LOUGHBOROUGH UNIVERSITY

ENHANCED GRADIENT CRYSTAL-PLASTICITY STUDY OF SIZE EFFECTS IN B.C.C. METAL

by

Murat Demiral

A Doctoral Thesis

Submitted in partial fulfilment of the requirements for the award of Doctor of Philosophy of Loughborough University

December 2012

ABSTRACT

Owing to continuous miniaturization, many modern high-technology applications such as medical and optical devices, thermal barrier coatings, electronics, micro- and nano-electro mechanical systems (MEMS and NEMS), gems industry and semiconductors increasingly use components with sizes down to a few micrometers and even smaller. Understanding their deformation mechanisms and assessing their mechanical performance help to achieve new insights or design new material systems with superior properties through controlled microstructure at the appropriate scales. However, a fundamental understanding of mechanical response in surface-dominated structures, different than their bulk behaviours, is still elusive.

In this thesis, the size effect in a single-crystal Ti alloy (Ti15V3Cr3Al3Sn) is investigated. To achieve this, nanoindentation and micropillar (with a square cross-section) compression tests were carried out in collaboration with Swiss Federal Laboratories for Materials Testing and Research (EMPA), Switzerland. Three-dimensional finite element models of compression and indentation with an implicit time-integration scheme incorporating a strain-gradient crystal-plasticity (SGCP) theory were developed to accurately represent deformation of the studied body-centered cubic metallic material. An appropriate hardening model was implemented to account for strain-hardening of the active slip systems, determined experimentally. The optimized set of parameters characterizing the deformation behaviour of Ti alloy was obtained based on a direct comparison of simulations and the experiments.

An enhanced model based on the SGCP theory (EMSGCP), accounting for an initial microstructure of samples in terms of different types of dislocations (statistically stored and geometrically necessary dislocations), was suggested and used in the numerical analysis. This meso-scale continuum theory bridges the gap between the discrete-dislocation dynamics theory, where simulations are performed at strain rates several orders of magnitude higher than those in experiments, and the

classical continuum-plasticity theory, which cannot explain the dependence of mechanical response on a specimen's size since there is no length scale in its constitutive description.

A case study was performed using a cylindrical pillar to examine, on the one hand, accuracy of the proposed EMSGCP theory and, on the other hand, its universality for different pillar geometries. An extensive numerical study of the size effect in micron-size pillars was also implemented. On the other hand, an anisotropic character of surface topographies around indents along different crystallographic orientations of single crystals obtained in numerical simulations was compared to experimental findings. The size effect in nano-indentation was studied numerically. The differences in the observed hardness values for various indenter types were investigated using the developed EMSGCP theory.

Keywords: Size effect; Micro-pillar-compression experiments; Nano-indentation experiments; Enhanced model of strain gradient crystal-plasticity theory; Ti alloy (Ti15V3Cr3Al3Sn); Geometrically necessary dislocations; Statistically stored dislocations

To my family and all my teachers

ACKNOWLEDGEMENTS

I would like to express my gratefulness and appreciation to Prof. Vadim V. Silberschmidt for guidance and insight in supervising the research, his invaluable help, and kindness. His knowledge, patience and understanding made possible the successful completion of the thesis. His sound advice, constructive criticisms and his ability to explain thing in a lucid manner shall always be remembered.

I would like to express my deepest gratitude and appreciation to my supervisor Dr Anish Roy, who inspired, encouraged and supported me for this study. He has helped me at various stages during my PhD studies and willingly sharing his knowledge and ideas with me. His active participation at every facet of my research work and mentoring has shaped my overall research outlook.

Many thanks to the members of Mechanics of Advanced Materials Research Group at Loughborough University, especially Dr Emrah Demirci, Mr Agostino Maurotto and Mr Riaz Muhammad, for their great support and invaluable friendship. My best wishes to Loughborough and Leicester Turkish communities for their strong fellowship and enthusiasm.

Special thanks to the Mr Kai Nowag from Swiss Federal Laboratories for Materials Testing and Research, Switzerland for his unique friendship and assistance in the performed experiments.

Funding from the European Union Seventh Framework Programme (FP7/2007-2013) during my study under grant agreement No. PITN-GA-2008-211536, project MaMiNa is gratefully acknowledged.

Finally, I would like to thank my wife, Selma, for her precious support, kindness, and being in my life with her endless love. I would like to appreciate my parents, Ömer & Seher Demiral, and my sister Fatma for their patience, love, encouragement and unique support during my studies. You are loved deeply.

PUBLICATIONS & CONFERENCES

Publications

A. Zahedi, M. Demiral, A. Roy, V. Babitsky, V.V. Silberschmidt. Indentation in fcc single crystals, *Solid State Phenomena*, Vol. 118, pp. 219-225, 2012.

M. Demiral, A. Roy, V. Silberschmidt. Repetitive indentation of Ti-based alloys: A numerical study, *IOP Conf. Series: Materials Science and Engineering*, Vol. 10 (012105), 2010.

Conferences

M. Demiral, A. Roy, V.V. Silberschmidt, Deformation mechanisms in advanced Ti-based alloy in indentation: Size effects, *10th world congress on Computational Mechanics (WCCM 2012)*, Sao Paulo, BRAZIL, 8-13 July 2012.

A. Zahedi, M. Demiral, A. Roy, V. Babitsky, V.V. Silberschmidt. Indentation in fcc single crystals, Timisoara, ROMANIA, 27-28 October 2011.

M. Demiral, A. Zahedi, A. Roy, V. V. Silberschmidt, Deformation mechanisms of advanced Ti-based alloy in nano-scale: A numerical study based on experiments, *2nd International Conference on Material Modelling*, Paris, FRANCE, 31 August - 2 September 2011.

M. Demiral, A. Roy, V.V. Silberschmidt, Deformation mechanisms of an advanced Ti-based alloy in indentation, *21th International Workshop on Computational Mechanics of Materials (IWCMM21)*, Limerick, IRELAND, 21-24 August 2011.

NOMENCLATURE

CHAPTER 2

A	Resulting imprint area
A_{proj}	Projected area for a spherical indenter
b	Burgers vector
C	Curvature of the loading
d	Grain size
E_{i}, E_{s}	Young`s modulus of the indenter and the specimen
E_r	Reduced modulus
H	The average contact pressure or hardness
H_0	Hardness in the limit of infinite depth
h^*	Characteristic length
h	Indentation depth
h_{c}	Contact depth
h_{f}	Residual depth after complete unloading
$h_{\mathrm{max}}, h_{\mathrm{m}}$	Displacement at the peak load
k	Hall-Petch slope
k_s	Source-hardening rate
l	Intrinsic material length-scale parameter
P	Load
P_{max}	Peak load
$(\frac{dP}{dh})_{h_{\mathrm{m}}}$	Stiffness measured from the unloading indentation curve at h_{m}
R	Radius of the spherical indenter
v_{i}, v_{s}	Poisson`s ratios of the indenter and the specimen
W_{e}	Elastic work
W_{p}	Plastic work
W_{t}	Total work done by loading
$\sigma_{0.08}$	Compressive stress of the material at a representative strain of approximately 8%
σ_Y, Y	Yield strength
σ_0	Friction stress
σ'_{ij}	Deviatoric part of the Cauchy stress
τ_s	Average source strength
τ'_{ijk}	Deviatoric part of Cauchy stress
ε_{g}	Geometrical parameter
μ	Shear modulus
λ	Average source length
θ	Angle of the indenter
β	Correction factor
δw	Work increment per unit volume

$\delta\varepsilon_{ij}$	Variation of strain
$\delta\eta_{ijk}$	Variation of strain gradient

CHAPTER 3-7

a, b, c	Lattice axial length
$\boldsymbol{B}$	Strain matrix
b	The magnitude of Burgers vector
$\boldsymbol{b}, \boldsymbol{g}$	Body and surface forces
$\boldsymbol{C}$	Tensor of elastic moduli
$\boldsymbol{d^e}$	Nodal displacement in the element e
$\boldsymbol{D}$	Symmetric parts of the $\boldsymbol{L}$
$f_{\alpha\beta}$	Magnitude of strength of a particular slip interaction
$\boldsymbol{F}$	Deformation gradient
$\boldsymbol{F^e}$	Deformation gradient for elastic stretching
$\boldsymbol{F^p}$	Deformation gradient for plastic stretching
$\boldsymbol{F^R}$	Deformation gradient for rigid body rotation of the lattice
f_{ext}	External forces
G	Interactive (cross) hardening that occurs between slip systems during the second and third stage of hardening
$g_T^\alpha \mid_{t=0}$	Incipient strength of slip systems
g^α	is the strength of each slip system α
h_s	Hardening modulus for the stage-I hardening
$h_{\alpha\beta}$	Slip hardening moduli
h_0	Initial hardening modulus
$\boldsymbol{I}$	Second-order identical tensor
$\boldsymbol{J}$	Jacobian, determinant of deformation gradient
k^e	Stiffness of the element e
l_{c}	Critical edge length of pillar
$\boldsymbol{L}$	Spatial velocity gradient
$\boldsymbol{N}(\boldsymbol{x})$	Shape function
$\boldsymbol{m}$	Slip-plane normal
NSLPTL	Total number of slip systems
n_G^α	Effective density of GNDs for slip system α
n	Rate sensitivity of the crystal
$\boldsymbol{P}$	First Piola-Kirchhoff (P-K) stress tensor
q	Latent to the self-hardening ratio
$\boldsymbol{R}$	Orthogonal rotation tensor
R	Reference, material or Lagrangean configuration
$r(d)$	Residual function
S	Current, spatial or Eulerian approach
$\boldsymbol{s}$	Slip direction
$\boldsymbol{S}$	Second P-K stress tensor
$S, \bar{S}$	Surface and normalized surface of the pillar
$T_{N\min}$	Smallest period in the finite-element mesh,
$\boldsymbol{U}, \boldsymbol{V}$	Right and left stretch tensors

$V, \bar{V}$	Volume and normalized volume of the pillar
$\boldsymbol{W}$	Skew-symmetric parts of the $\boldsymbol{L}$
$W_{N\max}$	Highest natural frequency of the system
α, β, γ	Inter-axial angles
α_{T}	Taylor coefficient
σ	Applied stress, Cauchy stress
ϕ	Angle between tensile axis and slip plane
λ	Angle between tensile axis and slip direction
$\cos\phi\cos\lambda$	Schmid factor
$\emptyset_t$	Frechet-derivative
$\gamma, \dot{\gamma}^{\alpha}$	Total plastic shear, plastic shear rate on slip system α
$\otimes$	Matrix product or the dyad of two vectors
dV	Deformed volume
$\boldsymbol{\tau}$	Kirchoff stress tensor
$\dot{\boldsymbol{F}}$	Time derivative of deformation gradient
$\dot{\boldsymbol{E}}$	Green-Lagrange strain tensor
$\hat{\dot{\boldsymbol{\sigma}}}$	Jaumann rate of the Cauchy stress
$\Delta\tau^{(\alpha)}, \Delta g^{(\alpha}$	Increments of resolved shear stress and current strength in slip system α
τ_0	Initial value of current strength of the slip systems
τ_s	Break-through stress
ρ_0, ρ	Mass density in the reference and current states
$\dot{\gamma_o}^{\alpha}$	Reference strain-rate on slip system α
$\mu_{ij}^{(\alpha)}$	Schmid factor
μ_s	Shear modulus
μ	Coefficient of friction
ξ, η, ρ	Isoparametric coordinates
$\boldsymbol{\nabla}_{\psi}$	Nabla operator relative to the isoparametric coordinate system
$\widetilde{\boldsymbol{b}}_k$	Unit vectors of dislocations k
$\widetilde{\boldsymbol{P}}^{\mathrm{T}}$	is the Mandel stress
$\widetilde{\boldsymbol{A}}$	Dislocation density tensor
$\tilde{\boldsymbol{\xi}}^{\boldsymbol{\alpha}}$	Projected density force
$n_{\odot}^{\alpha}$ and $n_{\vdash}^{\alpha}$	Densities of screw and edge dislocations
ξ_1	Correction factor accounting for the misalignment
ρ_s	Density of statistically stored dislocations (SSDs)
ρ_G	Density of geometrically necessary dislocations (GNDs)
$\rho_S\|_{t=0}$	Incipient density of SSDs
$\rho_G\|_{t=0}$	Incipient density of GNDs
$\nabla\gamma^{\beta}$	Shear strain gradient for slip system β
Ω	Domain of continuum and represents the traction boundary conditions
Γ	The traction boundary conditions
Δt_{cr}	Critical time step

CONTENTS

LIST OF FIGURES

LIST OF TABLES

Chapter I

1 Introduction

1.1 Motivation

Owing to continuous miniaturization, modern high-technology applications such as medical and optical devices, thermal barrier coatings, electronics, micro- and nano-electro mechanical systems (MEMS, NEMS), gems industry and semiconductors increasingly use components with sizes down to a few micrometers and even smaller. Recent advances in experimental characterization methods such as high-resolution load-displacement sensors and actuators, and micro-fabrication techniques as well as developments in computational capabilities assist exploration of material properties with decreasing sample dimensions, where (Stelmashenko *et al.*, 1993; McElhaney *et al.*, 1998; Greer and De Hosson, 2011). Understanding deformation mechanisms and assessing mechanical performance at micron and sub-micron scales provide insight helping to achieve or design new material systems with superior properties through controlled microstructure at the appropriate scales as an alternative to traditional strengthening techniques such as solution strengthening, cold working or alloying (Figure 1-1). Furthermore,

understanding the interaction between the mentioned extrinsic size effect and intrinsic size effect, i.e. strengthening due to microstructural constraints such as grain-size and second-phase particles [Zhu et al., 2008], contributes to enhancement in materials performance and sheds light on their design constraints.

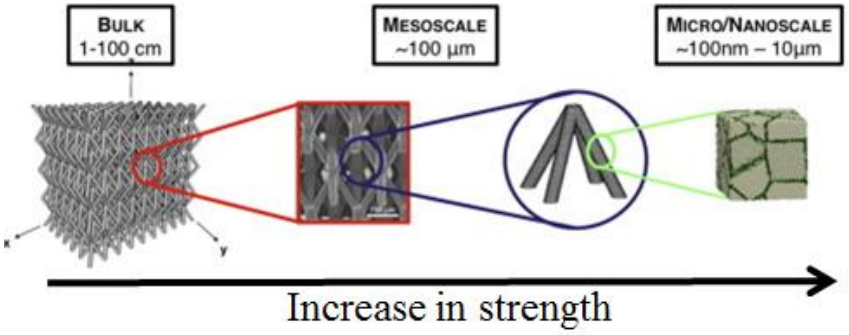

Figure 1-1: Micro-truss structure depicted at different length scales demonstrating concept of "architected" material. Reprinted with permission from (Jacobsen *et al*., 2007)

1.2 Goal and objectives

The goal of this research is to further the understanding of size effect in single-crystal base-centered-cubic (b.c.c.) Ti alloy, Ti15V3Cr3Al3Sn (Ti-15-3-3-3), experimentally and numerically, employing a non-local crystal-plasticity theory. To achieve the aim of the project, its major objectives are formulated in the following way:

- To investigate the size effects due to dimensional constraints, i.e. extrinsic size effect, in Ti alloy using micro-pillar-compression and nano-indentation experiments;
- To develop multi-scale continuum numerical models incorporating strain-gradient constitutive laws representing the mechanical performance of the Ti alloy in above mentioned tests. In connection with this to obtain an accurate description of local fields of strains and stresses inside the samples that is not possible to achieve in the experiments;

- To investigate the applicability of different continuum-plasticity theories such as classical plasticity, crystal-plasticity and strain gradient crystal-plasticity, at different length scales.

1.3 Methodology

This research employs a combined experimental and numerical study to describe the size effect in the material under investigation, Ti-15-3-3-3. To achieve this, several experimental and computational procedures described below were followed. This methodology is also described in a block diagram in Figure 1-2.

Initially, micro-pillars of Ti-15-3-3-3 with a square cross section of different dimensions were produced at EMPA, Switzerland using a focused-ion-beam (FIB) technique. To eliminate the influence of crystallographic orientation of the crystal, all pillars were produced from the same grain. In-parallel, nano-indentation tests for different crystal orientations were performed in the same alloy. Both experiments were implemented using quasi-static loading regimes.

As the material under investigation had a crystalline structure, a crystal-plasticity (CP) theory was planned to be used in numerical analysis. However, the classical continuum-plasticity theory cannot explain the dependence of mechanical response on size as no length scale enters the constitutive description. Discrete-dislocation dynamics (DDD) models are capable of modelling the size effect. However, it is still not possible with the current computational resources to perform those simulations on a realistic time scale and real-life structures; hence, they are necessarily performed at strain-rates several orders of magnitude higher than those in experiments. A multi-scale continuum theory, therefore, is needed to bridge the gap described above. The plasticity theories with gradient approaches have been successful in addressing the size-effect problem due to incorporation of a microstructural length-scale parameter in the governing equations of the deformation description. The strain gradient crystal-plasticity (SGCP) theory as well as its enhanced model is therefore used in numerical analysis within the framework of finite-element method (FEM).

The methodology followed in this thesis (Figure 1-2) can be described briefly as follows. Through multiple trial runs, material parameters of the studied single-crystal Ti alloy were determined by calibrating the developed FE models with the performed micro-pillar compression and nano-indentation experiments. Using the optimized set of material parameters, case studies were performed to verify the models. Ultimately, a thorough numerical investigation of size effects was implemented for each experiment separately.

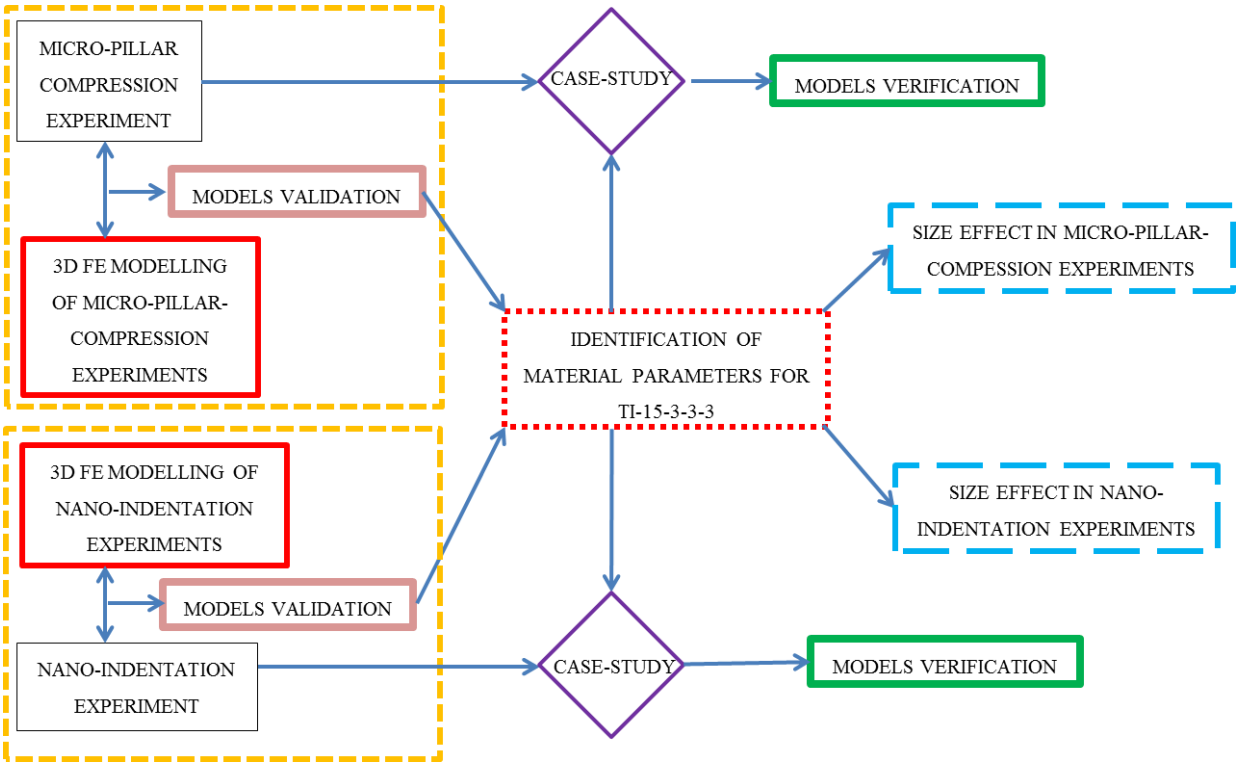

Figure 1-2: Research methodology used to describe size effects in micro-pillar-compression and nano-indentation experiments

Chapter II

2 Size effect in micro-pillar-compression and nano-indentation experiments

This chapter review pillar-compression and indentation experiments with regard to a size effect. In the first part of this chapter introductory information about the main aspects of size effect and the fundamentals of the mentioned experimental setups are given. A critical review about the observed size effects in pillar-compression and indentation experiments is given in the second and third parts of this chapter, respectively where the performed experiments and numerical analysis are documented extensively.

2.1 Introduction

Numerous experimental and numerical studies demonstrated that the strength of a material or plastic deformation at the micron or sub-micron scales is dramatically

different than that of macro-scale. This pronounced size effect have been observed in torsion (Fleck *et al*., 1994), bending (Stölken and Evans, 1998), indentation (Stelmashenko *et al*., 1993; McElhaney *et al*., 1998) and pillar-compression (Greer *et al*., 2005; Uchic *et al*., 2004) experiments. Size effects can be separated into two groups - "intrinsic" and "extrinsic". What is meant by intrinsic size effects is strengthening due to microstructural constraints such as grain size and second-phase particles (Zhu *et al*., 2008). On the other hand, extrinsic size effects arise from dimensional constraints due to a sample size. Although the intrinsic size effect has been studied by materials science community for more than a century, the extrinsic size effect was discovered in the last two decades and there is no full agreement about it, hence it is currently a topic of rigorous investigations. Understanding of interaction between these two size effects is beyond the scientific curiosity as elucidating the interplay between the microstructural and geometrical constraints can contribute to enhancement of materials performance and shed light on their design constraints.

The intrinsic size effects can be controlled by means of processing steps in material's production. Its quantification depends on the characteristic length scale of a particular microstructure, such as grain or precipitate size, twin-boundary spacing and dislocation density. This microstructural size governs mechanical properties and a plastic behaviour of the material at all dimensions; hence, its value does not depend on the size of the specimen (Greer and De Hosson, 2011). The grain size has long been known to have a significant effect on the mechanical behaviour of polycrystalline materials and metallic glasses. Hall (1951) and Petch (1953) experimentally justified that yield strength of iron changes inversely with the square root of grain size d and expressed this relation with the following universal equation:

$$\sigma_Y = \sigma_0 + k/\sqrt{d}, \qquad 2\text{-}1$$

where σ_0 is termed the friction stress and k is the Hall-Petch slope as a material constant. In polycrystalline materials, the interaction between defects and grain

boundaries is significant as a consequence of misorientation between grains. Grain boundaries act as pinning points impeding further dislocation propagation, i.e. resist to plastic deformation. This explains the physical mechanism of equation 2-1. The smaller the grains in polycrystalline sample, the larger the density of grain boundaries; hence, more energy is needed to move the dislocations. However, the Hall-Petch relation is valid for polycrystals down to the grain size of around 40 nm. When the grains are reduced to 40 nm, alternative plastic deformation mechanisms like grain-boundary sliding, partial dislocation emission and absorption at grain boundaries become important (Ke *et al.*, 1995; Van Swygenhoven and Derlet, 2001). At grain sizes below 20 nm, the inverse Hall-Petch relation manifested and attributed to diffusional creep in nano-crystalline samples (Chokshi *et al.*, 1989). Other researchers related this behaviour to grain-boundary sliding (Schiøtz *et al.*, 1999), individual dislocation motion (Louchet *et al.*, 2006) and atomic structure differences between grain boundary and inside the grain (Takeuchi, 2001). Figure 2 summarizes the yield stress-grain size relation for copper polycrystals from different studies. The general tendency of the curves indicates that an inverse Hall-Petch relation is valid in the region where the grain size is smaller than 25 nm ($\frac{1}{\sqrt{d}} = 0.2\ \mathrm{nm}^{-1}$), while beyond this size there exists a Hall-Petch relation.

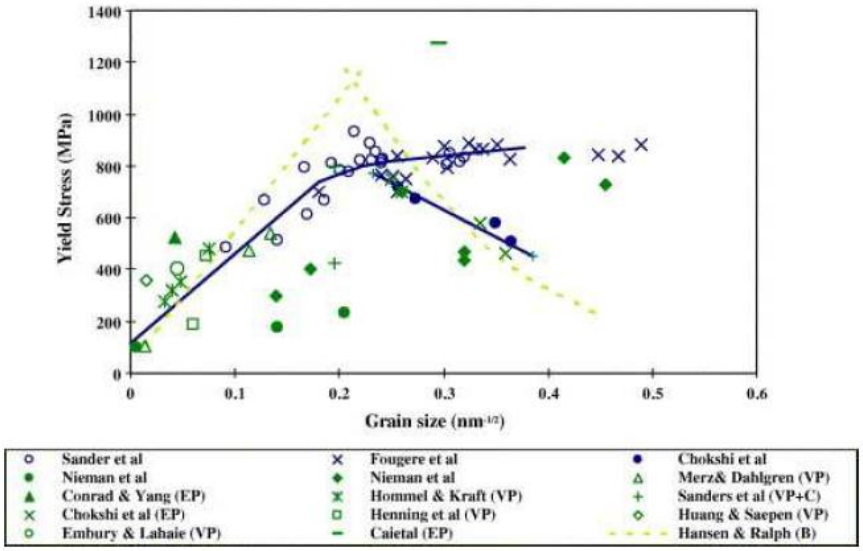

Figure 2-1: Yield stress versus grain size plot for Cu polycrystals from different studies. Reprinted with permission from (Meyers *et al.*, 2006)

In addition to grain-size-dependent plasticity, an extrinsic size effect has been reported in the last two decades. According to it, material strength scales inversely with sample dimensions such as diameter of micro- or nano-pillar or thin film thickness due to defect interaction with a free surface (Greer and De Hosson, 2011). Similarly, various indentation experiments performed by different research groups revealed that there exists a very strong relationship between material properties, such as hardness and indentation depth, i.e. a size of indentation (Stelmashenko *et al*., 1993; McElhaney *et al*., 1998; Ma and Clarke, 1995; Nix and Gao, 1998).

A single-crystal or monocrystalline solid is a material where the crystal lattice of the entire sample is continuous, without grain boundaries. The absence of defects associated with grain boundaries can give monocrystals unique mechanical, optical and electrical properties. On the other hand, in a polycrystalline material owing to misorientation of its grains, a collective behaviour of constitutive grains defines its performance, i.e. the macroscopic polygrain structure possesses almost isotropic properties. Figure 2-2 demonstrates the electron-back-scatter diffraction (EBSD) map of the polycrystalline surface of a Ti-alloy (Ti15V3Cr3Al3Sn) with an inserted inverse pole figure. In this figure two grains with different orientation and grain boundary are shown. Different colours for various grains represent the orientations shown in the inverse pole figure.

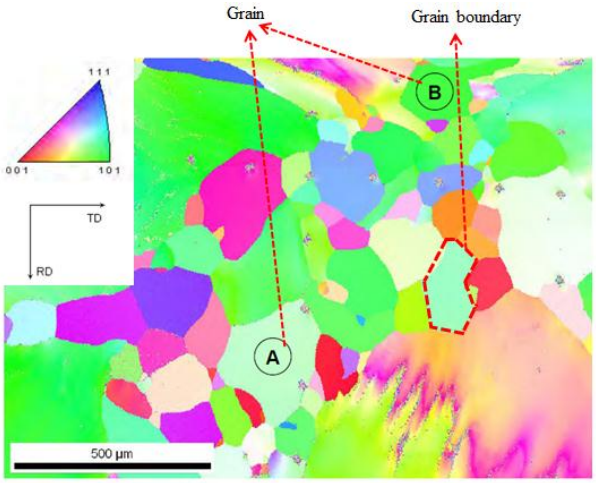

Figure 2-2: EBSD scan of the surface of the Ti 15-3-3-3 sample with the corresponding pole figure.

Single-crystal materials with their unique anisotropic properties have many different application areas. They are particularly used in optics, electronics, micro- and nano-electro mechanical systems, gems industry and semiconductors. The precise fabrication and reliable operation of single-crystal components at micron- or nano scale entails the exploration of their mechanical properties with a decreasing sample size as material behaviour diverge from that of the bulk material. Indentation and pillar-compression experiments are two experiments commonly used to assess the mechanical performance of materials at small scales. In indentation experiments plastic deformation induced by small loads and a nano-indenter tips is confined within a very small volume, which, in turn, leads to formation of non-uniform stresses and strains within the sample tested resulting in strong strain gradients (Figure 2-3). The observed size effect in indentation is ascribed to inherent gross gradients in strains (Abu Al-Rub, 2007). On the other hand, pillar-compression experiment can be considered as an extension of indentation, in which the indenter tip compresses the whole pillar in axial direction (Figure 2-3). In contrast to indentation experiment, deformation is applied homogeneously in this technique. However, deformation develops in an inhomogeneous manner from the onset of deformation and is confined to discrete slip bands (Maass *et al*., 2008; Zhang and Aifantis, 2011; Maass *et al*., 2007; Horstemeyer *et al*., 2001; Maass *et al*., 2007). This experiment therefore can be considered as macroscopically homogenous, but microscopically heterogeneous. Different explanation of size effects in pillar-compression experiment exist.

Indentation experiments are extensively used to characterize local deformations at various length scales and to identify material properties such as Young's modulus and hardness, based on the experimentally determined loading - unloading curves. However, interpretation of material properties such as yield stress or work-hardening rate (WHR) remains difficult owing to imposed gross strain gradients. On the other hand, relative experimental simplicity and minimal requirements for sample preparation assists ubiquitous use of indentation. Indentation can be performed several times on a single specimen and can be used to probe different volumes of materials (Gouldstone *et al*., 2007). Pillar-compression experiments are

performed without strain gradients at the macroscopic scale qualifying this method to attain critical parameters of pillars studied. The intrinsic complexity of the experiment such as precise fabrication of pillars without significant damage and performing the experiment with a perfect alignment of pillar and indenter tip entails a qualified person to carry out it.

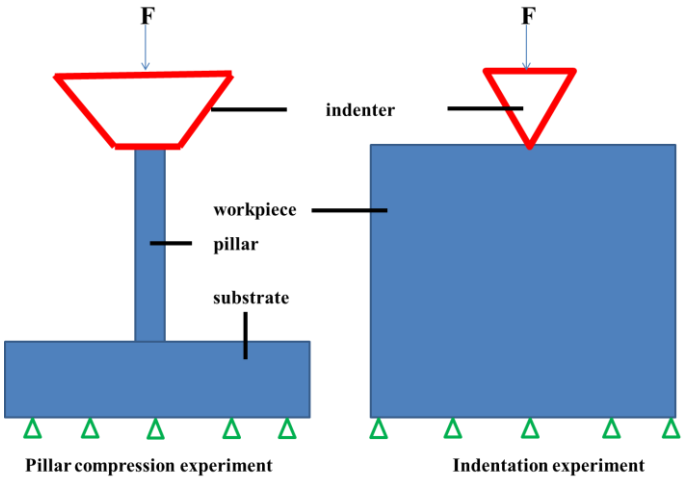

Figure 2-3: The schematic of pillar-compression (a) and nano-indentation (b) experiments

In this thesis the size effects in a single-crystal Ti alloy is explained with the aforementioned material characterization techniques, viz. pillar-compression and indentation. It is worth to mentioning that as the size of pillars considered in this study ranges from 1 μm to 32 μm, pillar-compression technique henceforth is referred as micro-pillar-compression experiment. On the other hand, indentation experiments are referred as nano-indentation since they are performed with indentation depths of up to 400 nm. In the next section, a detailed overview for both techniques in the context of size effects is given.

2.2 Micro-pillar-compression experiment

Investigations into the size-dependence of single-crystals can be traced back to mid- 20th century. However, these first experiments were performed partially for metal whiskers without any dislocations. In 1952, the study of Herring and Galt revealed that measured tensile strength of tin (Sn) whiskers (filamentary crystals

with diameter of a few micrometers) are likely to approach theoretical values for a perfect Sn lattice (Herring and Galt, 1952; Shan *et al*., 2008). Later Brenner reported that dislocation-free metal whiskers yielded at higher stress with smaller diameters (1956). Since then, the change in mechanical properties of crystalline materials with a size became the subject of numerous experimental studies (Brenner, 1958) and scientific discussions (Nix, 1989; Nix, 1998). Among the earliest works to explore the effect of dimensional constraint on mechanical behaviour, Suzuki *et al*. (1956) and Fourie (1967) studied a size effect in single-crystals of Cu. In the first study the extension of stage-I glide to higher strains with a decrease in the size of Cu single-crystals was reported, whereas critical resolved shear stress and work-hardening rate remained constant. In the second study it was observed that a stage-2 work-hardening rate dropped sharply when the size of Cu single-crystals decreased from 270 μm to 50 μm.

Several years ago, Uchic and co-workers (Uchic *et al*., 2004) developed a testing methodology to measure the flow behaviour of miniature samples in compression. In this technique micro-scale cylindrical samples fabricated using a focused-ion-beam (FIB) milling technique (Figure 2-4 (a)) were uniaxially compressed by nanoindentation system equipped with a flat punch (Uchic and Dimiduk, 2005; Uchic *et al*., 2009). This method was specifically designed to probe mechanical properties intrinsic to the material as a function of the decreasing sample size. Later this technique was extended by Greer *et al*. (2005) to perform uniaxial compression tests on Au nano-pillars with diameters less than those of studied in Uchic *et al* (2004).

The recent advances in the compression experimental setup enable to probe the size-dependent mechanical performance of materials in smaller dimensions. For instance Uchic *et al*. (2004) tested three different materials with a size from 1 to 40 μm: Ni, Ni3Al-1%Ta and a Ni-based super alloy with an (269) orientation. These experiments showed an increase in the strength of crystals up to 15 times compared to bulk Ni with a decrease in the sample size. However, no significant increase in the work-hardening rate of the crystals was observed. It was also reported that

frequent strain bursts, avalanches of dislocations, and increased finite discrete slip bands along the gauge length of the crystal were observed when the crystal size became smaller. In contrast to the smooth stress-strain curve obtained during compression of a bulk material, the stress-strain curves of small-sized pillars contain several discrete strain bursts, where strain jumps discontinuously to an increased value while the stress value remains constant or decreases. Figure 2-5 demonstrates typical strain bursts, more frequent in small-size pillars, observed in stress-strain curve of f.c.c. nano pillars. The group of Nix and Greer (2006) performed similar tests on (001) oriented Au crystals with dimensions of less than 1 μm. This study showed a trend of an increase in the strength of the pillar with a decrease in its size. It was also revealed that the flow-stress value of as high as 800 MPa was observed in the compression of 200 nm Au specimens, which is extraordinarily high compared to its bulk counterpart with corresponding value around 25 MPa at 10% strain.

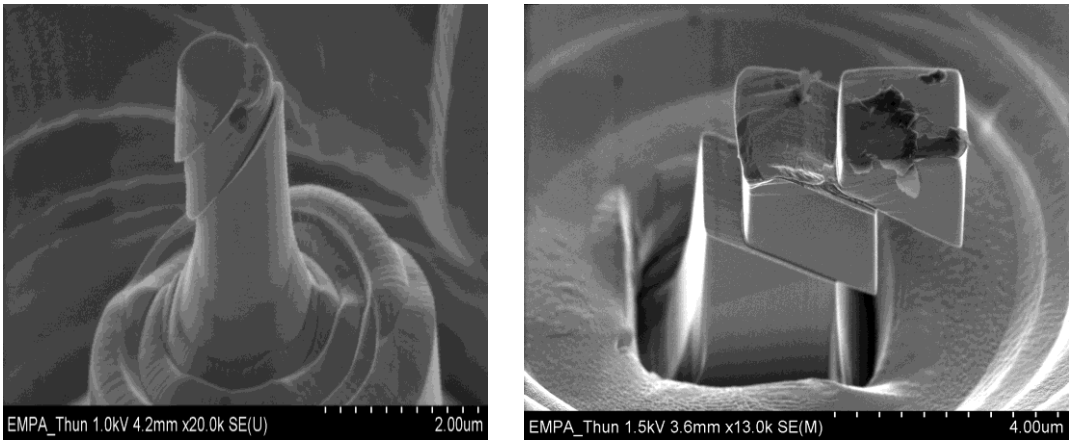

Figure 2-4: SEM images showing Ti-15-333 single-crystal micro-pillars with circular (a) and square (b) cross sections after compression

Due to the absence of commercial in-situ mechanical testing equipment and the challenge associated with sample preparation (dog-bone shape) in tensile test, mostly a compressive behaviour of materials at the micron and sub-micron scales have been reported. Recently, Kiener *et al*. (2009) reported a new method to measure tensile behaviour of single-crystals at the micro- and nano scales using the samples fabricated with FIB. The mechanical test was performed inside a scanning

electron microscope (SEM) and a transmission electron microscope (TEM). In this experiment, f.c.c. single-crystal Cu samples with diameters ranging from 500 nm to 8 μm and an aspect ratio from 1 to 13.5 were tested. This study revealed the presence of a size effect, which strongly depended on the sample's aspect ratio; however, the reported size effect was less pronounced than its compression counterpart. It was reported that size-dependent hardening was linked to dislocation pile-ups due to their constrained glide in the sample. Jennings and Greer (2010) performed in-situ tensile-deformation test with [111] oriented single-crystal Cu nano-pillars with diameters ranging from 75 nm to 165 nm fabricated by e-beam lithography and electroplating. A power-law relationship between strength and diameter of nano-pillar was reported similar to that for fabricated by FIB machining. In this study the inhomogeneous deformation is explained by annihilation of dislocations at free surfaces of the pillar.

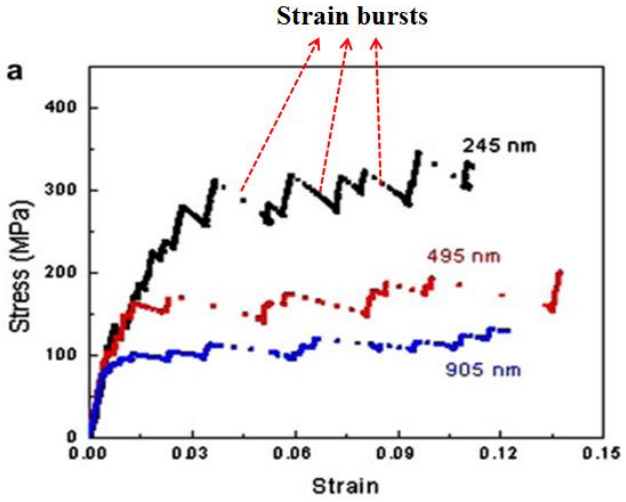

Figure 2-5: Typical stress-strain curves in compression of Au pillars with various diameters. Reprinted with permission from (Kim and Greer, 2009)

Brinckmann *et al*. (2008) did a comparative experimental study of face-centered cubic (f.c.c.) Au crystals and body-centered cubic (b.c.c.) Mo crystals at nanoscale. This study showed that Au specimens reached 44% of its theoretical strength but no strain-hardening was observed, whereas Mo specimens reached only 7% of its ideal strength but showed strain-hardening. The difference is ascribed to differences in dislocation behaviour during deformation: Dislocation starvation is

the predominant mechanism in nano scale f.c.c. crystals while junction formation and hardening characterize the plasticity in b.c.c. crystals.

Most of the reports explaining the size effects are focused on f.c.c. structures, with only several recent studies on b.c.c. crystalline pillars, due to lower complexity of internal microstructures of f.c.c. In the next part deformation mechanisms and detailed studies for these two crystal structures are explained. The relevant reviews for more complex microstructures such as non-cubic single-crystals hexagonal close-packed (Lilleodden, 2010; Sun *et al*., 2011) and tetragonal (Lee *et al*., 2010; Lee *et al*., 2011), shape memory alloys (Clark *et al*., 2010; Frick *et al*., 2007; Frick *et al*., 2008), nano-crystalline metals (Yamakov *et al*., 2002; Van Swygenhoven *et al*., 2002), nano-laminate composites (Mara *et al*., 2008) and metallic glasses (Telford, 2004) are not discussed in this thesis due to space limitations. The reader is referred to respective references and the references therein.

2.2.1 Face-centered cubic metals

Different deformation mechanisms have been interpreted for the nano- and micron-size f.c.c. pillars. Among the proposed theories "hardening by dislocation starvation" is the mostly accepted one to explain the size effects in f.c.c. nano-pillars (Frick *et al*., 2008) . The basic premise of the theory is as follows: Owing to smaller dimensions of the nano-size pillars the dislocations present at the onset of plastic deformation leave the specimen before they multiply. Having reached this "dislocation starvation" state, new dislocations are necessarily nucleated both at the sample surface and in the bulk of the crystal in the course of deformation since the movement of dislocations is required for a compatible plastic deformation. As the nucleation of these new dislocations requires high stresses approaching near-theoretical strength, the strength of nano-size pillars is observed to increase with decreasing sample size. This theory appears to be in good agreement with in-situ TEM performed by Shan *et al*. (2008). Figure 2-6 (a) demonstrates the FIB micro-fabricated (111) Ni pillar with 160 nm of diameter in this study. It is apparent that there is a high initial dislocation density in the pillar. However, the pre-existing dislocations progressively left the pillar during the initial compression stage, and a

completely dislocation-free pillar was ultimately obtained (Figure 2-6 (b)). Computational atomistic simulations performed by different research groups also justify this theory (Rabkin *et al*., 2007; Tang *et al*., 2007; Deshpande *et al*., 2005).

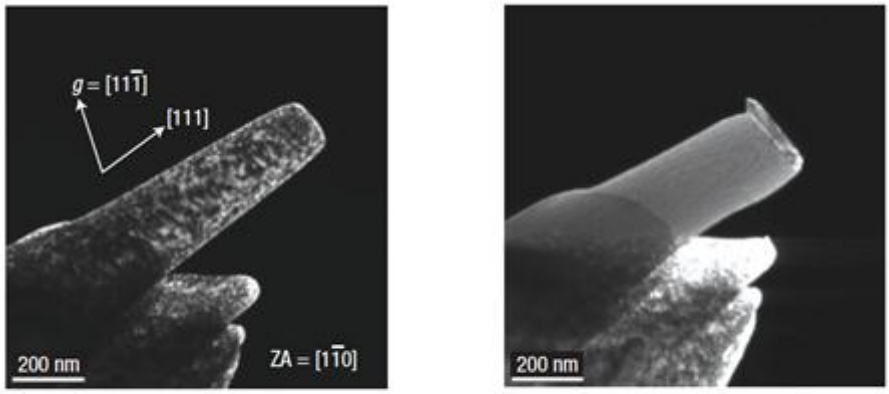

Figure 2-6: Dark-field TEM image of Ni pillar before tests (a) and after first compression (b). Reprinted with permission from (Shan *et al*., 2008)

The prominent deformation mechanism for the micron-sized pillars (larger than 500 nm-1000 nm) is the single-arm source theory proposed and developed by Parthasarathy *et al*. (2007) and Rao *et al*. (2008). In this theory, creation of dislocations occurs as a result of operation of partial Frank-Read sources or truncated sources also known as single-arm sources. This theory suggests that a random distribution of dislocation sources either exists initially in pillars or generated by interaction of initially present dislocations and the average source strength (τ_s) is related with the average source length (λ) by the following equation:

$$\tau_s = k_s \mu \frac{\ln(\lambda/b)}{(\lambda/b)}, \qquad 2\text{-}2$$

where k_s is a source-hardening rate, μ is the shear modulus and b is the Burgers vector. According to this equation, with a decrease in the diameter of pillar, the source length becomes smaller, hence overall strength increases. Ng and Nyan (2009) studied a size effect of Al micro-pillars with diameters changing from 1.2 micron to 6 micron either coated or center-filled with a tungsten-based compound.

A higher strain-hardening rate and a much smoother stress-strain curve suggest suppression of dislocation avalanches and a lack of nucleation-controlled plasticity. The TEM analysis reveals higher dislocation densities in the post-deformed specimens confirming the trapping of the dislocations inside the micro-pillars rather than annihilating at the free surface in contrast to nano-sized pillars (Greer and De Hosson, 2011).

Maass and co-workers studied the role of strain gradients on the plastic deformation of micron-size f.c.c. pillars using a synchrotron micro-diffraction technique (Maass *et al*., 2007; 2008; 2009). These studies demonstrate that geometrically necessary dislocations (GNDs) are generated during the deformation process leading to strain gradients. GNDs are the extra storage of dislocations required to accommodate the lattice curvature that arises in the presence of non-uniform plastic deformation (Gao and Huang, 2003). Section 2.3.2 provides further discussion of GNDs. The assumed dislocation starvation theory, therefore, is not applicable to micron-size pillars since it is impossible to squeeze all dislocations to the surface of the pillar. Likewise, Guruprasad and Benzerga (2008) argued that although the deformation in a pillar-compression test is macroscopically homogenous, it is heterogeneous microscopically, i.e. GNDs vanish macroscopically but present locally. Akarapu *et al*. (2010) numerically demonstrated that the deformation is heterogeneous from the onset of deformation and is confined to the discrete slip bands. On the other hand, SEM images of micron-sized pillars taken after the compression in (Dimiduk *et al*., 2005; Ng and Ngan, 2008) suggest that deformation evolves in an in-homogenous manner, though it is applied homogeneously as the end regions of the pillars appear non-deformed while the sample center is sheared by multiple slip zones (Zhang and Aifantis, 2011).

The FIB technique is the most prevalent method for producing small-size pillars to investigate the influence of sample's dimensions on mechanical properties. In this method Ga^{+} ions are bombarded and implanted to fabricate the pillars (Bei *et al*., 2007; Zhang and Aifantis, 2011; Hurtado and Ortiz, 2012). This process inevitably

introduces surface dislocation loops, and precipitates also instigate surface amorphization. The presence of FIB-induced defects led several researchers to infer that the fabrication process may play a significant role in the observed size effects. On the one hand, Bei *et al*. (2007) proposed that increasing strength of pillars with a decrease in the pillar size would be a consequence of the increased volume fraction of a FIB-damaged layer with a decreasing pillar diameter. But Kiener *et al*. (2007) investigated the Ga^+ ion-induced damage with TEM and Monte Carlo simulations, where a non-negligible influence of the ion damage in the order of 100 MPa (assuming Taylor hardening) was reported for submicron-sized samples. In order to understand the importance of fabrication technique on the size effects, Jennings *et al*. (2010) developed a FIB-less method to produce nanopillars. In this method arrays of vertically oriented gold and copper nanopillars are created based on patterning polymethylmethacrylate by electron beam lithography and subsequent electroplating into the prescribed template. In this technique the pillars are produced intentionally with non-zero dislocation densities to compare and contrast them with the pillars produced with the FIB method; otherwise the pillars without dislocations would render theoretical strengths regardless of size. This study demonstrated that nano-size pillars created without any Ga^+ bombardment and containing initial dislocations with density comparable with that for pillars created with Ga^+ bombardment exhibit an identical size effect with the pillars produced with the FIB method. This study evidently suggests that the observed size effect in small-size pillars is a function of microstructure rather than the fabrication technique.

2.2.2 Body-centered cubic structures

Experimental and computational studies of compression of single-crystal Mo nano-pillars showed that the deformation mechanism in b.c.c. nano-pillars is fundamentally different from that of f.c.c. nano-pillars (Kim *et al*., 2010). Brinckmann *et al*. (2008) reported a comparison of uniaxial compression results for Mo and Au nano-pillars. This study revealed that both methods provided different deformation mechanism. Especially, size-dependent strengths, stochastic discrete

bursts in their stress-strain curves, fractions of attained theoretical strength as well as extents of strengthening were different. These discrepancies were attributed to profound differences in the plasticity mechanisms of f.c.c. and b.c.c. metals as also confirmed by atomistic simulations (Greer *et al*., 2008). In b.c.c. metals, the screw components of a dislocation loop are not restricted to glide any particular single plane and can also cross-slip on any other favourable crystallographic plane during shearing of the crystal, whereas the edge components glide on a specific plane. The reason for the differences is attributed to dissimilar mobilities of dislocation components: In b.c.c. metals mobility of screw dislocations is estimated at around one fortieth of the motion of edge dislocations. The dislocations in b.c.c. nano-pillars, therefore, are likely to have a higher residence time inside a pillar rather than leaving it, significantly increasing the probability of individual dislocation interaction, multiplication of dislocations and formation of junctions, which, in turn lead to new dislocation sources (Kim *et al*., 2010). As the junction size is proportional to size of the pillars, the junctions are shorter for small-size b.c.c. pillars. It is therefore harder to break through the gliding mobile dislocations leading to an increase in strength of the pillar. On the other hand, as the increase in temperature greatly increases mobility of screw dislocations, the number of formed junctions is reduced requiring nucleation of new dislocations. The size effect, therefore, in b.c.c. metals would be expected to become closer to f.c.c. metals at higher temperatures. However, the b.c.c. pillars never become dislocation starved as in the f.c.c. nano-pillars, instead complex networks of short dislocation segments are formed (Greer *et al*., 2008). This is also consistent with molecular-dynamics (MD) and dislocations-dynamics (DD) simulation of Weinberger and Cai (2008).

Kim and Greer (2009) reported size-dependent strengths of (001) oriented Mo nano-pillars in compression and tension. The observed higher flow-stresses are explained by an increase in yield strength rather than strain-hardening. It was also reported that the amount of strain-hardening under tension is much lower compared to that under compression demonstrating a tension-compression asymmetry. This observed asymmetry is attributed to the differences in the Peierls stress, i.e. lattice resistance to dislocation motion, in twinning and anti-twinning direction (Gröger *et*

al., 2008). It is worth mentioning that friction stress or intrinsic lattice resistance, accounting for the flow-stress indirectly related to dislocation activities, is negligibly small in f.c.c. metals but it is significant in b.c.c. metals (Nix, 1989; Narutani and Takamura, 1991; Beltz *et al*., 1996). In (Kim and Greer, 2009; 2010) TEM images of Mo nano-pillars with diameter of 100 nm before and after the deformation were analyzed. The results indicate formation of an entangled dislocation substructure and justify differences in the deformation behaviour of f.c.c. and b.c.c. metals. The effect of crystal orientation on the tension-compression asymmetry of Mo nano-pillars was studied by Kim *et al*. (2009). It was shown that compressive flow-stresses are higher in (001) orientation and smaller in (011) orientation compared to tensile flow-stresses. This study revealed that tension-compression asymmetry was a function of size of the pillar for sizes less than 800 nm, whereas strength differential for larger pillars approaches size-independent bulk values (Greer and De Hosson, 2011).

The influence of applied strain-rate on the size effect in b.c.c. single-crystals was investigated by Kim and Greer (2010). Under a constant displacement rate the imposed strain-rate varied by around one order of magnitude between the largest and smallest Mo pillar that ranged from 200 nm to 800 nm. In this study, around 50% differential in the yield stress for the smallest and around 20% differential in the yield stress for the largest pillar were reported. This study revealed that the strain-rate had an influence on the observed size effects in nano-size pillars.

Kim and Greer (2010) also studied different b.c.c. metals in addition to Mo. The (011)-oriented single-crystal nano-size pillars of Ta, W, Nb and Mo were subjected to uniaxial compression and tension. This study demonstrated a power-law slope for size-dependent flow-stress of pillars. The corresponding slopes are -0.93 for Nb, -0.44 for W, Mo and Ta in compression and -0.80, -0.77, -0.58 and -0.43 for Ta, Nb, W and Mo in tension, respectively. The size-dependency of observed tension-compression asymmetry was also reported in this study. However, the authors did not observe any consistent correlation between the strain-hardening exponent and material type or size. That implies that strain-hardening is more likely to be a

function of the initial microstructure rather than the pillar size, whereas the yield and flow-stress fundamentally depends on the size of nano-pillar (Greer and De Hosson, 2011). On the other hand, the findings of Han *et al*. (2010) for b.c.c. V nano-pillars comply with the studies reported above.

The deformation mechanism in b.c.c. micron-sized pillars is similar to that in nano-sized pillars, unlike the different mechanism in f.c.c. nano- and micro-pillars. Therefore the mechanisms explained above for b.c.c. single-crystal nano-pillars can be generalized to micron-size pillars. The interpretation of deformation in micron-size pillars using a microscopic strain gradient concept owing to heterogeneous deformation occurring on discrete slip layers, as explained for f.c.c. metals in Section 2.2.1, can be extended for b.c.c. micron-scale single-crystals since the fundamental aspects of strain gradient theory is irrelevant of the crystal structure.

In summary, it is justified that in b.c.c. single-crystals a single dislocation can generate multiple new dislocations (Greer *et al*., 2008). Dislocation segments will further interact and form Frank-Read sources leading to an increase in dislocation density and requiring flow-stress due to inherent characteristic of screw dislocation gliding at different slip planes. It is worth mentioning that the hardening mechanism of b.c.c. single-crystals via entanglement of dislocation segments is similar to the forest-hardening model in bulk crystal-plasticity (Brinckmann *et al*., 2008).

Numerical modelling and simulations of pillar-compression experiment was performed by several teams. Among these works, Zhang *et al*. (2006) presented a parametric study of design of accurate pillar-compression experiments using 2D and 3D isotropic plasticity finite-element modeling. In these study geometric factors such as curvature at the bottom of the pillar connecting to the substrate, the aspect ratio and taper of the pillar, misalignment between indenter tip and pillar, material properties such as strain-hardening and strain-rate-sensitivity and plastic bucking phenomena were studied extensively. Schuster *et al*. (2008) followed this work and studied the effect of specimen taper on the compressive strength of metallic glass. On the other hand Chen *et al*. (2010) focused on local stress

concentration in metallic glass pillars using an isotropic plasticity model. Horstemeyer *et al*. (2001) performed atomistic simulations of plasticity via the embedded atom method (EAM) for single-crystal f.c.c. metals. The results of molecular-dynamics simulations indicated that plastic deformation was intrinsically inhomogeneous and the yield strength depended on the sample size, i.e. scaled inversely with the volume-to-surface area ratio, even in the absence of strain gradients. Raabe *et al*. (2007) used a crystal-plasticity FE model to investigate the influence of stability of the initial crystal orientation, aspect ratio and contact conditions between the indenter tip and pillar on anisotropy and changes in crystallographic orientation during the deformation. This study revealed that the evolution of orientation changes was in part due to shape inclination owing to buckling rather than crystallographic orientation solely. Shade *et al*. (2009) did a combined experimental and crystal-plasticity finite-element study to examine lateral constraint effects on compression of single-crystals. It was reported in this study that the degree of lateral constraint in a compression test system could influence the behaviour of the material tested. Finally, Zhang and Aifantis (2011) developed a strain gradient model for single-crystal Ni micro-pillars. In this study a higher-order strain gradient theory was used to capture the size effects and strain bursts that were experimentally observed in compression.

2.3 Indentation

An indentation test is one of the most commonly used experimental techniques to measure mechanical properties of small-size components as the conventional tensile tests are difficult to conduct at nano- or micro-scales. Another underlying reason for its ubiquitous use is its relative experimental simplicity and minimal requirements for sample preparation. Indentation can be performed several times on a single specimen and can be used to probe different volumes of materials (Gouldstone *et al*., 2007). Size effects in indentation have been reported by many authors (Stelmashenko *et al*., 1993; McElhaney *et al*., 1998; Ma and Clarke, 1995). It is interpreted as the increase in the hardness values of material with a decrease in the depth of indentation or a radius of the spherical indenter. A close relationship

exists between the observed size effect in indentation and the main features of the experiment. For instance, hardness of the indented specimen varies with respect to different types of indenter, contact conditions and surface profile of the indented surface besides the pronounced size effect. The main aspects of indentation therefore are described in the next section before starting to explain or interpret the size effects in micro- or nano-indentation.

2.3.1 Main aspects of indentation

In indentation a hard indenter with known mechanical properties is pushed into a test material and then withdrawn (Figure 2-7). The indentation load and the penetration depth into the material are simultaneously recorded, and a load-penetration depth curve is obtained (Figure 2-7). This curve contains a wealth of information relating to the deformation behaviour of materials and can be used to determine many mechanical properties such as hardness and an elastic modulus (Cheng and Cheng, 2004).

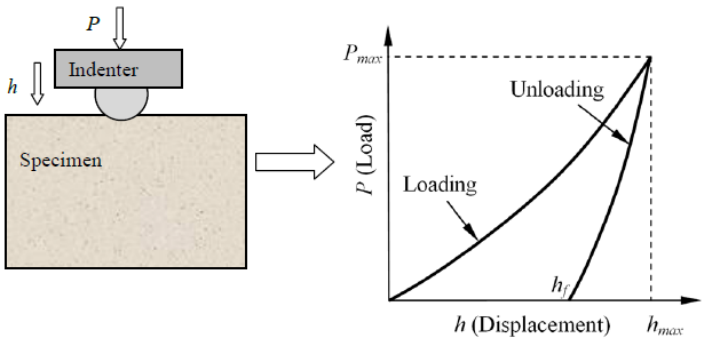

Figure 2-7: Schematic illustration of identification of bulk material (Guo, 2010)

Indentation testing has its origins from 1822 where German scientist Friedrich Mohs characterized scratch resistance of various minerals through the ability of a harder material to scratch a softer material (Fischer-Cripps, 2002). The indexing scheme, called as Mohs scale, ranges from 1 on the soft end for talc to 10 for diamond. The analytical approach to the contact problem in indentation testing traces back to the Hertz contact theory of 1881. Since that time, many methods were developed for hardness measurements, and various definitions for hardness

were proposed. The most-known of them, originated at the beginning of the 20th century, are Brinell, Vickers and Rockwell hardness tests.

The Brinell hardness test method was proposed at the very beginning of the twentieth century (Hutchungs, 2009). In this first widely used and standardised hardness test a 5 or 10 mm steel ball indenter with a load ranging from 5000 N to 30000 N is applied on a metal sample with a flat surface. The Brinell hardness value is calculated by dividing the maximum applied load to the imprint area after unloading. The Vickers hardness test was developed in 1922 (Hutchungs, 2009). Compared to the Brinell test, here a pyramidal diamond indenter with a square base is used and magnitude of the applied force is of the order of newtons. In this test, first of all, two diagonals of the imprint after unloading are measured using a microscope and then the average length is calculated to evaluate the square area of the imprint. The ratio of the maximum applied load to the imprint area gives us the Vickers hardness value. In the Rockwell hardness test method, developed in the early twentieth century (Hutchungs, 2009), the procedure is different. First, a diamond-cone (or hardened steel-ball) indenter is forced into a sample at a prescribed minor load, then a major load is applied and held for a set period of time and, finally, the force on the indenter is decreased back to the minor load. The Rockwell hardness is calculated from the difference in indenter positions before and after the application of the major load. The summary of those methods is presented in Table 2-1.

Table 2-1: Hardness-testing techniques (Callister, 1997)

Name of hardness test	Indenter	Applied load
Brinell	5 or 10 mm diameter steel ball	5000-15000 N (softer material) 30000 N (metal sample)
Vickers	Diamond pyramid	0.01-10 N

Rockwell	Diamond cone or spherical hardened balls with 1.588-12.70 mm diameters	100-1500 N

In general, the above-mentioned traditional hardness tests employ application of a single static force with a specified tip shape and tip material. The output of these hardness tests is typically a single indentation hardness value as a measure of the relative penetration depth of the indentation tip into the sample. On the other hand, in traditional indentation experiments optical imaging of the indented surface imposes a lower limit on the length scale of indentation. Since the early 1970s, instrumented micro- and nano-indentation techniques have been developed and are now widely available (Cheng and Cheng, 2004). Compared to traditional hardness tests, the load and the indenter displacement are recorded simultaneously during the entire loading and unloading processes in instrumented indentation. Instrumented indentation can be accurately conducted using force levels from hundreds mN to as small as a few micro-Newtons over depths from tens microns down to a nano-meter range. This technique, therefore, allows a single instrument to be used to characterize nearly all types of material systems. Instrumented indentation, also known as depth-sensing indentation, is being increasingly used to probe a mechanical response of wide range of materials, such as metals, polymers, ceramics, composites, biological materials (Hengsberger *et al*., 2003), rocks (Yoshioka and Yoshioka, 1995) and even food products (Liu and Scanlon, 2003). More specifically, the application area of instrumented indentation covers dislocation behaviour in metals (Nix and Gao, 1998); mechanical behaviour of thin films (Lilleodden, 2002; Huber *et al*., 2002; Saha and Nix, 2002)and bones (Fan *et al*., 2002); time dependent behaviour of polymers (VanLandingham *et al*., 2001; Oyen and Cook, 2003)and metals (Asif and Pethica, 1997; 1998); scratch resistance of coatings (Randall and Consiglio, 2000; Jardret *et al*., 2000) and wear resistance of metals (Li and Bhushan, 2001). Figure 2-8 provides a schematic illustration of an instrumented indentation system (IIS). In the IIS a force is applied using either electromagnetic or electrostatic actuator connected to the indenter shaft by a series of leaf springs where a capacitive sensor is typically used to measure displacement.

The coupled force and displacement data are measured at leaf springs. The deflection of the leaf springs is a measure of the load applied to the indenter.

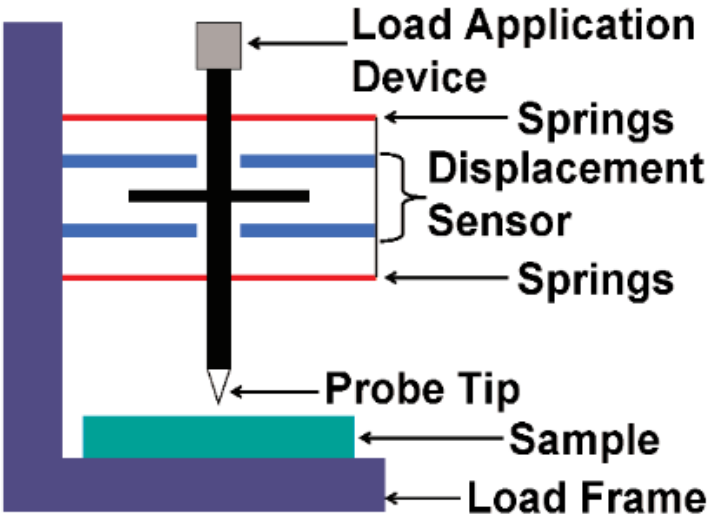

Figure 2-8: Schematic illustration of instrumented indentation system. Reprinted with permission from (VanLandingham, 2003)

Indenter types

In indentation experiments the most frequently used indenters are divided into two subgroups: The indenters with a revolutionary surface and pyramid indenters. Conical and spherical indenters constitute the first group, while three-sided Berkovich and four-sided Vickers indenters constitute the second group (Figure 2-9).

When a spherical indenter, i.e. spherical indenter tip, is used in an indentation experiment, contact stresses are initially small and produce only elastic deformation, later followed by a transition from elastic to plastic deformation. The spherical indenter (Figure 2-9(a)), therefore, has been widely used for brittle materials where a small-strain elastic deformation is required to avoid failure of the material. On the other hand for analysis of ductile materials sharp conical indenter (Figure 2-9(b)) is used, simplifying extraction of elastic-plastic properties. Self-similarity of indenters with a revolutionary surface makes them unique in the indentation of anisotropic crystalline materials as they do not introduce any kind of

anisotropy other than that of the tested specimen. Pyramid indenters are widely used when the desired level of strain is greater such as thin film coatings (Fischer-Cripps, 2003) or for analysis of ductile materials beside the application of a sharp conical indenter tip.

Extended information on how mechanical properties of materials are extracted with different indenter types can be found in the following works: For spherical indentation see (Taljat and Pharr, 2004; Harsono *et al*., 2009); for conical indentation see (Abu Al-Rub, 2007; Fischer-Cripps, 2003; Cheng, 1999; Durban and Masri, 2008; Berke *et al*., 2009); for Vickers indentation see (Antunes *et al*., 2006; 2007; Yin *et al*., 2007) and, finally, for Berkovich indentation see (Fischer-Cripps, 2001; Kese *et al*., 2005; Foerster *et al*., 2007; Sakharova *et al*., 2009).

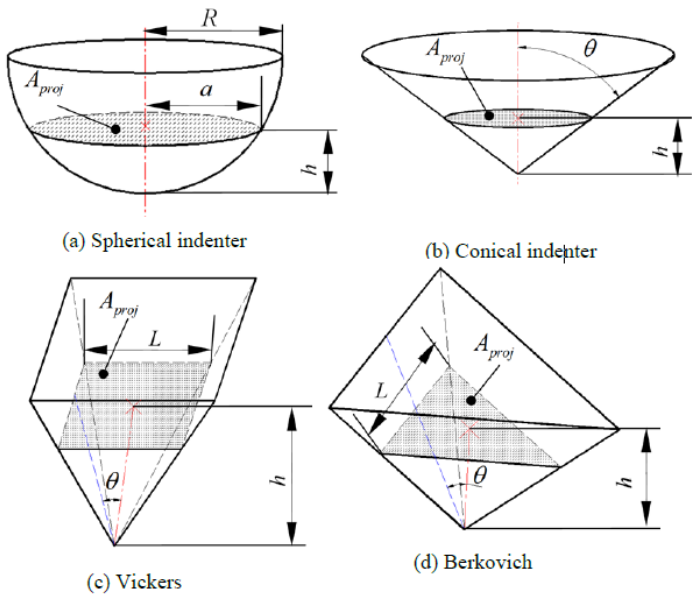

Figure 2-9: Geometries of indenters used in instrumented indentation (Fischer-Cripps, 2002)

In the use of identification to determine material properties such as hardness and the Young's modulus, the projected contact area as a function of penetration depth is required. The schematics of projected contact area for different indenter geometries are demonstrated in Figure 2-9. The area for a spherical indenter (Figure 2-9(a)) corresponds to

$$A^{S}_{\text{proj}} = \pi a^2 = \pi h(2R - h), \qquad 2\text{-}3$$

where a is the radius of the contact area and R is the radius of the spherical indenter. The contact area corresponds to a square cross section (Figure 2-9(c)) for a Vickers indenter with $\theta = 68°$ and calculated as

$$A^{V}_{\text{proj}} = L^2 = (2h\tan(68°))^2 \approx 24.504h^2. \qquad 2\text{-}4$$

In the case of Berkovich indenter ($\theta = 65.3°$), the equilateral-triangle projected contact area (Figure 2-9(d)) is expressed as,

$$A^{B}_{\text{proj}} = \sqrt{3}/4L^2 = \sqrt{3}/4(2h\cot 30°\tan 65.3°)^2 \approx 24.56h^2. \qquad 2\text{-}5$$

On the other hand, the circular contact area when the surface is indented with the conical indenter (Figure 2-9(b)) can be written as

$$A^{C}_{\text{proj}} = \pi\, h^2(\tan\theta)^2. \qquad 2\text{-}6$$

In the numerical modelling of indenter, some researchers (Cheng and Cheng, 2004; Mata *et al*., 2002a; Mata *et al*., 2002b; Mata and Alcala, 2004) preferred to replace their Vickers and Berkovich pyramidal indenters with a conical counterpart to use advantages of axisymmetric characteristics of a conical indenter in their 2D models. For such conditions, the half-apex angle of the conical indenter θ is chosen to impose an identical contact area penetration depth relation by using the Vickers or Berkovich pyramidal indenter. The following equation, as an equivalent of equations 2-4 and 2-6, therefore, should be satisfied for a Vickers indenter,

$$\pi\, h^2(\tan\theta)^2 = 24.504h^2. \qquad 2\text{-}7$$

Then the half apex angle of the equivalent conical indenter becomes $\theta \approx 70.30°$. Using the same way, $\theta \approx 70.32°$ is calculated for a Berkovich indenter. Vickers

and Berkovich indenters therefore can be replaced with a conical indenter in numerical models.

Analyzing mechanical properties using indentation curves

In the middle of the twentieth century, based on indentation experiments Tabor (1951) proposed the following relationship for a hardness value of the material:

$$H = \frac{P}{A} = 3\sigma_{0.08}, \qquad 2\text{-}8$$

where P is a load applied to a flat surface with a rigid pyramidal tip, A is the resulting imprint area and $\sigma_{0.08}$ corresponds to compressive stress of the tested material at a representative strain of approximately 8%. This relationship has been widely used in the materials science community century for more than half a century. Several other methods were also proposed in the mean-time to characterize the properties of materials from indentation tests. These methods are explained below.

Figure 2-10 shows a typical load-displacement curve of a homogeneous elastic-plastic material obtained with a sharp indenter tip. In this figure, $h_{\max}$ represents the displacement at the peak load, $P_{\max}$. h_c, h_f and θ correspond to the contact depth (defined as the depth of the indenter that is in contact with the sample under load), the residual depth or the final displacement after complete unloading and geometrical parameter (ε_g) in equation 2-14, respectively. The areas underneath the loading curve and unloading curves corresponds to the total work done by loading W_t and released by elastic unloading W_e, respectively. Then the plastic work (W_p) done by the indentation process equals to the differences between W_t and W_e, i.e. $W_p = W_t - W_e$.

The average contact pressure or hardness of the indented material is defined by

$$H = \frac{P_m}{A_{proj}}, \qquad 2\text{-}9$$

where A_{proj} is the true projected (real) contact area of the hardness impression. The following equations show how the elastic modulus of the indented sample is calculated:

$$E_r = \frac{\sqrt{\pi}}{2}\frac{1}{\beta A_{\text{proj}}}\left(\frac{dP}{dh}\right)_{h_{\max}}, \qquad 2\text{-}10$$

$$\frac{1}{E_{\text{r}}} = \frac{1-{v_{\text{i}}}^2}{E_{\text{i}}} + \frac{1-{v_{\text{s}}}^2}{E_{\text{s}}}, \qquad 2\text{-}11$$

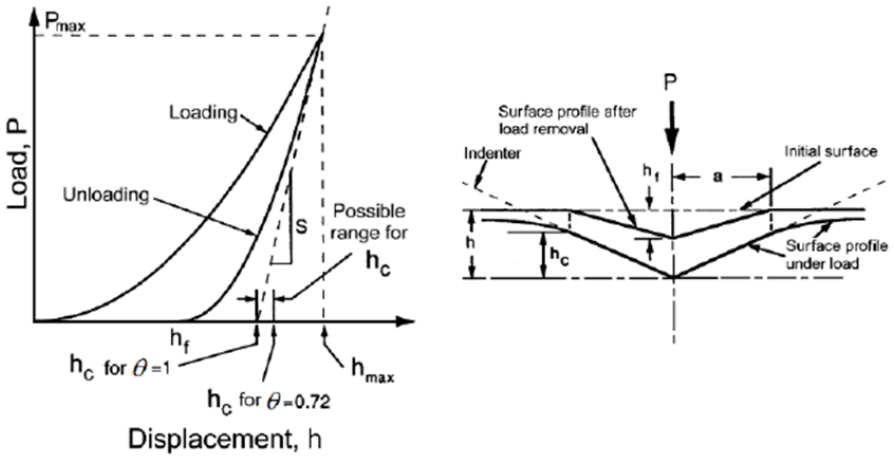

Figure 2-10: Schematic of load-depth curve for sharp indentation of ductile material (a) with deformed pattern of an elastic-plastic sample during and after indentation (b) (Gerday, 2009)

where β is a correction factor (constant) that depends on the geometry of the indenter (β=1.034 for a Berkovich indenter, β=1 for a conical indenter and $\beta = 1.012$ for Vickers indenter (Pharr, 1998; Poon *et al.*, 2008), E_r is the reduced modulus accounting for the fact that elastic deformation occurs in both the specimen and the indenter; E_{i}, E_{s} and v_{i}, v_{s} are the Young`s modulus and Poisson`s ratios of the indenter and the specimen; and $\left(\frac{dP}{dh}\right)_{h_{\text{m}}}$ corresponds to stiffness measured from the unloading indentation curve at h_{m}, i.e. the slope of the initial portion of the unloading curve. Equation 2-10 is derived from the Sneddon's

solution of the contact problem between a rigid indenter and compressed isotropic elastic half-space (Sneddon, 1965). It has been shown that this equation can be also extended to any indenter, which can be described as a solid of revolution of a smooth function (Pharr *et al*., 1992) and to indentation on elastic-plastic materials (Cheng and Cheng, 1997). The correction factor β is introduced to avoid overestimation of elastic modulus measured by indentation experiments (Cheng and Cheng, 1997; Dao *et al*., 2001).

Different methods were proposed to calculate the contact area. Pethicai, Hutchings and Oliver (1983) suggested a simple method based on measured load-displacement curve and the cross sectional area of the indenter as a function of the distance from the indenter tip, known as shape function. Two obvious choices - $h_{\max}$ and h_{f} - were suggested to establish the shape function. It was found that the final depth gives a better estimate of the contact area then the depth at peak load. A More comprehensive method was later proposed by Doerner and Nix (1986) to evaluate the contact area. Their approach is based on the observation that during the initial stages of unloading, the elastic behaviour of the indentation contact is similar to that of a flat cylindrical punch where the area of contact remains unchanged as the indenter retracts back, hence the initial unloading part of the curve is assumed to be linear. To estimate the contact area, they extrapolated the initial linear part of the unloading curve to zero loads linearly and the corresponding depth was used to determine the contact area. Experiments in iron-nickel based amorphous alloy (METGLAS 2826) revealed that the extrapolated depth gives a better estimate for the contact area then either the depth at maximum load or the final depth. This observation was later confirmed by FE simulations of the indentation on silicon and nickel using a conical indenter (Bhattacharya and Nix, 1988). However, indentation of a large number of materials with instrumented indentation demonstrated that the unloading curves obtained were rarely linear, even in the initial stages of unloading. Oliver and Pharr (1992) employed a special dynamic technique, where the contact stiffness can be measured continuously as the elastic recovery takes place during the unloading stage of indenter. They found out that unloading contact stiffness changes immediately and continuously. These

results revealed that the flat-punch approximation proposed by Doerner and Nix (1986) was not an entirely adequate description of a real material behaviour. Oliver and Pharr (1992) therefore suggested fitting the initial section of the unloading curve by a power law. Their developments estimate the contact area better and, hence, provide a more accurate evaluation of the elastic modulus and hardness.

The power-law relationship of Oliver and Pharr used to describe the initial unloading curve for the stiffness measurement is

$$P = B(h - h_{\mathrm{f}})^{m}, \tag{2-12}$$

where the constants B, m, h_{m} are determined by a least-squares fitting procedure (Oliver and Pharr, 1992). Then the initial unloading stiffness can be calculated as follows:

$$\left(\frac{dP}{dh}\right)_{h_{\mathrm{m}}} = Bm(h - h_{\mathrm{f}})^{m-1}. \tag{2-13}$$

According to the investigation of Oliver and Pharr, the projected contact area is a function of the contact depth h_{c} and equals to the following expression:

$$h_{\mathrm{c}} = h_{\max} - \varepsilon_{\mathrm{g}} \frac{P_{\mathrm{m}}}{\left(\frac{dP}{dh}\right)_{h_{\mathrm{m}}}} \tag{2-14}$$

where ε_{g} is a geometrical parameter that equals 1 for a flat punch, 0.72 for a conical indenter and 0.75 for a spherical or pyramidal indenter. On the other hand, the area function for a perfect sharp Berkovic indenter as explained in the previous section is given by

$$A_{\mathrm{proj}}(h_{\mathrm{c}}) = 24.56(h_{\mathrm{c}})^{2}. \tag{2-15}$$

The deviations from a perfect sharp Berkovic indenter owing to blunting at the tip is incorporated in the calculation of area function as follows;

$$A_{\text{proj}}(h_c) = 24.5(h_c)^2 + C_1(h_c)^1 + C_2(h_c)^{1/2} + C_3(h_c)^{1/4} + \ldots\ldots + C_8(h_c)^{1/128}, \quad \text{2-16}$$

where C_1 through C_8 are fit constants (Wang *et al.*, 2004). These values are calibrated for different indenter tips by means of various reference materials, which mechanical properties are already known such as copper, tin, the fused silica (Albrecht *et al.*, 2005). Once h_c is obtained through equation 2-14, the contact area can be computed using equations 2-15 and 2-16. Ultimately, the hardness and the elastic modulus of the indented specimen can be obtained from equations 2-9, 2-10 and 2-11.

Pile-up vs. sink-in behaviour

It is well known that the materials around the contact area usually deform and do not remain flat, instead they flow upwards (pile-up) or downwards (sink-in). For a heavily work-hardened metal, such as copper or mild steel, the material around the contact area bulges upwards or piles-up, whereas for a fully annealed metal the material around the contact area sinks in. Both phenomena are schematically illustrated in Figure 2-11. The occurrence of pile-up and sink-in patterns is related to the strain-hardening behaviour of the indented material (Pharr *et al.*, 1992; Chaudhri and Winter, 1988). Alcala *et al.* (2000) investigated piling-up and sinking-in of materials using Vickers and spherical indenters. Their research demonstrated that sinking-in predominates in materials with a strain-hardening value larger than 0.2. In the indentation of well-annealed soft metals, in the direct vicinity of the indenter tip, rapid strain-hardening leads plastic deformation to occur slowly further away from the contact region. That results in material to be displaced far away from the indentation zone leading to sink-in patterns. On the other hand, in indentation of strain-hardened samples, materials have only little reserves for further hardening and hence show a stronger localization in the plastic zone. A local pile-up instead of a sink-in displacement pattern around the indent, therefore, is observed (Wang *et al.*, 2004). Taljat and Pharr (2004), on the other

hand, reported that the surface profile of the indents is also a function of a non-dimensional ratio E/σ_Y. It was demonstrated that high values of the E/σ_Y ratio lead to development of a pile-up profile around the indenter; by contrast, small values of the E/σ_Y ratio lead to development of a sink-in profile.

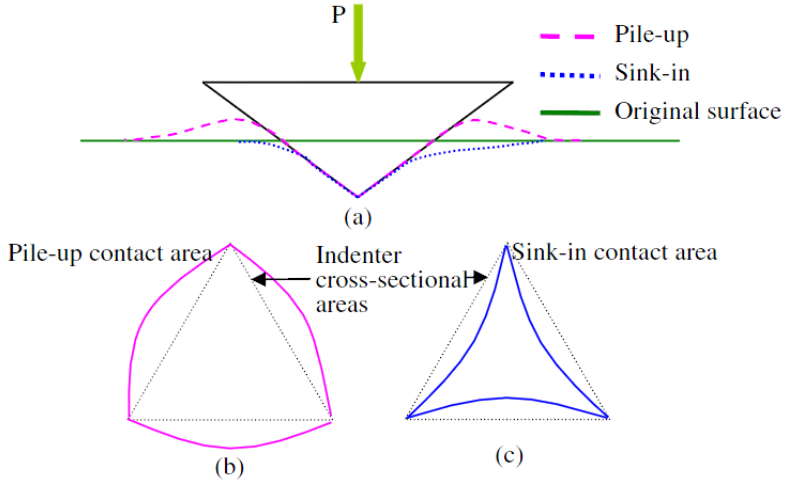

Figure 2-11: Schematic representation of pile-up and sink-in effects during micro-indentation (a), the cross section of pile-up contact area (b) and sink-in contact area (c). Reprinted with permission from (Lee and Chen, 2010)

The influence of temperature on surface profile of indented workpiece material was investigated by Huang *et al*. (2005). This study, where a micro-indentation of a NiTi shape-memory alloy was performed, demonstrated that the material showed a sink-in surface profile at low temperature whereas a pile-up surface profile was obtained at high temperature. Wang *et al*. (2004) demonstrated experimentally and using a crystal-plasticity finite-element model that the appearance of pile-up patterns in nano-indentation of single-crystals depended on crystallography and orientation of the indented workpiece material. On the other hand, Liu *et al*. (2005) and Bucaille *et al*. (2003) found that introduction of friction affected the indent surface pile-up profile. It was observed that an increase in the friction coefficient led to a reduction in the pile-up height. Liu *et al*. (2005) observed this reduction up to a friction coefficient value of 0.4, for a larger friction coefficient, no further reduction in pile-up heights was observed.

A surface profile of the indented sample is of great importance as it affects accurate determination of a contact area and, hence, hardness and elastic-modulus measurements. For instance, sink-in patterns reduce the contact area while pile-up patterns increase it and neglecting them can result in significant errors. For instance, Fischer-Cripps (2002) argues that the errors could give rise to 60%. To determine the actual contact area correctly, different techniques have been used. For instance, atomic force microscopy (AFM) has been used in indentation using a Berkovich indenter to determine the actual contact area. However, this procedure was observed to be limited as the continuous measurement of the contact area was impossible even during the elastic recovery. The finite-element (FE) method may constitute a helpful alternative to overcome this barrier, where the stress and deformation field can be predicted continuously. FE simulations accounting for pile-up or sink-in effects were performed by Mata *et al*. (2002) and Giannakopoulus and Suresh (1999) for Berkovich tips and Maneiro and Rodriquez (2005) and Ai and Dai (2008) for a spherical indenter.

Effect of friction

Several researchers (Mata and Alcala, 2004; Bucaille *et al*., 2003; Cai, 1993; Harsono *et al*., 2008) investigated experimentally and numerically the influence of friction in indentation. Cai (1993) conducted indentation experiments with both lubricated and non-lubricated pyramidal indenters into the annealed samples to study the influence of friction. That study demonstrated that the frictional effects became dominant when the angle of indenter decreased. Similar observation was also noticed by Bucaille (2003) who examined the influence of indenter tip's angle on the friction coefficient using an analytical model proposed by Taylor. Mata and Alcala (2004) carried out FE simulations of indentation by a rigid conical tip with a half-apex angle of 70.3°. In their study they used a Coulomb friction model. It was reported that in assessment of a mechanical behaviour of materials showing considerable piling-up, the effect of friction coefficient should not be neglected. Otherwise, the values of the yield stress and work-hardening exponent may be up to 50% larger than the actual ones. Harsono *et al*. (2008) did a parametric study for

various apex angles of conical and Berkovich indenter tips to investigate the effect of friction on the indentation parameters such as C/Y and W_p/W_T, where C correspond to the curvature of the loading. It was concluded that the influence of friction depended on material properties of the target and the type of indenter tips adopted in the tests.

Liu *et al*. (2008) performed nano-indentation experiments using a spherical indenter on single-crystal copper in different crystallographic orientations. In this study, the coefficient of friction between the indenter and workpiece material was predicted by calibrating a 3D crystal-plasticity finite-element model of nano-indentation with the experiments. It was reported that different friction coefficients were found to be appropriate for indentation of single-crystal with different crystal orientations. For instance, $\mu = 0.4$ is appropriate for (100) orientation, $\mu = 0.3$ for (011) orientation and $\mu = 0.2$ for (111) orientation. The role of friction coefficient in nano-indentation was also studied by Liu *et al*. (2005) and Bucaille *et al*. (2003). It was reported that the introduction of friction did not change the obtained load versus displacement relationship, but significantly changed the indent surface's pile-up profile. This observation was explained by Tabor (1951) analytically where the normal force applied by indenter is described by the following equation as a function of indenter angle, θ, and friction coefficient, μ, using a conical indenter:

$$F = \pi p (R_c)^2 (1 + \frac{\mu}{\tan\theta}), \qquad 2\text{-}17$$

where R_c is the contact radius and p is the contact pressure (Figure 2-12). According to equation 2-17, the force applied with the indenter is independent of the cone angle under frictionless conditions. On the other hand the contribution of friction is negligibly small for a conical indenter ($\theta = 70.3°$) as the ratio of $\mu/\tan\theta$ corresponds to 0.00716 and 0.0716, far less than 1 in equation 2-17, when $\mu = 0.02$ and $\mu = 0.2$, respectively.

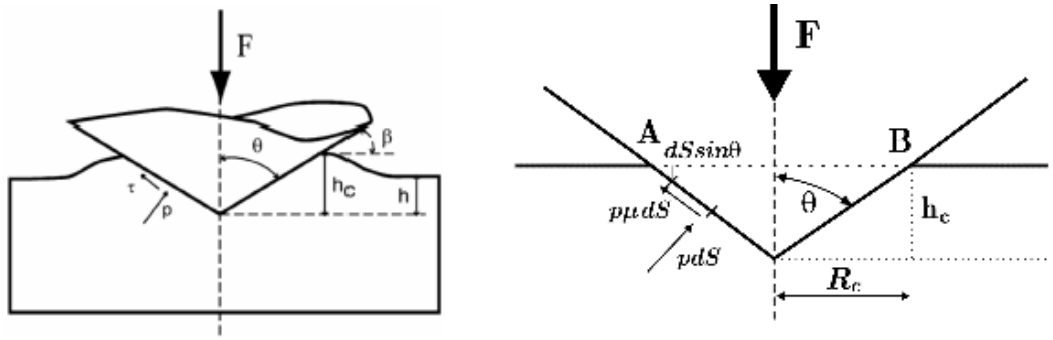

Figure 2-12: Schematics of conical indentation with frictional conditions. Reprinted with permission from (Bucaille et al., 2003)

2.3.2 Size effects in indentation

Experiments carried out in the past few decades demonstrated a strong size effects in indentation experiments when the material's length scale and the non-uniform plastic deformation were of the same order at micron or submicron levels. Stelmashenko *et al*. (1993), Ma and Clarke (1995), Nix and Gao (1998), McElhaney *et al*. (1998) reported that the measured hardness values were observed to increase with a decreasing indentation size, especially in the sub-micrometer depth regime. Figure 2-13 demonstrates a typical size effect observed in indentation. In this figure an experimentally obtained depth dependence of hardness value of a single-crystal copper and a cold worked polycrystalline copper is presented. Similar observations were also reported for yield strength and strain hardening by Fleck *et al*. (1994) in torsional experiments of copper wires and by Stolken and Evans (1998) in micro-bend tests.

Indeed, hardness measurements have been recognized to be size-dependent in the early 1950s by Tabor (1951). The research into the indentation size effect (ISE) has continuously increased over the last decades; this was partly motivated by the development of large-scale application of thin films in electronic components, and partly by the availability of novel methods of probing mechanical properties in very small volumes (Carpinteri and Puzzi, 2006). Many different mechanisms have been suggested to be responsible for the ISE. Several authors demonstrated that the following factors cannot be responsible solely for the strong dependence of

indentation hardness on the indentation depth even though they may have some influence: The pile-up or sink-in surface profile (McElhaney *et al*., 1998), loading rate of indenter (Lilleodden, 2002; Xue *et al*., 2002), grain size or Hall-Patch effect (Stelmashenko *et al*., 1993), oxidation layer or work-hardened surface layer (Lilleodden, 2002; Swadener *et al*., 2002) and indenter-tip radius (McElhaney *et al*., 1998; Xue *et al*., 2002).

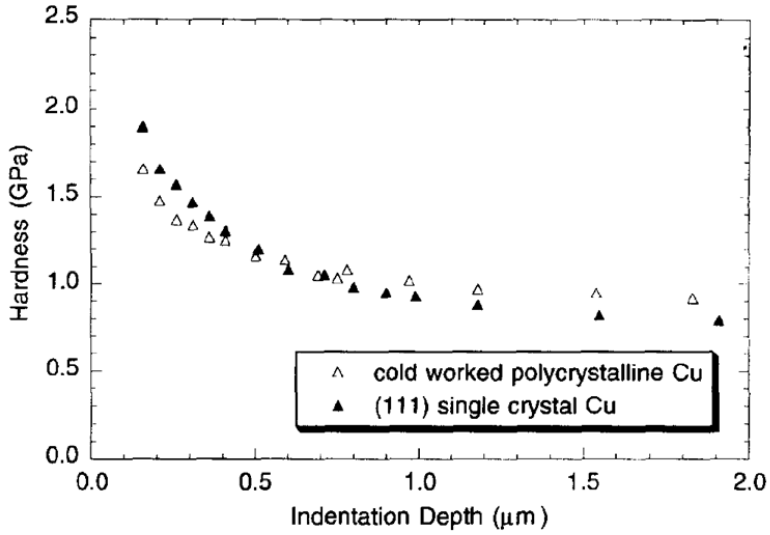

Figure 2-13: Indentation size effects in crystalline materials. Reprinted with permission from (McElhaney *et al*., 1998)

A number of authors argued that the size dependence of material's mechanical properties resulted from an increase in strain gradients inherent to small localized zones leading to presence of geometrically necessary dislocations, which, in turn resulted in additional hardening (Gao and Huang, 2003; Aifantis, 1984; Busso *et al*., 2000; Fleck and Hutchinson, 1997; Nix and Gao, 1998). The characteristic features of deformation in metals are dislocation formation, dislocation motion and dislocation storage. According to the Taylor's hardening rule, dislocation storage is responsible for material hardening (Carpinteri and Puzzi, 2006). Stored dislocations can be divided into two groups: Statistically stored dislocations (SSDs) and geometrically necessary dislocations (GNDs). SSDs are generated by trapping each other in a random way and believed to be dependent on the effective plastic strain (Ashby, 1970; Gao *et al*., 1999b). On the other hand, GNDs are the stored

dislocations that relieve plastic-deformation incompatibilities within the material caused by non-uniform dislocation slip. The density of GNDs is directly proportional to the gradients of effective plastic strain, and their presence causes additional storage of defects and, hence, increases the deformation resistance by acting as obstacles to SSDs (Fleck and Hutchinson, 1997; Ashby, 1970; Kröner, 1962; Arsenlis and Parks, 1999). The dependency of SSDs and GNDs on the effective plastic strain and gradients of the effective plastic strain, respectively, is responsible for the size effect. The smaller the length scale, the larger the density of GNDs relative to SSDs and, consequently, the larger the plastic strain gradients compared to average plastic strains. Using this concept, Nix and Gao (1998) modelled the indentation size effect for crystalline materials. The following characteristic form explaining the depth dependence of hardness is obtained from this model:

$$\frac{H}{H_0} = \sqrt{1 + \frac{h^*}{h}}, \qquad 2\text{-}18$$

where H is hardness for a given indentation depth h, H_0 is hardness in the limit of infinite depth and h^* is a characteristic length depending on the indenter shape, shear modulus and H_0 (Nix, 1998).

The classical continuum plasticity theory (Hill, 1950) cannot explain the dependence of mechanical response on size as no length scale enters the constitutive description. However, the plasticity theory with gradient approaches has been successful in addressing the size effect problem. This success is related to the integration of a microstructural length-scale parameter in the governing equations of the deformation description (Abu Al-Rub and Voyiadjis, 2004). Gradient approaches typically retain terms in the constitutive equations of higher- or lower-order gradients with coefficients that characterize length-scale measures of the deformation microstructure associated with the non-local continuum (Abu Al-Rub and Voyiadjis, 2004). On the other hand, the classical continuum plasticity theories including a strain gradient plasticity theory represent the collective

behavior of dislocations and their interactions at the micro-scale. Therefore, there must exist a lower limit on the length scale, below which the continuum plasticity theories are not applicable. In other words, the continuum plasticity theories are only applicable at a scale much larger than an individual dislocation spacing. This is similar to the relation between the elasticity and the lattice theories; where the elasticity theory is applicable to a few lattice spacing (atomic spacing) below which the lattice theory governs. Similarly, the continuum plasticity theories are applicable to a few dislocation spacings below which the dislocation theories govern. Gao *et al*. (1999) identified that the lower limit for the applicability of strain gradient plasticity theory was around 100 nm. In other words, only when the characteristic length of deformation is larger than 100 nm the pronounced strain gradient plasticity theories can be used (Xue *et al*., 2002).

The gradient regularization in solid mechanics was first studied by Aifantis (Aifantis, 1984). Later, the gradient terms were introduced in several plasticity models through the yield function (Gao *et al*., 1999b; Muhlhaus and Aifantis, 1991; De Borst and Mühlhaus, 1992; Fleck and Hutchinson, 2001; Chen and Wang, 2002). The gradient concept in damage was studied by Voyiadjis *et al*. (2001) for anisotropic damage. Extension of the gradient theory to rate-dependent plasticity/damage was succeeded by few authors (Wang *et al*., 1998; Aifantis, 1999; Oka *et al*., 2000; Voyiadjis *et al*., 2003; Gurtin, 2003). A reasonable agreement between gradient-plasticity theories and experiments was demonstrated in micro- and nano-indentation (Nix and Gao, 1998; Gao *et al*., 1999a; Shu and Fleck, 1999; Begley and Hutchinson, 1998; Huang *et al*., 2000; Yuan and Chen, 2001) in micro-bend and micro-twist experiments (Abu Al-Rub and Voyiadjis, 2004; Gao *et al*., 1999a; Tsagrakis and Aifantis, 2002). Crystal-plasticity models were also developed for the study of fatigue (Manonukul and Dunne, 2004; Bennett and McDowell, 2003; Dunne et al., 2007) and to predict the locations of fatigue crack nucleation in well-characterized f.c.c. polycrystals (Dunne et al., 2007).

In gradient-plasticity theories a constitutive length-scale parameter l is used to scale the effects of strain gradients and is thought of as an internal material length,

related to storage of GNDs. The strain gradient effects become important when the characteristic length associated with deformation becomes comparable to the intrinsic material length-scale parameter l. In other words, if the representative length of non-uniform deformation is much larger than l, strain gradient effects are negligible and the strain gradient theories degenerate to classical plasticity theories (Gao *et al*., 1999). The study of Begley and Hutchinson (1998) indicated that indentation experiments might be the most effective way of measuring the length-scale parameter as the typical tension test cannot be effectively used to determine the material properties of gradient theories due to uniform deformation, whereas in indentation experiment significant work-hardening evolves due to severe and non-uniform plastic and damage deformation concentrated in the localized region directly below the indenter (Abu Al-Rub and Voyiadjis, 2004).

Nix and Gao (1998) estimated the material length scale parameter l from the micro-indentation experiments of McElhaney *et al*. (1998) to be 12 μm and 5.84 μm for annealed single-crystal copper and for cold-worked polycrystalline copper, respectively. Yuan and Chen (2001) proposed that the unique intrinsic material length parameter l can be computationally determined by fitting the Nix and Gao (1998) model from micro-indentation experiments, and they identified $l = 6$ μm for polycrystal copper and $l = 20$ μm for single-crystal copper. Begley and Hutchinson (1998) estimated that the material length-scale associated with the stretch gradients ranged from $1/4$ to 1 μm, while the material lengths associated with rotation gradients were on the order of 4 μm by fitting micro-indentation hardness data (Abu Al-Rub and Voyiadjis, 2004). Different tests also have been used to determine the length scale parameter. For instance, Fleck *et al*. (1994) conducted micro-torsion tests of thin copper wires and predicted l to be 4 μm for copper, whereas Stolken and Evans (1998) did micro-bend tests of thin nickel beams and proposed $l = 5$ μm for nickel (Abu Al-Rub and Voyiadjis, 2004).

Strain gradient plasticity theories are classified into two frameworks: Higher-order and lower-order continuum theories. The higher-order theories belong to the Mindlin`s framework of higher-order continuum theories. In this theory, higher-

order stresses are involved as a work conjugate of the strain gradient with the following equation:

$$\delta w = \sigma'_{ij}\delta\varepsilon_{ij} + \tau'_{ijk}\delta\eta_{ijk}, \qquad 2\text{-}19$$

where δw is the work increment per unit volume of an incompressible solid due to a variation of displacement, σ'_{ij} is the deviatoric part of the Cauchy stress, $\delta\varepsilon_{ij}$ is the variation of strain, τ'_{ijk} is the deviatoric part of Cauchy stress and $\delta\eta_{ijk}$ is the variation of strain gradient. Here, the order of equilibrium equations is higher than that of the conventional continuum theories requiring additional boundary conditions. The theories developed by Fleck and Hutchinson (1997), Fleck *et al*. (1994), Gao *et al*. (1999), Huang *et al*. (2000), Gurtin (2000) are in this class. On the other hand, in the lower-order strain gradient plasticity theory, the higher-order stresses are not incorporated in the constitutive equations; hence, no additional boundary conditions are required. In this type of non-local plasticity theory, the strain gradient effects come into play through the incremental plastic modulus. The strain gradient theories proposed by Acharya and Bassani (2000), Acharya and Beaudoin (2000), Bassani (2001), Beaudoin and Acharya (2001) and Evers *et al*. (2002) are examples of this class. The mechanism-based strain gradient crystal-plasticity theory developed by Han *et al*. (2005) also belongs to this category, where size-dependent plastic deformation at micron and submicron length scales is modelled. The core idea in this theory is to incorporate the concept of geometrically necessary dislocations into the continuum plastic constitutive laws using the Taylor function.

Huang *et al*. (2004) compared the obtained solutions using higher-order and lower-order strain gradient theories for a one-dimensional example, where a bar was fixed at one end and subjected to a constant body force and a uniform stress at the free end along the direction of the bar (Figure 2-14). Figure 2-14 demonstrates the distribution of strain gradient in the bar using lower-order and higher-order strain gradient theories. It is clearly visible that both theories agree very well except near

the two ends of the bar. As the higher-order stresses become significant at the boundaries, different strain gradient distributions are obtained using different frameworks of the theories.

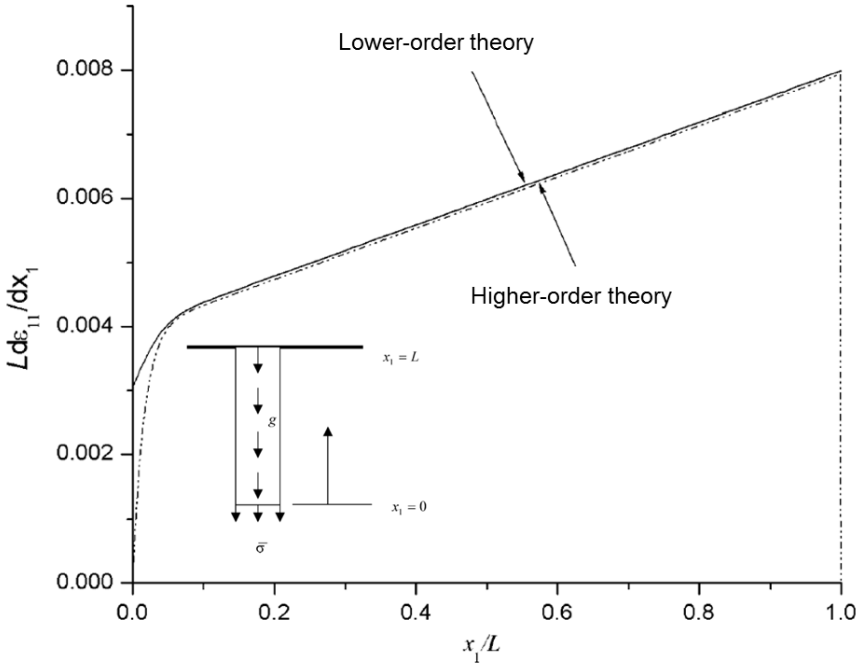

Figure 2-14: Distribution of strain gradients in bar predicted by lower-order (conventional theory of mechanism-based strain gradient) and higher-order (mechanism-based strain gradient theory) theories. Reprinted with permission from (Huang *et al*., 2004)

Different indenter types were also used to study size effects in indentation. For instance, Qu *et al*. (2006) used five different spherical indenter tips with radius ranging from 14 μm to 1600 μm to measure the size effect in indentation. It was observed that indentation hardness H increased with an increase in the ratio of contact radius a to the indenter radius R (Figure 2-15). Swadener *et al*. (2002) and Tymiak *et al*. (2001) also observed that the indentation hardness increased systematically with an increase in the indentation depth using a spherical indenter, i.e., the so-called reversed size effect, contrary to the usual size effect observed in sharp indentation. The opposite dependence of indentation hardness on indentation depth is explained by different dislocation densities underneath the indenters. In the case of a sharp indenter, the average density of SSDs is independent of the

indentation depth (Ma and Clarke, 1995; Arsenlis and Parks, 1999), while the density of GNDs is inversely proportional to it (Gurtin, 2000). On the other hand, in the case of indentation using a spherical indenter, although the density of SSDs increases with an increase in the indentation depth (through a contact radius) the density of GNDs becomes essentially independent (Fleck and Hutchinson, 1997; Fleck and Hutchinson, 1993). The total dislocation density, therefore, displays an opposite depth dependence for sharp and spherical indenters, so does the indentation hardness values (Xue *et al.*, 2002). However, Abu Al-Rub and Voyiadjis (2004) interpreted the size effect in hardness experiments with a spherical indenters in a different way. It was explained in this study that to get an analogy on the ISE in spherical indentation similar to sharp indentation, plastic strain was required to be independent of the sphere size as in the case of sharp indentation, where the plastic strain is independent of indentation depth. In this study, the hardness values obtained using different spherical indenters were compared for the same a/R ratio representing the same plastic strain value. A decrease in the hardness value with an increasing spherical indenter size was reported, which can be also interpreted from Figure 2-15.

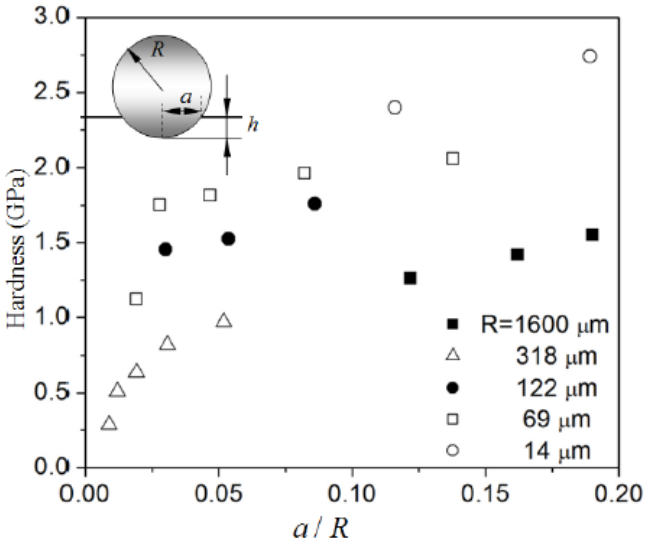

Figure 2-15: Indentation hardness of iridium versus ratio of contact radius (a) to spherical indenter radius (R). Reprinted with permission from (Qu *et al.*, 2006)

The calibration of different material parameters in the models incorporating strain gradient theories plays a significant role in understanding the physical role of the gradient. This necessitates carrying out truly definite experiments at those scales, where their influences can be traced from the deformation patterns. In other words, the calibration of constitutive coefficients of a gradient-dependent model should not rely on the mechanical tests, where gradient effects are comparatively less, but draw information from the experiments at a compatible scale, where the gradient effects become significant. Micro/nano-indentation, micro-bending, micro-torsion experiments can be counted as gradient-dominant tests (Abu Al-Rub and Voyiadjis, 2004).

Chapter III

3 Strain gradient crystal-plasticity theory

Constitutive modeling of crystalline deformation accounting for size effects is dealt with in this chapter. The chapter begins with a description of fundamental mechanics of crystalline solids in terms of their atomic structure followed by analysis of plastic-deformation mechanisms in crystals. In the second part, constitutive modelling of crystalline deformation is explained, where the kinematics of finite deformation is described briefly and later a crystal-plasticity framework with appropriate constitutive laws is introduced. In the final part of this chapter, detailed information about the strain gradient theory is given.

3.1 Fundamentals of crystals

3.1.1 Crystal structures

Metals, alloys, and some ceramic materials are examples of crystalline materials. In crystalline material, or crystalline solid, atoms are arranged in a pattern repeating itself in three dimensions and thus forming a solid with a crystal structure. The arrangement of atoms in crystalline solids is described by referring atoms to the points of intersection of a network of lines in three dimensions. Such a network is called a *space lattice*, which can be also described as an infinite three-dimensional array of points (Figure 3-1) (William and Javad, 2004). In crystalline solids the atomic order shows that small groups of atoms are forming a repetitive pattern. Hence, it is often convenient in describing crystal structures to subdivide the structure into small repeating entities called *unit cells* (Figure 3-1). As the unit cell is chosen to represent the symmetry, it is the basic structural unit, or building block, of the crystal structure (Callister, 1997). By assigning specific values for axial lengths (a, b, c) and inter-axial angles (α, β, γ) (Figure 3-1), different types of unit cells can be constructed.

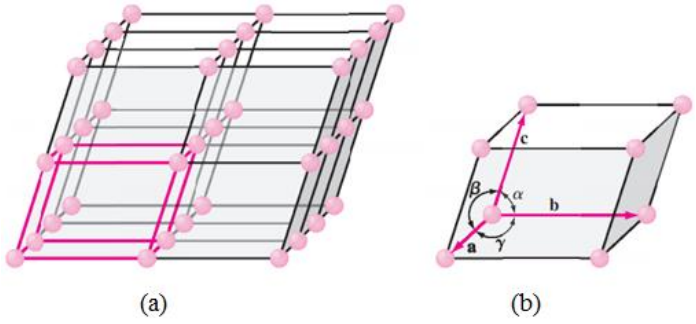

Figure 3-1: Space lattice of crystalline solid (a) and one unit cell showing lattice constants (b) (William and Javad, 2004)

Most elemental metals (about 90 %) crystallize upon solidification into three densely packed crystal structures: body-centered cubic (b.c.c.), face-centered cubic (f.c.c.) and hexagonal close-packed (h.c.p.) (Figure 3-2). In cubic crystal structures three axes intersect each other at right angles and in hexagonal crystal structure two axes intersect at 120° and third axis at right angle (William and Javad, 2004).

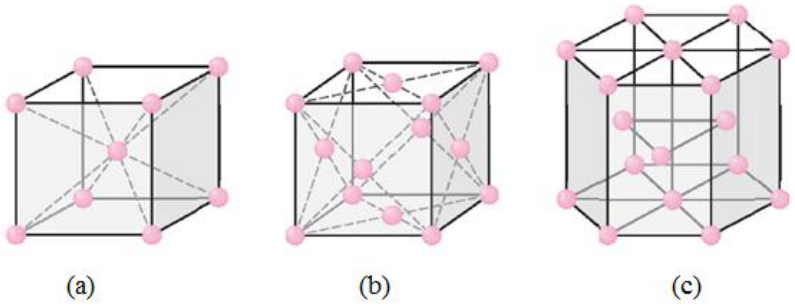

Figure 3-2: Crystal structures: body-centered cubic (a), face-centered cubic (b) and hexagonal close-packed (c) (William and Javad, 2004)

As Ti15V3Cr3Al3Sn (Ti-15-3-3-3) (a titanium-based beta-alloy), the material studied in this thesis, belongs to a group of metastable β-titanium alloy possessing a single phase b.c.c. crystal structure, this crystal structure is discussed below. In the b.c.c. unit cell, one atom is in contact with eight identical atoms located at the corners of an imaginary cube (Figure 3-3). The atomic packing factor (APF) for the unit cell is calculated to be 68%, i.e. 68% of the unit cell volume is occupied by atoms and 32% is empty space. The b.c.c. crystal structure is not a close-packed structure since the atoms could be packed closer together as in the f.c.c. and h.c.p. crystal structure where the APF corresponds to 74%. As the b.c.c. structure is not a close-packed structure, it does not have close-packed planes like the {111} planes in the f.c.c. structure or the {0001} planes in the h.c.p. structure (Sun *et al*., 2011). The most densely packed planes in the b.c.c. structure are the {110} family of planes. However, the atoms in the b.c.c. structure do have close-packed directions <111> along the cube diagonals. Figure 3-4 presents how the directions and planes are defined in cubic unit cells.

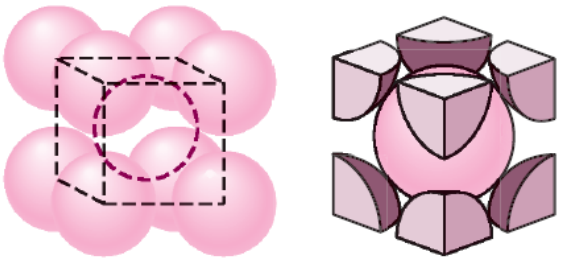

Figure 3-3: Different representation of b.c.c. unit cell (William and Javad, 2004)

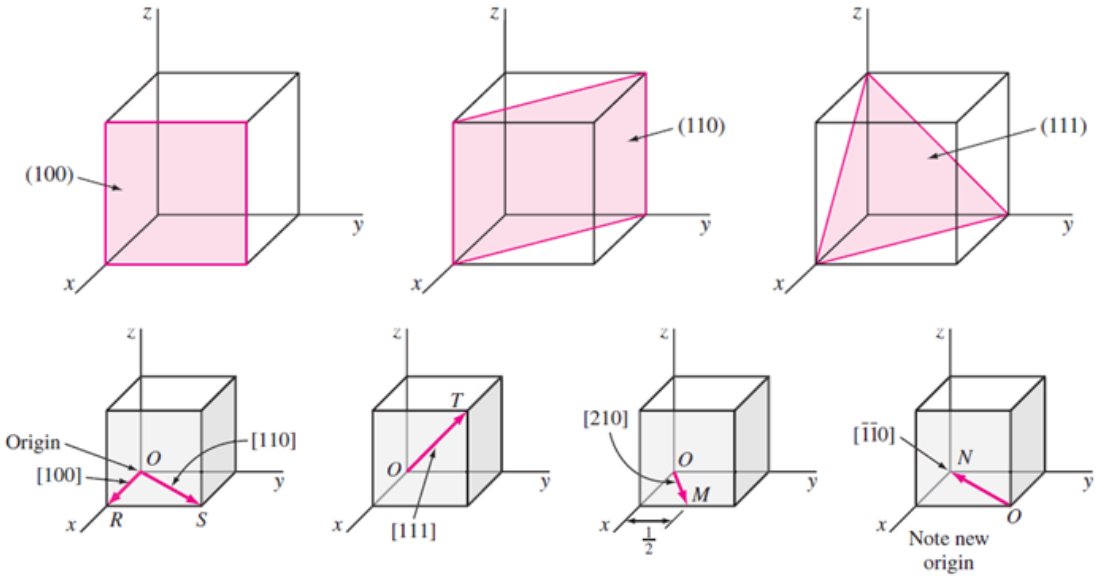

Figure 3-4: Some planes and directions in cubic unit cells (William and Javad, 2004)

3.1.2 Slip in crystals

Crystallographic slip is the governing mechanism of plastic deformation in metals and alloys driven by the motion of dislocations. Dislocations are crystallographic defects, or irregularities, within a crystal structure, which can be introduced in materials either during plastic deformation, during solidification or as a result of thermal stresses owing to rapid cooling (Callister, 1997). An interesting analogy to dislocation motion can be considered as the movement of a worm where the worm propels itself by stretching out a section of its body and thus moving its head forward. The fundamental dislocation types are edge and screw. In real materials dislocations exist as a mixture of both dislocation types. In an edge dislocation, there exists a localized lattice distortion along the end of an extra half-plane of atoms whereas in screw dislocation a helical path is traced around the linear defect by the atomic planes in the crystal lattice (Figure 3-5).

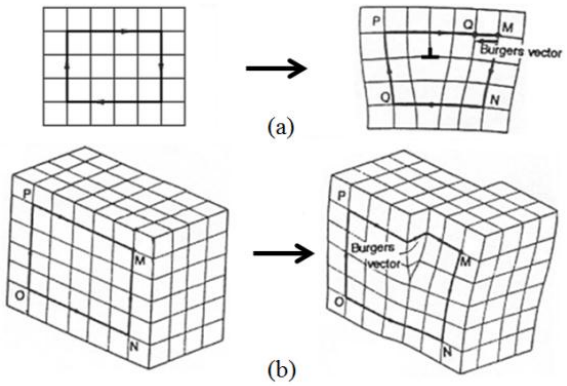

Figure 3-5: Schematic of edge (a) and screw dislocations (b) (Wk, 2008)

The movement of dislocations is not with the same degree of ease on all crystallographic planes of atoms and in all crystallographic directions. Instead, there is a preferred plane, called *slip plane*, and in that plane there are specific directions, along which dislocation motion occurs, called *slip directions*. The combination of the slip plane and the slip direction is called *slip system*. In b.c.c. materials there are 48 slip systems, viz. 6 slip planes of type (110), each with 2 [111] directions makes 12 systems, 24 (123) and 12 (112) planes each with [111] direction makes 24 and 12 systems, respectively (Figure 3-6).

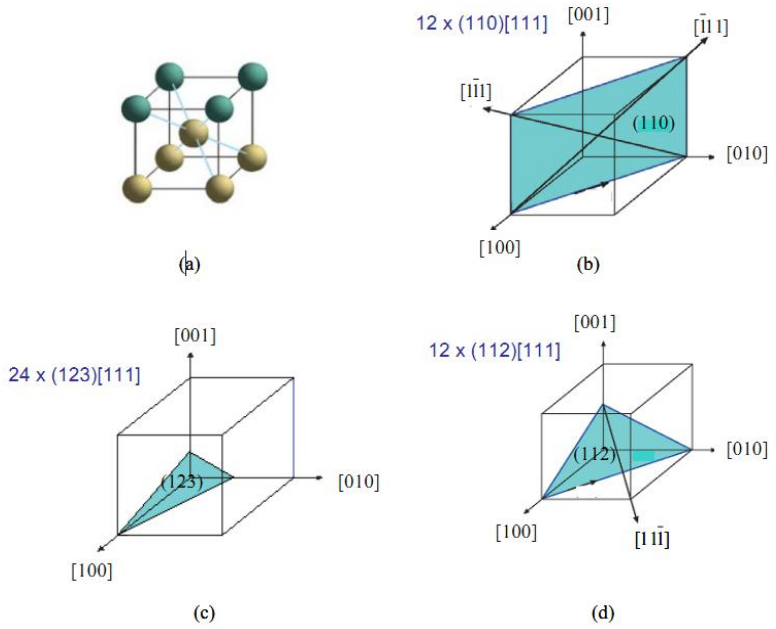

Figure 3-6: B.c.c. crystal structure (a) with three types of glide planes (b-d) and 48 slip systems in total (Siddiq, 2006)

Slip in single-crystals occurs in response to shear stress applied along a slip plane and in a slip direction. The shear component of applied stress is called as *resolved shear stress* and depends on the applied stress and orientation of the slip system. Slip begins when this value reaches a threshold value known as *critical resolved shear stress*. The relation, known as *Schmid's law*, between resolved shear stress and applied stress can be written as

$$\boldsymbol{\tau_R} = \boldsymbol{\sigma} \cos\phi \cos\lambda, \qquad 3\text{-}1$$

where σ is the applied stress (equals to P/A) and $\cos\phi\cos\lambda$ is called the *Schmid factor*. During plastic deformation of a single-crystal, each existing slip system has a potential to be activated. However, one slip system is generally oriented most favourably with the largest Schmid factor ($\cos\phi\cos\lambda$), and, hence, the highest resolved shear stress, known as *primary slip system*. For instance, the orientation $\phi = \lambda = 45°$ corresponds to the most favourable slip system where the Schmid factor is the highest attainable one.

In fact the Schmid law has two distinct assertions. The first one is that plastic flow begins when the resolved shear stress on a possible slip system reaches a CRSS, which is a constant, independent of the slip system and of the sense of slip. The second one states that this critical stress is not influenced by any other component of the applied stress tensor (Duesbery and Vitek, 1998). These assumptions are valid in metals with close-packed crystal structures for which the Schmid law was established (Ito and Vitek, 2001). However, many authors observed that there exist difference in CRSS for tension and compression loading, i.e. an intrinsic anisotropic resistance to slip, in materials crystallizing in the b.c.c. structure proving the evidence of deficiencies in the Schmid law (Taylor and Elam, 1926; Vitek *et al*., 1970, Duesbery and Vitek, 1998). In fact, in the b.c.c. lattice {111} planes are not mirror planes, hence shearing in opposite direction along <111> differs in contrast with the <110> slip direction of f.c.c. crystals since {110} planes

are mirror planes, which, in turn, guarantees the equivalence of the two senses of slip (Ito and Vitek, 2001). Nowag et al (Nowag et al., 2012) demonstrated experimentally that the investigated material in this thesis, b.c.c. Ti alloy, does not violate the Schmid's law. Therefore, the finite-strain continuum theory assuming the Schmid-type constitutive behaviour is a reasonable choice for this study. However, for some b.c.c. materials, plasticity may start on a slip system that is geometrically not predicted, i.e. breakdown of Schmid's law. In such cases, the present continuum model cannot predict the material's deformation response accurately.

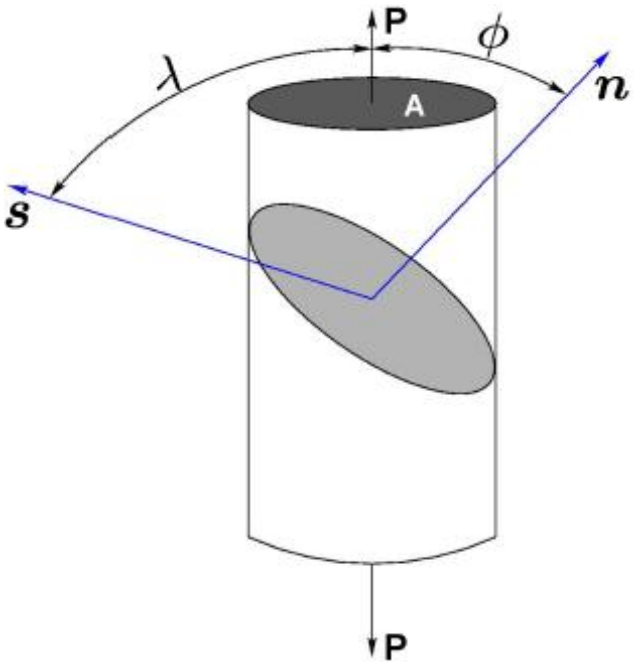

Figure 3-7: Geometrical relationship between the tensile axis, slip plane and slip direction (Callister, 1997)

The critical resolved shear stress required for activation of a slip system is not a constant value, but evolves with an increase in deformation, known as strain- or work-hardening. Strain-hardening is caused basically due to interaction of dislocations in different slip systems. An extended discussion regarding this phenomenon is presented in Section 3.2.2.

Deformation in polycrystals is relatively complicated compared to single-crystals. Polycrystalline materials are the aggregation of many single-crystals, each of which

has a different crystallographic orientation Due to existing geometrical constraints between crystals in polycrystalline aggregate, a single grain, which is favourably oriented, cannot deform until the adjacent or less favourably oriented grains are capable of slip also, which in turn leads to higher forces. Polycrystalline materials, therefore, are stronger compared to their single-crystal counterparts (Callister, 1997).

3.2 Constitutive modelling of crystalline deformation

The main aspects of continuum mechanics used in this thesis are reviewed in this section. Here, first the fundamentals of finite deformation are explained kinematically, later this concept is extended to the crystal-plasticity framework.

3.2.1 Kinematics of finite deformation

The motion of a deformable body from a reference configuration to a current configuration is denoted by continuous, invertible, one-to-one function $\emptyset_t = \boldsymbol{X} \rightarrow \boldsymbol{x} : R \rightarrow S$. Here R represents the reference, material or Lagrangean configuration and S represents the current, spatial or Eulerian approach. The fundamental descriptor of kinematics of deformable bodies is the deformation gradient ($\boldsymbol{F}$), defined as the tangent of mapping vector, where the Frechet-derivative of the motion function, $\emptyset_t$ is taken (Ogden, 1997).

$$\boldsymbol{F}(\boldsymbol{X}) = \nabla_{\boldsymbol{x}} \emptyset_t(X) = \frac{\partial \boldsymbol{x}}{\partial \boldsymbol{X}}, \qquad 3\text{-}2$$

where $\partial \boldsymbol{X}$ is an infinitesimal material line element in the reference configuration and $\partial \boldsymbol{x}$ in the deformed configuration. The deformation gradient $\boldsymbol{F}$ can be decomposed into a product of two second-order tensors using the polar decomposition theory as follows (Figure 3-8):

$$\boldsymbol{F} = \boldsymbol{RU} = \boldsymbol{VR}, \qquad 3\text{-}3$$

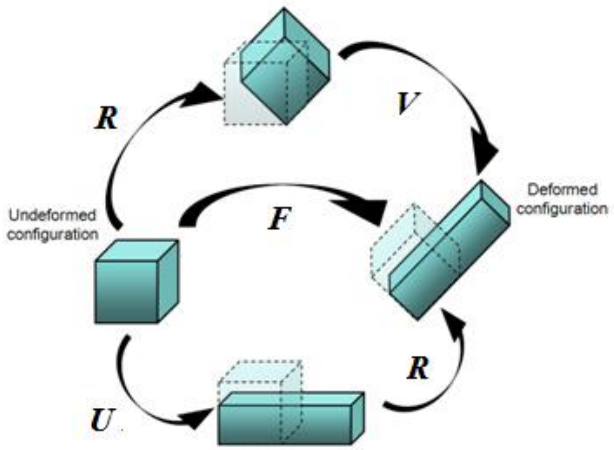

Figure 3-8: Polar decomposition of the the deformation gradient

where $\boldsymbol{U}$ and $\boldsymbol{V}$ denote right and left stretch tensors, respectively. $\boldsymbol{U}$ and $\boldsymbol{V}$ are both positive definite and symmetric tensors, hence can be related to each other by

$$\boldsymbol{V} = \boldsymbol{R}\boldsymbol{U}\boldsymbol{R}^{\mathrm{T}}, \tag{3-4}$$

where $\boldsymbol{R}$ is a orthogonal rotation tensor with the following properties:

$$\boldsymbol{R}^{\mathrm{T}} = \boldsymbol{R}^{-1}, \tag{3-5}$$

$$\det \boldsymbol{R} = 1. \tag{3-6}$$

The material time derivative of equation 3-2 gives us the velocity difference in the current configuration of a line element $d\boldsymbol{X}$ in the reference frame

$$\frac{\partial \boldsymbol{F}}{\partial t} = \frac{\partial}{\partial t}\left(\frac{\partial \boldsymbol{x}}{\partial \boldsymbol{X}}\right), \tag{3-7}$$

$$\dot{\boldsymbol{F}} = \frac{d\boldsymbol{v}}{d\boldsymbol{X}}. \tag{3-8}$$

$d\boldsymbol{v}$ can be also described as the velocity difference of the end points of a line element $d\boldsymbol{x}$ in the spatial frame as

$$d\boldsymbol{v} = \boldsymbol{L} \cdot d\boldsymbol{x}, \tag{3-9}$$

where $\boldsymbol{L}$ is the spatial velocity gradient. If equations 3-2, 3-8 and 3-9 are combined, the following equations are obtained:

$$\dot{\boldsymbol{F}} = \boldsymbol{L}\boldsymbol{F}\,,$$
$$\boldsymbol{L} = \dot{\boldsymbol{F}}\boldsymbol{F}^{-1}. \tag{3-10}$$

If equation 3-3 is put with the right stretch tensor into equation 3-10, the following equations are obtained:

$$\boldsymbol{L} = (\boldsymbol{R}\dot{\boldsymbol{U}})(\boldsymbol{R}\boldsymbol{U})^{-1},$$
$$\boldsymbol{L} = \boldsymbol{R}\dot{\boldsymbol{U}}\boldsymbol{U}^{-1}\boldsymbol{R}^{\boldsymbol{T}} + \dot{\boldsymbol{R}}\boldsymbol{R}^{\boldsymbol{T}}. \tag{3-11}$$

The symmetric and skew-symmetric parts of the spatial velocity gradient represent the spatial rate of deformation and rigid-body rotation rate, respectively.

$$\boldsymbol{D} = \boldsymbol{L}^{\mathbf{sym}} = \boldsymbol{R}[\dot{\boldsymbol{U}}\boldsymbol{U}^{-1}]^{\mathbf{sym}}\boldsymbol{R}^{\boldsymbol{T}},$$
$$\boldsymbol{W} = \boldsymbol{L}^{\mathbf{skw}} = \boldsymbol{R}[\dot{\boldsymbol{U}}\boldsymbol{U}^{-1}]^{\mathbf{skw}}\boldsymbol{R}^{\boldsymbol{T}} + \dot{\boldsymbol{R}}\boldsymbol{R}^{\boldsymbol{T}}. \tag{3-12}$$

3.2.2 Crystal-plasticity theory

In this section the kinematical theory of Taylor (1938) describing the mechanics of crystals and its precise mathematical theory developed by Hill (1966), Rice (1971), Hill and Rice (1972) is used for the crystal-plasticity theory. The key equations of the crystal-plasticity theory are summarized below following the works of Rice (1970) and Asaro (1983). The reader is referred to Dunne and Petrinic (2005) and the references therein for extended information.

The basic idea of crystal-plasticity formulation described here rests on the fact that a material flows through a crystal lattice via dislocation motion, whereas the lattice itself undergoes elastic deformations. In other words, a crystalline slip triggers inelastic deformation of a single-crystal, but does not distort the crystal lattice (Figure 3-9).

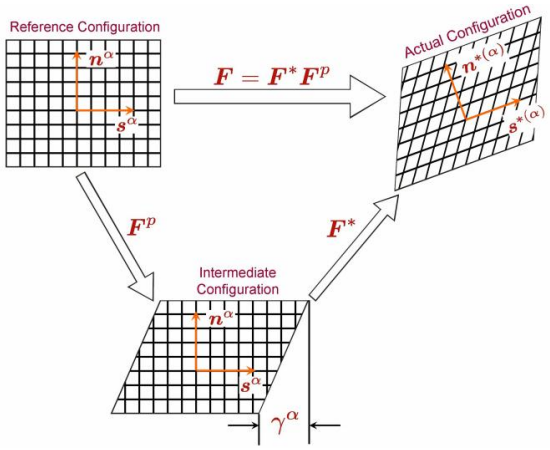

Figure 3-9: Kinematics of crystalline deformation (Prakash, 2009)

For finite deformation, mapping a reference configuration of the material to the deformed configuration is denoted by the total deformation gradient $\boldsymbol{F}$, which can be decomposed as

$$\boldsymbol{F} = \boldsymbol{F}^* \boldsymbol{F}^{\boldsymbol{p}} , \tag{3-13}$$

where $\boldsymbol{F}^*$ accounts for elastic stretching ($\boldsymbol{F}^{\boldsymbol{e}}$) and rigid body rotation of the lattice ($\boldsymbol{F}^{\boldsymbol{R}}$), and hence described as

$$\boldsymbol{F}^* = \boldsymbol{F}^{\boldsymbol{e}} \boldsymbol{F}^{\boldsymbol{R}} . \tag{3-14}$$

$\boldsymbol{F}^{\boldsymbol{p}}$ represents material's plastic shear and corresponds to the amount of deformation that remains in the crystal after the load has been removed, i.e. the crystal lattice is brought back to its original configuration (Prakash, 2009). According to the crystal-plasticity theory, deformation remaining in the crystal after elastic recovery corresponds to $\boldsymbol{F}^{\boldsymbol{R}} \boldsymbol{F}^{\boldsymbol{p}}$.

The deformation gradient for a single slip in crystals can be written as

$$\boldsymbol{F}^{\boldsymbol{p}} = \mathbf{1} + \gamma \boldsymbol{s} \otimes \boldsymbol{m} , \tag{3-15}$$

where $\boldsymbol{s}$ is the slip direction, $\boldsymbol{m}$ is the slip-plane normal, γ is the total plastic shear and $\otimes$ represents the matrix product or the dyad of two vectors. In the case of

multiple slip, the evolution of $\boldsymbol{F^p}$ is the sum of shears on individual slip systems (α) and related to the slipping rate ($\dot{\gamma}^{\alpha}$) by

$$\dot{\boldsymbol{F}}^{\boldsymbol{p}}(\boldsymbol{F}^{\boldsymbol{p}})^{-\boldsymbol{1}} = \sum_{\alpha=1}^{N} \dot{\gamma}^{\alpha} \boldsymbol{s}^{\alpha} \boldsymbol{m}^{\alpha}. \tag{3-16}$$

In the deformation of crystal, vectors connecting lattice sites are stretched and rotated according to $\boldsymbol{F}^*$. The slip direction and slip plane normal in deformed configuration are therefore defined by:

$$\boldsymbol{s}^{*(\alpha)} = \boldsymbol{F}^* \boldsymbol{s}^{\alpha} , \tag{3-17}$$

$$\boldsymbol{m}^{*(\alpha)} = \boldsymbol{m}^{\alpha} \boldsymbol{F}^{*-\boldsymbol{1}} . \tag{3-18}$$

Here, the deformed vectors of slip direction ($\boldsymbol{s}^{*(\alpha)}$) and slip plane normal ($\boldsymbol{m}^{*(\alpha)}$) are not unit vectors, unlike the undeformed ones ($\boldsymbol{s}^{\alpha}, \boldsymbol{m}^{\alpha}$), but remain orthogonal to each other (Figure 3-9).

The spatial velocity gradient can be rewritten as a function of $\boldsymbol{F}^*$and $\boldsymbol{F^p}$ when the equation 3-13 is inserted into equation 3-10. Then the following equation is obtained:

$$\begin{aligned} \boldsymbol{L} = \boldsymbol{\nabla v} = \dot{\boldsymbol{F}}\boldsymbol{F}^{-\boldsymbol{1}} &= (\boldsymbol{F}^{*}\dot{\boldsymbol{F}}^{\boldsymbol{p}})(\boldsymbol{F}^{*}\boldsymbol{F}^{\boldsymbol{p}})^{-\boldsymbol{1}} \\ &= (\dot{\boldsymbol{F}}^{*}\boldsymbol{F}^{\boldsymbol{p}} + \boldsymbol{F}^{*}\dot{\boldsymbol{F}}^{\boldsymbol{p}})(\boldsymbol{F}^{\boldsymbol{p}})^{-\boldsymbol{1}}(\boldsymbol{F}^{*})^{-\boldsymbol{1}} \\ &= \dot{\boldsymbol{F}}^{*}(\boldsymbol{F}^{*})^{-\boldsymbol{1}} + \boldsymbol{F}^{*}\dot{\boldsymbol{F}}^{\boldsymbol{p}}(\boldsymbol{F}^{\boldsymbol{p}})^{-\boldsymbol{1}}(\boldsymbol{F}^{*})^{-\boldsymbol{1}} . \end{aligned} \tag{3-19}$$

Here the velocity gradient contains two terms; the first term measures the lattice deformation ($\boldsymbol{L}^*$) and the second term measures plastic slip ($\boldsymbol{L^P}$), i.e.

$$\boldsymbol{L}^{*} = \dot{\boldsymbol{F}}^{*}(\boldsymbol{F}^{*})^{-\boldsymbol{1}}, \ \boldsymbol{L}^{\boldsymbol{p}} = \boldsymbol{F}^{*}\dot{\boldsymbol{F}}^{\boldsymbol{p}}(\boldsymbol{F}^{\boldsymbol{p}})^{-\boldsymbol{1}}(\boldsymbol{F}^{*})^{-\boldsymbol{1}} . \tag{3-20}$$

Then the plastic velocity gradient in the current configuration due to shearing of a set of slip systems can be rewritten using the equation 3-16:

$$\boldsymbol{L^p} = \dot{\boldsymbol{F}}^{\boldsymbol{p}}(\boldsymbol{F^p})^{-\mathbf{1}} = \sum_{\alpha=1}^{N} \dot{\gamma}^{\alpha} \boldsymbol{s}^{\alpha} \boldsymbol{m}^{\alpha} = \sum_{\alpha=1}^{N} \dot{\gamma}^{\alpha} \boldsymbol{s}^{*\alpha} \boldsymbol{m}^{*\alpha}. \quad 3\text{-}21$$

The velocity gradient can be also decomposed into symmetric and skew symmetric parts representing stretching ($\boldsymbol{D}$) and spin ($\boldsymbol{W}$), respectively:

$$\boldsymbol{L^{sym}} = \boldsymbol{D} = \boldsymbol{D}^{*} + \boldsymbol{D^p} \text{ and } \boldsymbol{L^{skw}} = \boldsymbol{W} = \boldsymbol{W}^{*} + \boldsymbol{W^p}. \quad 3\text{-}22$$

In the first section of crystal-plasticity theory, the kinematics of crystalline deformation are introduced. What follows next is the constitutive equations used in crystal-plasticity theory.

Constitutive equations

Many constitutive equations used in crystal-plasticity theory are given in a rate form as a relation between stress rate and strain-rate. The rate definition of the stress tensors requires invariance of the material frame (objective) to ensure objectivity of the constitutive response of a material. If the stress and strain measures are material quantities then objectivity is automatically satisfied. However, if the quantities are spatial, then the objectivity of stress rate is not guaranteed even if the strain-rate is objective (Simo and Hughes, 1998). To preserve objectivity, modified time derivatives of stress tensors are used. Among numerous objective stress rates in the literature on continuum mechanics, three widely used are the Truesdell rate, the Green-Naghdi rate and the Jaumann rate. The Jaumann rate used in the formulation of crystal-plasticity theory is briefly explained here.

Stress rates used in crystal-plasticity

The objective stress rates are obtained by taking the derivative of equations transforming different stress tensors. Here, first the definitions of different stress tensors are given used in crystal-plasticity.

The Cauchy ("true") stress ($\boldsymbol{\sigma}$) represents the force per unit deformed area in the solid. The definition of the work using the Cauchy stress over a deformed volume (dV) is given by

$$w = \int \boldsymbol{\sigma} : \boldsymbol{D}\, dV\ . \tag{3-23}$$

Equation 3-23 can be described with different stress tensors and their work conjugates as follows:

$$w = \int \boldsymbol{\sigma} : \boldsymbol{D}\, dV = \int \boldsymbol{\tau} : \boldsymbol{D}\, dV_0 = \int \boldsymbol{P} : \dot{\boldsymbol{F}}\, dV_0 = \int \boldsymbol{S} : \dot{\boldsymbol{E}}\, dV_0\ , \tag{3-24}$$

where $\boldsymbol{\tau}$ corresponds to the Kirchoff stress tensor, $\boldsymbol{P}$ corresponds to the first Piola-Kirchhoff (P-K) stress tensor, $\boldsymbol{S}$ corresponds to second P-K stress tensor, $\dot{\boldsymbol{F}}$ is time derivative of deformation gradient, $\dot{\boldsymbol{E}}$ is Green-Lagrange strain tensor and, ultimately, dV_0 denotes undeformed volume. The definition of Green-Lagrange strain tensor is

$$\begin{aligned} \boldsymbol{E} &= \frac{1}{2}(\boldsymbol{F}\boldsymbol{F}^{\boldsymbol{T}} - 1), \\ \dot{\boldsymbol{E}} &= \boldsymbol{F}\boldsymbol{D}\boldsymbol{F}^{\boldsymbol{T}}. \end{aligned} \tag{3-25}$$

The relation between the Cauchy stress and the 2nd P-K stress is called *the Piola transformation* which can be written as

$$\boldsymbol{\sigma} = \boldsymbol{J}^{-1}\boldsymbol{F}\,\boldsymbol{S}\,\boldsymbol{F}^{\boldsymbol{T}}\ , \tag{3-26}$$

where $\boldsymbol{J}$ (Jacobian) corresponds to determinant of deformation gradient. The Jaumann rate of the Cauchy stress ($\boldsymbol{\sigma}$), $\hat{\dot{\boldsymbol{\sigma}}}$, is defined as material time derivative of equation 3-26

$$\hat{\dot{\boldsymbol{\sigma}}} = \boldsymbol{J}^{-1}\boldsymbol{F}\,\dot{\boldsymbol{S}}\boldsymbol{F}^{\boldsymbol{T}}. \tag{3-27}$$

This equation can be rewritten in an open form if equation 3-26 is inserted in equation 3-27:

$$\hat{\dot{\boldsymbol{\sigma}}} = \boldsymbol{J}^{-1}\boldsymbol{F}\frac{d}{dt}(\boldsymbol{J}\boldsymbol{F}^{-1}\boldsymbol{\sigma}\boldsymbol{F}^{-T})\,\boldsymbol{F}^{\boldsymbol{T}}\ . \tag{3-28}$$

For the purpose of defining an objective stress rate, it is assumed that $\boldsymbol{U} = 1$, then $\boldsymbol{F} = \boldsymbol{R}$ is obtained from equation 3-3, i.e. there is no stretch ($\boldsymbol{J}$ = 1). Then equation 3-28 is simplified to

$$\hat{\dot{\boldsymbol{\sigma}}} = \boldsymbol{R}\frac{d}{dt}(\boldsymbol{R^{-1}\sigma R^{-T}})\,\boldsymbol{R}^{T}\,. \tag{3-29}$$

Expanding out the derivative of equation 3-29 leads to the following:

$$\begin{gathered}\hat{\dot{\boldsymbol{\sigma}}} = \boldsymbol{R\dot{R}^{-1}\sigma R^{-T}R}^{T} + \boldsymbol{RR^{-1}\dot{\sigma}R^{-T}R}^{T} + \boldsymbol{RR^{-1}\sigma\dot{R}^{-T}R}^{T}\,, \\ \hat{\dot{\boldsymbol{\sigma}}} = \boldsymbol{R\dot{R}^{-1}\sigma} + \dot{\boldsymbol{\sigma}} + \boldsymbol{\sigma\dot{R}^{-T}R}^{T}.\end{gathered} \tag{3-30}$$

It is known from equation 3-5 that

$$\boldsymbol{RR}^{T} = 1\,. \tag{3-31}$$

When the derivative of both sides is taken the following equation is obtained:

$$\begin{gathered}\frac{d}{dt}(\boldsymbol{RR}^{T}) = 0\,, \\ \boldsymbol{\dot{R}R}^{T} + \boldsymbol{R\dot{R}}^{T} = 0\,, \\ \boldsymbol{\dot{R}R}^{T} = -\boldsymbol{R\dot{R}}^{T},\end{gathered} \tag{3-32}$$

If equations 3-31 and 3-32 are inserted into equation 3-30, the following is obtained:

$$\hat{\dot{\boldsymbol{\sigma}}} = -\boldsymbol{\dot{R}R}^{T}\boldsymbol{\sigma} + \dot{\boldsymbol{\sigma}} + \boldsymbol{\sigma\dot{R}R}^{T}. \tag{3-33}$$

Recall that the spin tensor $\boldsymbol{W}$ (equation 3-22) is the skew part of the velocity gradient and can be expressed as

$$\begin{gathered}\boldsymbol{W} = \mathrm{skew}(\boldsymbol{L}) = \mathrm{skew}\big(\boldsymbol{R\dot{U}U^{-1}R}^{T} + \boldsymbol{\dot{R}R}^{T}\big), \\ = \frac{\mathbf{1}}{\mathbf{2}}\,\boldsymbol{R}\big(\boldsymbol{\dot{U}U^{-1}} - \boldsymbol{U^{-1}\dot{U}}\big)\boldsymbol{R}^{T} + \boldsymbol{\dot{R}R}^{T}\,\cdot\end{gathered} \tag{3-34}$$

The first term in equation 3-34 is negligibly small compared to the second term. The skew tensor, therefore, can be simplified as

$$\boldsymbol{W} \approx \dot{\boldsymbol{R}}\boldsymbol{R}^{T}. \tag{3-35}$$

Then the Jaumann rate of the Cauchy stress on axes rotating with the material takes the following final form

$$\hat{\dot{\boldsymbol{\sigma}}} = \dot{\boldsymbol{\sigma}} - \boldsymbol{W}\boldsymbol{\sigma} + \boldsymbol{\sigma}\boldsymbol{W}. \tag{3-36}$$

The objectivity of the material constitutive response entails the objectivity of the Jaumann rate of the Cauchy stress (Holzapfel, 2000).

Constitutive laws

A constitutive law describing the relation between the symmetric rate of stretching the lattice ($\boldsymbol{D}^{*}$) and the Jaumann rate of Cauchy stress $\hat{\boldsymbol{\sigma}}$ ($\hat{\dot{\boldsymbol{\sigma}}}$) is given by (Hill and Rice, 1972)

$$\hat{\dot{\boldsymbol{\sigma}}} + \boldsymbol{\sigma}\,(\boldsymbol{I}{:}\,\boldsymbol{D}^{*}) = \boldsymbol{C}{:}\,\boldsymbol{D}^{*}, \tag{3-37}$$

where $\boldsymbol{I}$ is the second-order identical tensor and $\boldsymbol{C}$ is the tensor of elastic moduli having the following symmetries:

$$C_{ijkl} = C_{jikl} = C_{ijlk} = C_{klij}. \tag{3-38}$$

The f.c.c. and b.c.c. metals have cubic symmetry. The elastic moduli for such crystals is particularly simple, and can be parameterized by only 3 material constants, C_{11}, C_{12}, C_{44}. The following matrix expresses the elastic moduli of such materials:

$$\boldsymbol{C} = \begin{bmatrix} C_{11} & C_{12} & C_{12} & 0 & 0 & 0 \\ C_{12} & C_{11} & C_{12} & 0 & 0 & 0 \\ C_{12} & C_{12} & C_{11} & 0 & 0 & 0 \\ 0 & 0 & 0 & C_{44} & 0 & 0 \\ 0 & 0 & 0 & 0 & C_{44} & 0 \\ 0 & 0 & 0 & 0 & 0 & C_{44} \end{bmatrix}. \tag{3-39}$$

Equation 3-37 is formed on the axes that rotate with the crystal lattice and related to the co-rotational stress rate on axes rotating with the material ($\hat{\boldsymbol{\sigma}}$) by

$$\dot{\hat{\boldsymbol{\sigma}}} = \hat{\boldsymbol{\sigma}} - \boldsymbol{W}^{\boldsymbol{p}}\boldsymbol{\sigma} + \boldsymbol{\sigma}\boldsymbol{W}^{\boldsymbol{p}} . \tag{3-40}$$

The crystalline slip is governed by the Schmid's law, in which the slipping rate ($\dot{\gamma}$) in any particular slip system is assumed to depend on the so-called *Schmid stress* $\boldsymbol{\tau}^{(\alpha)}$, just the resolved shear stress when elastic distortions are negligible. The relation between the Schmid stress and the current Cauchy stress ($\boldsymbol{\sigma}$) is given by the equation (Rice, 1970; Hill, 1967; Mandel, 1965)

$$\boldsymbol{\tau}^{\alpha} = \boldsymbol{m}^{*\alpha}\frac{\rho_0}{\rho}\boldsymbol{\sigma}\boldsymbol{s}^{*(\alpha)}, \tag{3-41}$$

where ρ_0 and ρ are the mass density in the reference and current states. The rate of change of Schmid stress ultimately is given by the equation in (Hill and Rice, 1972) as

$$\dot{\boldsymbol{\tau}}^{(\alpha)} = \boldsymbol{m}^{*\alpha}\left[\dot{\hat{\boldsymbol{\sigma}}} + \boldsymbol{\sigma}\,(\boldsymbol{I}:\boldsymbol{D}^{*}) - \boldsymbol{D}^{*}\boldsymbol{\sigma} + \boldsymbol{\sigma}\boldsymbol{D}^{*}\right]\boldsymbol{s}^{*(\boldsymbol{\alpha})} . \tag{3-42}$$

Now the next step is to determine the evolution of shear-strain $\dot{\gamma^{\alpha}}$ by the corresponding τ^{α}. A Power law (Hutchinson, 1976) is used to predict the plastic slip-rates in a single-crystal. The viscoplastic expression of flow rule is as follows:

$$\dot{\gamma^{\alpha}} = \dot{\gamma_o^{\alpha}}\ \mathrm{sgn}\,(\tau^{\alpha})\left|\frac{\tau^{\alpha}}{g^{\alpha}}\right|^{n}, \tag{3-43}$$

where $\dot{\gamma_o^{\alpha}}$ is the reference strain-rate on slip system α, g^{α} is the strength of each slip system and a functional of the past slip history, i.e., accumulated plastic strains during previous increments of loading, sgn (·) returns an integer indicating the sign of an argument (·) and n represents the rate sensitivity of the crystal. A rate-independent material (n goes to large numbers) is treated as a limit of rate-dependent plasticity.

Strain-hardening of each slip system is characterized by the evolution of strengths through the incremental relation:

$$\dot{g}^{(\alpha)} = \sum_{\beta} h_{\alpha\beta}\dot{\gamma}^{(\beta)}, \qquad 3\text{-}44$$

where $h_{\alpha\beta}$ are the slip hardening moduli and summation is performed over all activated slip systems. In this equation $h_{\alpha\alpha}$ represent the self-hardening moduli where no summation is done and $h_{\alpha\beta}$ $(\alpha \neq \beta)$ represent latent hardening moduli relating the rate of hardening on each system, which is most naturally defined w.r.t. the rotating crystal lattice (Wu *et al.*, 1991). Different hardening models used in crystal-plasticity are presented in Table 3-1.

Table 3-1: Different hardening models

Hardening model	Description	Observation
(Taylor, 1938)	Isotropic hardening	No information about latent hardening
(Nakada and Keh, 1966) (Havner and Shalaby, 1978)	Latent hardening is incorporated.	Predicts strong latent hardening.
(Peirce *et al.*, 1982) (PAN)	A modified model of latent hardening is suggested.	More in accord with experimental results, but Bauschinger effect is neglected.
(Wu *et al.*, 1991) (BW)	Three-stage hardening of crystalline materials is described.	An explicit expression of slip interactions between slip systems

As the PAN and BW models described in Table 3-1 are more in accord with experimental results, they are used in our numerical models. The self-hardening moduli in the PAN model are described by the following equation:

$$h_{\alpha\alpha} = h(\gamma) = h_0 \,\mathrm{sech}^2 \left|\frac{h_0\gamma}{\tau_s - \tau_0}\right|, \qquad 3\text{-}45$$

where h_0 is the initial hardening modulus, τ_0 is the yield stress equivalent to the initial value of current strength of the slip systems ($g^{(\alpha)}(0)$), τ_s is the break-through stress, where large plastic flow initiates, and γ corresponds to cumulative shear-strain on all slip systems and is described by

$$\gamma = \sum_{\alpha} \int_0^t \left|\dot{\gamma}^{(\alpha)}\right| dt \,. \qquad 3\text{-}46$$

In equation 3-45 the hyperbolic secant function is used to describe self-hardening starting with higher initial hardening and vanishing after reaching a saturation resolved shear stress (Figure 3-10). The latent hardening moduli are given by the following equation:

$$h_{\alpha\beta} = qh(\gamma)\ (\alpha \neq \beta), \qquad 3\text{-}47$$

where q is a latent to the self-hardening ratio. These expressions for hardening moduli neglect the Bauschinger effect in a crystalline solid.

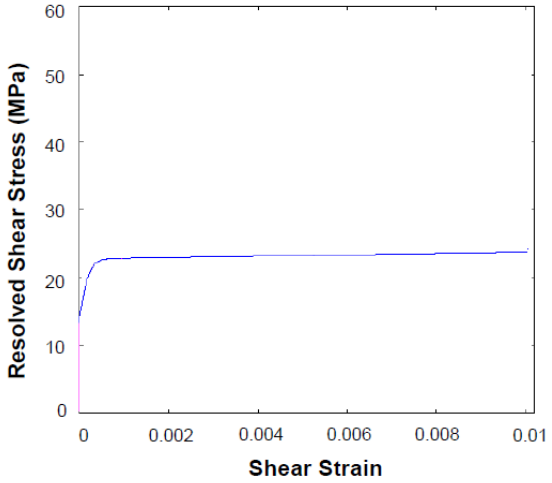

Figure 3-10: PAN model for self-hardening of slip system in single-crystal materials (Siddiq *et al.*, 2007)

In the BW model, a different expression for the hardening moduli is used to describe three-stage hardening of crystalline materials (Figure 3-11). In Figure

3-11, stage I corresponds to easy glide, where the crystal extends considerably at almost constant stress and slips on the primary slip system. In stage II as the geometry of the crystal changes as slip proceeds, slip may begin on a second slip system when the corresponding Schmid factor becomes compatible to that of the primary slip system with dislocations starting to glide on two slip systems; hence, further glide is inhibited due to interaction of slip systems. This phenomenon is called *work-hardening*. Stage III corresponds to extension at high stresses, where the applied force saturates sufficiently to overcome the obstacles. Therefore, the slope of the graph becomes progressively less steep. In stage III work-hardening saturates and it is finalized by the crystal's failure.

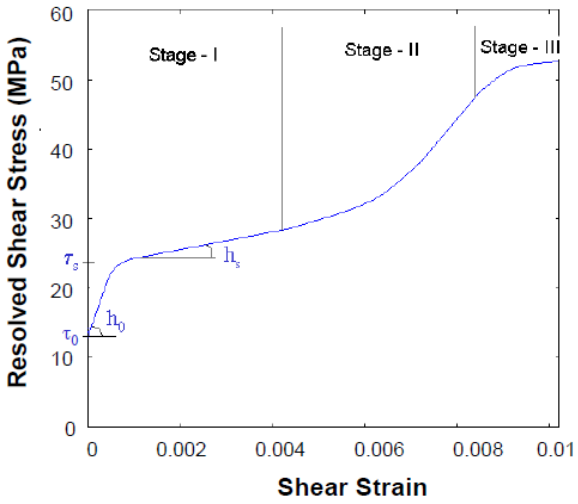

Figure 3-11: BW model for self hardening of slip system in single-crystal materials (Siddiq *et al*., 2007)

The hardening moduli in the BW model are described by the following equation depending on the shear-strains of all slip systems:

$$h_{\alpha\alpha} = \left\{(h_0 - h_s)sech^2\left[\frac{(h_0 - h_s)\gamma^{(\alpha)}}{(\tau_s - \tau_0)}\right] + h_s\right\} G\left(\gamma^{(\beta)}\right)\ (\beta \neq \alpha),$$
$$h_{\beta\alpha} = q h_{\alpha\alpha}\ (\beta \neq \alpha), \qquad 3\text{-}48$$

where h_s is the hardening modulus for the stage-I hardening (Figure 3-11), $\gamma^{(\alpha)}$ is the total shear-strain in slip system α and $\gamma^{(\beta)}$ is the total shear-strain in slip system

β. Here the function G represents interactive (cross) hardening that occurs between slip systems during the second and third stage of hardening and expressed by the following equation:

$$G\left(\gamma^{(\beta)}\right) = 1 + \sum_{\beta \neq \alpha} f_{\alpha\beta} \tan h\left(\gamma^{(\beta)}/\gamma_0\right) (\beta \neq \alpha), \quad 3\text{-}49$$

where γ_0 is the amount of slip, after which the interaction between slip systems reaches peak strength, and $f_{\alpha\beta}$ denotes the magnitude of strength of a particular slip interaction.

3.3 Mechanism-based strain gradient crystal-plasticity (MBSGCP) theory

The mechanism-based strain gradient crystal-plasticity theory (MBSGCP) used in this thesis was developed by Han *et al*. (2005) following the basic idea of mechanism-based strain gradient plasticity theory (MBSG), where the geometrically necessary dislocations are incorporated into the continuum plastic formulation via the Taylor relation (Taylor, 1938):

$$\tau = \alpha_{\mathrm{T}} \mu_s b \sqrt{\rho_s + \rho_G}, \quad 3\text{-}50$$

where α_{T} is an empirical coefficient, μ_s is the shear modulus, b is the magnitude of Burgers vector, and ρ_s, ρ_G are densities of statistically stored dislocations and geometrically necessary dislocations, respectively. In this theory an effective density of GNDs for a specific slip system is defined via a continuum analog of the Peach-Koehler force in dislocation theory (Han *et al*., 2005). This theory, belonging to the category of lower-order strain gradient models, is generalization of the conventional crystal-plasticity theory, i.e. the mechanism-based strain gradient crystal-plasticity theory reduces to a conventional crystal-plasticity theory when the strain gradient vanishes or the level of non-uniform deformation is larger than the intrinsic length scale of the material.

In dislocation theory, Peach-Koehler force is one of the most important concepts to describe the energetic force on a dislocation line element and given by for a volume element as

$$\tilde{\boldsymbol{\zeta}}_{\mathrm{L}}^{\mathrm{net}} = \sum_{k} \tilde{\boldsymbol{\zeta}}_{\mathrm{L}}^{k} = \sum_{k} -\tilde{\boldsymbol{l}}_{k} \times (\tilde{\boldsymbol{P}}^{\mathrm{T}} + \sum_{j \neq k} \tilde{\boldsymbol{P}}_{j}^{\mathrm{T}})\, \tilde{\boldsymbol{b}}_{k}, \tag{3-51}$$

where $\tilde{\boldsymbol{b}}_{k}$, $\tilde{\boldsymbol{l}}_{k}$ are unit vectors of dislocations k and $\tilde{\boldsymbol{P}}^{\mathrm{T}}$ is the Mandel stress. For a group of dislocations, $\tilde{\boldsymbol{\zeta}}_{\mathrm{L}}^{\mathrm{net}}$ can be written as (Han *et al.*, 2005)

$$\tilde{\boldsymbol{\xi}} = -\tilde{\boldsymbol{A}} \times \tilde{\boldsymbol{P}}^{\mathrm{T}}, \tag{3-52}$$

where $\tilde{\boldsymbol{A}}$ is the dislocation density tensor and corresponds to $\tilde{\boldsymbol{A}} = (J_{\mathrm{p}})^{-1} \boldsymbol{F}^{\mathbf{p}} \mathrm{Curl} \boldsymbol{F}^{\mathbf{p}}$ with $J_{\mathrm{p}} = \det(\boldsymbol{F}^{\mathbf{p}})$. The dislocation density tensor defined here has a dimension of [1/Length] deviating slightly from a more common definition of [1/(Length)^2] due to direct linkage of $\tilde{\boldsymbol{A}}$ with the strain gradient (Han *et al.*, 2005). Equation 3-52 can be considered as a dislocation density force $\tilde{\boldsymbol{\xi}}$ acting on GNDs by $\tilde{\boldsymbol{P}}$. As the shear stress resolved onto a specific slip system α is $\tau^{\alpha} = \tilde{\boldsymbol{P}}.(\tilde{\boldsymbol{s}}^{\alpha} \otimes \tilde{\boldsymbol{m}}^{\alpha})$, the resolved dislocation density force can be written as

$$\tilde{\boldsymbol{\xi}}^{\boldsymbol{\alpha}} = -\tau^{\alpha} \tilde{\boldsymbol{A}} \times (\tilde{\boldsymbol{s}}^{\alpha} \otimes \tilde{\boldsymbol{m}}^{\alpha})^{\mathrm{T}}. \tag{3-53}$$

The projected density force $\tilde{\boldsymbol{\xi}}^{\boldsymbol{\alpha}}$ in this equation can be interpreted as a force acting on GNDs due to τ^{α}. When $\tilde{\boldsymbol{A}}$ is expanded as in (Arsenlis and Parks, 1999; Gurtin, 2002, Cermelli and Gurtin, 2002)

$$\tilde{\boldsymbol{A}} = \sum_{\alpha} (n_{\odot}^{\alpha} \tilde{\boldsymbol{s}}^{\alpha} \otimes \tilde{\boldsymbol{s}}^{\alpha} + n_{\perp}^{\alpha} \tilde{\boldsymbol{t}}^{\alpha} \otimes \tilde{\boldsymbol{s}}^{\alpha}), \tag{3-54}$$

where $\tilde{\boldsymbol{t}}^{\alpha} = \tilde{\boldsymbol{s}}^{\alpha} \times \tilde{\boldsymbol{m}}^{\alpha}$, $n_{\odot}^{\alpha}$ and $n_{\perp}^{\alpha}$ are the densities of screw and edge dislocations on slip system α. Then the equation 3-60 can be rewritten as

$$\tilde{\boldsymbol{\xi}}^{\boldsymbol{\alpha}} = -\tau^{\alpha}\tilde{\boldsymbol{m}}^{\alpha} \times \sum_{\beta} \tilde{\boldsymbol{s}}^{\alpha\beta}(n_{\odot}^{\beta}\tilde{\boldsymbol{s}}^{\beta} + n_{\vdash}^{\beta}\tilde{\boldsymbol{t}}^{\beta}) \qquad 3\text{-}55$$

As $\tilde{\boldsymbol{\xi}}^{\boldsymbol{\alpha}}$ is parallel to the slip plane, it can be expressed as

$$\tilde{\boldsymbol{\xi}}^{\boldsymbol{\alpha}} = -\tau^{\alpha}(\tilde{n}_{\vdash}^{\alpha}\tilde{\boldsymbol{s}}^{\alpha} - \tilde{n}_{\odot}^{\alpha}\tilde{\boldsymbol{t}}^{\alpha}), \qquad 3\text{-}56$$

where $\tilde{n}_{\vdash}^{\alpha}$ and $\tilde{n}_{\odot}^{\alpha}$ are effective dislocation densities associated with edge and screw dislocations of the slip system α. Then the norm $|\tilde{\boldsymbol{\xi}}^{\boldsymbol{\alpha}}| = |\tau^{\alpha}|\ n_G^{\alpha}$ provides an effective measure of dislocation density as $n_G^{\alpha} = \sqrt{(n_{\vdash}^{\alpha})^2 + (n_{\odot}^{\alpha})^2}$. The resolved dislocation force in equation 3-53 defines an effective density of GNDs on the slip system α as

$$n_G^{\alpha} = |\widetilde{\boldsymbol{A}} \times (\tilde{\boldsymbol{s}}^{\alpha} \otimes \tilde{\boldsymbol{m}}^{\alpha})^{\mathrm{T}}|. \qquad 3\text{-}57$$

In Fleck *et al.* (1994), it was demonstrated that for a single slip system strain gradients normal to the slip plane do not introduce lattice distortions; hence, do not contribute to the hardening of the slip system and are not contained in $\widetilde{\boldsymbol{A}}$. On the other hand; although, in the case of multiple slip systems, $\widetilde{\boldsymbol{A}}$ and $n^G = |\widetilde{\boldsymbol{A}}|$ can contain strain gradients normal to a given slip plane, equation 3-64 ensures that gradients normal to the specific slip plane α are excepted from contribution to the hardening on this specific system (Han *et al.*, 2005). This complies with the physical picture given by in Fleck *et al.* (1994).

Strain gradient formulations of crystal-plasticity were previously proposed by many authors. In the higher order strain gradient theories, such as proposed by Smyshlyaev and Fleck (1996) and Shu and Fleck (1999) higher order stresses and additional boundary conditions were required. In this framework, Regueiro *et al.* (2002) suggested a relationship between the dislocation density tensor and back stresses. Cermelli and Gurtin (2000) developed a general theory of GNDs by characterizing dislocations through a tensor measuring the local Burger's vector

per unit area. Gao *et al.* (1999) proposed a mechanism-based strain gradient plasticity theory (MBSGP) based on a multi-sale framework linking the micro-scale notion of SSDs and GNDs to the meso-scale notion of plastic strain and strain gradient. Shizawa and Zbib (1999), Menzel and Steinmann (2000) and Gurtin (2002) used kinematic hardening formulations, where second-order strain gradients were related to back stresses resulting from dislocation pile-ups in front of obstacles. In the case of problems with constant strain gradients such as plastically bent beam, these formulations predict no size dependence in contrast to experiments (Stölken and Evans, 1998) and discrete-dislocation simulations (Cleveringa *et al*., 1999).

In the lower order strain gradient theories the strain gradient effects are introduced directly into the evolutionary laws of the internal slip system variables. Although, these theories provide more physically intuitive approach to describe strain gradient effects without the need to include higher order stresses or additional boundary conditions, they are unable to describe problems which may require non-standard boundary conditions, such as the problem given in Shu *et al.* (2001). In this framework, Acharya and Bassani (2000) described a dependence of the work-hardening moduli on strain gradients with the help of a quadratic norm of a dislocation-density tensor. In the model of Arsenlis and Parks (2002), dislocation density state variables evolve from initial conditions according to equations based on fundamental concepts in dislocation mechanics such as the conservation of Burgers vector in multiplication and annihilation processes. Groma (1997) and Groma *et al*. (2003) developed models using a statistical description of dislocation interactions. Although these models are in good agreement with dislocation simulations (Yefimov *et al*., 2004), the classical hardening laws used in crystal-plasticity were abandoned in these models. On the other hand, Busso *et al*. (2000) and Han *et al*. (2005) attempted to link the evolution of slip system strength to the presence of GNDs; where, while in the former one the evolution of GNDs were linked to local slip rate gradients, in the latter MBSGCP model, GND densities were obtained from spatial gradients of the plastic shear strain on slip systems.

MBSGCP is a crystal-plasticity formulation of MBSG accounting for the effects of lattice anisotropy on size-dependent deformation due to dislocation hardening in a crystal (Han *et al*., 2005). In this model the intrinsic length scale of a material is given by:

$$l = \frac{{\alpha_{\mathrm{T}}}^2 {\mu_s}^2 b}{(g_0)^2}, \tag{3-58}$$

where g_0 stands for a reference slip resistance which is taken to be $\mu/100$. In this model, the effective slip resistance (g_T^α) takes the contribution of geometrically necessary dislocations g_G^α into account besides strain-hardening caused by SSDs (g_s^α) for slip system α as follows:

$$g_T^\alpha = \sqrt{(g_s^\alpha)^2 + (g_G^\alpha)^2}. \tag{3-59}$$

The slip resistance g_s^α is obtained using equation 3-44 as in the conventional crystal-plasticity theory, whereas the slip resistance g_G^α is calculated by

$$g_G^\alpha = g_0 \sqrt{l n_G^\alpha}, \tag{3-60}$$

where n_G^α stands for the effective density of GNDs. In the case of comparatively small deformation and negligible elastic strains, the displacement gradient can be decomposed additively such as $\nabla \boldsymbol{u} = \boldsymbol{H}_* + \boldsymbol{H}_{\mathrm{p}}$, where $\boldsymbol{H}_{\mathrm{p}}$ corresponds to the plastic distortion and $\boldsymbol{H}_*$ the lattice rotation (Cermelli and Gurtin, 2001). In the case of multiple slip, $\boldsymbol{H}_{\mathrm{p}}$ can be written as $\sum_\alpha (\gamma^\alpha \boldsymbol{s}^\alpha \otimes \boldsymbol{m}^\alpha)$ and the effective dislocation density tensor $\widetilde{\boldsymbol{A}}$ is reduced to $\widetilde{\boldsymbol{A}} = \sum_\alpha (\nabla \gamma^\alpha \times \boldsymbol{m}^\alpha) \otimes \boldsymbol{s}^\alpha$. This leads equation 3-57 to take the following form to compute the effective density of GNDs:

$$n_G^\alpha = \left| \boldsymbol{m}^\alpha \times \sum_\beta s^{\alpha\beta} \nabla \gamma^\beta \times \boldsymbol{m}^\beta \right|. \tag{3-61}$$

It is worth mentioning that finite strain theory was used in the simulations of the following chapters, where only the formulation of n_G^α is obtained based on the assumption of small deformation theory.

Equation 3-60 can be rewritten as follows using equation 3-58:

$$g_G^\alpha = \alpha_{\mathrm{T}} \mu_s \sqrt{b n_G^\alpha}. \tag{3-62}$$

Having calculated the effective slip resistance due to both SSDs and GNDs using the above equations, the plastic slip-rate is obtained using the following equation

$$\dot{\gamma^\alpha} = \dot{\gamma_o}^\alpha \operatorname{sgn}(\tau^\alpha) \left| \frac{\tau^\alpha}{g_T^\alpha} \right|^n, \tag{3-63}$$

where g_T^α corresponds to

$$g_T^\alpha = \sqrt{(g_s^\alpha)^2 + (\alpha_{\mathrm{T}} \mu_s)^2 b n_G^\alpha}. \tag{3-64}$$

The numerical procedure and the details of the implementation of the MBSGCP theory (equation 3-58 to 3-64) into conventional crystal-plasticity are discussed in the next chapter.

Chapter IV

4 Computational frameworks for strain gradient crystal-plasticity theory

In this chapter the solution framework for the strain gradient crystal-plasticity theory using the finite-element method (FEM) is presented. Here, the aspects of FEM pertaining to coupling with the constitutive equations are first dealt with. In the second part, an incremental formulation of the crystal-plasticity theory is explained. This chapter closes with the details regarding implementation of the mechanism-based strain gradient crystal-plasticity theory into the conventional crystal-plasticity theory.

The crystal-plasticity model was implemented in the implicit finite-element code ABAQUS/Standard using the user-defined material subroutine (UMAT), initially developed by Huang (1991) and modified by Kysar (1997). The UMAT subroutine has been further modified to account for the strain gradient theory. The details of the extension of the code are given at the end of this chapter. The reader is referred

to Dunne and Petrinic (2005) and the references therein for extended information about the computational plasticity.

4.1 Finite-element model

FEM is a general numerical scheme to solve complex engineering problems, where the application of the conventional analytical methods may be limited or impractical. The general premise of this method is to discretize an arbitrary domain into an assembly of simply shaped elements, in which differential equations are approximately solved (Figure 4-1). In each element, a convenient approximate solution is assumed and the conditions of overall equilibrium of the structure derived. Satisfaction of these conditions result in approximate solutions for the unknowns such as displacements, strains and stresses (Rao, 1999).

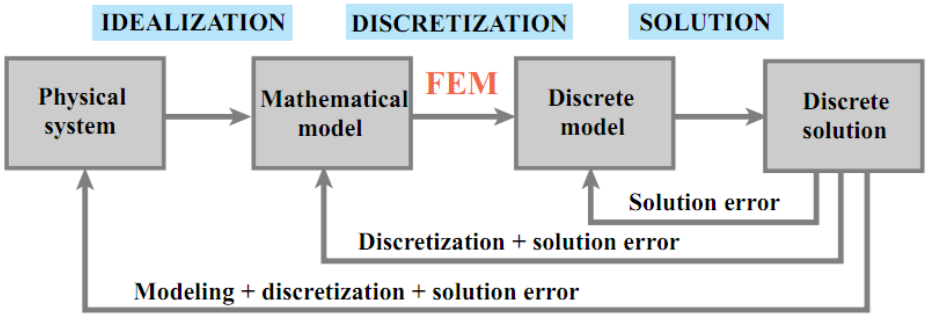

Figure 4-1: Steps of physical simulation process (Felippa, 2007)

An extended step-by-step process of FEM can be listed as follows (Huebner *et al.*, 2001):

- **Discretize the continuum**

The continuum is divided into elements.

- **Select interpolation functions**

Nodes are assigned to each element and the interpolation function represented by polynomials is chosen to represent the variation of the field variable over the element. Here, a displacement field is described using the shape function, $\boldsymbol{N}(\boldsymbol{x})$, with FE Ansatz as

$$\boldsymbol{u}(\boldsymbol{x}) = \boldsymbol{N}(\boldsymbol{x})\boldsymbol{d}^{\boldsymbol{e}} , \tag{4-1}$$

where $\boldsymbol{d}^{\boldsymbol{e}}$ represents the nodal displacement in the element e. $\boldsymbol{N}(\boldsymbol{x})$ describes how the nodal displacements are distributed throughout the element corresponding to 1 at the node location and 0 at the neighbouring nodes.

- **Find the element properties**

The matrix equations expressing the properties of individual elements are determined. The FEM expresses the dependent fields such as elastic strain $\boldsymbol{D}^*$ and stress $\boldsymbol{\sigma}$ as follows:

$$\boldsymbol{D}^* = \boldsymbol{u}' = \boldsymbol{B}\boldsymbol{d}^{\boldsymbol{e}} , \tag{4-2}$$

$$\boldsymbol{\sigma} = \boldsymbol{C}{:}\,\boldsymbol{D}^*, \tag{4-3}$$

where $\boldsymbol{u}'$ is the displacement gradient, $\boldsymbol{C}$ is the elasticity tensor and $\boldsymbol{B}$ is the strain matrix.

- **Assemble the element properties to obtain the system equations**

The matrix equations are combined to express the behaviour of the entire system with the following equilibrium equation:

$$\boldsymbol{\sigma}' + \rho\boldsymbol{b} = 0 , \tag{4-4}$$

where ρ is the density and $\boldsymbol{b}$ corresponds to body forces. Equation 4-4, written in a strong form, can be formulated in a weak form by introducing a field of test functions $\delta\boldsymbol{u}(\boldsymbol{x})$, selected to satisfy any prescribed kinematic constraint. The principle of virtual work now becomes

$$-\delta W = \int_{\Omega} \boldsymbol{\sigma}\delta\boldsymbol{D}^{*} d\,\Omega - \int_{\Omega} \rho\boldsymbol{b}\delta\boldsymbol{u} d\,\Omega - \int_{\Gamma} \boldsymbol{g}\delta\boldsymbol{u} d\,\Gamma\,, \tag{4-5}$$

where $\boldsymbol{b}$ and $\boldsymbol{g}$ are the components of body and surface loads, respectively, Ω represents the domain of continuum and Γ represents the traction boundary conditions. When equations 4-1 and 4-2 are inserted into equation 4-5, the following boundary-value problem is obtained:

$$\sum_{i=1}^{n_{el}} \delta\boldsymbol{d}^{i^{T}} \left\{ \int_{\Omega} \boldsymbol{B}^{T}\boldsymbol{\sigma} d\,\Omega - \int_{\Omega} \boldsymbol{N}^{T}\rho\boldsymbol{b} d\,\Omega - \int_{\Gamma} \boldsymbol{N}^{T}\boldsymbol{g} d\,\Gamma \right\} = 0\,. \tag{4-6}$$

Here, the assembly operator assembles the system of equations for each element.

- **Impose the boundary conditions**

The equations of the system are modified to account for the boundary conditions at the nodes or the elements.

- **Solve the system equations**

The set of simultaneous equations are solved to obtain the unknown nodal values such as displacement. In equation 4-6, the first term is called as internal nodal forces due to the induced stresses (equation 4-7) whereas the remaining part corresponds to external nodal forces due to body and traction forces (equation 4-8).

$$\boldsymbol{f_{int}} = \int_{\Omega} \boldsymbol{B}^{T}\boldsymbol{\sigma} d\,\Omega = \boldsymbol{k^{e}}\boldsymbol{d^{e}}, \tag{4-7}$$

$$\boldsymbol{f_{ext}} = \int_{\Omega} \boldsymbol{N}^{T}\rho\boldsymbol{b} d\,\Omega + \int_{\Gamma} \boldsymbol{N}^{T}\boldsymbol{g} d\,\Gamma. \tag{4-8}$$

The algebraic system of equations 4-7 and 4-8 constitutes equilibrium between internal and external nodal forces. Solving them using an iterative scheme reveals the solution, i.e. the displacement field. In equation 4-7 $\boldsymbol{k}^{\boldsymbol{e}}$ representing the stiffness of the element e is a function of displacement field for nonlinear systems, i.e. $\boldsymbol{k}^{\boldsymbol{e}} = \boldsymbol{k}^{\boldsymbol{e}}(\boldsymbol{d}^{\boldsymbol{e}})$.

- **Computation of other variables**

The other important fields such as strains and stresses are calculated from displacement field using equations 4-2 and 4-3.

4.1.1 Iterative Solution Technique

Iterative solution techniques in FE analysis are used to find the unknowns in nonlinear systems. The nonlinearity is defined as the dependence of the stiffness matrix on displacement and/or force. A nonlinear behaviour in solid mechanics may exist due to geometrical, material and contact nonlinearities.

Large rotations and displacements even with small strains cause geometric nonlinearity. In such cases, where deformation of a body is sufficiently large, the finite-deformation theory (see Section 3.2.1) is used rather than a small-strain theory. Nonlinearity may also be observed in case of relatively small displacements that exceed a dimension of the deformed body such as thin-sheet metals (Bathe, 1996).

Material nonlinearity occurs also when there exists a nonlinear relationship between strains and stresses, where a material behaviour depends on the current deformation state and past history of the deformation. It is worth pointing out that material nonlinearity should not necessarily be present only in non-elastic region, it can also be observed in the elastic region such as hyperplastic materials like rubber. On the other hand, gradual interaction of deformable bodies with other bodies during the deformation process is the source of contact nonlinearity.

Solution of nonlinear equations can be performed using various solution techniques, such as the Euler method, direct iteration method, modified Newton-Raphson method, quasi-Newton-Raphson method and Newton-Raphson method.

The Newton-Raphson method is selected for the solution of nonlinear equation systems studied in this thesis. The main motivation for this choice is the quick convergence rate of this method compared to others (Systemes, 2010).

The Newton-Raphson method is an iterative procedure and generally used to find a root of an equation. The nonlinear equation $f_{ext} = k^e d^e$ is written as the equilibrium of equations 4-7 and 4-8. To find the solution of this equation a residual function, $r(d) = f - k(d)d$, is defined. Here the main purpose is to minimize the residual, i.e. the displacement value, d, is recalculated until a certain amount of accuracy is reached.

Equation $r\left(d^{i-1}\right) = f - k\left(d^{i-1}\right)d^{i-1}$ describes how the residual is calculated after each iteration. The Taylor series expansion of the residual at the i^{th}iteration with an increment Δd^i is written as follows:

$$r\left(d^i\right) = r\left(d^{i-1} + \Delta d^i\right) = r\left(d^{i-1}\right) + \left[\frac{\partial r(d)}{\partial d}\right]_{d^{i-1}} \Delta d^i + \text{high} - \text{order terms}\,. \tag{4-9}$$

As the iteration advances the residual force, $r\left(d^i\right)$, is supposed to approach zero. When the high order terms are neglected due to their negligible contribution, it gives a rise to the following linear equation calculating the displacement increment:

$$\Delta d^i = \frac{-r\left(d^{i-1}\right)}{\left[\frac{\partial r(d)}{\partial d}\right]_{d^{i-1}}}, \tag{4-10}$$

where the denominator at the right-hand side is called the *Jacobian matrix*. The next approximation to the solution after each iteration is calculated as follows:

$$d^i = d^{i-1} + \Delta d^i\,. \tag{4-11}$$

The iteration continues until a certain amount of tolerance is reached.

The Newton-Raphson method is expensive per iteration as the Jacobian must be formed and solved at each iteration. Alternative methods such as the modified Newton-Raphson method, where the Jacobian is recalculated occasionally, or the approximate Newton-Raphson method, where an approximation to the Jacobian matrix is calculated, can be used for the solution of nonlinear problems (Systemes, 2010). However, these methods are not suitable in terms of accuracy for severely nonlinear cases, though they could lead to a shorter total solution time.

4.1.2 Convergence Control

The convergence criteria are assigned in the calculations in order to conclude the iterations when a desired value of accuracy is reached. There must be a compromise between accuracy and computational time for an effective computation. If a tight tolerance is selected, excessive computation effort is spent on unnecessary accuracy. If the tolerance is set too loose, the equilibrium error may be excessive and an inaccurate solution resulted. In the commercial FE software, the convergence criteria are based on a relative and/or an absolute value of residual forces, $\frac{(r(\Delta d^i))^T r(\Delta d^i)}{(r(d^i))^T r(d^i)} < \mathrm{TOL}$, and/or displacements, $\frac{(\Delta d^i)^T \Delta d^i}{(d^i)^T d^i} < \mathrm{TOL}$. Equilibrium is only assumed when both of the equilibrium checks for each iteration is satisfied. In our FE simulations 5×10^{-3} is taken as the criterion for residual force value.

4.1.3 Time Integration methods

To find the unknowns in the numerical analysis such as displacements, stresses and strains, the rate equations must be integrated with respect to time. As the constitutive rate equations are highly non-linear, integration is usually achieved incrementally, and stress and other state variables are updated in every increment. The computational algorithms for the time integration fall into two general classes: Explicit and implicit algorithms.

In an explicit algorithm, the information at time t is used to get the unknowns at time $t + \Delta t$ directly. The well-known explicit methods are a simple/forward Euler

method and Runge-Kutta method (Huang, 1991). In an explicit FEM analysis, the stiffness matrix is updated at the end of each increment, and then the next increment of load (or displacement) is applied to the system. One drawback of this method is that smaller time increments are required to have an accurate solution which in turn leads to longer computational time. Otherwise, the solution tends to drift from the correct solution. The time step for explicit methods is limited by the time that the physical wave crosses the element; therefore the solution time is comparable to the time required for the wave to propagate through the structure (Bathe, 1996). The critical time Δt_{cr} can be calculated from the mass and stiffness properties of the complete element assemblage:

$$\Delta t \leq \Delta t_{\mathrm{cr}} = \frac{T_{N\mathrm{min}}}{\pi} = \frac{2}{W_{N\mathrm{max}}} \leq \frac{2}{W_{E\mathrm{max}}}, \qquad 4\text{-}12$$

where Δt_{cr} is the critical time step size, $T_{N\mathrm{min}}$is the smallest period in the finite-element mesh, $W_{N\mathrm{max}}$ is the highest natural frequency of the system and $W_{E\mathrm{max}}$ is the highest natural frequency of all individual elements in a model (Bathe, 1996).

In an implicit algorithm, information at times t and $t + \Delta t$ is used to get the unknowns at time $t + \Delta t$. An example of a fully implicit method is the backward Euler method. In an implicit method, after each increment the analysis does Newton-Raphson iterations to enforce equilibrium of the internal structure forces with the externally applied loads within some user-specified tolerance (see Section 4.1.2). On the other hand, explicit analysis does not enforce any equilibrium. This fundamental difference qualifies implicit analysis to be more accurate. In implicit analysis, challenging problems can be handled quite efficiently such as cyclic loading, snap through, and snap back as long as sophisticated control methods such as arc length control, generalized displacement control are used. Since the stiffness matrix (Jacobian) in implicit analysis must be updated and reconstructed after each iteration, it is expensive computationally.

4.2 Incremental formulation of crystal-plasticity

In this section, the incremental formulation and complete algorithm of the crystal-plasticity theory discussed in Section 3.2.2 is explained. Geometric and/or material nonlinearity in crystal-plasticity require an incremental approach for integration of equilibrium equations. The tangent modulus method (Peirce *et al*., 1984) is used to determine the increment of plastic shear-strain in slip system α within the time increment Δt by the equation

$$\Delta\gamma^{(\alpha)} = \Delta t[(1-\theta_1)\dot{\gamma}_t^{(\alpha)} + \theta_1\dot{\gamma}_{t+\Delta t}^{(\alpha)}], \tag{4-13}$$

where θ_1 is an integration constant ranging from 0 to 1 depending on the implicit or explicit method. $\theta_1 = 0$ corresponds to the simple Euler time integration scheme, an explicit method, and if θ_1 varies between 0 and 1, it becomes a backward Euler integration scheme, which is an implicit method.

The Taylor expansion of slipping rate gives

$$\dot{\gamma}_{t+\Delta t}^{(\alpha)} = \dot{\gamma}_t^{(\alpha)} + \frac{\partial\dot{\gamma}^{(\alpha)}}{\partial\tau^{(\alpha)}}\Delta\tau^{(\alpha)} + \frac{\partial\dot{\gamma}^{(\alpha)}}{\partial g^{(\alpha)}}\Delta g^{(\alpha)}, \tag{4-14}$$

where $\Delta\tau^{(\alpha)}$ and $\Delta g^{(\alpha)}$ are the increments of resolved shear stress and current strength in slip system α within the time increment Δt, respectively. When equation 4-14 is inserted into equation 4-13, the following incremental relation is obtained:

$$\Delta\gamma^{(\alpha)} = \Delta t\left[\dot{\gamma}_t^{(\alpha)} + \theta_1\frac{\partial\dot{\gamma}^{(\alpha)}}{\partial\tau^{(\alpha)}}\Delta\tau^{(\alpha)} + \theta_1\frac{\partial\dot{\gamma}^{(\alpha)}}{\partial g^{(\alpha)}}\Delta g^{(\alpha)}\right]. \tag{4-15}$$

From equation 3-44, the incremental formulation of current hardening function can be written as

$$\Delta g^{(\alpha)} = \sum_{\beta} h_{\alpha\beta}\,\Delta\gamma^{(\beta)}. \tag{4-16}$$

The increments of resolved shear stress $\Delta\tau^{(\alpha)}$ can be obtained through equations 3-21, 3-37 and 3-42 as follows:

$$\partial\tau^{(\alpha)} = \left[C_{ijkl}\mu_{kl}^{(\alpha)} + w_{ik}^{(\alpha)}\sigma_{jk} + w_{jk}^{(\alpha)}\sigma_{ik}\right]\left[\Delta\varepsilon_{ij} - \sum_{\beta}\mu_{kl}^{(\beta)}\Delta\gamma^{(\beta)}\right], \tag{4-17}$$

where C_{ijkl} are the elastic moduli. $\mu_{ij}^{(\alpha)}$ and $w_{ij}^{(\alpha)}$ are "Schmid factors" for each slip system (α) and defined as

$$\begin{aligned} \mu_{ij}^{(\alpha)} &= \frac{1}{2}\left[s_i^{\alpha}m_j^{\alpha} + s_j^{\alpha}m_i^{\alpha}\right], \\ w_{ij}^{(\alpha)} &= \frac{1}{2}\left[s_i^{\alpha}m_j^{\alpha} - s_j^{\alpha}m_i^{\alpha}\right]. \end{aligned} \tag{4-18}$$

To compute the incremental relation for the shear-strain increment $\Delta\gamma$, equations 4-16 and 4-17 are inserted into equation 4-15, then the following equation is obtained:

$$\begin{aligned} \sum\Bigg\{\delta_{\alpha\beta} + \theta_1\Delta t\frac{\partial\dot{\gamma}^{(\alpha)}}{\partial\tau^{(\alpha)}}\left[C_{ijkl}\mu_{kl}^{(\alpha)} + w_{ik}^{(\alpha)}\sigma_{jk} + w_{jk}^{(\alpha)}\sigma_{ik}\right]\mu_{kl}^{(\alpha)} \\ - \theta_1\Delta t\frac{\partial\dot{\gamma}^{(\alpha)}}{\partial g^{(\alpha)}}h_{\alpha\beta}sign\left(\dot{\gamma}^{(\beta)}\right)\Bigg\}\Delta\gamma^{(\beta)} = \\ = \dot{\gamma}^{(\alpha)}\Delta t + \theta_1\Delta t\frac{\partial\dot{\gamma}^{(\alpha)}}{\partial\tau^{(\alpha)}}\left[C_{ijkl}\mu_{kl}^{(\alpha)} + w_{ik}^{(\alpha)}\sigma_{jk} + w_{jk}^{(\alpha)}\sigma_{ik}\right]\Delta\varepsilon_{ij}\,. \end{aligned} \tag{4-19}$$

The co-rotational stress increment $\Delta\sigma_{ij} = \hat{\dot{\sigma}}_{ij}\Delta t$ given in equation 3-36 can be written as

$$\Delta\sigma_{ij} = C_{ijkl}\Delta\varepsilon_{kl} - \sigma_{ij}\Delta\varepsilon_{kk} - \sum_{\alpha}\left[C_{ijkl}\mu_{kl}^{(\alpha)} + w_{ik}^{(\alpha)}\sigma_{jk} + w_{jk}^{(\alpha)}\sigma_{ik}\right]\Delta\gamma^{(\alpha)}. \tag{4-20}$$

The algorithm used in a UMAT subroutine is as follows. The first step is using the known strain, strain increment, orientation of the grain, current strength of a slip system and resolved shear stress at time t, the Schmid tensor and the shear-strain-rate are calculated using equations 4-18 and 3-43 and an initial value of $\Delta\gamma$ is predicted using equation 4-19. Next, new increments for the current strength of slip systems, the resolved shear stress and the stress increments are calculated with

equations 4-16, 4-17 and 4-20, respectively. Finally, the Newton-Raphson iterative scheme is applied until the convergence is reached according to the following residual equation

$$\Delta\gamma^{(\alpha)} - (1-\theta_1)\Delta t\dot{\gamma}_t^{(\alpha)} - \theta_1\Delta t\dot{\gamma}_{t+\Delta t} \leq \varepsilon, \qquad 4\text{-}21$$

where ε corresponding to an absolute error of shear-strains in slip systems is taken 10^{-5} in our simulations. Once the iteration has converged, the orientation update is performed for the crystal lattice with the following equations.

$$\Delta s_i^{*(\alpha)} = \left[\Delta\varepsilon_{ij} + W_{ij}\Delta t - \sum_{\beta} (\mu_{ij}^{(\beta)} + w_{ij}^{(\beta)})\Delta\gamma^{(\beta)}\right] s_j^{*(\alpha)}, \qquad 4\text{-}22$$

$$\Delta n_i^{*(\alpha)} = n_j^{*(\alpha)}\left[\Delta\varepsilon_{ij} + W_{ij}\Delta t - \sum_{\beta} (\mu_{ij}^{(\beta)} + w_{ij}^{(\beta)})\Delta\gamma^{(\beta)}\right]. \qquad 4\text{-}23$$

4.3 Numerical procedure in implementation of strain gradient theory

The mechanism-based strain gradient crystal-plasticity theory (MBSGCP) belongs to the category of the lower-order strain gradient theory. In this type of non-local plasticity theory neither higher-order stress nor additional boundary conditions are involved as in the conventional crystal-plasticity (CP) theory, only the strain gradient effects come into play through the incremental plastic modulus as explained in Section 3.3. All constitutive equations are therefore identical to those in CP; hence, the incremental formulation explained in Section 4.2 is also applicable for MBSGCP. The only modification is performed while calculating the shear-strain-rate, i.e. equation 3-63 is used in MBSGCP rather than equation 3-43. As the strain gradient in this theory is not calculated directly as an independent variable, unlike higher-order theories, linear hexahedral C3D8 brick element (Figure 4-2) can be used. In other words an inherent constant strain field in this element type does not restrict the application of the lower-order theory; however, it cannot be used in higher-order theories as no strain gradient evolves due to the

constant strain field. For such theories higher-order elements should be used (Busso *et al.*, 2000).

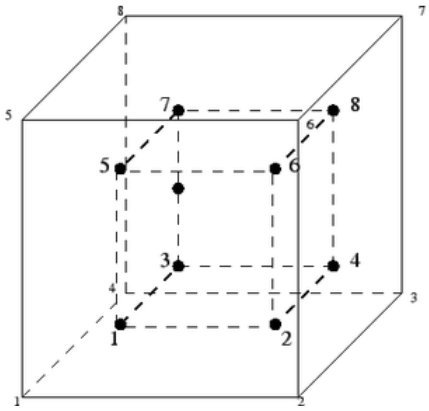

Figure 4-2: 2x2x2 integration points in eight-node hexahedral C3D8 brick element

To implement the MBSGCP constitutive model in UMAT, the strategic step is how to calculate the gradient of shear-strain $\nabla\gamma^{\beta}$ for each slip system (β) in equation 3-61 while calculating the incremental plastic modulus. To achieve this, the following steps are followed:

- At the end of each time increment, the shear-strain value ($\gamma_G^{(\alpha)(i)}$) at each gauss point (i, integration point) and slip system (α) is saved by means of the UMAT inherent looping over Gauss points for each element. As the shear-strain values are defined as state variables in the UMAT subroutine, they are updated for each time increment; hence, the state variables from the previous steps must be stored in a COMMON block.
- In the next step, the extrapolation scheme presented in equation 4-24 (Busso *et al.*, 2000) is employed to obtain shear-strain values at nodes $\gamma_N^{(\alpha)(i)}$ using the isoparametric shape functions $N^i(\psi)$ (Table 4-1)

$$\gamma_G^{(\alpha)(i)} = \sum_{i=1}^{8} N^i(\psi)\gamma_N^{(\alpha)(i)}, \qquad 4\text{-}24$$

where ψ given in

Table 4-2 corresponds to the isoparametric coordinates of the integration point. In this section, to distinguish the representation of integration point and node, non-bold (i) and bold characters ($\boldsymbol{i}$) are used, respectively. The isoparametric shape functions in equation 4-24 are constructed in such a way that it takes a unit value at node ($\boldsymbol{i}$) and is zero at all other nodes (Bathe, 1996). For instance, the value of first shape function is zero at all the nodes except the first node with coordinates (1, -1, -1). It is worth mentioning here that the sequence of nodes and integration points with respect to their coordinates (Figure 4-2) needs to be cared and addressed properly in equation 4-24. By inverting equation 4-24, the unknown corner nodal values can readily be determined from the solution of the inverse problem.

As an alternative way to the methodology explained above, another user subroutine, URDFIL, is used besides the UMAT subroutine to determine the shear-strain values at the nodes. As the subroutine URDFIL permits the user to read the results at the nodes at the end of each time increment while the analysis is running, the shear-strain values can be stored in COMMON blocks and passed into UMAT subroutine. Both methods were used in our FE simulations and give exactly the same results.

Table 4-1: Shape functions of the C3D8 linear brick element (Figure 4-2)

N^1	$\frac{1}{8}(1+\xi)(1-\eta)(1-\rho)$	N^5	$\frac{1}{8}(1+\xi)(1-\eta)(1+\rho)$
N^2	$\frac{1}{8}(1+\xi)(1+\eta)(1-\rho)$	N^6	$\frac{1}{8}(1+\xi)(1+\eta)(1+\rho)$
N^3	$\frac{1}{8}(1-\xi)(1+\eta)(1-\rho)$	N^7	$\frac{1}{8}(1-\xi)(1+\eta)(1+\rho)$
N^4	$\frac{1}{8}(1-\xi)(1-\eta)(1-\rho)$	N^8	$\frac{1}{8}(1-\xi)(1-\eta)(1+\rho)$

Table 4-2: Isoparametric coordinates $\boldsymbol{\psi}(\xi,\eta,\rho)$ of integration points

Integration point(i)	ξ	η	ρ
1	0.577	-0.577	-0.577
2	0.577	0.577	-0.577
3	-0.577	-0.577	-0.577
4	-0.577	0.577	-0.577
5	0.577	-0.577	0.577
6	0.577	0.577	0.577
7	-0.577	-0.577	0.577
8	-0.577	0.577	0.577

- Having obtained the shear-strain values at 8 nodes, the shear-strain gradients at 8 integration points are determined by calculating the spatial derivatives of linear shape functions, i.e. the spatial derivative of equation 4-24 as given in (Dunne *et al.*, 2007; Liang and Dunne, 2009 ; Busso *et al.*, 2000)

$$\nabla\gamma_G^{(\alpha)(i)} = \frac{\partial\gamma_G^{(\alpha)(i)}}{\partial \boldsymbol{x}} = \frac{\partial\gamma_G^{(\alpha)(i)}}{\partial(\psi)}\frac{\partial(\psi)}{\partial \boldsymbol{x}} = \sum_{i=1}^{8}(N^i(\boldsymbol{\psi})\nabla_{\boldsymbol{\psi}})\gamma_N^{(\alpha)(\boldsymbol{i})}J^{-1}, \qquad 4\text{-}25$$

where

$$J = \frac{\partial \boldsymbol{x}}{\partial(\boldsymbol{\psi})} = \sum_{i=1}^{8}\mathbf{Y}^i(N^i(\boldsymbol{\psi})\nabla_{\boldsymbol{\psi}}). \qquad 4\text{-}26$$

Here, $\nabla_{\boldsymbol{\psi}}$ is the nabla operator relative to the isoparametric coordinate system, J is the Jacobian matrix and $\mathbf{Y}^i$is the position of the integration points. With the known nodal values, $\gamma_N^{(\alpha)(\boldsymbol{i})}$, equation 4-25 is used to calculate the gradient of shear-strain $\nabla\gamma_G^{(\alpha)(i)}$ at each integration point (i) and for each slip system (α) based on the spatial derivative of shape functions given in Table 4-3, which depends on the isoparametric coordinates of the integration points (Table 4-2). For the convenience

of the reader, the values of spatial derivative of shape functions w.r.t. ξ were presented in Table 4-4. This methodology aids to calculate the gradients of strains from first order finite elements (C3D8). Similar approaches were also used in Siddiq et al. (2007) and Lee and Chen (2010).

Table 4-3: Spatial derivative of isoparametric shape functions $(N^i(\boldsymbol{\psi})\nabla_{\psi})$

Shape function (i)	$\frac{\partial N^i}{\partial \xi}$	$\frac{\partial N^i}{\partial \eta}$	$\frac{\partial N^i}{\partial \rho}$
1	$\frac{1}{8}(1-\eta)(1-\rho)$	$-\frac{1}{8}(1+\xi)(1-\rho)$	$-\frac{1}{8}(1+\xi)(1-\eta)$
2	$\frac{1}{8}(1+\eta)(1-\rho)$	$\frac{1}{8}(1+\xi)(1-\rho)$	$-\frac{1}{8}(1+\xi)(1+\eta)$
…….	…….	…….	…….
8	$-\frac{1}{8}(1-\eta)(1+\rho)$	$-\frac{1}{8}(1-\xi)(1+\rho)$	$\frac{1}{8}(1-\xi)(1-\eta)$

Table 4-4: The values of spatial derivative of isoparametric shape functions w.r.t. ξ $(N^i(\boldsymbol{\psi})\nabla_{\xi})$ at the integration points

(i)	ξ	η	ρ	$\frac{\partial N^1}{\partial \xi}$	$\frac{\partial N^2}{\partial \xi}$	….	$\frac{\partial N^7}{\partial \xi}$	$\frac{\partial N^8}{\partial \xi}$
1	0.577	-0.577	-0.577	0.083	0.022	….	-0.311	-0.083
2	0.577	0.577	-0.577	0.022	0.083	….	-0.083	-0.311
3	-0.577	-0.577	-0.577	0.083	0.311	….	-0.022	-0.083
4	-0.577	0.577	-0.577	0.311	0.083	….	-0.083	-0.022
5	0.577	-0.577	0.577	0.083	0.022	….	-0.311	-0.083
6	0.577	0.577	0.577	0.022	0.083	….	-0.083	-0.311

7	-0.577	-0.577	0.577	0.083	0.311	….	-0.022	-0.083
8	-0.577	0.577	0.577	0.311	0.083		-0.083	-0.022

In the following chapter, the material parameters of single-crystal b.c.c. Ti alloy are identified using the model of nano-indentation and micro-pillar-compression experiments. The strain gradient crystal-plasticity model is used therein. This constitutive law was implemented in the implicit finite-element code ABAQUS/Standard using the user-defined material subroutine (UMAT), initially developed by Huang (1991) and modified by Kysar (1997). This code is further developed by the author with regard to several aspects as follows:

- The mechanism-based strain gradient theory was implemented in the subroutine. To achieve this, UMAT and URDFIL subroutines are used within two different methods. The details can be found in Section 4.3.
- The implicit UMAT subroutine was converted to its explicit counterpart, VUMAT. This amendment enables to run simulations within an explicit analysis since the implicit one has convergence difficulties and needs enormous computational time. Of course, very fine time increments are needed in an explicit analysis of a model having rather small element sizes, which, in turn, leads to longer computational times. In this thesis mainly the implicit analysis is used.
- In the UMAT subroutine the parameters of the slip hardening model are assumed to be the same as those for the same set of crystallographically identical slip systems, although it could be different from those in other sets. Here the code is adjusted in such a way that it gives flexibility to define the slip hardening parameters individually even in the same set of slip systems. This modification enables to evaluate the local fields accurately for a b.c.c. crystal structure, where there exists a difference in the Peierls stress, i.e. different lattice resistance to dislocation motion in

twinning and anti-twinning direction corresponding to different slip parameters in the same set of slip systems.

- In the UMAT material subroutine, the shear-strain-rate value for each slip system is calculated using equation 3-43. During the calculations, when the resolved shear stress value (τ^{α}) exceeds strength of the slip system (g^{α}) as a result of any finite strain increment, $\dot{\gamma}^{\alpha}$ reaches very large values, especially becoming infinitely large when rate sensitivity (n) is large, such as 50 or 100, which, in turn, leads to termination of the analysis. To avoid this, smaller strain increments along the whole computational time domain should be used. This leads to very long computational time. To circumvent this problem, an additional statement is inserted in the code checking the ratio (τ^{α}/g^{α}). When this ratio reaches a critical threshold value (selected 1.3 in our analysis), the UMAT assigns a smaller time increment using the variable "PNEWDT", i.e. the code abandons the current time increment in favor of a time increment given by PNEWDT*DTIME (Systemes, 2010), where DTIME corresponds to the present time increment. This variable, PNEWDT, was selected 0.25 in our simulations.

- It is well known that deformation of the crystals leads to change in its orientation. Such orientation gradients need to be evaluated as they give hints about the deformation mechanism. In the subroutine, the lattice deformation and rotation are fully characterized by reciprocal vectors coinciding with slip directions and normal to slip planes in the deformed configuration. The modification is done in the following way: The initial orientation of the crystal ($ANGINIT(I,1)$, $ANGINIT(I,2)$, $ANGINIT(I,3)$) is saved in the COMMON blocks. The underlying reason is the slip directions and normals to slip planes defined as state variables in the subroutine are updated after each time increment; hence, the history of state variables should be saved in a common block, which could be accessed by the UMAT subroutine. In the second step, using the ATAN2 function and the present (($STATEV(34+3*I)$, $STATEV(35+3*I)$, $STATEV(36+3*I)$) and initial orientation of the crystal for each slip system (I), the

orientation changes are computed in all directions, defined as state variables ($STATEV(11 * NSLPTL + I)$, $STATEV(12 * NSLPTL + I)$, $STATEV(13 * NSLPTL + I)$) with the following formulations:

$$STATEV(11 * NSLPTL + I) = \Big(\mathrm{ATAN2}\big(STATEV(36 + 3 * I), STATEV(35 + 3 * I)\big) - \mathrm{ATAN2}\big(ANGINIT(I, 3), ANGINIT(I, 2)\big)\Big) * 180/\pi \quad 4\text{-}27$$

$$STATEV(12 * NSLPTL + I) = \Big(\mathrm{ATAN2}\big(STATEV(34 + 3 * I), STATEV(36 + 3 * I)\big) - \mathrm{ATAN2}\big(ANGINIT(\mathrm{I}, 1), ANGINIT(\mathrm{I}, 3)\big)\Big) * 180/\pi \quad 4\text{-}28$$

$$STATEV(13 * NSLPTL + I) = \Big(\mathrm{ATAN2}\big(STATEV(35 + 3 * I), STATEV(34 + 3 * I)\big) - \mathrm{ATAN2}\big(ANGINIT(I, 2), ANGINIT(I, 1)\big)\Big) * 180/\pi, \quad 4\text{-}29$$

where *NSLPTL* refers to the total number of slip systems.

Our first 3D FE nano-indentation simulations demonstrated that the solutions obtained using MBSGCP is time-increment-dependent; hence, temporal convergence cannot be obtained (Figure 4-3). The underlying reason is differences in the frequency of the updating of shear-strain values for each slip system due to existing strain gradients for different time increments. As explained in Section 4.3, strain gradients at present time for each slip systems are calculated using the shear-strain values from the previous time increment. When the smaller time increments are used, on the one hand, the slip systems evolves quicker as the contribution of GNDs is accounted for more frequently compared to larger time increments. To circumvent this problem, the formulation of strain gradient in equation 3-62 is modified as follows:

$$(g_G^{\alpha}) = \alpha_{\mathrm{T}} \mu_s \sqrt{b n_G^{\alpha}} . \frac{\Delta t}{t_{\mathrm{total}}} \quad 4\text{-}30$$

These two modifications can be also presented in a single equation by reformulating equation 3-61 as

$$n_G^{\alpha} = \left| m^{\alpha} \times \sum_{\beta} s^{\alpha\beta} \nabla \gamma_G^{(\alpha)(i)} \left(\frac{\Delta t}{t_{\text{total}}}\right)^2 \times m^{\beta} \right|. \qquad 4\text{-}31$$

The change in equation 4-30 is performed to correlate the slip resistance due to GNDs with the used time increment. With these modifications, the dependency of solutions on the time increment is not allowed as seen from Figure 4-4. Detailed information about the obtained load-displacement curves can be found in Chapter 6.

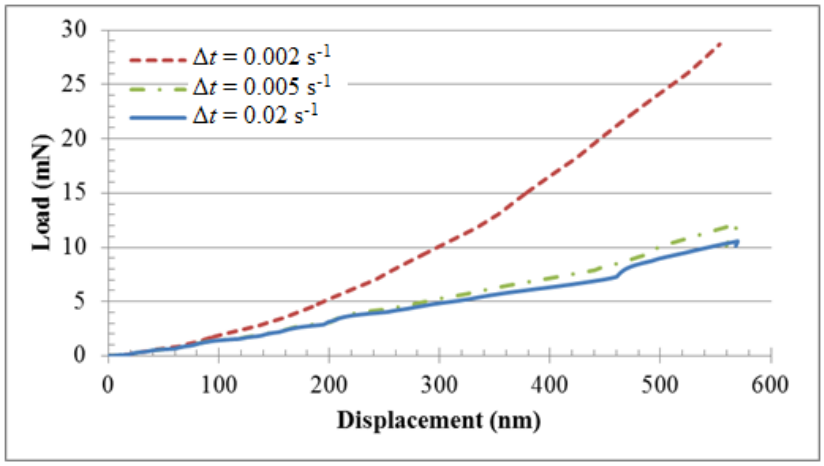

Figure 4-3: Nano-indentation simulations: Load-displacement curves obtained using different time increments with MBSGCP

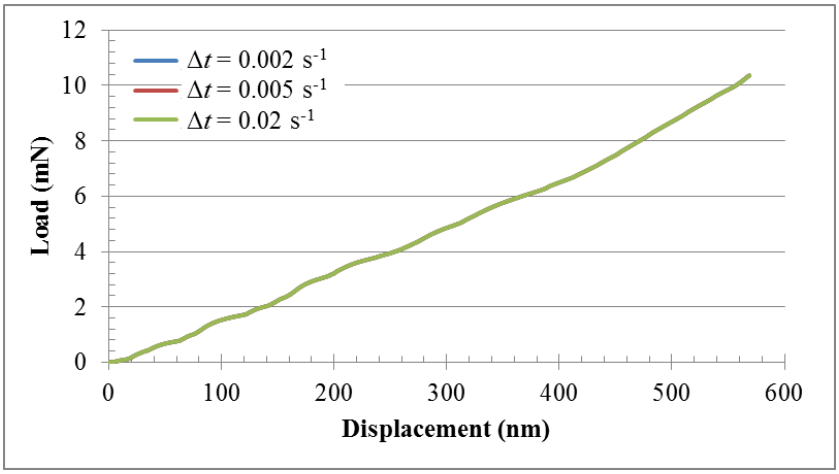

Figure 4-4: Nano-indentation simulations: Load-displacement curves obtained using different time increments with modified MBSGCP

To demonstrate the successful implementation of the MBSGCP theory in UMAT subroutine, here a simple bending problem was studied. As seen in Figure 4-5, a rectangular f.c.c. single crystal in the unrotated state ((100) orientation) with dimensions of 2.5 μm × 1.0 μm × 4.0 μm was deformed by imposing a displacement constraint on the side surfaces with a maximum displacement value of 0.5 μm on the top and bottom lines whilst decreasing linearly towards the center and become zero at the center line. This model was developed intentionally to obtain a constant strain gradient through the specimen's height.

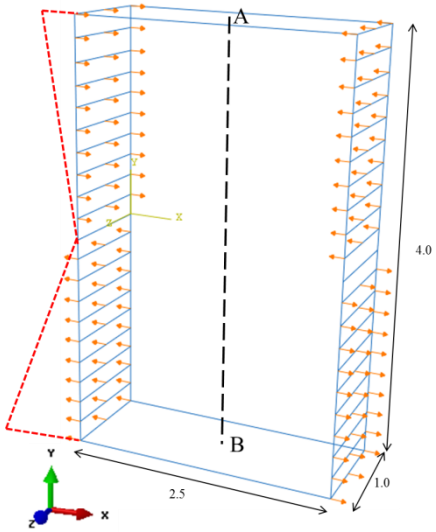

Figure 4-5: Bending model. Purple lines represent the direction of the displacement imposed on the edges and red lines represent the magnitude of its variation through the thickness (Dimensions in μm)

Figure 4-6 demonstrates the resulting distribution of total cumulative shear strains on all slip systems (sum of the absolute values of shear strains in all slip systems) in the deformed body (for the undeformed shape) while Figure 4-7 shows its variation through path A-B (Figure 4-5). As expected cumulative shear values were largest at points A and B and decreases towards the center and insignificant at the

very center of this path. To evaluate the influence of strain gradients, effective density of GNDs on the first slip system (at full loading) ($n_G^{(1)}$), correlated with the shear strain gradients in equation 4-31, was plotted. Figure 4-8 revealed that the GNDs were observed to be similar through the height of the deformed sample as expected due to a linear variation of shear strains on path A-B, i.e. constant gradients. However, as this variation was not linear in the center of this path and was not as steep as the other sections (Figure 4-6 and Figure 4-7), the corresponding effective density of GNDs was observed to be less. This study justified the successful implementation of the shear strain gradient theory as the constant GNDs were predicted on the respective path successfully.

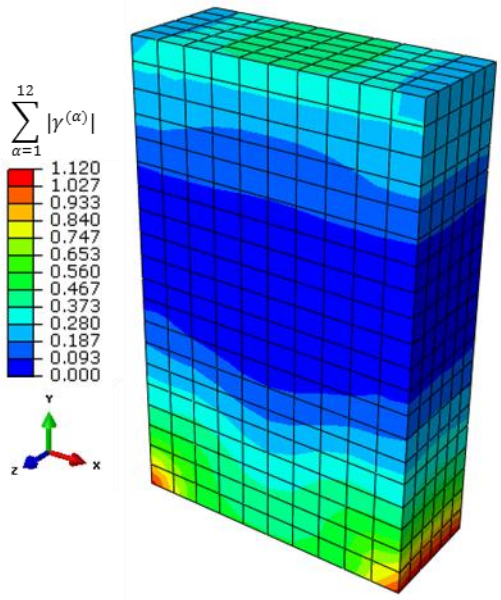

Figure 4-6: Distribution of total cumulative shear strains on all slip systems (sum of the absolute values of shear strains in all slip systems) obtained with FE simulations of the bending problem

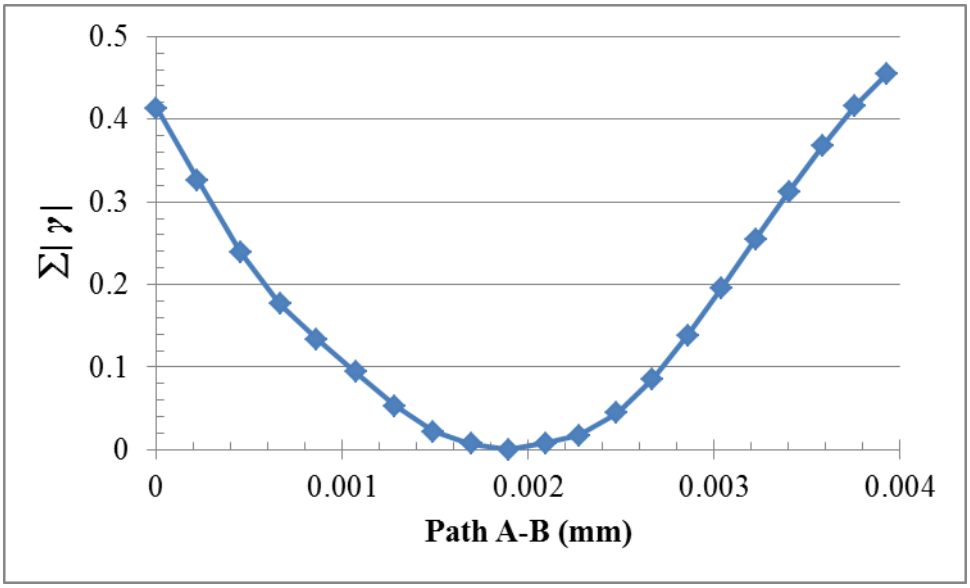

Figure 4-7: Distribution of total cumulative shear strains on all slip systems (sum of the absolute values of shear strains in all slip systems) at full loading obtained with FE simulations through path A-B.

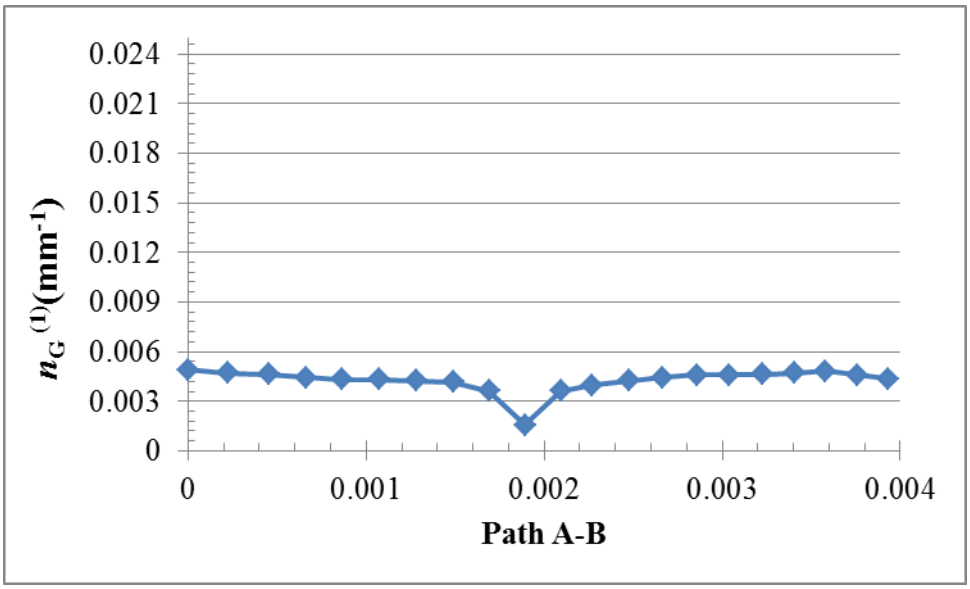

Figure 4-8: Distribution of effective density of GNDs ($n_G^{(1)}$) at full loading obtained with FE simulations through path A-B.

In the next two chapters, the size effect in micro-pillar compression and nano-indentation experiments for single crystal b.c.c. Ti alloy were discussed extensively,

respectively. The block diagram (Figure 4-9), as an extension of Figure 1-2, demonstrates the detailed methodology used in the relevant chapters.

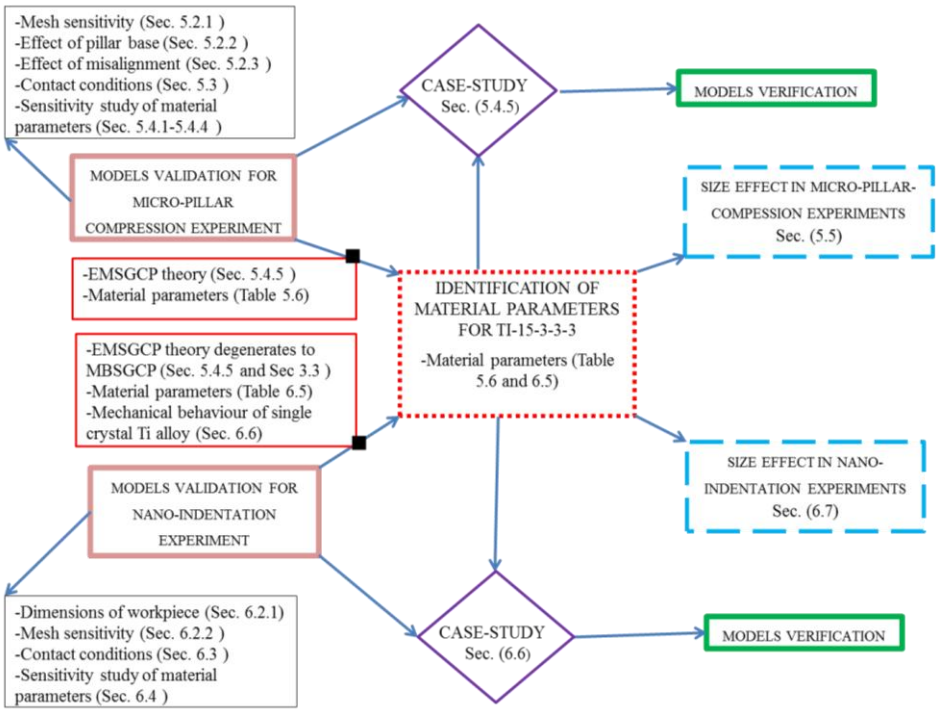

Figure 4-9: Summary of the research methodology to describe size effects in micro-pillar compression and nano-indentation experiment

Chapter V

5 Size effect in beta-phase Ti alloy

The aim of this chapter is to characterize a size effect in b.c.c. cubic beta phase of Ti alloy at micron-scale. To achieve this, a micro-pillar-compression experiment for different pillar sizes is performed. A FE model of this experiment is developed for identification of material parameters. This also enables extraction of information, which is not possible in the experiments, such as local fields of stresses and strains inside the pillar body or contribution of different slip systems during deformation.

In the first part of this chapter, the details regarding the performed experiments are given. In the second part, numerical modelling of the experiment is discussed and a 3D FE model is developed on the study of its different aspects such as mesh sensitivity, effect of substrate, misalignment between an indenter's tip and a pillar's top surface. It is followed by a thorough analysis of contact conditions in the model. In the following of this chapter, material parameters of beta-phase Ti alloy is determined using a strain gradient crystal-plasticity constitutive law and an extensive sensitivity analysis of the material parameters is performed and different

notions are considered to model the size effect such as fabrication of pillars or pre-existing strain gradients. This chapter closes with a thorough numerical analysis of the studied micro-pillar-compression experiment using the set of parameters obtained in the chapter.

5.1 Experimental details

This section starts with analysis of information about the material under investigation followed by the details of the performed experiments.

5.1.1 Material under investigation: Ti15V3Cr3Al3Sn

The material under investigation in this thesis is Ti15V3Cr3Al3Sn (Ti-15-3-3-3) (a titanium-based beta-alloy). Ti-15-3-3-3 belongs to the group of metastable β-titanium alloys and it has a single-phase b.c.c. crystal structure. In the following the material properties of Ti alloy are explained.

Titanium after aluminium, iron and magnesium is the fourth most popular metal on this planet with a fraction of about 0.6 % (Lütjering and Williams, 2007). Titanium is known for its high strength-to-weight ratio but it is an expensive material. The reason for its high price is due to its high reactivity with oxygen, which entails the use of an inert atmosphere or a vacuum during production and the melting process. Titanium is a strong metal with low density. Aluminium challenges titanium in lightweight structural applications, but this metal has a lower melting point (Table 5-1), thereby making titanium convenient in high-temperature applications (Lütjering and Williams, 2007). Titanium is a quite ductile metal especially in an oxygen-free environment and it has a fairly low electrical and thermal conductivity (Table 5-1).

Table 5-1: Comparison of titanium with aluminium (Lütjering and Williams, 2007)

Material features	Ti	Al
Melting temperature (°C)	1670	660

Density (g/cm^3)	4.5	2.7
Young`s modulus	115	72
Yield stress (MPa)	1000	~500
Thermal conductivity (W/m.K)	21.9	237
Comparative price	Expensive	Medium
Comparative corrosion resistance and reactivity with oxygen	Very high	High

Pure titanium, depending on a temperature range, exists in different crystallographic structures. The transus temperature, the temperature that separates different crystal structures, of Ti is 882°C. Below the transus temperature, titanium is stable in the α-phase and above the transus temperature it is stable in β-phase. The alpha stabilizers such as aluminium (Al), gallium (Ga), germanium (Ge), carbon (C), oxygen (O), and nitrogen (N) raise the α - β transition temperature. On the other hand, beta stabilizers such as molybdenum (Mo), vanadium (V), tantalum (Ta), niobium (Ni), manganese (Mn), iron (Fe), chromium (Cr), cobalt (Co), nickel (Ni), copper (Cu) and silicon (Si) lower the transition temperature (Joshi, 2006). β-phase titanium is known to be more ductile, whereas its α-phase counterpart is less ductile.

Pure Ti has acceptable mechanical properties and has been used in medical applications such as orthopaedic, dental implants, artificial hips, etc. as it does not react within the human body. For advanced engineering applications, the mechanical performance of Ti needs to be improved. This is accomplished by titanium alloys, where alloying elements are mixed with titanium. This mixture has a solid solubility assisting by undergoing precipitation strengthening. For instance, alloying elements like aluminium (Al), vanadium (V), iron (Fe), chromium (Cr), tin (Sn) and silicon (Si) increase the tensile yield strength value significantly. Titanium alloys have very high tensile strength and toughness, light weight (even at extreme temperatures) and extraordinary corrosion resistance. However, the high cost of production of titanium alloys limits their use to military applications,

spacecraft, medical devices and special components (connecting rods, engine) of expensive cars.

In this thesis based on research performed within the MaMiNa[1] project (Macro, Micro and Nano aspects of Machining), the size effect in Ti-15-3-3-3 is investigated. The chemical composition of the alloy is given in Table 5-2. The Ti-15-3-3-3 alloy is developed during the 1970`s on an Air Force contract to lower the cost of titanium sheet metal parts by reducing processing cost through the capability of being strip producible and its excellent room-temperature formability (Siemers, 2010). This solute-rich titanium alloy belongs to the group of metastable β-titanium alloys with martensite start temperature of below room temperature, thereby leading to the formation of an oversaturated β-microstructure when it is water-quenched or air-cooled from above β-transus temperature (Siemers, 2010).

Table 5-2: Composition of Ti-15-3-3-3

	Ti	V	Cr	Al	Sn
Ti-15-3-3-3	76%	15%	3%	3%	3%

The alloy Ti-15-3-3-3 was produced at *GfE Metalle and Materialien GmbH* in Germany. In the first stage of production, titanium sponge coming from Kazakhstan has been mixed with different pre alloys (85V-15Al and 50V-40Cr-10Al) and pure tin (Sn) which compacted to an electrode of 120 mm diameter. In the second stage the electrode was molten into a first ingot (160 mm diameter) in a VAR furnace followed by VAR remelting step, which, in turn led to the final ingot diameter of 200 mm. In the third stage these round bars were deformed at 850°C by rotary swaging in several steps to reduce the diameter of bars to 78 mm, which were later water-quenched from 700°C (as received state). Ultimately the material was solution-treated at 790°C for 30 minutes followed by air cooling. This final process led to microstructure consisting of pure β-grains, without any α- or γ'-precipitates. The average grain size of the body-centred cubic (b.c.c.) Ti alloy was

[1] The MaMiNa project combine the work of seventeen European universities, research institutions and industrial companies to analyse and improve the machinability of three selected alloys that are widely used in the industry, namely Ti15V3Cr3Al3Sn, Ni-based alloy 625 and Ti6Al2Sn4Zr6Mo.

about 1000 µm (Siemers, 2010). The microstructure analysis was performed by optical microscopy and electron backscatter diffraction (EBSD).

The specimen was polished before performing the experiments. The mechanical polishing procedure was followed by 12 hours of vibratory polishing in a solution of oxide polish suspension (OPS, containing silicon dioxide particles with diameter of 0.04 µm) and hydrogen peroxide in a proportion of 4:1 to remove the damage induced by mechanical polishing. Indentation tests were conducted on the present vibro-polished sample and an electro-polished sample for comparison, showing good agreement of the mechanical properties. Thus, vibratory polishing was shown to be a sufficient technique to remove the surface damage layer induced during mechanical polishing.

5.1.2 Micro-pillar compression experiment

The micro-pillar compression experiments were performed at Swiss Federal Laboratories for Materials Testing and Research (EMPA). Micro-pillars with square cross sections, with the edge length varying between 1 µm and 2 µm were fabricated in a single grain of a polycrystalline sample, by using a dual beam FIB / SEM Tescan FIB Lyra instrument (Figure 5-1 and Figure 5-4). The exact orientation of the grain, along the compression axis of the micro-pillars was (0.489 0.443 0.751). The aspect ratio (i.e. a ratio of height to the edge length) was kept constant at approx. 2.1.

To find a compromise between a fabrication time and accuracy of the process, pillars were produced in consecutive steps using different energies. The first step was conducted using a current of approx. 4 nA; for obtaining the final shape lower energies were used, approx. 0.15 nA (for a micro-pillar with a 1 µm edge length) and 0.79 nA (2 µm), respectively, while the voltage was kept constant at 30 kV.

All the compression tests were carried out inside a Zeiss DSM 962 scanning electron microscope (SEM), using a micro-indenter designed by EMPA in cooperation with the Institute of Materials Science, Swiss Federal Institute of Technology Lausanne (Rabe *et al.*, 2004), which allows precise pillar-punch

positioning and *in situ* characterization of deformation events. A flat punch tip was used to compress the pillars in order to achieve a homogeneous contact over the whole surface of the pillar and, thus, to enable an ideally uniaxial state of stress (In fact, the stress state is not fully uniaxial due to the tapered shape of the pillar and misalignment between the tip and pillar). All the pillars were compressed in a displacement controlled mode at a strain-rate of approx. 1×10^{-4} s^{-1}. A Hitachi S4800 high-resolution SEM system was used for imaging the pillars before and after compression.

The active slip system was identified by comparing SEM pictures of the compressed pillar and pole-figures of the EBSD scan (Figure 5-2). It should be emphasized that the typical uncertainty in EBSD measurements was between 0.5° and 1.4° (Nowag *et al.*, 2012). The slip direction / Burgers vector was assigned by the projected direction, in which the top part of the pillar moved, as indicated in Figure 5-2 by the red arrows in the SEM picture (top right) and {111} pole-figure (top left). This direction is in compliance with exactly one {111} direction, represented by an intersection point in the pole-figure. The direction $[1\bar{1}1]$ is therefore found to be the active slip direction.

Second, a line of intersection between the active slip-plane and pillar surface, highlighted in Figure 5-2 (top right) in green, can be used to identify the active slip plane. However, as pole-figures depict only crystallographic directions and no planes, the active slip plane has to be determined via direction of its corresponding normal, as shown in the {112} pole-figure (Figure 5-2, bottom left). Again, exactly one matching plane was found and no compliance was achieved for other possible families of slip planes - {011} and {123}. Hence, the matching point is the normal of our slip-plane, identified to be (121). This result is manifested by comparison of the angle between the surface and slip plane measured using SEM (Figure 5-2, bottom right) and its theoretically calculated magnitude. They were found to be 30° and 29.7°, respectively, and thus exhibit excellent agreement.

A similar analysis was conducted for all the pillars, and it was found that, irrespective of the pillar-size, deformation took places by single slip on the slip

system $(121)[1\bar{1}1]$. This particular system exhibits a Schmid factor of 0.4, the highest of all possible slip systems of {112} <111> type.

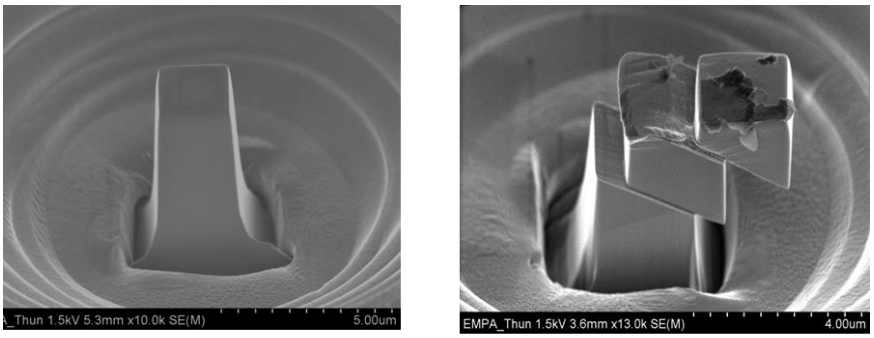

(a) (b)

Figure 5-1: SEM images showing Ti-15-333 single-crystal micro-pillar C (Figure 5-4) before (a) and after (b) compression

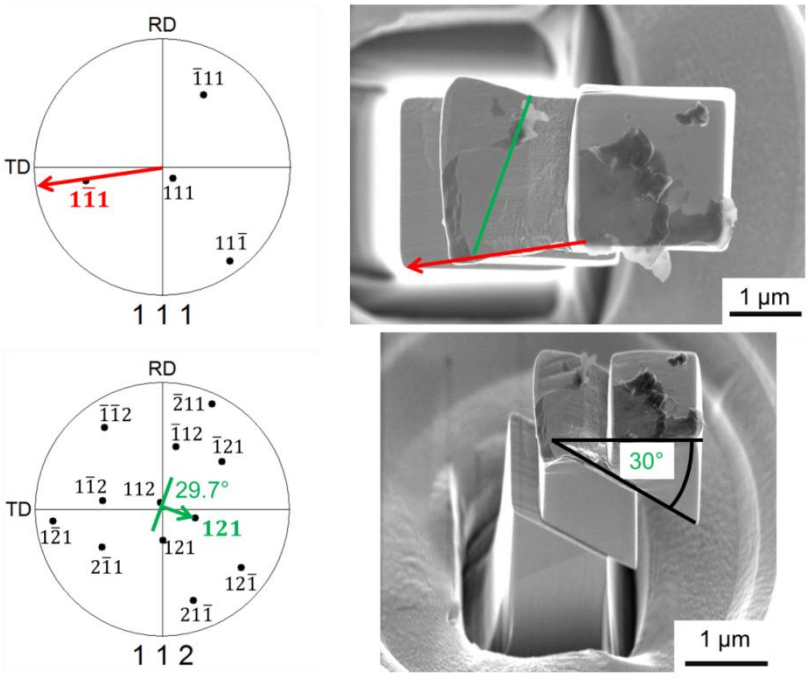

Figure 5-2: Determination of active slip system by comparing EBSD pole-figures for {111} (top left) and {112} directions (bottom left) with SEM images taken after compression from top (top right) and under 45° tilt (bottom right, dimensions corrected for tilt). The active slip system was found to be $(121)[1\bar{1}1]$.

Figure 5-3 demonstrates experimentally obtained average stress-strain curves for pillars A, B and C, where pillar A is the smallest pillar and pillar C is to the largest one (Figure 5-4). Average yield strength of micro-pillars is observed to increase greatly with decreasing edge length, which provides evidence of a strong size effect. It should be pointed out that due to limitations in the accessibility of the micro-pillar compression experimental set up at EMPA, single tests were performed. The obtained results seem to be promising and consistent with the studies in the literature (Greer and De Hosson, 2011). Based on these results, the material parameters of single crystal Ti alloy were determined using the methodology explained in this and next chapters.

In the experimental procedure of micropillar compression experiments several errors may occur due to following reasons. Firstly, tapered shape of the pillars induced during FIB milling could lead to a comparatively non-homogenous state of stress (Kiener *et al.*, 2007; 2009). Secondly, due to misalignment between pillar's upper surface and the indenter tip, stress concentrations may occur on this region of pillar, which, in turn, leads to its buckling and hence induce a bending component (Kiener *et al.*, 2007; 2009). Thirdly, due to FIB milling process, a damaged layer (range of several tens of nm, additional defects and dislocation loops) on the pillar surface may be introduced, which may influence the observed size effect in the experiments. The possible stress concentrations located on the transition region between the pillar and its substrate may also affect the resulting measurements. These points were discussed in detail numerically in Section 5.2.2, 5.2.3, 5.3 and 5.4.5 to get an idea about their affects on the obtained results.

It is worth mentioning about how average stress and average strain values plotted in Figure 5-3 were calculated. The definitions for these terms are $|\sum RF_3|/A_\mathrm{p}$ and $-\ln(L_\mathrm{p}/L_0)$, respectively, where $|\sum RF_3|$ corresponds to the overall reaction force on the contact pillar surface in the vertical direction, A_p corresponds to instant (during deformation) middle cross-sectional area of the pillar, and L_p and L_0 corresponds to instant and initial height of the pillar, respectively. As the stress state is not fully uniaxial due to the tapered shape of the pillar and misalignment

between the indenter's tip and pillar surface, here average stress and average strain are not equal to true stress and true strain, respectively.

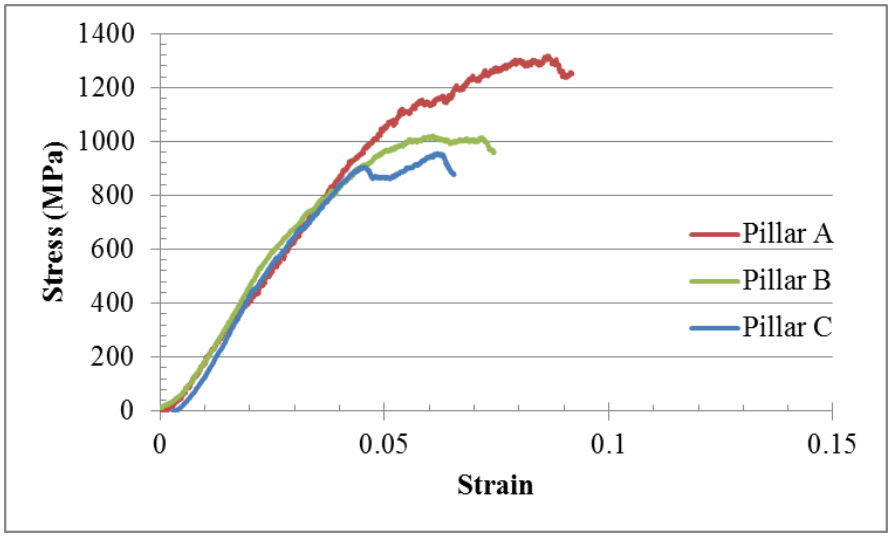

Figure 5-3: Experimental average stress-strain curves of pillars A, B and C (Figure 5-4)

5.2 Modelling considerations

A three-dimensional finite-element model of micro-pillar-compression experiment was developed to represent deformation of a single-crystal of Ti-based alloy. Numerical simulations were performed using the crystalline plasticity-based constitutive law incorporating the strain gradient theory implemented in a UMAT subroutine (see Section 4.3 for the details of the material subroutine). As the experimental study suggested that $(121)[1\bar{1}1]$ was found to be the dominant slip system during deformation, only the set {112} <111> is switched on among the potential three different sets in the following FE simulations. Nowag *et al.* (2012) also investigated the active slip systems for different sizes, orientations and geometries of micropillars (Ti-15-333 with b.c.c. crystal structure) and it was observed that slip was generally found to occur on {112} <111> slip-systems (by single slip). In connection with this, Lewis *et al.* (2010) did a FE investigation of b.c.c. titanium alloy using three separate single-crystal plasticity formulations for each loading: reduced 12 slip systems, reduced 24 slip systems and full 48 slip

systems. This study revealed that 12-slip-system model generally followed the full model results and provided reasonable predictions in the global stress-strain curve of the material with an error less than 10%. In this chapter the material parameters were calibrated with the experiments w.r.t. macroscopic stress-strain curves; hence, activating one set of slip system in the simulations seems to be an acceptable assumption. On the other hand, identical conditions were considered for all the investigated pillar sizes; hence, the influence of including all set of available slip systems on the size effect was not considered in this thesis and assumed to be negligible.

To explore the size effect in a single-crystal Ti alloy observed in experiments, three pillars with different sizes were modelled. Dimensions of the micro-pillar models are demonstrated in Figure 5-4 (a), and the schematic of the micro-pillar-compression model is shown in Figure 5-4 (b). When the pillars are produced with a FIB milling, some amount of taper is typically introduced in the sample as also observed in (Zhang *et al*., 2006; Shan *et al*., 2008). The taper is defined as an angle between the wall of the pillar and its axis, i.e. the top of the pillar is smaller compared to its bottom. In the milled samples an angle of 2.5° taper was measured and this value was introduced into the model (Figure 5-4). As the modulus of the diamond indenter used in the experiments was one order of magnitude higher than, that of Ti-alloy single-crystal workpiece (Section 5.4.1), the indenter was modeled as a rigid body in the simulations. The relative movement of the workpiece and indenter was introduced as translation of the indenter in the negative y-direction (Figure 5-4). Kinematic boundary conditions were imposed on the bottom face of the pillars by constraining modal displacements in all the directions since the micro-pillars fabricated by FIB are tightly bonded to a substrate. The Coulomb's friction law was used to model frictional interaction between the indenter tip and the pillar's top surface.

In the next part, different aspects of numerical modelling of the micro-pillar-compression experiment are discussed. First, a mesh-sensitivity analysis for the workpiece material is performed to find a compromise between the computational

cost and numerical accuracy in simulations. In the second part, the effect of substrate on the numerical solutions is analyzed followed by a thorough investigation of misalignment between the indenter's flat punch tip and the pillar's top surface. In the simulations of the following sections, unless otherwise stated, the elastic and plastic parameters presented in Table 5-3 are used.

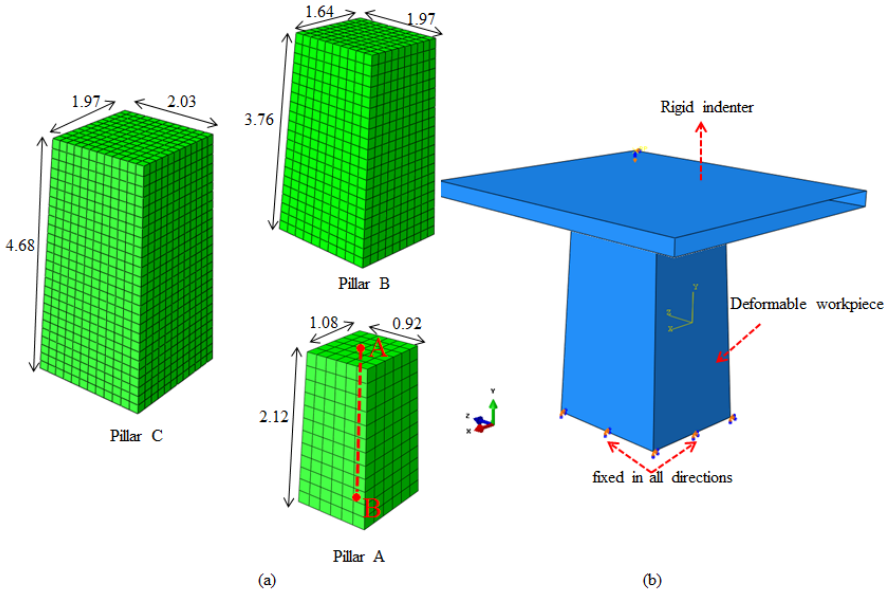

Figure 5-4: Dimensions of micro-pillars (in µm) (a); 3D model of micro-pillar-compression experiment (b)

Table 5-3: Crystal-plasticity parameters used in simulations to optimize FE model of micro-pillar-compression experiment

Elastic constants	$C_{11} = 127740$ MPa
	$C_{12} = 118850$ MPa
	$C_{44} = 43997$ MPa
Hardening parameters (PAN model)	$\dot{\gamma_o}^{\alpha} = 0.0001$
	$n = 15$
	$q = 1$
	$h_0 = 2000$ MPa
	$\tau_0 = 310$ MPa
	$\tau_s = 280$ MPa

Strain gradient parameters	$\alpha_T = 0.8$
	$\mu_s = 13980$ MPa
	$b = 2.802 \times 10^{-7}$ mm

5.2.1 Mesh sensitivity

In this section, a mesh-sensitivity analysis of the model is performed to find a compromise between conflicting requirements of accuracy and computational cost. Eight-node linear brick elements (C3D8) were used to discretize the workpiece sample. In this part, a friction coefficient value μ of 0.1 is considered to characterize the contact condition between the indenter tip and (001) crystallographically oriented pillar to avoid geometrical softening in the pillars assuring to demonstrate the influence of strain gradients on the mesh-sensitivity analysis properly.

Three different meshes were used to discretize pillar A, i.e. the smallest pillar, viz. Mesh 1, Mesh 2 and Mesh 3. The sizes of the elements in each mesh were similar, and in Mesh 1, on average, 140 nm × 140 nm × 140 nm. In Mesh 2 and Mesh 3, the corresponding sizes were 210 nm × 210 nm × 210 nm and 280 nm × 280 nm × 280 nm, respectively. Figure 5-5 demonstrates the average stress-strain curve obtained for pillar A in FE simulations using different mesh sizes. The definition of average stress and average strain was given in Section 5.1.2. The FE model predicts the same stress-strain curve for all the meshes. It can be therefore concluded that any of the mesh sizes studied here can be used to discretize pillar A. However, a choice of the coarsest mesh, Mesh 3 is, naturally, more beneficial as it leads to lower computational times compared to other meshes.

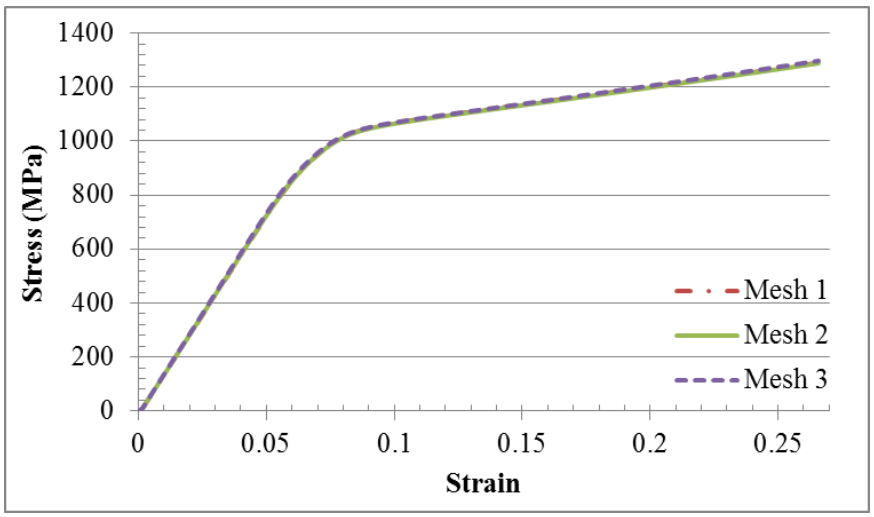

Figure 5-5: Average stress-strain curves obtained with MBSGCP simulations using different meshes

Of particular interest in this thesis are material's local fields such as stresses, strains, strain gradients etc., especially when the size of deformed volume is decreased. So, variations of fields for different mesh sizes were, therefore, investigated. Figure 5-6 presents a distribution of von Mises stress through the centre y-axis of pillar A for different FE meshes at 10% strain. This strain value was selected intentionally, as in the experiments the pillars were compressed approximately up to that strain level (Figure 5-3). It is observed that the FE model with Mesh 3 predicts a higher stress value between middle- and bottom-center of the pillar compared to other two meshes. As the prediction based on Mesh 2 in FE simulation is in good agreement with its finer counter-part, Mesh3, the former provides a compromise between the computational accuracy and computational cost. Therefore, Mesh 2 is used in the following sections of this chapter.

In the lower-order MBSGCP theory implemented here, shear-strain gradients evaluated at the integration points were computed by averaging the shear-strain values at corner nodes using the weighting functions, the spatial derivatives of linear shape functions. The mesh resolution used for the pillar, therefore, influences the magnitude of strain gradients, hence, affecting a macroscopic response of the material, e.g., the reaction force. Such an observation was also reported by Cheong

et al. (2005). In their study, mesh sensitivity of the FE results in the deformation behaviour of Cu polycrystals was investigated over a spectrum of length scales. The study revealed that in the case of predominance of geometrically necessary dislocations over statistically stored ones, the polycrystalline response became increasingly mesh-sensitive. Similar observations were also reported in our simulations as demonstrated in case study B in Section 5.5.1. It is therefore ensured that the same mesh size was used in FE modelling of pillars B and C to characterize the evolved strain gradients (Figure 5-4). The mesh convergence is automatically satisfied for these pillars since it already corresponds to a finer mesh for both pillars.

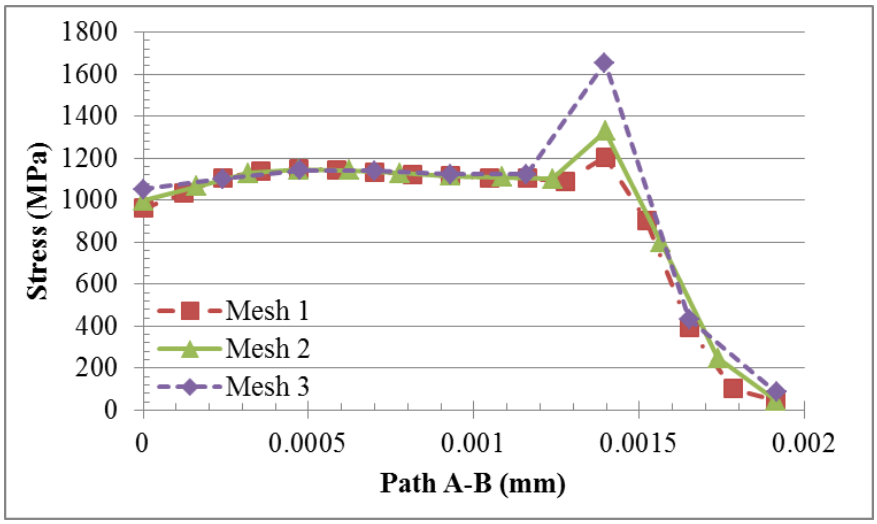

Figure 5-6: Distribution of von-Mises stress along path A-B (see Figure 5-4) at 10% average strain for pillar A

5.2.2 Effect of pillar base

In this section, the effect of pillar base on results of numerical solutions is studied. The term "substrate" is used below synonymously to the term "base". It should be also emphasized that here and in the following sections, unless stated otherwise, $\mu = 0.05$ is used to characterize the contact condition between the indenter tip and the pillar with a crystallographic orientation of (0.489 0.443 0.751). The micro-pillar compressed in the experiment was modelled as a prism with a rectangular cross-section and a specific taper; the micro-pillar was assumed to be ideally

bonded to a substrate and, hence, modelled with nodes of the bottom face of the pillars constrained in all directions (Figure 5-4). This assumption needs to be checked for the sake of accuracy of the results. To achieve this, two models were considered. In addition to the discussed one, another model was created, with the substrate introduced directly into simulations. In the latter FE model, the same mesh size and crystal orientation were considered for the substrate (Figure 5-7).

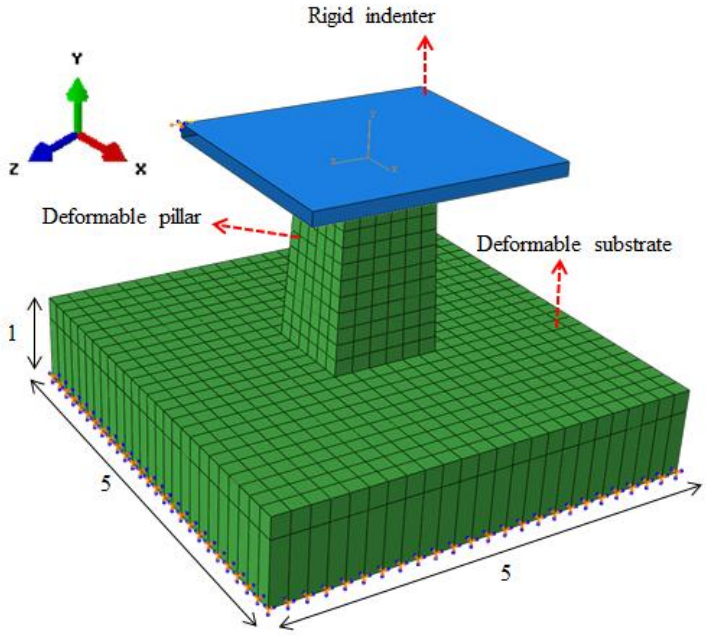

Figure 5-7: 3D FE model of micro-pillar with substrate (dimensions in µm)

Zhang *et al*. (2006) performed a parametric study to design an accurate compression experiment. One of particular interests in that study was the effect of curvature of transition of the micro-pillar into the bulk substrate. Depending on the ratio of the curvature radius to the radius of pillar, the flow-stress in the material was evaluated (Figure 5-8). The study suggested that the curvature did not change the material's response significantly. For instance, for the aspect ratio of 2, similar to the case studied here, even for the largest studied ratio of curvature radius to the radius of micro-pillar, the error in flow-stress was less than 6%. Hence, this curvature therefore was not taken into account in our model.

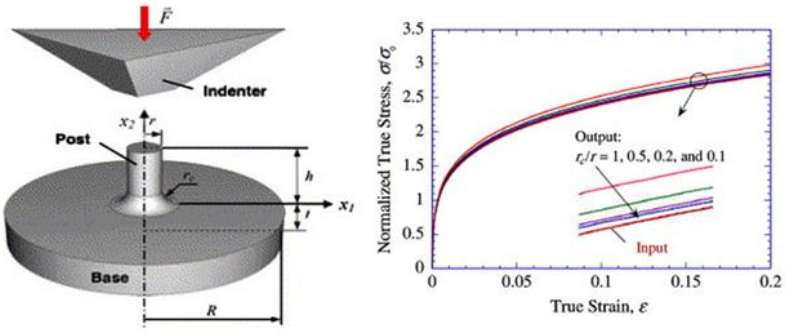

Figure 5-8: Schematic of cylindrical pillar and its substrate (a). Effect of radius of curvature on FE simulation output (b). The inset demonstrates the zoomed view of the circled region to facilitate comparison. Different output curves correspond to different ratios of the radii of pillar curvature to the pillar radius. Reprinted with permission from (Zhang *et al.*, 2006)

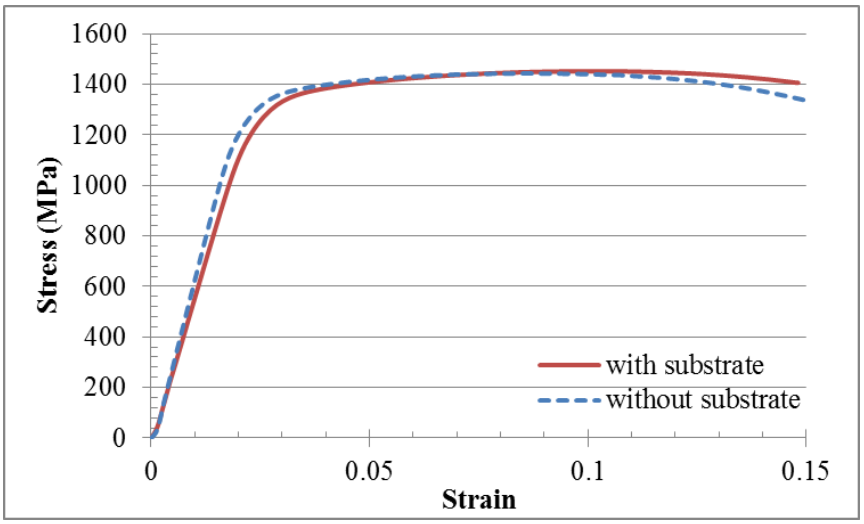

Figure 5-9: Average stress-strain curves obtained in FE simulations with substrate and without substrate

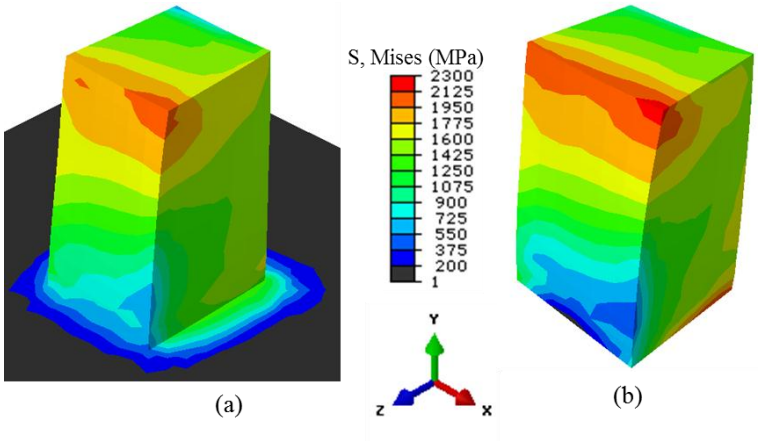

Figure 5-10: Distributions of von Mises stress at 8% average strain obtained in FE simulations with substrate (a) and without substrate (b)

The numerical results demonstrate that the stress-strain curve of the material with base and without base does not differ significantly (Figure 5-9). Of a special interest in this plot here is underestimation of the elastic modulus when the substrate is accounted for. Zhang *et al*. (2006) ascribed this difference to the neglection of the contribution of substrate compliance to the overall compliance. In other words, although the substrate was deformed along with the pillar and this deformation contributes to the system compliance, it was not accounted in the collected displacement data. The influence of substrate on local fields was also analysed. The distribution of von Mises stress on the pillar surface was calculated at 8% strain to comply with the experiments as the pillars are compressed up to that strain level in the experiment (Figure 5-10). This figure demonstrates that the obtained stress distribution for both models are very similar confirm a relatively good approximation when neglecting the substrate in the model. This simplification in the model also allows reduction of computational times as simulations for a pillar with the base run longer. The finding of the Jerusalem *et al*. (2012) where the base of the cylindrical pillar was also neglected is akin to our observations.

5.2.3 Effect of misalignment

Our first FE simulation results demonstrate that there exists discrepancy between simulations and the experiments at the initial stage of compression. This

disagreement arises due to underestimation of stiffness in the experiments. Such observations were also made in other studies (Zhang *et al*., 2006; Schuster *et al*., 2008; Jérusalem *et al*., 2012; Kunz *et al*., 2011), where the reason was linked to misalignment between the indenter's flat punch tip and the pillar's top surface. It was reported that when the misalignment increased, a decrease in the measured elastic modulus was observed. Zhang *et al*. (2006) characterized this relationship in 3D FE simulations with an isotropic constitutive law (Figure 5-11). This figure indicates that even a 1° of misalignment leads to underestimation of the elastic modulus by approx. 55%. Therefore, a special care is needed to reduce or eliminate the misalignment in the test system.

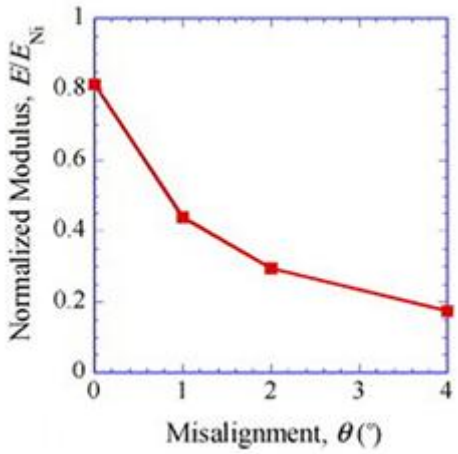

Figure 5-11: Effect of system misalignment on error in elastic modulus. Reprinted with permission from (Zhang *et al*., 2006)

In this section the effect of misalignment of the system on the initial portion of the loading is numerically studied. In the model, the misalignment is represented as an angle (θ_p) between the indenter's tip and the pillar's axis; when θ_p=0°, the system is perfectly aligned. Figure 5-12 demonstrates the effect of various magnitudes of θ_p on the stress-strain curve. The FE simulations suggest that the material's elastic modulus is underestimated when a misalignment is introduced into the model, i.e. with an increase in the misalignment, the elastic modulus is increasingly underestimated. This finding is in agreement with observations in other studies (Zhang *et al*., 2006; Schuster *et al*., 2008; Jérusalem *et al*., 2012; Kunz *et al*., 2011).

Figure 5-12 suggests that misalignment of 6° exists in the experiment between indenter's tip and the pillar's axis. It should be emphasized that this value also accounts for the contribution arising due to neglection of substrate compliance to the overall system's compliance. This implies that misalignment in the experiments was less than 6°. Figure 5-11 also supports this fact where the elastic modulus is underestimated even for a perfect alignment.

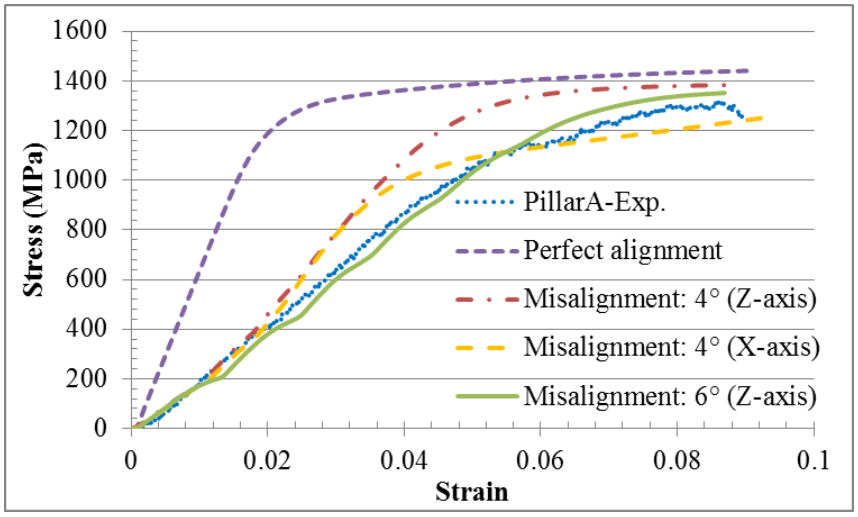

Figure 5-12: Average stress-strain curves obtained with FE simulations for different misalignments (for direction of axes see Figure 5-4)

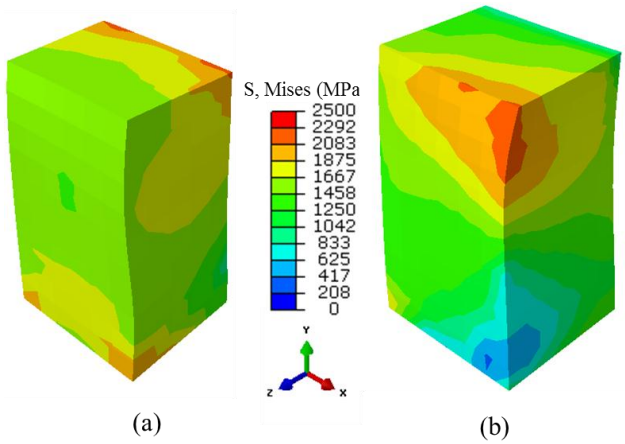

Figure 5-13: Distribution of von Mises stress at full loading from FE simulation of misalignment w.r.t. to x-axis (a) and z-axis (b)

Misalignment, on the other hand, causes contact anisotropy in the system that is especially significant at the beginning of the compression, i.e. while a portion of the pillar is in contact with the indenter, and other parts remaining without contact. This also leads to differences between the obtained solution and the test results. For instance, although the misalignment in the system is introduced with the same amount (4°) w.r.t. x- and z-axis, the obtained stress-strain curves (Figure 5-12) and the corresponding stress distributions on the surface of the pillars (Figure 5-13) are different.

Since in this thesis, the main focus is on the deformation behaviour of a single-crystal Ti alloy where only the material anisotropy is accounted for, it is tried to avoid introducing any anisotropy in the model other than those due to the crystal structure. It is, therefore, preferred not to introduce any misalignment in our 3D FE model; instead the misalignment will be accounted for in the models by introducing a correction factor ξ_1 in the constitutive laws. This factor is introduced in the constitutive equation 3-37 and in the equations incorporating equation 3-37 . This pronounced equation after ξ is introduced becomes

$$\hat{\boldsymbol{\sigma}} + \boldsymbol{\sigma}\,(\boldsymbol{I}:\boldsymbol{D}^*) = \xi_1\,\boldsymbol{C}:\boldsymbol{D}^*. \qquad 5\text{-}1$$

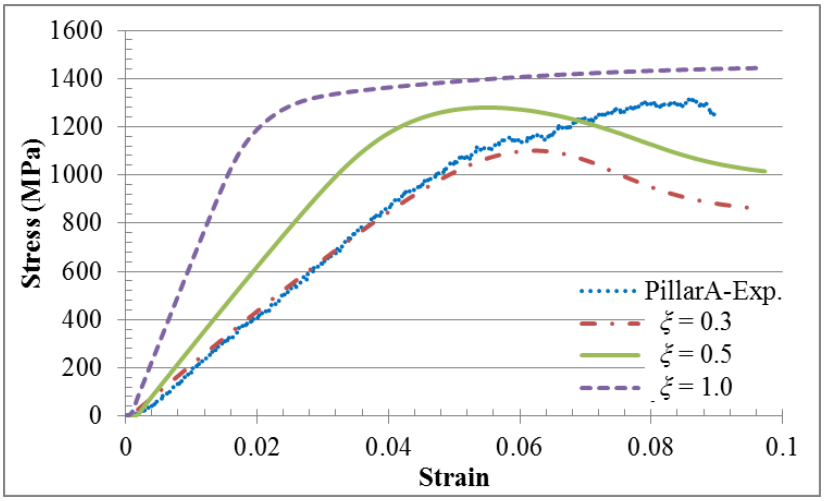

Figure 5-14: Average stress-strain curves obtained with FE simulations for different correction factors accounting for misalignments

The modified constitutive law is used to study the influence of different correction factors ranging from 0.3 to 1 on the load-displacement curve, where ξ_1 =1 corresponds to perfect alignment in the system. Figure 5-14 demonstrates that the correction factor value of 0.3 accounts correctly for misalignment in the experiments correctly. This correction factor henceforth is used in the constitutive laws in the simulations for the respective experiment as a fitting parameter.

5.3 Contact conditions

The effect of friction characteristics at the indenter-workpiece interface is studied in this section. As mentioned earlier, the Coulomb's friction law was used to model the frictional interaction. In this linear model when the shear stress at the interface exceeds the critical shear stress τ_{cr} that is equal to the product of the friction coefficient μ and contact pressure, slipping will occur; otherwise, there exists a sticking regime at the interface between the contacting bodies. Three different idealised friction conditions were studied. First, $\mu = 0$ was considered to represent the effect of a well-lubricated indenter-workpiece interface followed by two dry (non-lubricated interface) contact conditions: $\mu = 0.1$ was considered to represent the extreme contact condition and $\mu = 0.05$ corresponds to a medium friction coefficient between two extremes. It is worth mentioning that $\mu = 0.05$ is between the lower ($\mu = 0.03$) and upper ($\mu = 0.06$) bounds for a contact condition of a diamond-metal surface interface given in the literature (Spear, 1989). The lateral displacement of the pillar at 10% strain for different contact conditions was compared. It was observed in numerical simulations that the pillar with $\mu = 0$ and $\mu = 0.05$ showed buckling during compression, i.e. geometric softening, whereas the pillar with $\mu = 0.1$ revealed a more stable evolution of the shape during deformation (Figure 5-15). The *in-situ* videos recorded during the compression experiments indicate that the lateral slipping of the pillar occured during the deformation process. It was therefore concluded that $\mu = 0.1$ does not represent the contact conditions accurately. The contact condition without friction also does not reflect the reality as the presence of at least a small amount of friction is intrinsic to these experiments (Zhang *et al*., 2006). A friction-coefficient value of

0.05, therefore, seemed to be an appropriate choice to represent the contact conditions in the experiments; hence, it was used in the subsequent simulations.

The influence of friction is also observed in the corresponding flow curves (Figure 5-16). In the case of $\mu = 0$, the stress-strain curve becomes unstable at an early stage of deformation, whereas in the case of $\mu = 0.05$ the instability in the stress-strain curve starts at strain of approx. 4%. The instability here is defined as the deviation of the flow curve from the one for $\mu = 0.1$. On the other hand, buckling observed in Figure 5-15 may appear at first sight like classical elastic-plastic buckling. However, classical analytical models predict that buckling is expected to occur for pillars, which are at least 20 times longer than the present pillars for the same cross-section (Raabe *et al*., 2007). Buckling observed here occurs rather due to crystalline anisotropy, which promotes shape instability. The finding of Raabe *et al*. (2007) confirms this argument and demonstrated that a stable deformation process can be achieved for a pillar with a stable orientation such as (100) even with $\mu = 0$.

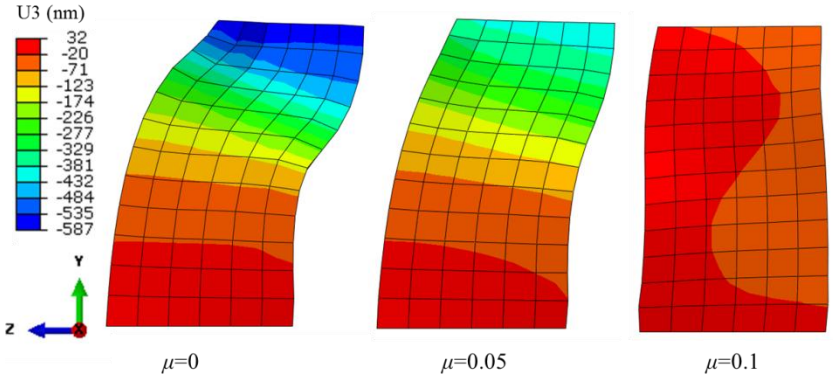

Figure 5-15: Distribution of displacements in z-direction at full loading in FE simulations for different contact conditions

5.4 Determination of material parameters

In this section the appropriate values of material parameters for the studied single-crystal Ti alloy are determined based on a direct comparison between simulations and the experiments. It should be emphasized that the optimized set of parameters

representing the deformation behaviour of Ti alloy was obtained based on both micro-pillar-compression and nano-indentation experiments.

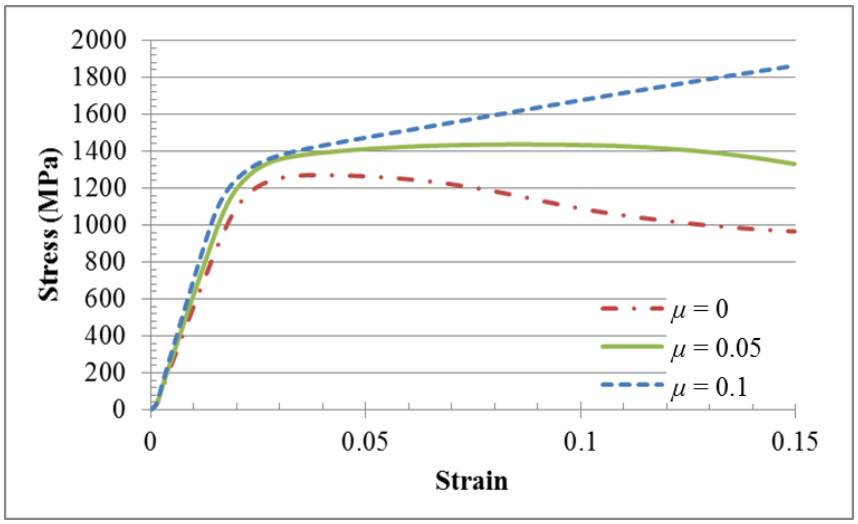

Figure 5-16: Average stress-strain curves obtained with FE simulations for different contact conditions

5.4.1 Elastic properties

Elastic properties of the single-crystal Titanium alloy are represented by three material constants, C_{11}, C_{12}, C_{44} as given in equation 3-39. Two different sets for those constants are considered (Table 5-4). The first set of elastic parameters was obtained using *ab-initio* simulations performed at 0 K for b.c.c. Ti alloys (Tegner *et al.*, 2012). The second set was obtained from the experimental results for the b.c.c. titanium single-crystal performed at high temperature (1273 K) using resonant-ultrasound spectroscopy (Ledbetter *et al.*, 2004). To find the material's elastic constants for Ti alloy at room temperature (300 K), at which the micro-pillar-compression experiments were performed, these two different sets were considered. The dependence of elastic constants on temperature was studied for different metals by Varshni (1970). This study demonstrated that elastic constants decreased linearly with an increase in temperature except at very low temperatures (0-50 K) where an exponential change occured. As a first estimate, the two different sets were interpolated linearly; the obtained values are presented in Table 5-4. Since the stress-strain curve obtained from the micro-pillar-compression experiment was

affected by misalignment between the indenter's tip and the pillar's top surface as explained in Section 5.2.3, the exact elastic parameters cannot be predicted properly from this experiment. The first estimation of the material's elastic parameters therefore was tested with the data from the nano-indentation experiments, with the slope of the unloading curve describing the material's elastic behaviour. The FE simulations (see Chapter 6) demonstrated that using those elastic parameters the slope of the unloading curve in experiments was predicted accurately. It was, therefore, decided to use those elastic parameters in this thesis without any additional corrections. Based on these elastic constants, the value of shear modulus μ_s presented in Table 5-4 was calculated using the equation proposed by Schulze (1979) in the following form:

$$\mu_s = \sqrt{(C_{11} - C_{12})C_{44}/2}. \qquad 5\text{-}2$$

Table 5-4: Elastic constants for Ti alloy

	T (K)	C_{11} (GPa)	C_{12} (GPa)	C_{44} (GPa)	A (Anisotr. fac.)	μ_s (GPa)
Ab-initio sim.	0	137.00	130.00	46.00	13.14	12.68
Experiments	1273	97.70	82.70	37.50	5.00	16.77
Interpolated (linear)	300	127.74	118.85	43.99	11.22	13.98

The sensitivity analysis of material's plastic parameters is performed in the next section describing how parameters giving the best fit to the experimental stress-strain curves were obtained through multiple trial runs. The influence of different material's plastic parameters such as n, α , τ_0, τ_s and h_0 on the stress-strain curve of the deformed pillar is studied for pillar A with ξ_1 =0.3.

5.4.2 Effect of strain-rate sensitivity

The strain-rate sensitivity n of the material should be determined for each set of slip systems for evolution of the plastic strain-rate $\dot{\gamma}^{\alpha}$ in equation 3-63. It is worth mentioning that the reference strain-rate $\dot{\gamma_o}^{\alpha}$ in this equation is taken as 10^{-4} s^{-1}

since the compression experiments were performed approximately at that strain-rate. Smaller values of n such as 1, 2 or 5 represent a strain-rate-sensitive, whereas larger values such as 20, 50, 100 correspond to a strain-rate-insensitive model. As the rate sensitivity of single-crystal Ti alloy, from which the pillars were produced, is not known, this was assumed to be strain-rate insensitive, hence n was selected as large as possible to represent the material behaviour close to rate-independent plasticity. It was, therefore, first, assumed that n = 100, and both micro-pillar-compression and nano-indentation simulations were performed with that level in parallel. It was observed that while the former simulations ran smoothly, very long computational times were required in the latter case due to convergence problems. The reason for this was a noticeable difference in strain gradients imposed in those two different processes. It seemed therefore plausible to select this parameter based on the nano-indentations simulations that required reasonably well computational stability. The computational analysis presented in Section 6.4.1 suggested n to be 15 and this value still corresponds to the strain-rate insensitive material's behaviour of the single-crystal Ti alloy. The extended information about selection of n is given in the next chapter, where the sensitivity to n in nano-indentation simulations is investigated thoroughly.

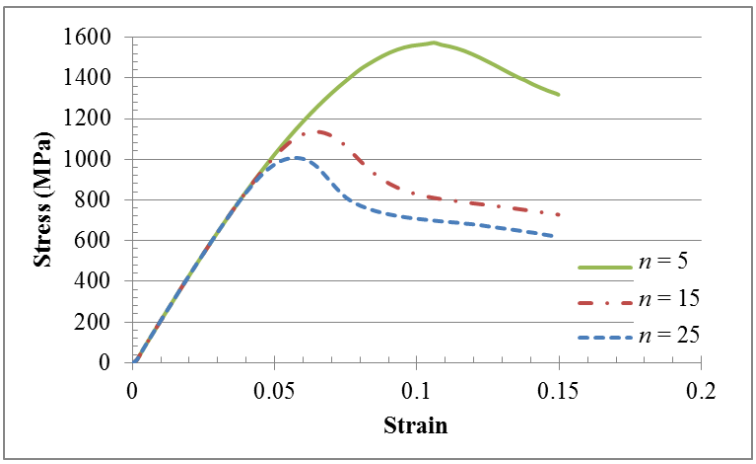

Figure 5-17: Average stress-strain curves obtained with FE simulations of micro-pillar compression for different values of n

The stress-strain curves for different n values obtained for micro-pillar compression are presented in Figure 5-17. A decrease in value of n moves this curve upwards. This can be explained by the fact that for larger values of n, which represent rate-independent behaviour, the hardening saturates earlier compared to that of smaller values of n, which represent rate-sensitive behaviour. It is worth mentioning that the softening part in the curves (after the ultimate tensile strength is reached) arises due to geometrical softening (similar to Figure 5-15).

5.4.3 Effect of Taylor coefficient

The α_T value in Equation 3-50 is an empirical coefficient in the well-known Taylor relation (Taylor, 1938) describing the shear flow-stress in terms of dislocation density. The Taylor coefficient enters in the constitutive equations through MBSGCP theory (Section 3.3).

In this section, the influence of α_T value on the stress-strain behaviour of the single-crystal micro-pillar is studied. Three different values of α_T were considered, viz. 0.0, 0.8 and 0.16. Here, α_T = 0.0 represents the solution obtained using CP while other values represent the solution obtained using MBSGCP. Figure 5-18 demonstrates how different values of α_T affect a simulated stress-strain behaviour of the micro-pillar. It is clear that with an increase in the value of α_T, the flow-stress increases after strain of 5% since the contribution of strain gradients to the overall response is negligibly small at the beginning of deformation and increases gradually with its increase. In the micro-pillar-compression experiment, deformation was macroscopically homogenous, which, in turn, led to a lower effect of strain gradients. On the other hand, gradual development of strain gradients justifies that deformation was microscopically heterogeneous. Similar observations were also made by Maass *et al*. (2007) experimentally and by Zhang and Aifantis (2011) numerically, where the presence of GNDs in the micro-pillars was justified though it vanishes macroscopically. On the other hand, strain gradients are more profound in nano-indentation experiments compared to micro-pillar experiments. The value of α_T was therefore determined using nano-indentation experiments. Through multiple trial runs, α_T = 0.7 was found to give a reasonably good

agreement by comparing the results of numerical models with the experiments (Section 6.5). This value will be used in the simulations described below.

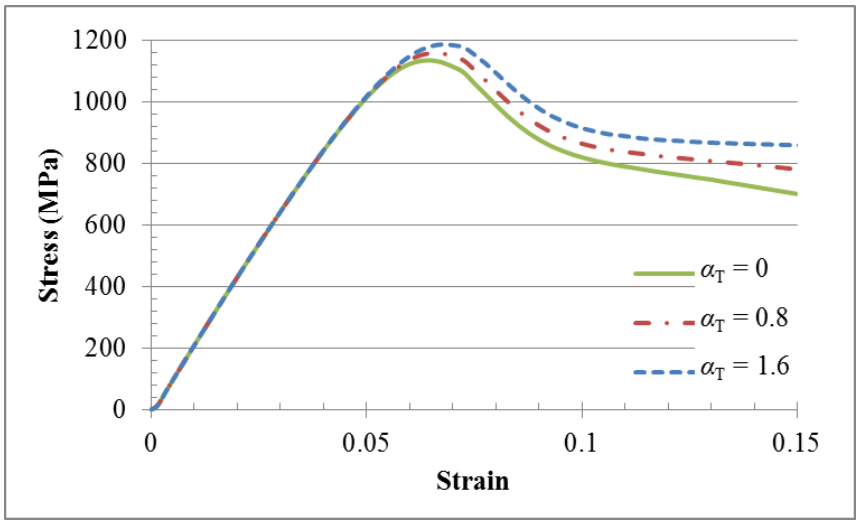

Figure 5-18: Average stress-strain curves obtained with FE simulations for different values of α_T

5.4.4 Effect of other plastic parameters

In this section, the influence of τ_0, τ_s and h_0 on the stress-strain relationship for simulation of micro-pillar-compression is analysed. The stress-strain curves for different τ_0 values for a constant value of $\tau_s = 210$ MPa are presented in Figure 5-19. An increase in τ_0 value moves this curve up. This can be explained by the fact that larger force value is needed to activate slips systems for larger value of τ_0.

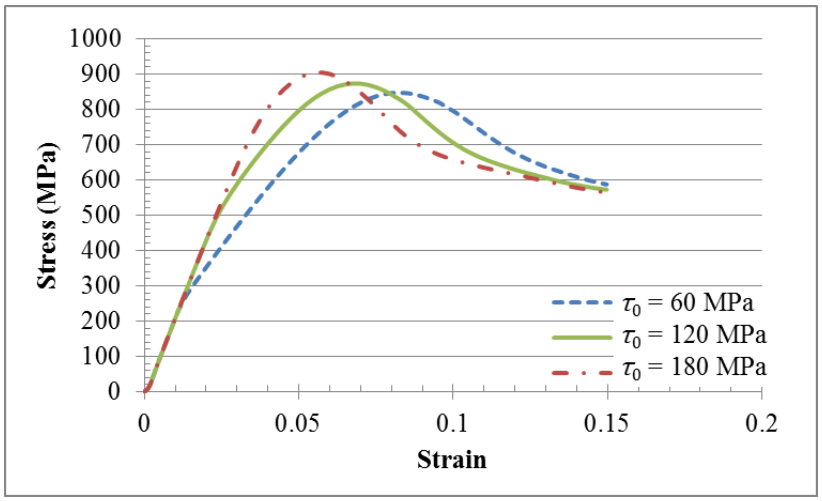

Figure 5-19: Average stress-strain curves obtained with FE simulations for different values of τ_0

The influence of saturation stress τ_s and initial hardening modulus h_0 on the stress-strain curve is in the same line with τ_0. An increase in the value of τ_s for a constant value of $\tau_0 = 120$ MPa leads to a shift of the curves upwards as larger force values are needed to saturate the hardening behaviour of material for larger τ_s values (Figure 5-20 (a)). That also results in an increase in the plastic work done by the indentation process. Likewise, with an increase in the value of h_0 for constant values of $\tau_0 = 60$ MPa and $\tau_s = 210$ MPa, the stress value increases at the same strain value, hence the amount of work done by the indenter tip increases (Figure 5-20 (b)).

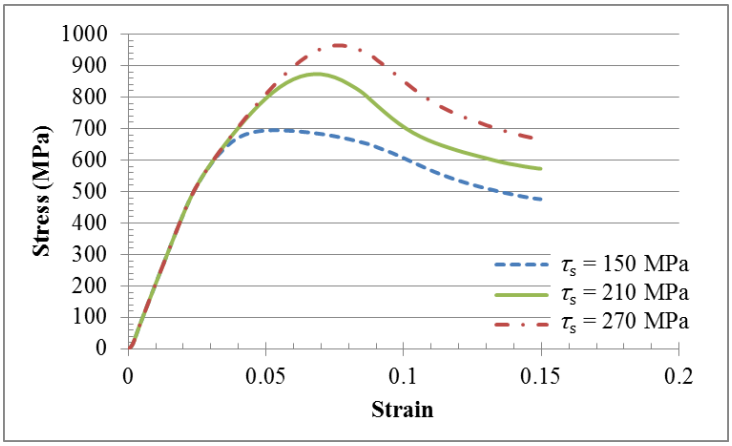

(a)

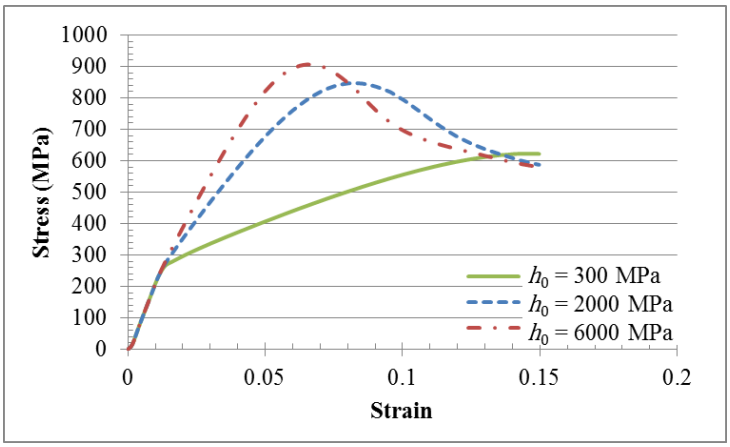

(b)

Figure 5-20: Average stress-strain curves obtained with FE simulations for different values of τ_s (a) and h_0 (b)

5.4.5 Determination of material parameters of single-crystal Ti alloy

In this section, through multiple trial runs the material parameters of the single-crystal Ti alloy are determined using the MBSGCP theory by comparing the simulated stress-strain responses with those from the experiments (Figure 5-3). It should be emphasized that the general trends of the curves obtained in the previous section provide hints to determine the material parameters. Different cases are considered below.

In the first case, the flow curve of pillar C was used to identify plastic parameters. As demonstrated in Figure 5-21, a reasonably good match between experiments and simulations was obtained for pillars B and C using the parameters presented in Table 5-5; however, prediction of the stress-strain relation prediction for pillar A was unsuccessful. Different cases were also considered, for instance, the experimental flow curves of pillars B and C were also considered individually to identify plastic parameters. It was recognized that fitting the numerical stress-strain curve of all the pillars to the experimental results using the MBSGCP theory was not possible. These observations led to the conclusion that different approaches should be considered to describe the size effects observed in the experiments. In the next, the influence of production of pillars on the size effect is discussed.

Table 5-5: Crystal-plasticity parameters used in FE simulations to determine material plastic parameters of Ti alloy

Plastic parameters (PAN model)	$h_0 = 10000$ MPa
	$\tau_0 = 221$ MPa
	$\tau_s = 247$ MPa

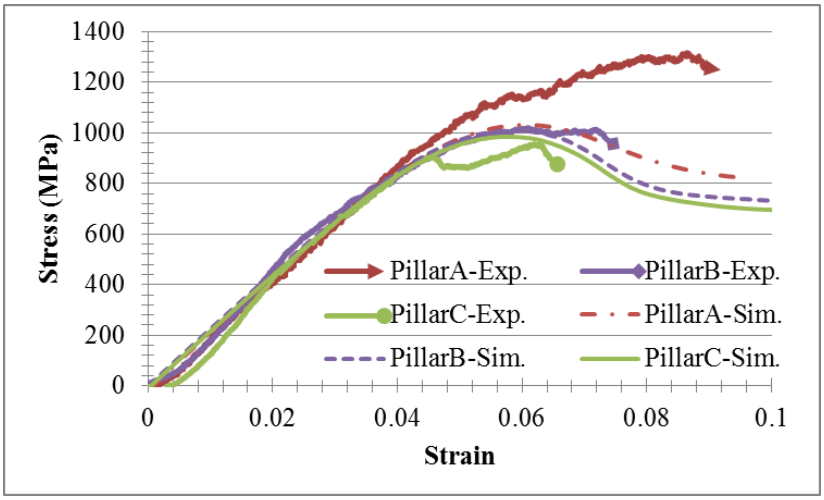

Figure 5-21: Average stress-strain curves obtained from experiments and FE simulations of pillars A, B and C using MBSGCP theory

The focussed ion beam (FIB) technique is the most prevalent method for producing small-size pillars to investigate the influence of sample dimensions on mechanical properties. In the FIB method, Ga^+ ions are bombarded and implanted to fabricate the pillars. This process inevitably introduces surface dislocation loops and precipitates also instigating surface amorphization. The presence of FIB-induced defects led several researchers to infer that the fabrication process may play a significant role in the observed size effects. For instance, Bei *et al*. (2007) proposed that increased strength of a pillar with a decrease in its size would be a consequence of the increased volume fraction of the FIB-damaged layer with a decrease in pillar diameter. Similarly Kiener *et al*. (2007) investigated Ga^+ ion-induced damage by means of TEM investigation and Monte Carlo simulations. In this study a non-negligible influence of the ion damage in the order of 100 MPa assuming Taylor hardening for submicron-sized samples was reported. To understand the importance of fabrication technique on the size effects, Jennings *et al*. (2010) developed a FIB-less method to produce nanopillars. In this method, arrays of vertically oriented gold and copper nanopillars were created based on patterning polymethylmethacrylate by electron-beam lithography and subsequent electroplating into the provided template. In this technique the pillars were produced intentionally with none zero dislocation densities to compare and contrast

them with the pillars produced with FIB, since the pillars without dislocations would render theoretical strengths regardless of size. This study demonstrated that nano-size pillars created without Ga+ bombardment (containing initial dislocations with the density of the same order with that of the pillars created with Ga+ bombardment) exhibited an identical size effect with the pillars produced with the FIB method. This study evidently suggested that the observed size effect in small-size pillars is a function of microstructure rather than the fabrication technique. The production method of pillars, therefore, is not taken into account while reformulating the constitutive equations.

The influence of microstructure on strength of the nano- and micro-pillars was studied by a few researchers. The experimental study of Maass and co-workers (2007) revealed that a significant density of geometrically necessary dislocations was generated during compression and giving a rise to strain gradients; this was also demonstrated by the discrete-dislocation analysis (Guruprasad and Benzerga, 2008; Akarapu *et al*., 2010). On the other hand, Maass *et al*. (2008) investigated the initial microstructure of undeformed Au, Ni, Cu and NiTi micro-pillars using a white-beam Laue micro-diffraction technique. In this method, continuous streaking of Laue diffraction peaks was related to internal strain gradients and discontinuous streaking to the presence of dislocation walls as white-beam Laue diffraction patterns are sensitive to microstructure (Maass *et al*., 2009; Maass *et al*., 2007; Maass *et al*., 2006). In the cited work, anisotropic peak shapes of several micro-pillars were analysed as indicators of strain gradients. This study suggested that strain gradients existed predominantly in the initial microstructure of micro-pillars with diameters less than 5 μm, consistent with the observations of Maass *et al*. (2006) and it was also suggested that a higher surface-to-volume ratio in smaller pillars increased the occurrence of pre-existing strain gradients. The following may give an idea about these observations. During the fabrication process of pillars, e.g. with the FIB method, pillars become work-hardened, hence finite stresses evolve in their body. It is well known that traction-free surfaces of pillars dictate a zero stress value on their surfaces. This difference in the stress distribution results in stress gradients, i.e. strain gradients in the body. For instance, for the smaller pillar size,

where the traction-free surfaces are closer to the pillar's axis, physically (and numerically) strain gradients become more pronounced compared to larger pillar sizes. Accordingly, the smaller the size of pillar is, the higher the density of GNDs and thus higher the pillar strength. Based on these observations in this study, an enhanced model of strain gradient crystal-plasticity (EMSGCP) theory is suggested, where the initial microstructure of pillars as a function of surface-to-volume ratio is accounted for. This multi-scale continuum theory promising to explain the size effect for different micron-size pillar characteristics bridges the gap between the discrete-dislocation-dynamics (DDD) theory (Tang *et al*., 2007; Deshpande *et al*., 2005; Benzerga and Shaver, 2006), where simulations are performed at strain-rates several orders of magnitude higher than those in real experiments, and the classical continuum plasticity theory, which cannot explain the dependence of mechanical response on a specimen's size since there is no length scale in its constitutive description (Raabe *et al*., 2007; Wang *et al*., 2004). The presented model here complies with the recent studies of Fan *et al*. (2012) and Hurtado and Ortiz (2012), where the contribution of surface effects to the size effect was demonstrated using DDD and non-local continuum models, respectively.

Enhanced modelling of strain gradient crystal-plasticity theory

EMSGCP theory requires the constitutive equation relating the incipient density of dislocations with the initial strengths of the slip systems (CRSS, τ_0 or $g_T^{\alpha}\,|_{t=0}$). The following equation, which has a similar structure with the Taylor equation, is suggested.

$$\tau_0 = K\sqrt{\rho|_{t=0}}, \qquad 5\text{-}3$$

where K is a constant and taken as 0.0392 MPa.mm, and $\rho|_{t=0}$ is the incipient density of the dislocations. In the MBSGCP theory, the contribution of pre-existing strain gradients due to GNDs to the CRSS value is not accounted for, only the initial SSDs determine the initial shearing of the slip systems as shown in equation 5-4.

$$g_T^{\alpha}\,|_{t=0} = K\sqrt{\rho_S|_{t=0}}, \qquad 5\text{-}4$$

In other words the pillars initially are assumed to be strain gradient free. In the EMSGCP theory, the pre-existing strain gradients in the pillar are accounted for by incorporating the contribution of GNDs in the overall hardening function of the slip systems. However, the interaction between SSDs and GNDs in the constitutive equation needs to be identified first.

The following general expression for the flow-stress accounting for the coupling between SSDs and GNDs has been proposed by Columbus and Grujicic (2002):

$$\tau = \left[(\tau_S)^{\beta_1} + (\tau_G)^{\beta_1}\right]^{1/\beta_1}, \qquad 5\text{-}5$$

where β_1 is the interaction coefficient, τ_S and τ_G are given by the Taylors hardening law as

$$\tau_S = \alpha\mu b\sqrt{\rho_S} \text{ and } \tau_G = \alpha\mu b\sqrt{\rho_G}. \qquad 5\text{-}6$$

Different values of β_1 were investigated in the literature. Two mostly considered values for β_1 are 1 and 2, where

- $\beta_1 = 1$ corresponds to a superposition of contributions of SSDs and GNDs to the flow-stress, where $\tau = \alpha_{\mathrm{T}}\mu b(\sqrt{\rho_S} + \sqrt{\rho_G})$ and the total dislocation density ρ_T is expressed as the sum of square roots of SSD and GND densities, $\rho_T = (\sqrt{\rho_S} + \sqrt{\rho_G})^2$. This type of expression for the flow-stress as a coupling of SSDs and GNDs was studied by Columbus and Grujicic (2002)
- $\beta_1 = 2$ corresponds to a simple arithmetic sum of SSD and GND densities, i.e. $\rho_T = \rho_S + \rho_G$. The flow-stress is expressed as $\tau = \alpha_{\mathrm{T}}\mu b\sqrt{\rho_S + \rho_G}$. This type of expression for the flow-stress was studied by many authors

(Abu Al-Rub and Voyiadjis, 2004; Stelmashenko *et al*., 1993; Ma and Clarke, 1995; Busso *et al*., 2000).

Another way of a coupling between SSD and GND densities was proposed by Fleck and Hutchinson (1997), where ρ_T equals to a harmonic sum of ρ_S and ρ_G, i.e. $\rho_T = \sqrt{(\rho_S)^2 + (\rho_G)^2}$. These different types of interactions between SSDs and GNDs in the formulation of flow stress were also considered to express CRSS. The followings can be written when $\beta_1 = 1$ and 2, respectively.

$$\tau_0 = g_T^{\alpha}\,|_{t=0} = K\sqrt{\rho_S|_{t=0}} + K\sqrt{(\frac{\bar{S}}{\bar{V}})^2\rho_G|_{t=0}}\,, \qquad 5\text{-}7$$

$$\tau_0 = g_T^{\alpha}\,|_{t=0} = K\sqrt{\rho_S|_{t=0} + (\frac{\bar{S}}{\bar{V}})^2\rho_G|_{t=0}}\,. \qquad 5\text{-}8$$

In these equations the contribution of pre-existing GNDs is correlated with the ratio of normalized surface ($\bar{S}$) to normalized volume ($\bar{V}$) of micro-pillar as complementary to the approach discussed. The surface and volume of the pillar are normalized by the corresponding values of the benchmark pillar C. With this new reformulation of the CRSS, the plastic parameters of the single-crystal Ti alloy for different pillar sizes are given in Table 5-6, where the given density values are compatible in magnitude with those in (Norfleet et al., 2008). It is worth mentioning that the saturation stress value ($g_T^{\alpha}\,|_{\mathrm{sat}}$) is also reformulated in a same manner since the pre-existing strain gradients do also influence the break-through stress where large plastic flow initiates.

The FE simulation results for different pillar sizes using $\beta_1 = 1$ and 2 are presented in Figure 5-22. These results demonstrate that the experimental stress-strain curves of pillars A, B and C are predicted appropriately using both interaction coefficients. In this study, it is decided to use $\beta_1 = 2$; hence only equation 5-8 will be used below. It should be emphasized that, as expected from the continuum nature of the constitutive model, the discrete strain bursts observed

in the experiments are not captured by the calculations. However, the overall trends with regards to hardening rates and the yield stresses are well captured using the EMSGCP theory.

Table 5-6: EMSGCP parameters used in FE simulations for different β_1 values

Pillar type	$\frac{\bar{S}}{\bar{V}}$	$\beta_1 = 1$	$\beta_1 = 2$
		$\rho_G\|_{t=0} = 3.4 \times 10^6$ mm^{-2} $\rho_S\|_{t=0} = 1.538 \times 10^7$ mm^{-2}	$\rho_G\|_{t=0} = 1.510 \times 10^7$ mm^{-2} $\rho_S\|_{t=0} = 1.538 \times 10^7$ mm^{-2}
Pillar A	2.033	$g_T^\alpha\|_{t=0} = 293$ MPa	$g_T^\alpha\|_{t=0} = 337$ MPa
		$g_T^\alpha\|_{\text{sat}} = 326$ MPa	$g_T^\alpha\|_{\text{sat}} = 357$ MPa
Pillar B	1.182	$g_T^\alpha\|_{t=0} = 233$ MPa	$g_T^\alpha\|_{t=0} = 231$ MPa
		$g_T^\alpha\|_{\text{sat}} = 261$ MPa	$g_T^\alpha\|_{\text{sat}} = 250$ MPa
Pillar C	1.0	$g_T^\alpha\|_{t=0} = 221$ MPa	$g_T^\alpha\|_{t=0} = 211$ MPa
		$g_T^\alpha\|_{\text{sat}} = 247$ MPa	$g_T^\alpha\|_{\text{sat}} = 230$ MPa

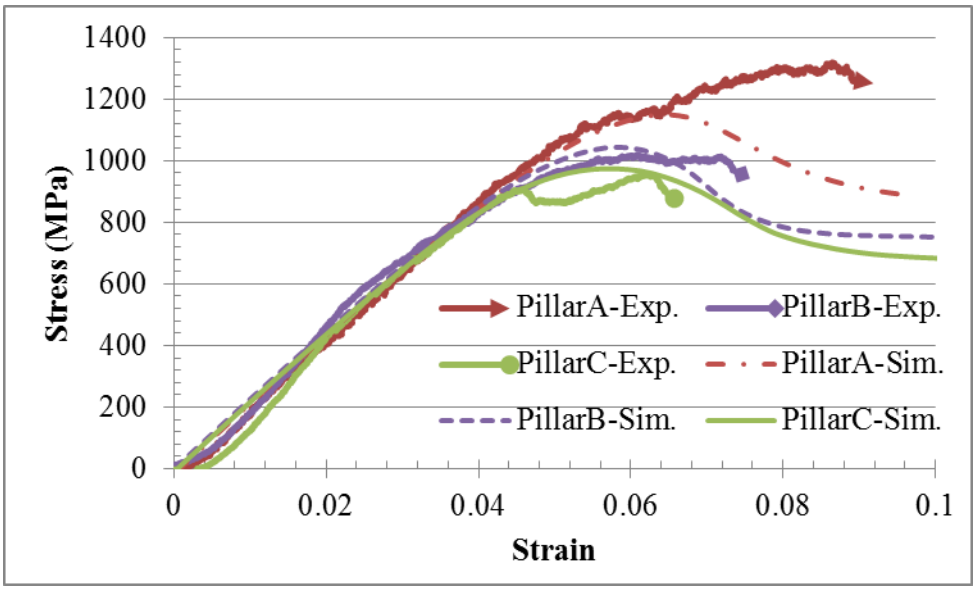

(a)

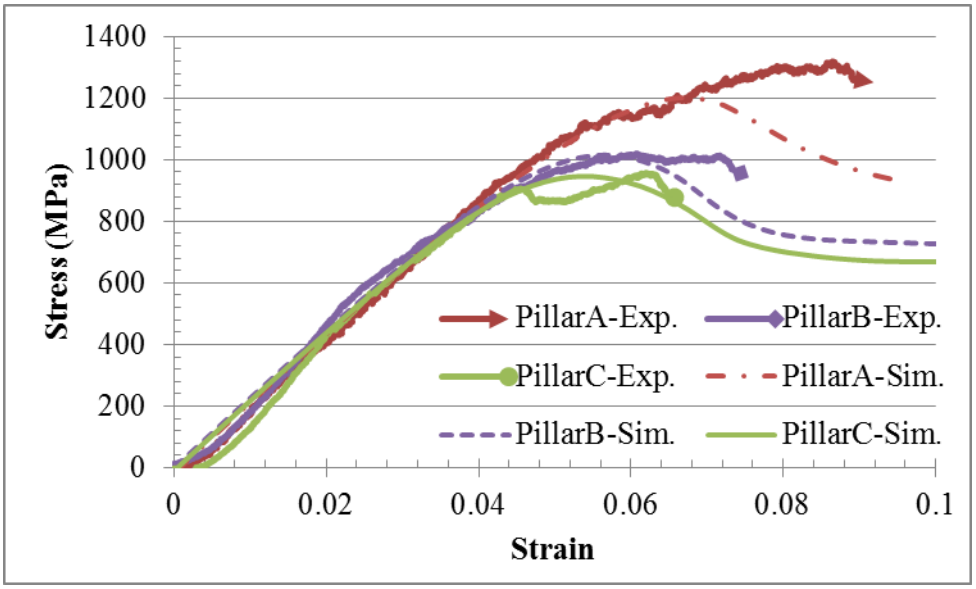

(b)

Figure 5-22: Average stress-strain curves for pillars A, B and C obtained from experiments and with FE simulations using EMSGCP theory with $\beta_1 = 1$ (a) and $\beta_1 = 2$

At the next step, a case study is performed where a cylindrical pillar with an orientation of (0.538 0.532 0.652) is compressed (Figure 5-23). The pillar's dimensions are 0.955 μm in diameter and 2.73 μm in height. This study enables us to examine, on the one hand, accuracy of the proposed the EMSGCP theory and, on the other hand, universality of the theory for different pillar geometries. The FE model was developed consistent with the considerations explained in Section 5.2. The normalized surface-to-volume ratio of the cylindrical pillar is 2.055, and the corresponding material parameters used in the simulations are presented in Table 5-7. Our first FE simulation suggested a misalignment between the indenter's tip and the cylindrical pillar since the elastic modulus was underestimated in the experiment (Figure 5-24). It was found that with an introduction of misalignment of 2.5° into the model, the elastic modulus of the pillar was estimated accurately; hence, the found misalignment was adopted in the FE model. As demonstrated in Figure 5-24, a reasonably well match was obtained between the experiment and the simulation using the EMSGCP theory, justifying the accuracy of the proposed model.

It should be emphasized that geometrical softening observed in the experiment was not captured in simulations; hence, the flow curves in Figure 5-24 start diverging after initial strain of 2.2%. It is important to underline that geometrical softening observed in the experiments and in the simulations are not similar to each other. In the experiment, the upper surface of the pillar starts to slip w.r.t. the indenter's tip, and at some instance a part of the pillar begins to shears off at certain plane, most likely where the Schmid factor is the highest. This leads to geometrical softening in the experiment due to decrease in cross-sectional area (Figure 5-24). On the other hand, in the simulations, geometrical softening arises only due to slip between the upper surface of the pillar and the indenter's tip, where no explicit tearing of the material occurs (as in the experiments) since such a mechanism is not introduced into the model. This pronounced difference between the experiments and the simulations results in deviation of the obtained stress-strain curve. However, this occurs beyond the yield point as seen from Figure 5-24, thereby the first part of the stress-strain curve obtained from the simulations do represent the experiments accurately. It should be mentioned that in the case of compression of a pillar with a stable orientation such as (001), where slip systems have an identical Schmid factor, the specimen do not undergo any buckling during compression (Raabe *et al*., 2007); hence, the above-mentioned difference between the experiment and simulation does not appear. For such orientations, it is more likely to accurately predict the material response numerically even at higher strain values. It must be emphasized that the continuum crystal plasticity approach presented here is limited to interpret the experimental results up to the development of planar slip nucleation, beyond this point the pillar's behaviour cannot be predicted numerically.

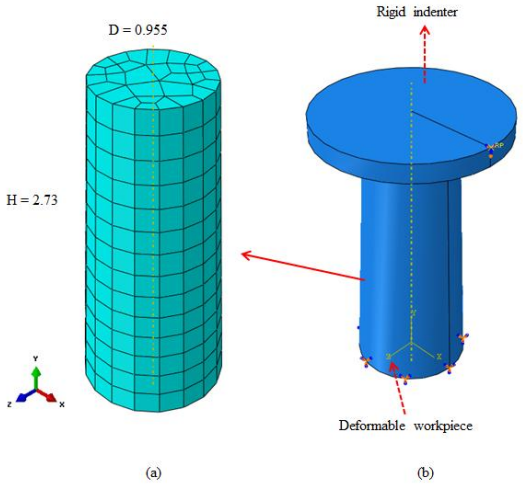

Figure 5-23: (a) Dimensions of cylindrical micro-pillar (in µm); (b) 3D FE model of micro-pillar-compression experiment

Table 5-7: EMSGCP parameters for modelled cylindrical pillar

Pillar type	$\frac{\bar{S}}{\bar{V}}$	$g_T^\alpha \mid_{t=0}$	$g_T^\alpha \mid_{\text{sat}}$
Pillar D	2.055	340 MPa	360 MPa

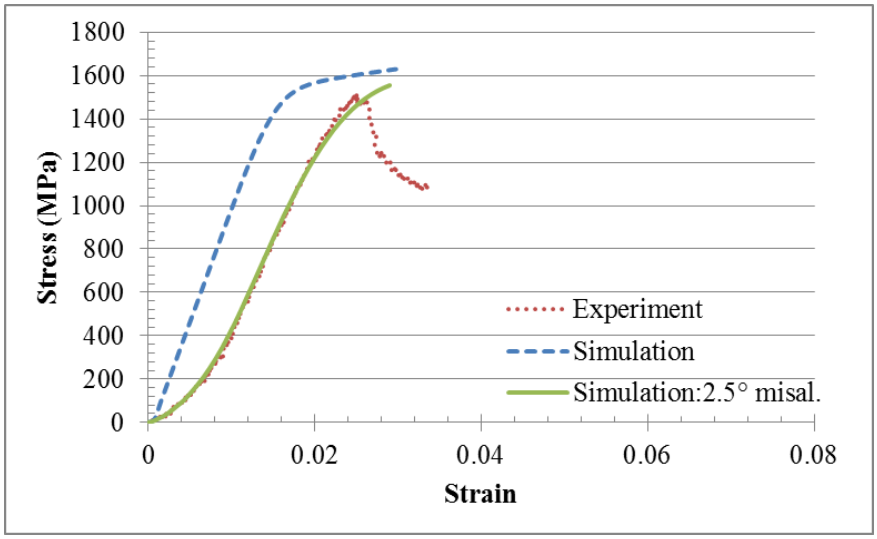

Figure 5-24: Average stress-strain curves for pillar D obtained from experiment and with FE simulations for different misalignments

5.5 Numerical predictions of size effects in pillars

In this section, the size effect in the single-crystal Ti alloy is studied, with the factors such as different aspect ratios, misalignment in the test system (ξ_1 =1 is therefore used in the followings, see Section 5.2.3) and taper of pillars, which may influence the size effect, are eliminated. On the other hand, that leads fully homogenized deformation macroscopically; hence, the average stress and strain values whose definitions were given in Section 5.1.2 corresponds to true stress and true strain values, respectively in the followings. Pillars having a square cross-section with an edge length of 1, 2, 4, 8 and 16 μm were modelled. The height-to-edge length aspect ratio was fixed at 2.1 in all the models. The material's plastic parameters for different pillar sizes are presented in Table 5-8. Consistent with the mesh-sensitivity analysis performed in Section 5.2.1, the mesh size of 210 nm × 210 nm × 210 nm was used to discretize the pillars. The crystal was oriented so that the micro-pillar axis was in the (010) direction enabling to avoid geometrical softening in simulations. For such an orientation of the crystal, four slip systems, viz. the fifth, sixth, seventh and eighth are expected to be activated according to the Schmid's law (see Table 5-9).

Table 5-8: EMSGCP parameters for different sizes of pillars

Pillar type	$\frac{\bar{S}}{\bar{V}}$	Pillar dimensions (width × length × height, μm)	$g_T^\alpha \mid_{t=0}$	$g_T^\alpha \mid_{\text{sat}}$
Pillar E	2.208	1 × 1 × 2.1	361 MPa	381 MPa
Pillar F	1.104	2 × 2 × 4.2	222 MPa	242 MPa
Pillar G	0.552	4 × 4 × 8.4	171 MPa	191 MPa
Pillar H	0.276	8 × 8 × 16.8	156 MPa	176 MPa
Pillar I	0.138	16 × 16 × 33.6	152 MPa	172 MPa
Pillar J	0.069	32 × 32 × 67.2	151 MPa	171 MPa

Table 5-9: Schmid factors of different slip systems for (0 1 0) crystallographic orientation

Slip system							Schmid factor
number	plane			direction			(0 1 0)
1	1	1	2	1	1	-1	0.236
2	-1	1	2	1	-1	1	-0.236
3	1	-1	2	-1	1	1	-0.236
4	1	1	-2	1	1	1	0.236
5	1	2	1	1	-1	1	-0.471
6	-1	2	1	1	1	-1	0.471
7	1	-2	1	1	1	1	-0.471
8	1	2	-1	-1	1	1	0.471
9	2	1	1	-1	1	1	0.236
10	-2	1	1	1	1	1	0.236
11	2	-1	1	1	1	-1	-0.236
12	2	1	-1	1	-1	1	-0.236

5.5.1 Case studies

This section starts with case studies to demonstrate the influence of boundary conditions and crystal orientation on the evolved strain gradients during loading (compressed to 76% of its height at full loading). To achieve this, following cases were studied.

- Case A: Pillar E was deformed by fixing its bottom surface only in the loading direction and allowed to move in the lateral directions. This enabled us to obtain a homogenous, uniform uniaxial strain and stress distribution (Figure 5-25 (a, b)), which, in turn, generates a zero plastic strain gradient as seen in Figure 5-25 (c).

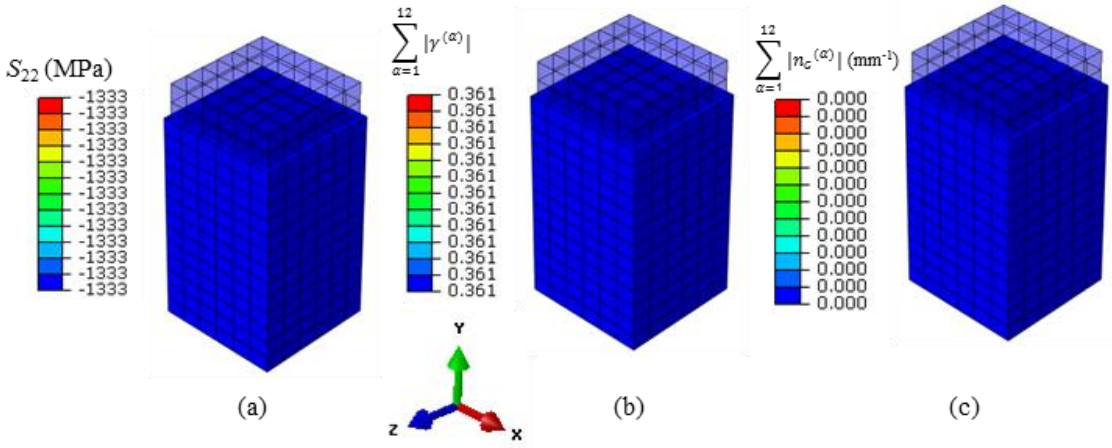

Figure 5-25: Distribution of stress values in the loading direction (a), total cumulative shear strains on all slip systems (sum of the absolute values of shear strains in all slip systems) (b) and sum of the absolute values of effective density of GNDs in all slip systems ($\sum |n_G^{(\alpha)}|$) (c) obtained with FE simulations for pillar E in case study A

- Case B: The bottom surface of Pillar E was fixed in all directions. This leads to a heterogeneous deformation as seen from in Figure 5-26 (a, b) where the stress distribution in the loading direction and total cumulative shear strains on all slip systems (sum of the absolute values of shear strains in all slip systems) were non-uniform. Also due to variation in the obtained total shear strain values, GNDs were generated in the deformed body as demonstrated in Figure 5-26 (c) where the effective density of GNDs on all slip systems (sum of the absolute values of effective density of GNDs in all slip systems) were observed to be non-uniform and mostly populated around the bottom corner nodes.

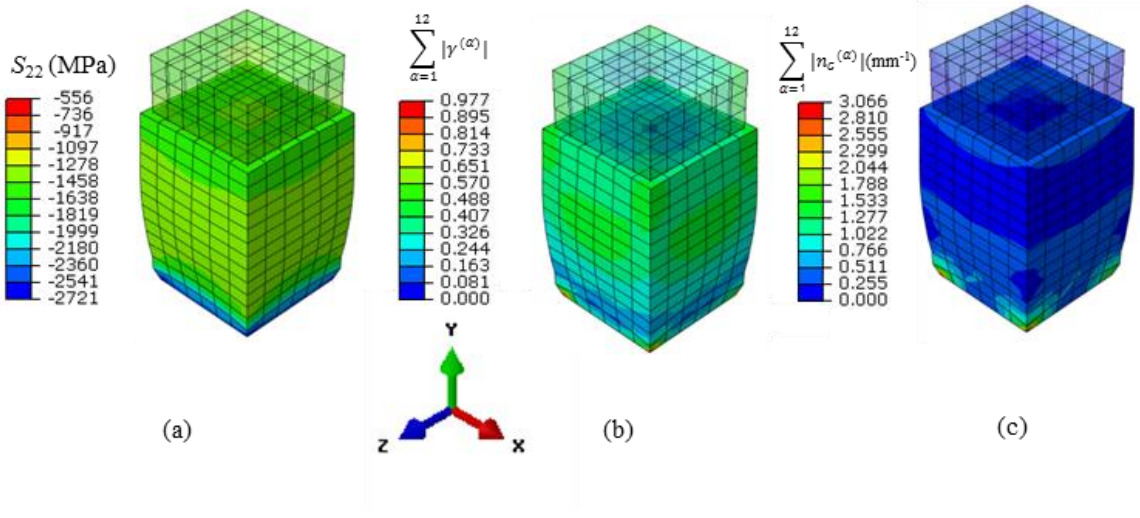

Figure 5-26: Distribution of stress values in the loading direction (a), total cumulative shear strains on all slip systems (b) and sum of the absolute values

of effective density of GNDs in all slip systems (c) obtained with FE simulations for pillar E in case study B

To fully understand the developed heterogeneous deformation, total accumulated plastic strain values in the loading direction and evolved GNDs on Y-Z center plane at half- ($t = t1$) and full-loading ($t = t2$) were analyzed. Figure 5-27 clearly demonstrated that with an increase in the amount of deformation, the accumulated plastic strain increased and more GNDs were evolved. Especially the distribution of ε_{22} at full loading ($t = t2$) indicated that the plastic strain was confined to the center of the plane and its variation was much more significant between center and bottom parts compared to other areas. The distribution of $\sum |n_G^{(\alpha)}|$ also justified this observation that GNDs were mostly populated on the respective areas (Figure 5-27 (b)). At this point, to demonstrate the proper implementation of strain gradient theory, the variation of shear strain values ($|(\varepsilon_{22})^{i+1}-(\varepsilon_{22})^{i}|$) and $\sum |n_G^{(\alpha)}|$ on path X-Y (Figure 5-27) were plotted, where i corresponds to number of nodes on the path (Figure 5-29). Here the first parameter characterizing roughly the gradients in the total plastic strain value in the loading direction should be in the same line with the latter parameter, which is in fact the measure of shear strain gradients. Figure 5-29 showed that the general trend of these two curves at half- and full-loading resembles to each other confirming that the strain gradient theory used in this study addressed the variation in the shear strain values accurately.

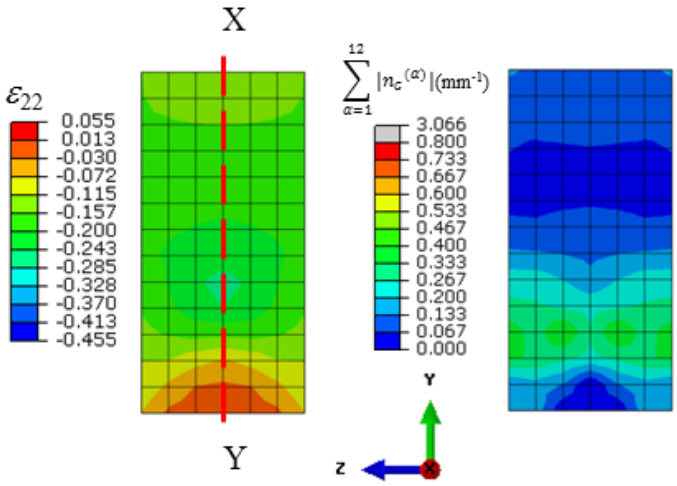

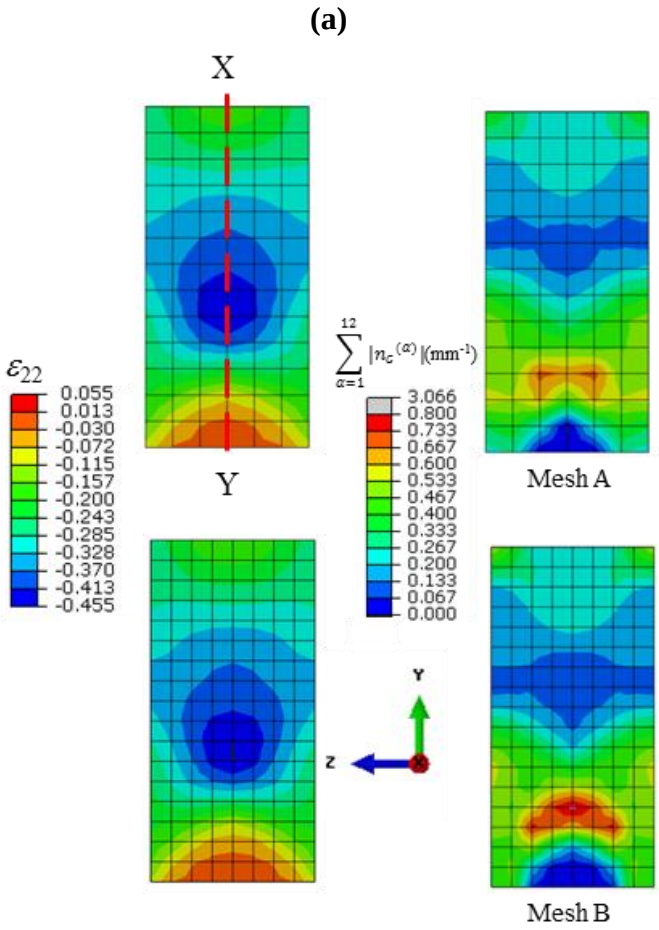

Figure 5-27: Distribution of accumulated plastic strain values in the loading direction (left) and sum of the absolute values of effective density of GNDs in all slip systems (right) at half- (*t=t1*) (a) and full-loading (*t=t2*) for different mesh sizes (b) on the mid-plane of pillar E obtained with FE simulations in case study B

The influence of mesh on the calculated strain gradients was also analyzed. Figure 5-27 (b) clearly indicates that the distribution of $\sum |n_G^{(\alpha)}|$ were not identical when a different level of mesh refinement is used in the discretization of the deformed body, even though the strain distribution for both were very similar to each other. Figure 5-28 demonstrated the computed sum of the absolute values of effective density of GNDs in all slip systems at full-loading (*t=t2*) on path X-Y (Figure 5-27) for different mesh sizes, where mesh C corresponds the coarsest mesh and mesh A

and mesh B are demonstrated in Figure 5-27. This plot also confirmed the mesh dependency of the computed strain gradients. The study of Cheong *et al.* (2005) also revealed that in the case of predominance of GNDs over SSDs, the structure response became increasingly mesh-sensitive. The same mesh size was therefore used in the discretization of the different size of pillars in this study.

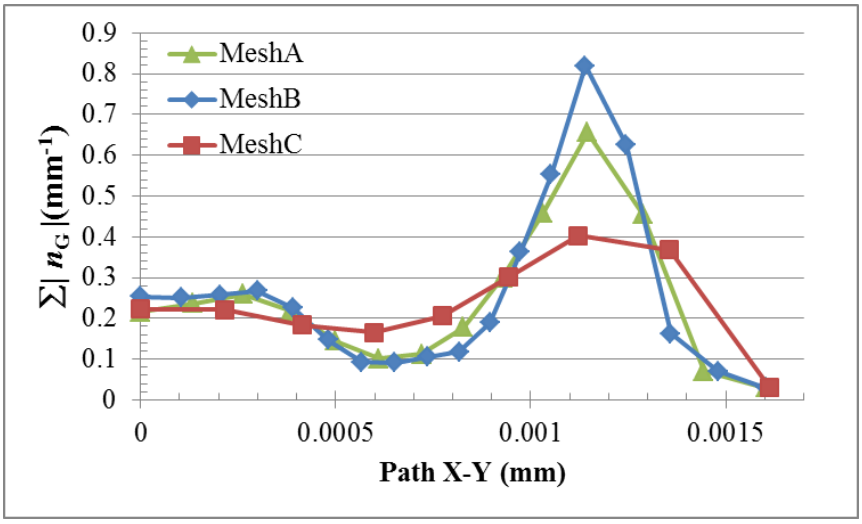

Figure 5-28: The plot of the sum of the absolute values of effective density of GNDs in all slip systems ($\sum|n_G|$) at full-loading (*t=t2*) on path X-Y (Figure 5-27) obtained with FE simulations for different mesh sizes

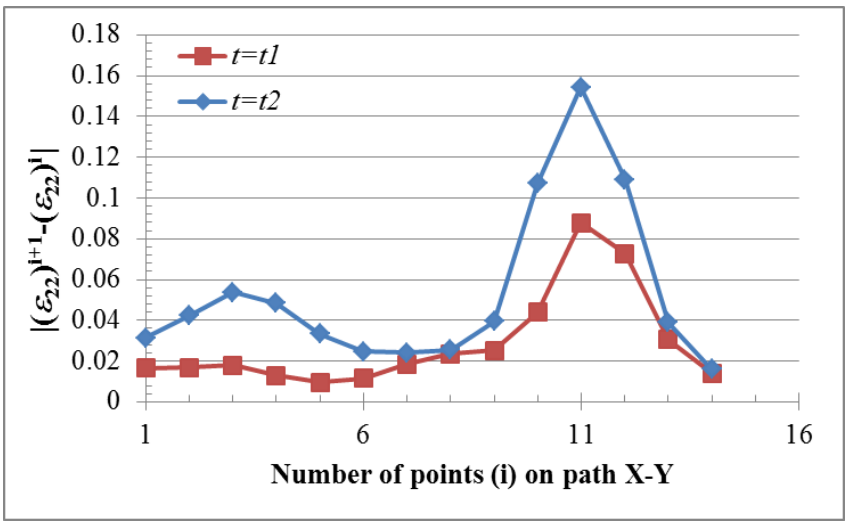

(a)

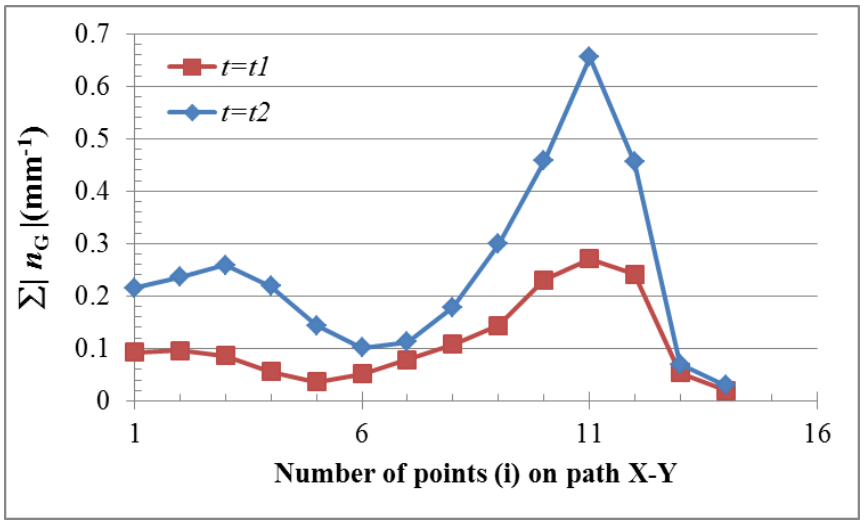

(b)

Figure 5-29: The plot of variation in the accumulated plastic strain values in the loading direction $|(\varepsilon_{22})^{i+1}-(\varepsilon_{22})^{i}|$ (a) and sum of the absolute values of effective density of GNDs in all slip systems (b) at half- (*t=t1*) and full-loading (*t=t2*) on path X-Y (Figure 5-27) obtained with FE simulations in case study B

- Case C: Compared to case B, the compressed crystal was rotated to (0.489 0.443 0.751) orientation in this case study. As seen in Figure 5-30 (a), due to slip between pillar's upper surface and the indenter, the pillar's two corners were in tension, while the others were in compression. The resulting total shear strain values (on all slip systems) were significant between the upper left corner and lower right corner of the pillar (Figure 5-30 (b)) as most of the load was carried with this portion. The shear strain gradients were therefore larger on these areas (Figure 5-30 (c)). The distribution of ε_{22} and $\sum|n_G^{(\alpha)}|$ values on Y-Z center plane at full-loading also clearly indicated that the shear activity and its variation were confined to this region and hence the gradients were there significant (Figure 5-31).

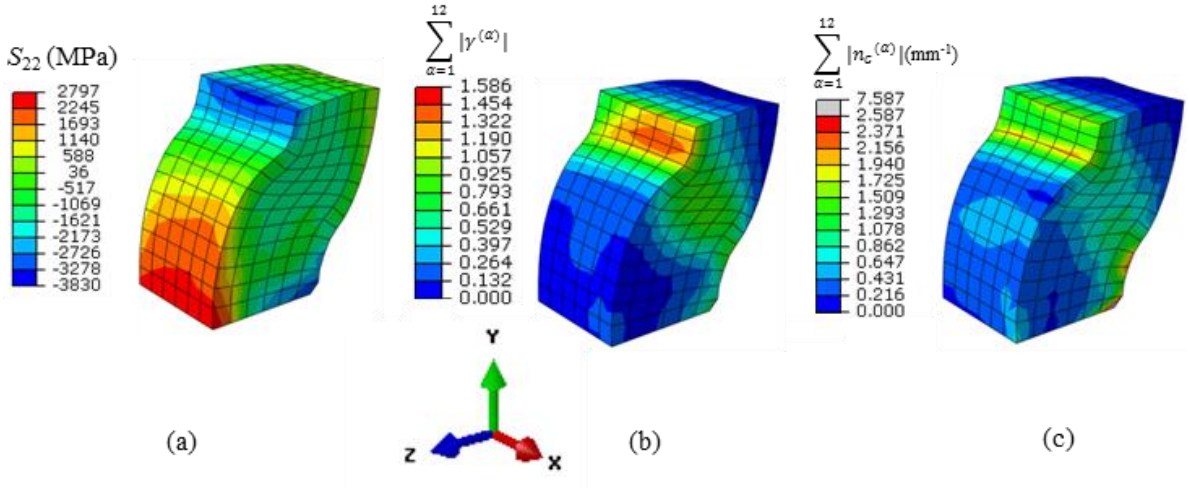

Figure 5-30: Distribution of stress values in the loading direction (a), total cumulative shear strains on all slip systems (b) and sum of the absolute values of effective density of GNDs in all slip systems (c) obtained with FE simulations for pillar E in case study C

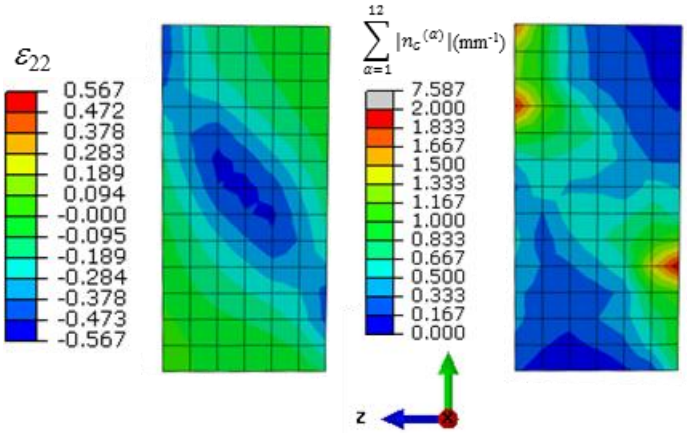

Figure 5-31: Distribution of accumulated plastic strain values in the loading direction (left) and sum of the absolute values of effective density of GNDs in all slip systems (right) on the mid-plane of pillar E obtained with FE simulations in case study C

5.5.2 Size effects in different size of pillars

The obtained true stress-strain curves for Ti micro-pillars E, F, G, H and I are compared in Figure 5-32. Yield strength of micro-pillars is observed to increase

with a decreasing pillar size, providing evidence of a strong size effect. It may be noted that the phenomena is more pronounced for pillars of smaller sizes compared to those of larger ones. This figure also suggests that no size effect is observed for pillars H and I since their flow curves are almost identical, implying that the effect of initial microstructure for both pillars is very similar. The flow curve of pillar I, indeed, forms a lower bound for all the flow curves since its CRSS value, 152 MPa, is very close to the corresponding value obtained from the nano-indentation experiments, 150 MPa, where the influence of incipient strain gradients was negligibly small (Figure 5-32). From these results it was concluded that the "smaller is stronger" phenomena was observed for pillars E, F, G and H, and pillar H had the critical size, with no observable size effect for larger pillar sizes. The edge length of this pillar, 8 μm, is therefore considered as the critical edge length l_c, below which the relative change in the corresponding stress value is less than 5%.

The value of critical resolved shear stress can be scaled with respect to the diameter d of the micro-pillar using the following power-law form:

$$\frac{\mathrm{CRSS}}{\mu_s} = A\left(\frac{d}{b}\right)^{M}, \qquad 5\text{-}9$$

where μ_s is the shear modulus, b is the Burgers vector magnitude, and A and M are constants. Dou and Derby (2009) obtained the universal constants $A = 0.71$ and $M = -0.66$ by using a least-squares fit to the experimental data for Al, Au and Ni micro-pillars. The corresponding curve for Ti alloy is plotted using the material parameters of pillars E, F, G and H (it should be emphasized that one of the edge lengths of square pillars is used to replace the diameter term in equation 5-9). It is worth mentioning here that is since the size effect was not observed for pillars H and I, pillar I was not considered in the fitting. As seen from the logarithmic plot shown in Figure 5-33, the obtained constants are 0.63 and -0.40 for A and M, respectively. A comparatively good agreement was achieved for constant A, whereas a lower value of constant M was predicted, i.e. the curve for Ti alloy is not steep as compared to the universal curve. This difference can be ascribed to the

difference in the range of pillar size considered: while for the universal curve both nano and micron-size pillars were considered to determine the constants, here only micron-size pillars were considered.

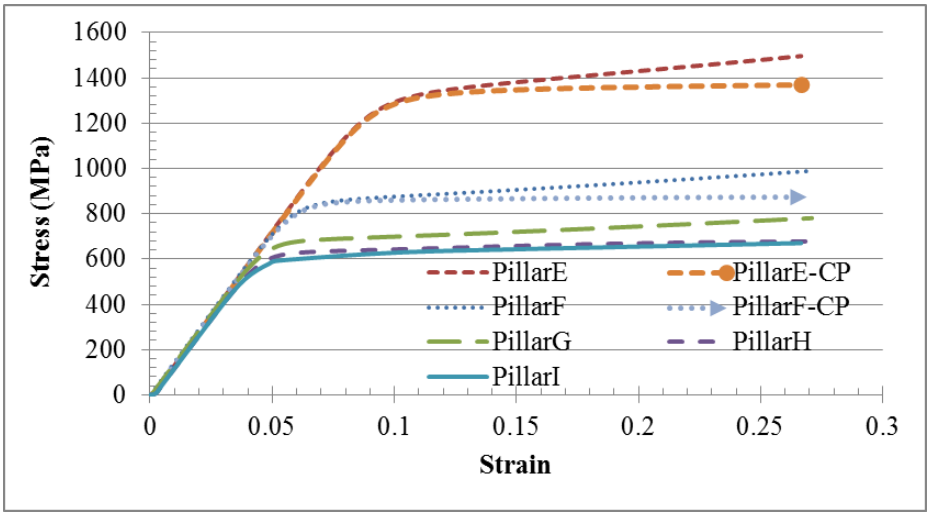

Figure 5-32: True stress-strain curves for pillars E, F, G, H and I obtained with FE simulations using EMSGCP theory and for pillars E and F using CP theory

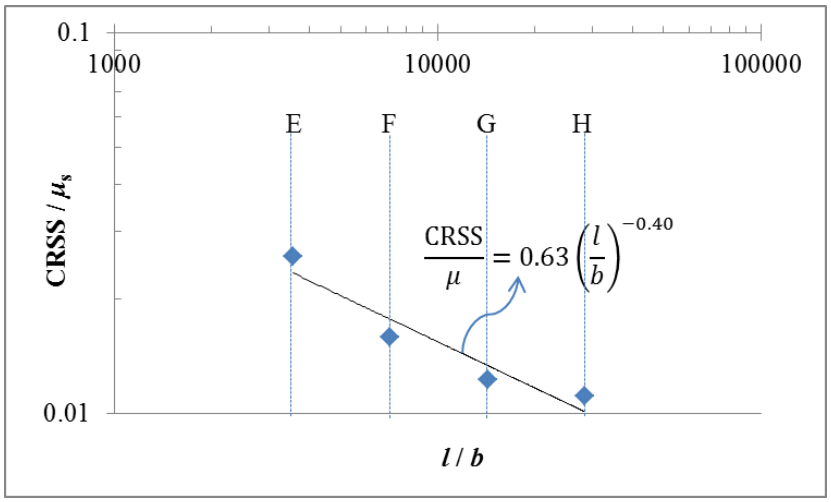

Figure 5-33: Logarithmic plot of CRSS normalized with μ_s versus l normalized with b for pillars E, F, G and H

In Figure 5-32 the solutions for pillars E and F obtained using the CP theory with incipient strain gradients accounted for, but not strain gradients introduced during

deformation are also plotted. In these solutions, however, the incipient strain gradients are considered while obtaining values of CRSS ($g_T^{\alpha}\,|_{t=0}$) for slip systems. It is observed that the hardening rate for the CP theory based results is small and border on ideal plasticity, this can be explained by the used PAN hardening model (Figure 3-10). However, the solutions obtained using the EMSGCP theory demonstrate that the hardening rates are higher due to the strain gradients developed during deformation. To quantify the evolved strain gradients as a function of pillar size, the work-hardening rate (WHR) for pillars E, F, G and H were determined (Table 5-10). The WHR was defined as a slope of the curve between true stress-strain data values for strains of 15 and 20%. Interestingly, a significant increase in WHR is observed with a decreasing pillar size, with a best fit line of WHR $\propto (l)^{-0.675}$ justifying the fact that size effect is pronounced in the WHR as well (Figure 5-37). The evolved strain gradients for different size of pillars were also investigated. To explain it properly, firstly the accumulated plastic strain values in the loading directions (ε_{22}) for the mid-plane of pillar E, F and G at full loading (strain of approx. 27%) were compared. Figure 5-34 demonstrated that the values were similar to each other. As mentioned earlier the same mesh size was used in all the pillars to eliminate the influence of mesh on the predictions since the calculated strain gradients are mesh dependent (see case study B in Section 5.5.1). The variation of ε_{22} values on path X-Y (Figure 5-34) were plotted to get a rough idea about the amount of strain gradients evolved during loading. Figure 5-35 demonstrated that they were largest for the smallest pillar and decreases with an increase in the pillar's size. The distribution of the sum of the absolute values of effective density of GNDs in all slip systems ($\sum |n_G^{(\alpha)}|$) in Figure 5-36 also supports this observation. The contour plots in this figure indicated that the GNDs were significant for pillar E, modest for pillar F and lowest for pillar G. Also the GNDs were mostly populated between the middle and bottom sections of the pillars' mid-planes since the variations in total shear strain values on these regions were more significant as demonstrated earlier in Figure 5-35. It should be emphasized that although the strain distributions of different pillar sizes were similar to each other, their gradients, i.e. their variation through the dimensions, became different due to

their different geometrical sizes. These results justify that the smaller the pillar, the higher strain gradients evolve during deformation.

Table 5-10: Work-hardening rates for pillars of different sizes

Pillar	Work-hardening rate (MPa)
Pillar E	981
Pillar F	659
Pillar G	480
Pillar H	229

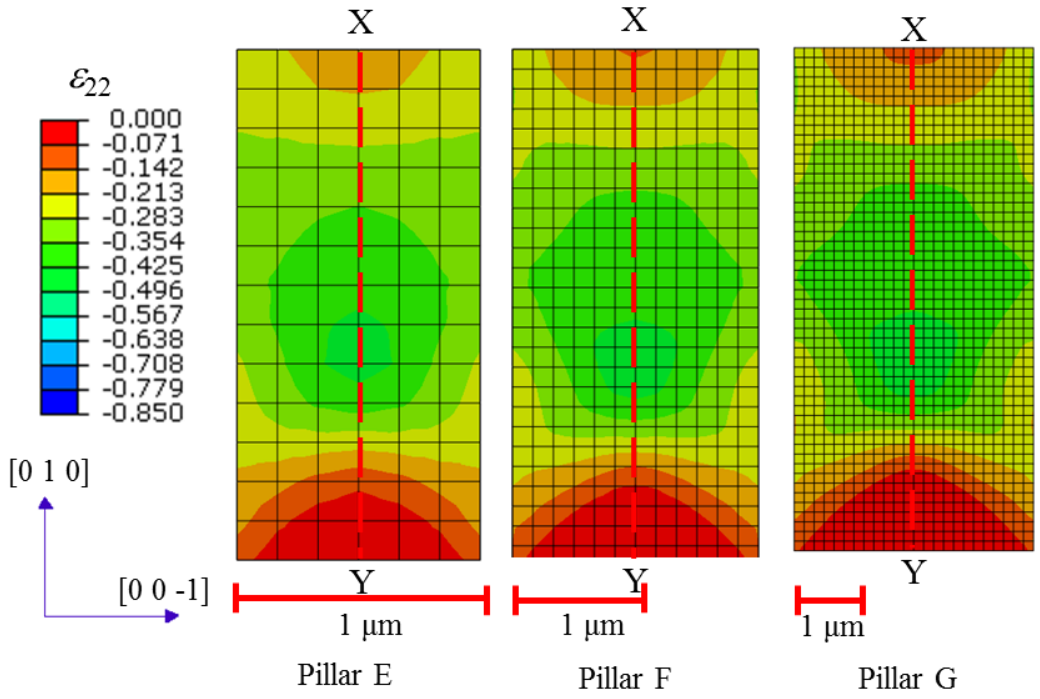

Figure 5-34: Distribution of accumulated plastic strain values in the loading direction at full loading obtained with FE simulations for mid-plane of pillars E, F and G (consider different length scales)

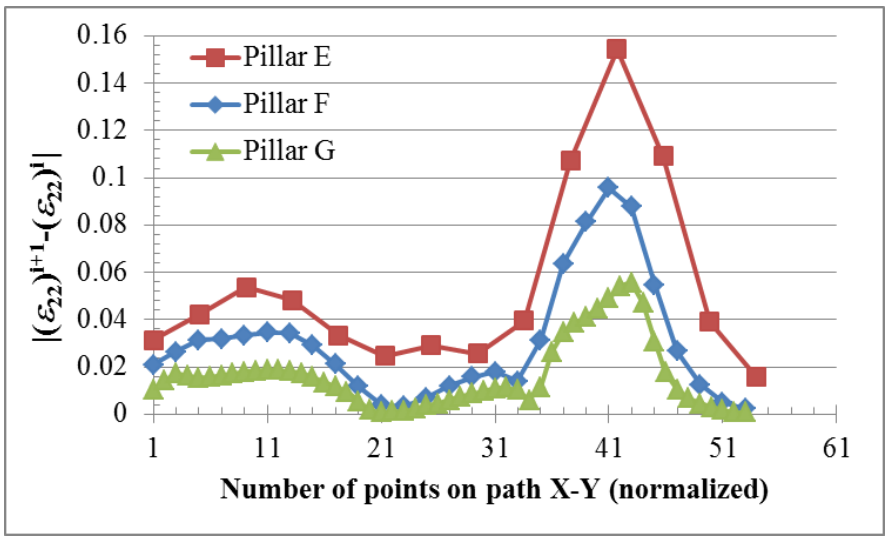

Figure 5-35: The plot of variation in the accumulated plastic strain values in the loading direction $|(\varepsilon_{22})^{i+1}-(\varepsilon_{22})^{i}|$ at full-loading on path X-Y (Figure 5-27) obtained with FE simulations for pillars E, F and G

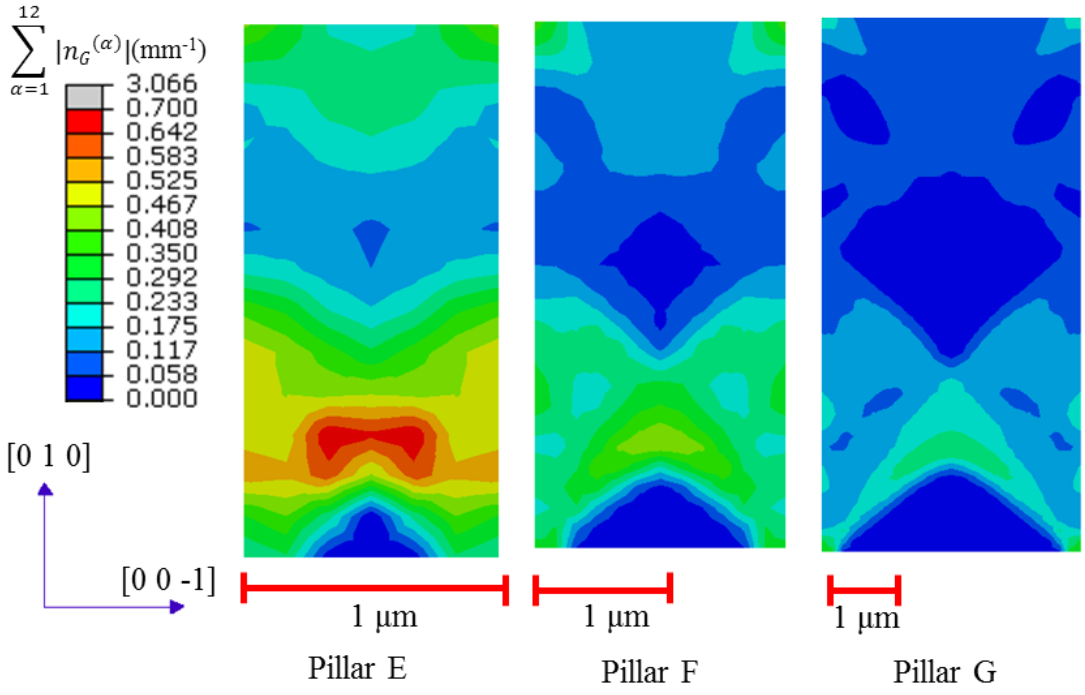

Figure 5-36: Distribution of the sum of the absolute values of effective density of GNDs in all slip systems at full loading obtained with FE simulations for mid-plane of pillars E, F and G (consider different length scales)

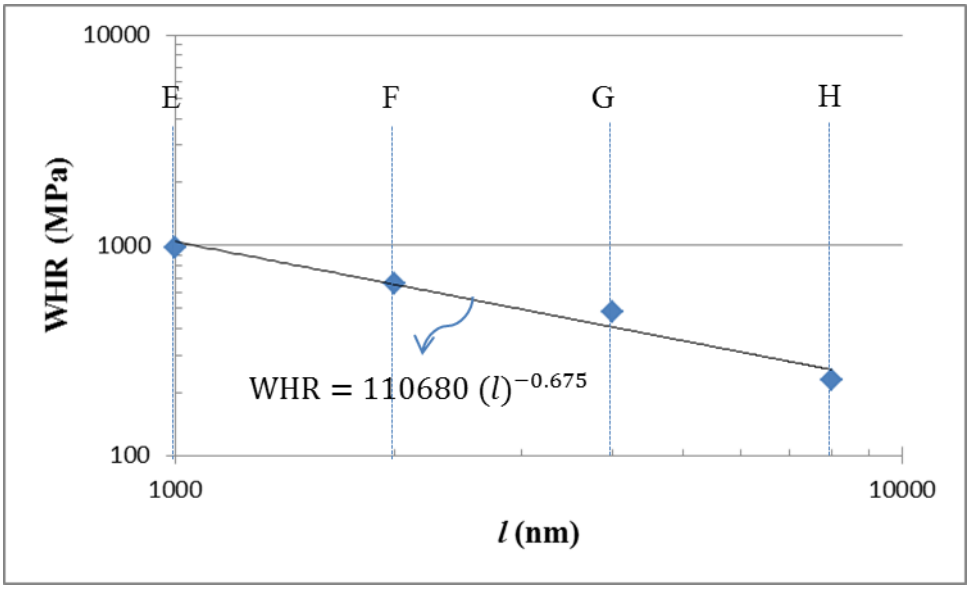

Figure 5-37: Logarithmic plot of work-hardening rate (WHR) versus *l* for pillars E, F, G and H

5.5.3 Sensitivity of characteristic length

In the previous section, the range of pillar sizes, where the size effect is significant, is determined. For the Ti alloy the edge length of 8 μm is observed to be the critical length (l_c), below which effectively no size effect is observed. Here, the sensitivity of this critical length is investigated with respect to different material parameters representing different material characteristics, e.g. CRSS, K and dislocation interaction coefficient. Since CRSS ($g_T^\alpha|_{t=0}$) is a function of incipient density of SSDs ($\rho_S|_{t=0}$) and incipient density of GNDs ($\rho_G|_{t=0}$) as demonstrated in equation 5-8, different cases are considered here for varying relative magnitudes of ρ_S and ρ_G. In addition to already determined values of densities presented in Table 5-6, labelled as "Present", two cases with different density values were also analysed as shown in Table 5-11. In the first case $\rho_G|_{t=0}$ was kept the same and $\rho_S|_{t=0}$ was decreased, whereas in the second case $\rho_S|_{t=0}$ was kept the same, while $\rho_G|_{t=0}$ was decreased.

The change in the CRSS value with the edge length of pillars E to J for different cases is shown in a logarithmic plot in Figure 5-38. This plot reveals that the

critical edge length varies for different cases. For instance, l_c is 16 μm for case 1 and the corresponding value for case 2 is 4 μm, whereas, as mentioned above, l_c is 8 μm for the present case. This result suggests that a decrease in $\rho_S|_{t=0}$ causes an increase in l_c; hence, the size effect can be observed for a larger range of pillar edge length. On the other hand, a decrease in $\rho_G|_{t=0}$ leads to a smaller l_c. In the case of smaller values of $\rho_S|_{t=0}$ and larger values of $\rho_G|_{t=0}$, the size effect is observed for a larger range of pillar size and similarly in the case of larger values of $\rho_S|_{t=0}$ and smaller values of $\rho_G|_{t=0}$, the size effect is observed for a smaller range of pillar size.

Table 5-11: EMSGCP parameters for different cases

Cases	Density values, 10^4 mm^{-2}
Present	$\rho_S\|_{t=0} = 1538$
	$\rho_G\|_{t=0} = 1510$
Case 1	$\rho_S\|_{t=0} = 700$
	$\rho_G\|_{t=0} = 1510$
Case 2	$\rho_S\|_{t=0} = 1538$
	$\rho_G\|_{t=0} = 500$

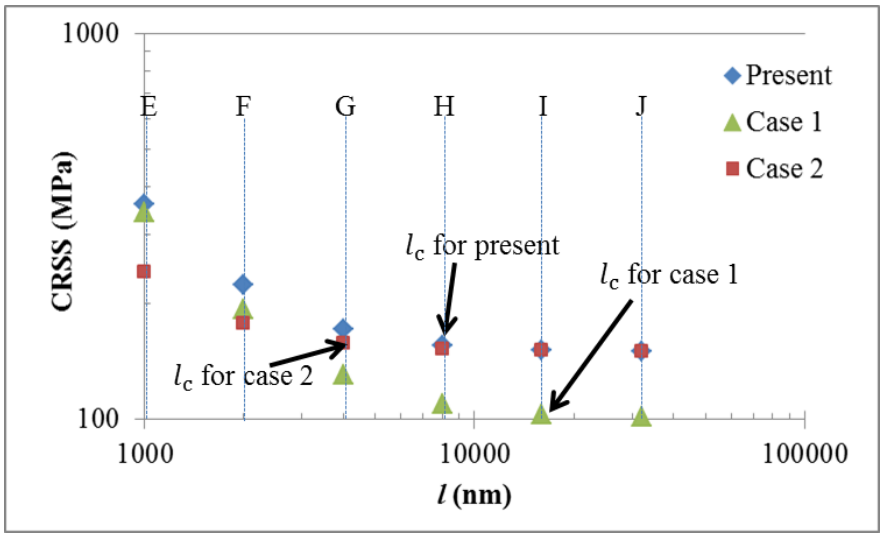

Figure 5-38: Logarithmic plot of CRSS versus *l* for different cases (see Table 5-11)

The sensitivity of l_c was also investigated for other material properties - K and β. The former one correlates the initial strength of slip system to the incipient density of dislocations and the latter one represents the sensitivity to coupling between $\rho_S|_{t=0}$ and $\rho_G|_{t=0}$. In the first study here in addition to K = 0.04 that was used for the above analysis, K = 0.02 and 0.08 are also considered. The CRSS value for pillars E to J as a function of pillar edge length in a logarithmic plot is shown in Figure 5-39. This plot indicates that l_c is 8 μm for all K values, implying that l_c is not sensitive to parameter K.

To see the influence of β_1 on l_c, two different values of β_1 - 1 and 2 - were considered. Figure 5-40 demonstrates the corresponding CRSS value for pillars E to J as a function of pillar edge length in a logarithmic plot. This plot suggests that $l_c = 64$ μm for β_1 = 1 and, as known from the previous analysis, $l_c = 8$ μm for β_1 = 2. It is worth mentioning that the CRSS value of a pillar with dimensions of 32 μm × 32 μm × 67.2 μm is checked. This demonstrates a less than 5% difference in CRSS value compared to corresponding value of pillar J, hence justifying that $l_c = 64$ μm for β_1 =1. Figure 5-40 suggests that an increase in the β_1 value leads to a decrease in l_c. Abu Al-Rub and Voyiadjis (2004) demonstrated that the smaller the interaction coefficient β_1, the more significant interaction between SSDs and GNDs. Based on this it is concluded here that the stronger interaction of incipient SSDs and incipient GNDs leads to a larger range of pillar size with the size effect.

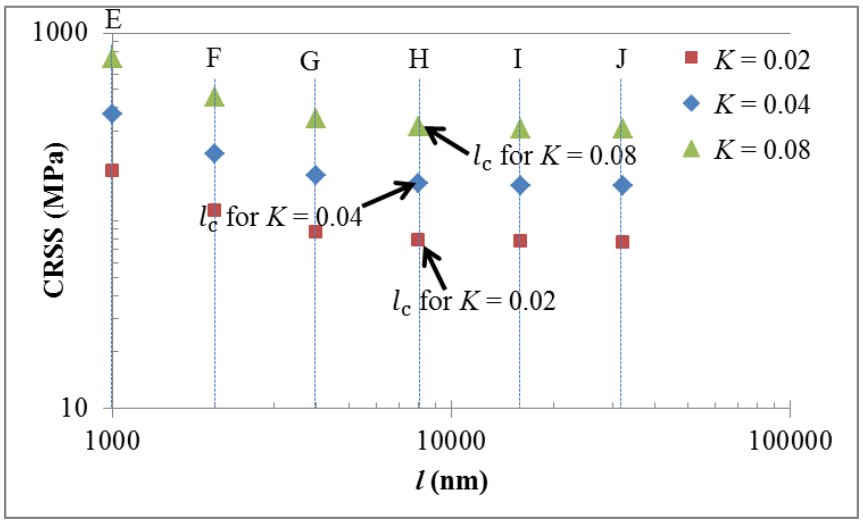

Figure 5-39: Logarithmic plot of CRSS versus *l* for different *K* values

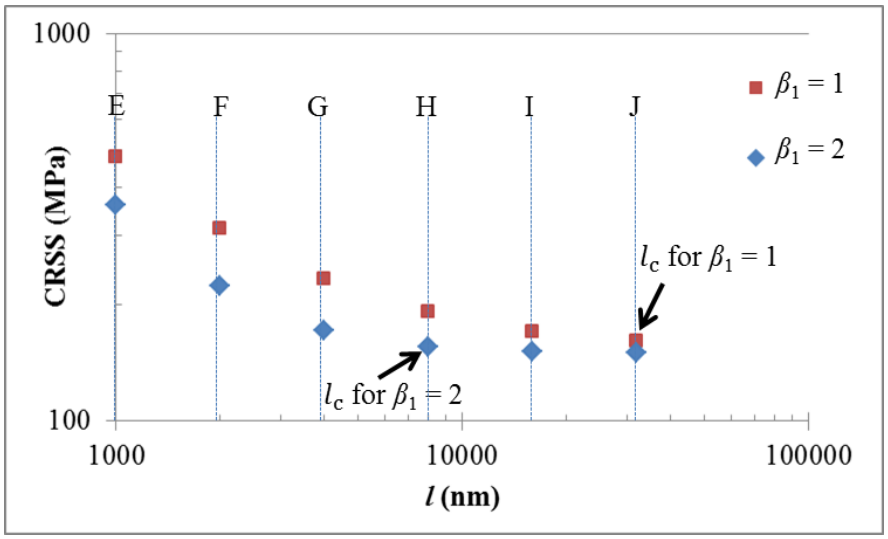

Figure 5-40: Logarithmic plot of CRSS versus *l* for different β_1 values

5.5.4 Influence of size effect on local properties

In this section the change in local mechanical properties of pillar with a change in pillar size was investigated. Figure 5-41 compares the calculated contour plots on deformed shape of the von Mises stress for the mid-plane of pillar E, F and G at full loading. The first noteworthy feature of the finite deformation is the barreling of pillars under compression regardless of the size. As expected, the stress values of smallest pillar are largest, and with an increase in the size a decrease in the obtained stress levels is observed. This can be explained by the fact that as the total density of dislocations is larger for smaller-size pillars, larger forces are required to move dislocations, leading to higher stress values in the body of the pillar.

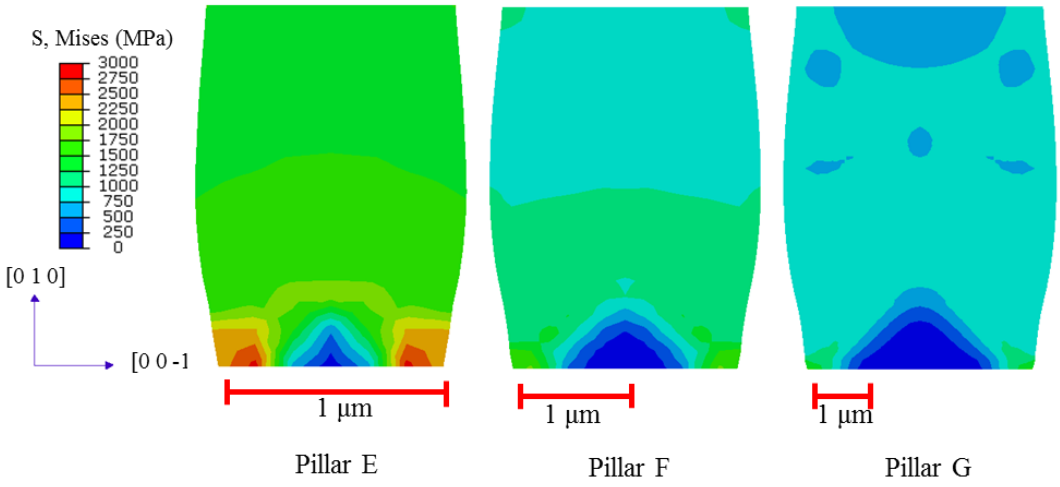

Figure 5-41: Distribution of von Mises stress at full loading obtained with FE simulations for mid-plane of pillars E, F and G (consider different length scales)

Compared to distribution of von Mises stress, a completely inhomogeneous distribution of shear-strains for different active slip systems is observed in pillar E (Figure 5-42). The contour plots in this figure suggest that the shear activity takes place basically on slip systems 5, 6, 7 and 8, whereas negligibly small shear happens on all other slip systems. This result complies with Table 5-9 where the Schmid factor was calculated before the start of deformation. This justifies that in the course of loading the local boundary conditions of each material point do not change since the deformation is macroscopically homogenous, i.e. the Schmid factor does not evolve with an increase in deformation.

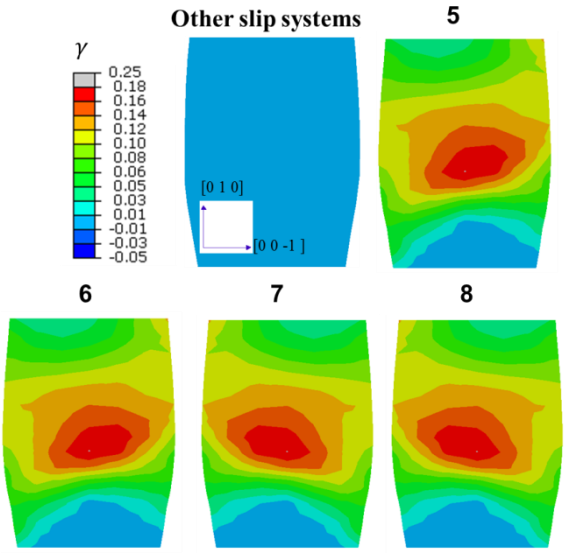

Figure 5-42: Distribution of shear-strains (γ) for different slip systems at full loading from FE simulations on the mid-plane of pillar E

5.6 Conclusions

The performed micro-pillar compression experiment demonstrated that the size effect was observed in the beta phase of Ti-15-333, i.e. the material behaviour diverged from that of the bulk material. A 3D FE model of this experiment was developed to get an insight about the underlying reason for this phenomenon.

At the first attempt, constitutive laws of the MBSGCP theory were used in the numerical model. However, as the CRSS values for slip systems in this theory are independent of the pillar size, this theory was found to be insufficient to explain the size effect. A novel enhanced model of strain gradient theory was suggested, where the initial microstructure of pillars as a function of the micro-pillar's surface-to-volume ratio was accounted for, based on some experimental evidence (Maass et al., 2006; 2007; 2009). This multi-scale continuum theory bridges the gap between the discrete-dislocation-dynamics (DDD) theory, where simulations are performed at strain-rates several orders of magnitude higher than those in experiments, and the classical continuum-plasticity theory, which cannot explain the dependence of mechanical response on a specimen's size since there is no length scale in its constitutive description. The numerical results demonstrated that the experimental

stress-strain curves of pillars were predicted appropriately using the EMSGCP theory, which accounts for the incipient GNDs in the pillar's body. It was also demonstrated that, although deformation was applied uniaxially in the micro-pillar compression experiment, heterogeneity evolved during loading due to boundary conditions and orientation of the pillar itself, leading, in its turn, to strain gradients as also suggested by Zhang and Aifantis (2011) and Maass et al. (2007). These findings also justified that strain-gradient theories can be used to explain the size effect in micro-pillars.

The edge length of the pillar, below which the relative change in the corresponding stress value was less than 5%, was considered as the critical edge length l_{c}. It was observed that l_{c} was a function of material parameters $\rho_S|_{t=0}$, $\rho_G|_{t=0}$ and β_1, whereas it was insensitive to parameter *K*.

The next chapter aims to characterize the material behaviour of the Ti alloy using nano-indentation experiments, where the induced strain gradients during loading are more profound. The EMSGCP FE model of this experiment also enables to identify some material parameters of the studied alloy, e.g. $\rho_S|_{t=0}$ and α_{T}, which are difficult to obtain using micro-pillar compression experiments.

Chapter VI

6 FE model of nano-indentation experiments based on EMSGCP theory

The goal of this chapter is to characterize the material's behaviour of Ti-15-3-3-3 at micron scale in nano-indentation experiment using the EMSGCP theory. In the previous chapter material parameters of the Ti alloy were identified by accounting for incipient strain gradients in the pillar sample. In micro-pillar-compression experiments, the studied volumes are not constrained by the surrounding material; however, in indentation experiments, deformation of indented volume of workpiece material is restricted by the neighbouring material. As the traction-free surfaces are sufficiently away in the nanoindentation sample, the effect of pre-existing strain gradients is insignificant, in contrast to the samples in micro-pillar-compression experiments.

3D FE modelling of nano-indentation experiments is developed here using the EMSGCP theory. It should be emphasized that the EMSGCP theory degenerates to the SGCP theory in case of nanoindentation experiment model as the incipient

strain gradients are negligibly small ($\rho_S|_{t=0} \approx 0$) in the indented workpiece material, as mentioned above, i.e. $\bar{S}/\bar{V}$ is effectively vanishes. This numerical model, on the other hand, enables us to characterize material properties of the single-crystal Ti alloy such as CRSS value, which cannot be directly determined from the load-displacement curve obtained in nano-indentation experiment due to its inherent smooth character, i.e. there exists no obvious transition from elastic to plastic deformation. The identified material parameter $\rho_S|_{t=0}$ also helps here to characterize the contribution of $\rho_S|_{t=0}$ and $\rho_G|_{t=0}$ to CRSS in micro-pillar-compression experiment, where their relative magnitudes cannot be determined directly from this experiment. The investigation in this chapter sheds light on the characterization of the evolved strain gradients in the indented workpiece material during deformation, which cannot be achieved in micro-pillar-compression experiments, where the strain gradients induced in the course of deformation are less profound.

In the first part of this chapter, details of the performed nano-indentation experiments are given, and the obtained load-displacement curves and surface profiles of indents are presented. In the second part, a FE model of nanoindentation experiments is discussed including mesh-sensitivity analysis and the appropriate selection of workpiece dimensions. This part is followed by determination of material parameters, including an extensive analysis of sensitivity of material parameters. Using the optimized set of material parameter, a comprehensive analysis of the mechanical behaviour of the single-crystal Ti alloy at nano scale is performed. In the final part of this chapter, a complete numerical analysis of the size effects in indentation is performed.

6.1 Nanoindentation experiment

Nanoindentation experiments on Ti-15-3-3-3 were performed at EMPA, Switzerland. Detailed information about the indented material is given in Section 5.1.1. *Ex-situ* nanoindentation experiments with a SEM instrument have been performed using a commercial nano-indenter Hysitron UBI equipped with a

conical indenter (tip radius: 1 μm; opening angle: 90°). This symmetrical indenter is selected to avoid symmetries other than those of the crystal structure. Nanoindentation tests were conducted five times for the each orientations (with a maximum deviation of ±0.02% and ±0.05% in the obtained maximum load and maximum displacement, respectively), viz. (0.641 0.078 0.764), (0.579 0.417 0.702) and (0.114 0.107 0.988), of the single-crystal metastable β-Titanium alloy Ti-15V-3Al-3Sn-3Cr. The crystal orientations were determined by electron back scattering diffraction (EBSD). The maximum load of 6 mN was used to analyse deformation anisotropy of the Ti alloy. The loading and unloading rate was kept constant at 0.1 mN/s. Figure 6-1 demonstrates the obtained load-displacement curves from the nanoindentation experiments.

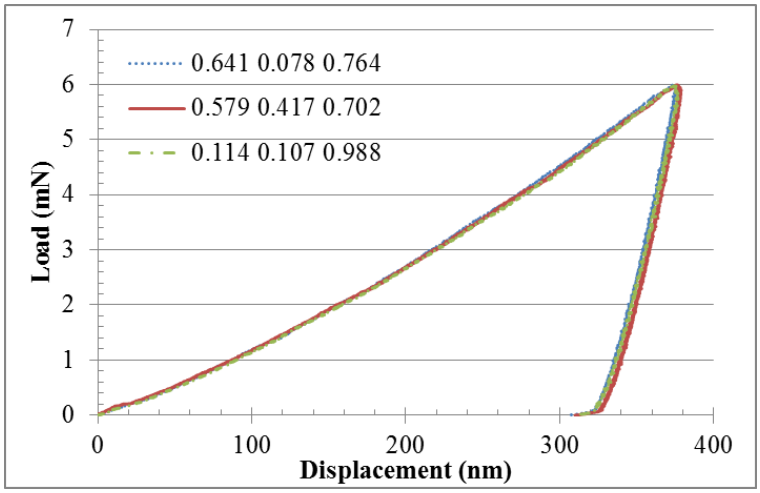

Figure 6-1: Load-displacement curves obtained from nanoindentation experiments for different crystallographic orientations

After the indentation all indents were characterized by atomic force microscopy (AFM) and with a field emission Hitachi SEM S4800 system to get more detailed information on the deformed material such as the shape of the piled-up material. As seen in Figure 6-2, different surface topographies were obtained for different orientations although the used indenter tip was symmetric. For the crystal with orientation (0.641 0.078 0.764), two-fold symmetry is observed, while orientations (0.114 0.107 0.988) and (0.549 0.417 0.702) resulted in a four-fold symmetry and three-fold symmetry, respectively. Different pile-up patterns can be explained in

terms of the strong crystallographic anisotropy of the out-of plane displacements around the indents. The scanned surface profiles of the indents through the paths shown in Figure 6-2 are plotted in Figure 6-3, revealing the fact that the obtained pile-up height is maximum for the indentation for (0.114 0.107 0.988) and minimum for the orientation (0.549 0.417 0.702).

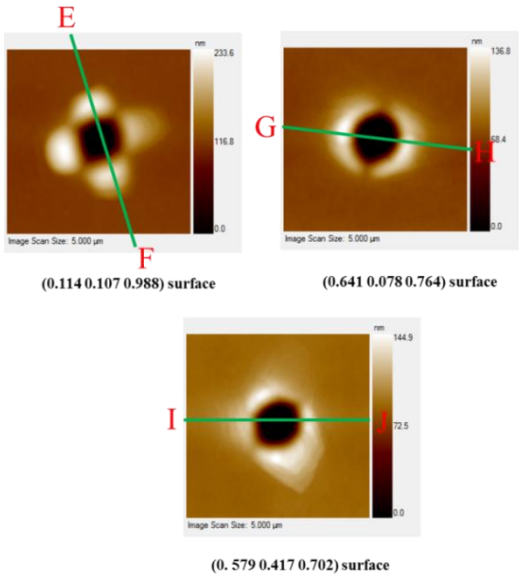

Figure 6-2: Pile-up structures of imprints taken by AFM-topography measurement and SEM imaging for different crystallographic orientations

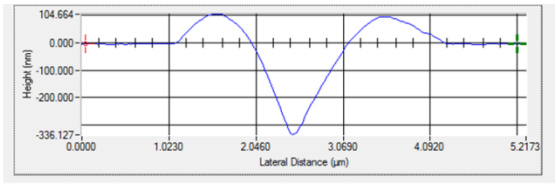

(0.114 0.107 0.988) surface, Path E-F

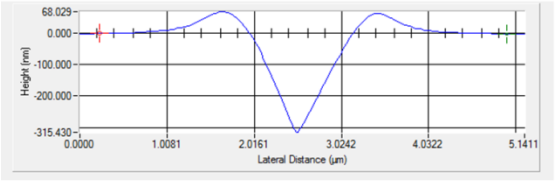

(0.641 0.078 0.764) surface, Path G-H

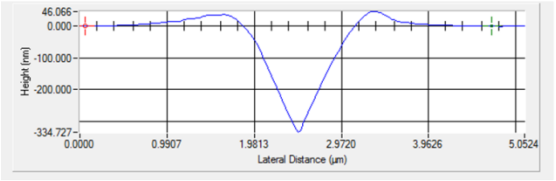

(0. 579 0.417 0.702) surface, Path I-J

Figure 6-3: Pile-up profiles of indents through different paths (see Figure 6-2) for different crystallographic orientations

The beta phase of Ti-15-3-3-3 has a b.c.c. crystal structure. In such materials slip may occur on 48 individual slip systems in three different sets: 12 slip systems from {110} <111> and {112} <111> families each and 24 slip systems from {123} <111> family. These three different sets are presented in Figure 3-6. The positions of the pile-up and orientations of slip lines around the imprints are determined by the active slip system. It is generally accepted that material is piling up in positions, where the active slip plane intersects the materials surface (Wang *et al*., 2004). It is therefore possible to distinguish between the possible glide planes of b.c.c. crystals by observing the position of slip lines surrounding the indentation imprint at the material surface and EBSD. For the investigated Ti alloy, Nowag *et al* (2012) compared the experimentally observed and theoretically expected positions of the slip bands for all possible glide planes for a grain close to (001) orientation including Schmid factors for all possible slip systems (Figure 6-4). In this study the investigation of {011} planes showed that there was no match between the theory and experimental results, i.e. the observed positions of pile-up and orientations of slip lines did not follow theoretical predictions. The analysis of {123} planes indicated that some of the experimentally observed slip-lines matched the theoretically calculated ones. However, not all of the observed slip lines could be correlated to a corresponding {123} plane. It should be emphasized that due to the high number of {123} planes it is not surprising that some matches were found. On the other hand, the comparison of slip lines with the theoretical positions of {112} planes showed a remarkable match: all the experimentally observed slip bands could be correlated to a particular {112} plane. In that study, (101) - and (111) - oriented crystals were also indented, and their analysis produced similar observations. In summary, the study suggested that {112} <111> was the dominant slip system during deformation. In the FE simulations of this chapter only this set is therefore switched on out of three different potential sets.

The detailed explanation of the experimental results will be given in Section 6.5, where the material parameters are defined, and in Section 6.6, where the mechanical behaviour of the Ti alloy is studied numerically. In the next section, the steps in developing a 3D FE model of nano-indentation experiment are shown.

6.2 Modelling consideration

A three-dimensional FE model of indentation was developed to represent the deformation of the single-crystal Ti-based alloy. Numerical simulations were performed using the EMSGCP theory implemented in the UMAT subroutine. This section starts with the justification for using the CP-based constitutive laws in FE simulations of this thesis rather than isotropic constitutive equations. Figure 6-2 demonstrates the indent impressions made on the workpiece material with a conical indenter. It is visible that the pile-up patterns on the (0.641 0.078 0.764) surface forms a two-fold symmetry. This experimental result can be predicted correctly using the CP-based constitutive law, where crystalline nature of the material is accounted for (Figure 6-5 (b)). On the other hand, the isotropic material model cannot predict the material behaviour accurately since the classical isotropic continuum mechanics do not account for crystallographic rotations, and hence, orientation effects, as there is no anti-symmetric term in the constitutive equations associated with the dyadic nature of crystallographic dislocation slip (Raabe *et al*., 2007).

A schematic of the developed indentation model is shown in Figure 6-6. Dimensions of the workpiece sample used in FE model were 10 μm × 10 μm × 6 μm to represent the single-crystal in a polycrystalline sample with dimensions of around 2 mm × 2 mm × 1 mm; justification for this selection is given in Section 6.2.1. Eight-node linear brick elements (C3D8) were used to discretise the workpiece sample. As the gradients of stress and strain fields reaches their highest value underneath the indenter, a finer mesh was used near the indenter's tip and a coarser one for the remaining regions (Figure 6-6). As mentioned earlier, to avoid asymmetries other than those of the crystal structure, a conical indenter with $\theta = 90°$

and a tip radius of 1.0 μm was used in the experiment. This was modelled exactly in the simulations (Figure 6-6). On the other hand, as the diamond indenter used in the experiments has a one-order-of-magnitude higher modulus compared to that of the Ti-alloy single-crystal workpiece, the indenter was modelled as a rigid body.

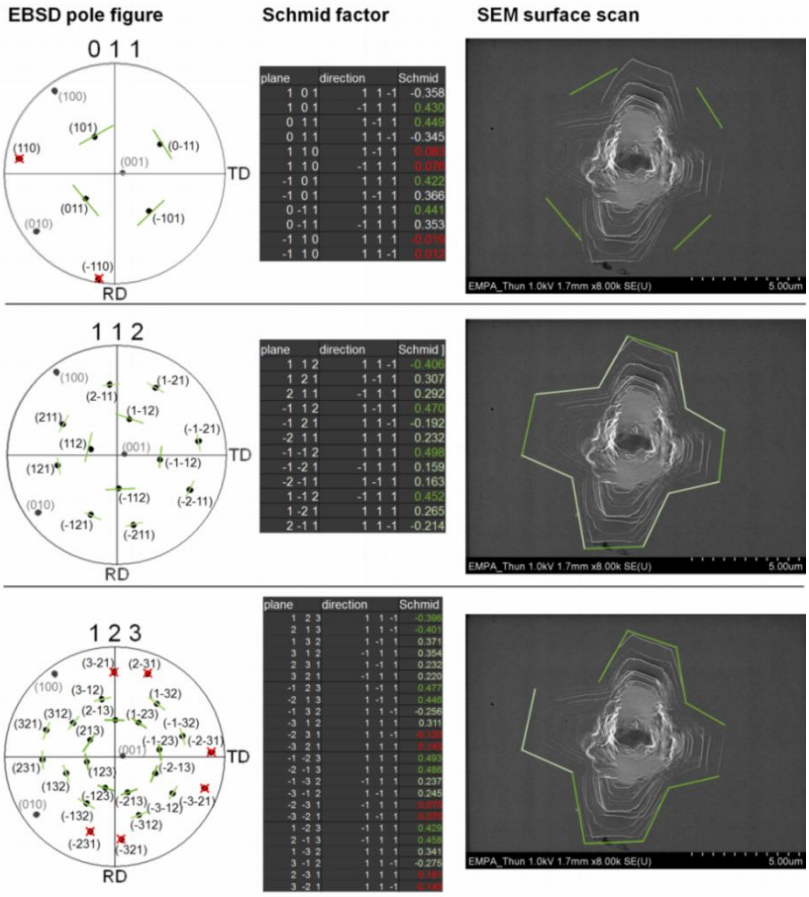

Figure 6-4: Comparison of theoretically expected positions of slip-lines determined by EBSD (left) and experimentally observed positions of slip-lines (right), with respect to Schmid factors of all systems (middle column) of (011) [111] (top), (112) [111] (middle row) and (123) [111] (bottom). Reprinted with permission from (Nowag *et al.*, 2012)

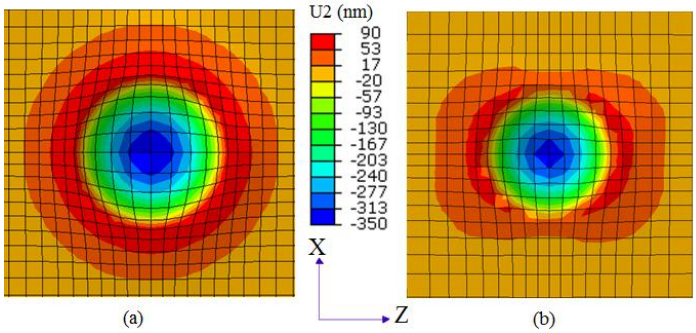

Figure 6-5: Distribution of displacement in y-direction on indent obtained in two different types of FE simulations: (a) FE simulation with isotropic plastic constitutive J2 model (no preferred direction, J2 is second invariant of stress deviator used as isotropic yield criterion); (b) FE simulation with anisotropic SGCP constitutive model

The relative movement of the workpiece and indenter was monitored by the translation of the latter in the negative y-direction (Figure 6-6). Kinematic boundary conditions were imposed on the bottom face of the workpiece by constraining displacements in all directions, whereas the faces of the workpiece perpendicular to x- and z-directions were constrained in x- and z-direction, respectively. On the other hand, the top face was free to deform. Such boundary conditions were imposed to represent the indentation of a single-crystal in a polycrystalline sample. The Coulomb's friction law was used to model the frictional interaction between the indenter and the surface of the workpiece material.

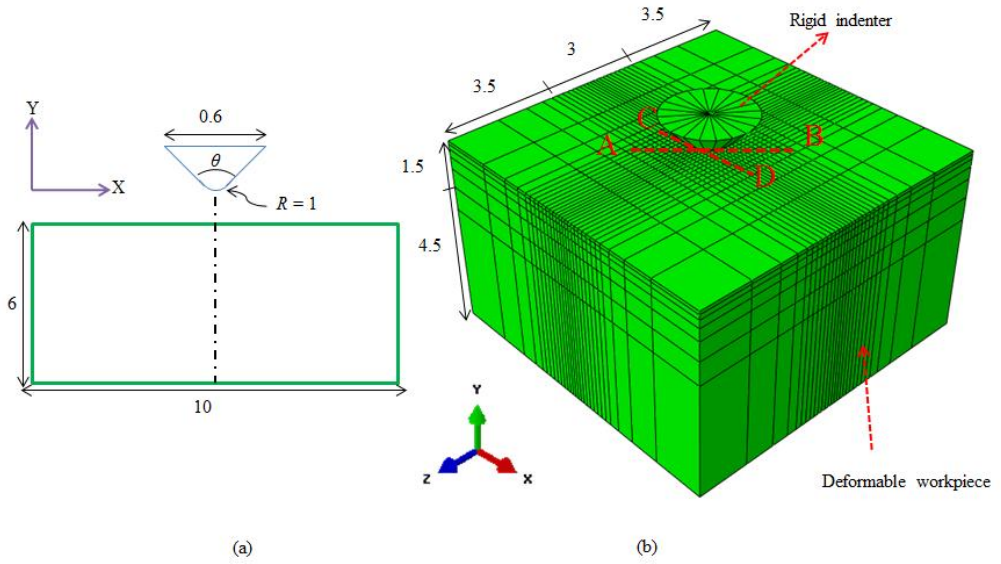

Figure 6-6: Dimensions of indenter and workpiece (in µm) (a); 3D finite-element model of nanoindentation using Mesh 3 (b) (see Section 6.2.2)

As optimization of material parameters will be performed by calibrating the numerical model with the experiments in Section 6.5, the first estimate for them presented in Table 6-1 is used in the following sections. Indentation simulations were carried out on a single-crystal of the studied Ti alloy in (001) orientation, where frictionless contact pair was defined between the indenter and the workpiece material.

Table 6-1: Crystal-plasticity parameters used in mesh-convergency study

Elastic constants	$C_{11} = 127740$ MPa
	$C_{12} = 118850$ MPa
	$C_{44} = 43997$ MPa
Hardening parameters (PAN model)	$\dot{\gamma_o}^{\alpha} = 0.0001$
	$n = 15$
	$q = 1$
	$h_0 = 4000$ MPa
	$g_T^{\alpha}\|_{t=0} = \tau_0 = 250$ MPa ($K = 0.0392$ MPa.mm)

	$g_T^{\alpha}\,\vert_{\mathrm{sat}} = \tau_{\mathrm{s}} = 300$ MPa
Strain gradient parameters	$\alpha_{\mathrm{T}} = 0.8$
	$\mu_{\mathrm{s}} = 13980$ MPa
	$b = 2.802 \times 10^{-7}$ mm

6.2.1 Dimensions of workpiece

In this section the following steps are performed to find the suitable dimensions for the modelled workpiece to represent the experiments accurately. These dimensions should be selected in such a way that they are large enough to circumvent the influence of traction free surfaces. At the same time, they should be small enough to have a computationally less expensive model. Under these circumstances, three different sets of dimensions for the workpiece material were considered: 5 µm × 5 µm × 3 µm (first set); 10 µm × 10 µm × 6 µm (second set) and 15 µm × 15 µm × 9 µm (third set). It is worth mentioning that the form factor of the workpiece was kept the same for all the sets. In this part of the study, the indenter penetrates to the workpiece with a maximum indentation depth of 570 nm and later retracts back. This value was selected deliberately to make the model more flexible for future studies as the maximum indentation depth in the experiments was smaller - 370 nm. Identical finite-element sizes with a minimum of 200 nm directly underneath the indenter were used to discretize the workpiece for all the three sets of their dimensions. This element size was selected, on the one hand, as large as possible to avoid very long computational times, on the other hand, as small as possible to have a promising accuracy in the solutions. The appropriateness of this mesh size was proven in the mesh-sensitivity analysis presented in the following section. Figure 6-7 (a) demonstrates the obtained nano-indentation load–displacement curves for different workpiece dimensions. This plot shows that all the models predict identical reaction to indentation. The first set was therefore considered to be optimal as it is computationally less expensive.

In the developed FE model, all the surfaces except for the workpiece's top face were constrained to represent nano-indentation of a single-crystal embedded in a polycrystalline aggregate. The aim here was to extend the model to account for

nano-indentation of a single-crystal, which can be possibly cut from the whole sample of a polycrystalline material or fabricated as a single-crystal. This adjustment was allowed in the model by relieving the constraints on the side surfaces. Figure 6-7 (b) presents the obtained load-displacement curve for the modified model. This figure clearly indicates that workpiece dimensions of 10 μm × 10 μm × 6 μm are ideal for our modelling efforts as the maximum error for the curve was only 5.2% compared to results obtained for larger dimensions. This study also revealed that a smaller workpiece (dimensions, 5 μm × 5 μm × 3 μm) was not sufficient to model the nano-indentation of a single-crystal due to a large deviation in the maximum load, - 17.1%, compared to that for the assumed benchmark workpiece dimensions (15 μm × 15 μm × 9 μm). The reason for this discrepancy is as follows: as dimensions of the workpiece become smaller, the influence of traction-free surfaces becomes significant, i.e. the indenter can penetrate into the workpiece material with a lower force as the constraints imposed by the bulk volume of the single-crystal to the indented surface are lessened. Based on the above analysis, it was decided to use dimensions of 10 μm × 10 μm × 6 μm for the workpiece in the nano-indentation model.

Guo (2010) studied the influence of workpiece dimensions on the indentation load-displacement curve. In a 2D axisymmetric FE model, a spherical indenter with a radius of 2.5 mm was penetrating the workpiece material, whose bottom surface is fixed in all directions, at a maximum distance of 0.3 mm. This numerical study revealed that when the ratio of workpiece height to indentation depth was 7 or less, the applied load decreased by approx. 16% compared to that in the model with extremely high workpiece height to indentation depth ratio. This study suggested that the height of the indented workpiece should be at least 10 times larger than the maximum indentation depth to eliminate the effects of imposed boundary conditions at the bottom surface. This ratio is 15.78 in this study, with the workpiece height being 6000 nm and maximum indentation depth 380 nm; hence, the requirement of the mentioned study was met (Guo, 2010). It is also worth mentioning that the dimensions of the workpiece used in our model comply with the nano-indentation models developed by different research groups to study the

deformation behaviour of different material crystals (Liu *et al*., 2005; Liu *et al*., 2008; Gerday *et al*., 2009).

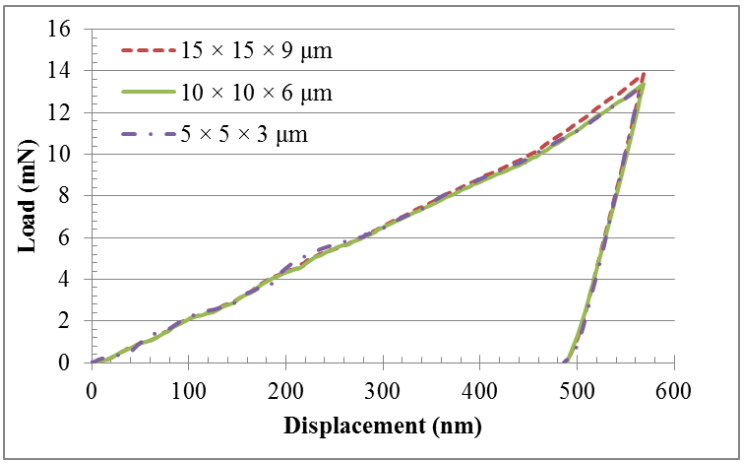

(a)

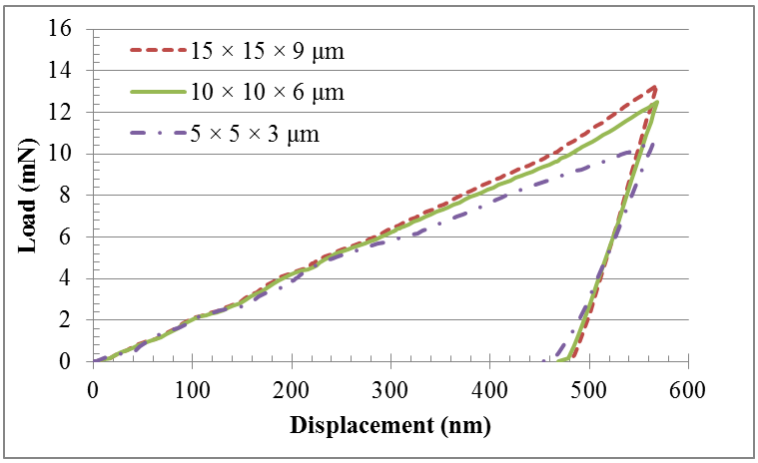

(b)

Figure 6-7: Load-displacement curves obtained from nanoindentation simulations for different workpiece dimensions, for the workpiece constrained at side surfaces (a) and without such constraints (b)

6.2.2 Mesh-sensitivity analysis

After defining the dimensions of the workpiece in the previous section, a mesh-sensitivity analysis of the model is performed here to find a compromise between the conflicting requirements of accuracy and computational cost before performing the planned program of simulations.

As stresses and strain gradients reach their highest value underneath the indenter region, this area was meshed with a finer mesh and other parts were meshed with a coarser one (Figure 6-6). To find the appropriate mesh, numerical simulations with different mesh sizes of the workpiece with dimensions of 10 × 10 × 6 μm were performed. To achieve this, the edges of this volume were discretized with a bias of 1.7, viz. double bias towards to center at the width and length edges and single bias upwards the height. The total number of elements in the first mesh is 2400 and the corresponding dimensions of the smallest element being 200 nm × 200 nm × 200 nm. The respective parameters for the second and third mesh are 3456 elements and 5488 elements and 150 nm × 150 nm × 150 nm and 100 nm × 100 nm × 100 nm, respectively. Table 6-2 shows the details of the meshes used in the mesh-sensitivity analysis. A maximum indentation depth of 300 nm was considered in this part to reduce the overall computational time. The load-depth relations obtained for different meshes are presented in Figure 6-8. Apparently, the features of curves are very similar to each other. It is therefore concluded that the coarsest mesh was the optimum choice for the study as it was computationally less expensive.

Table 6-2: Details of meshes used in mesh-sensitivity analysis: numbers of elements for respective dimensions

element dimension	Mesh1 (2400 elements)	Mesh 2 (3456 elements)	Mesh 3 (5488 elements)
width and length	20	24	28
Height	6	6	7

Of special interest in Figure 6-8 could be oscillations observed in the load-displacement curves. These are more pronounced in the coarsest mesh, especially at certain indentation depths, such as 110 nm or 170 nm. In fact, the solution obtained using the coarsest mesh owing to its inherent oscillatory trend deviates from and approaches to the results of the finest mesh sequentially, but the deviations are within an acceptable range. Many authors reported such non-smooth loading curves in nano-indentation simulations. Gerday *et al*. (2009) ascribed this

problem to the new material points entering into contact with penetration. Smith *et al*. (2001) and Kalidindi *et al*. (1992) attributed this problem to the finite size of the elements and proposed that the jagged load-displacement curve can be circumvented by using a finer mesh of the workpiece. On the other hand, Bocciarelli (2005) linked this with possible model errors associated with moving contact conditions between the indenter and the workpiece material. Our observation - the finer the mesh, the smaller oscillations - complies with conclusions by Kalidindi *et al*. (1992).

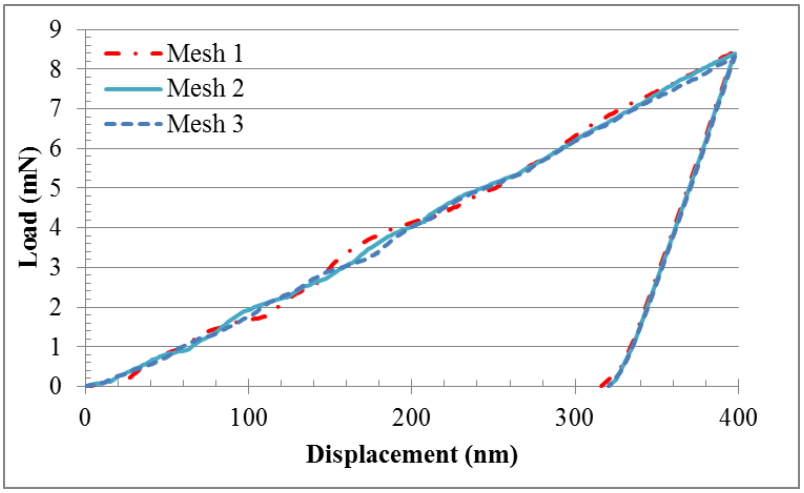

Figure 6-8: Load-displacement curves obtained from nanoindentation simulations with different FE meshes

An important aspect of indentation is the obtained surface profile of the indented surface, e.g. pile-up or sink-in. Such profiles affect the results of contact area calculations as its true value increases when the piling-up predominates and decreases when the sinking-in occurs. Neglecting these surface-deformation modes can result in significant errors for properties extracted from the experimental data (Wang *et al*., 2004). It is, therefore, investigated how the surface profile varies with different meshes. Figure 6-9 demonstrates surface profiles of the indented workpiece material along path A-B (Figure 6-6) for different element sizes. Here, all the models predict a pile-up surface profile and they also agree qualitatively. However, the maximum pile-up height was predicted as 54 nm for the coarsest mesh, whereas for the medium and the finest mesh, it was 64 nm and 68 nm,

respectively. Another important point here is that the indent's surface profile at zero surface height obtained using Mesh 1 deviates from other profiles (Figure 6-9). To characterize the differences in the surface profile using different meshes, the contact area was measured. This analysis revealed that the contact area is underestimated by 7% and 2% when the coarsest and medium meshes were used, respectively, assuming that the contact area of the finest mesh is the benchmark solution.

Based on the above analyses it was concluded that Mesh 2 with a minimum element size of 150 nm at the indentation region was sufficient to characterize the experimental workpiece accurately.

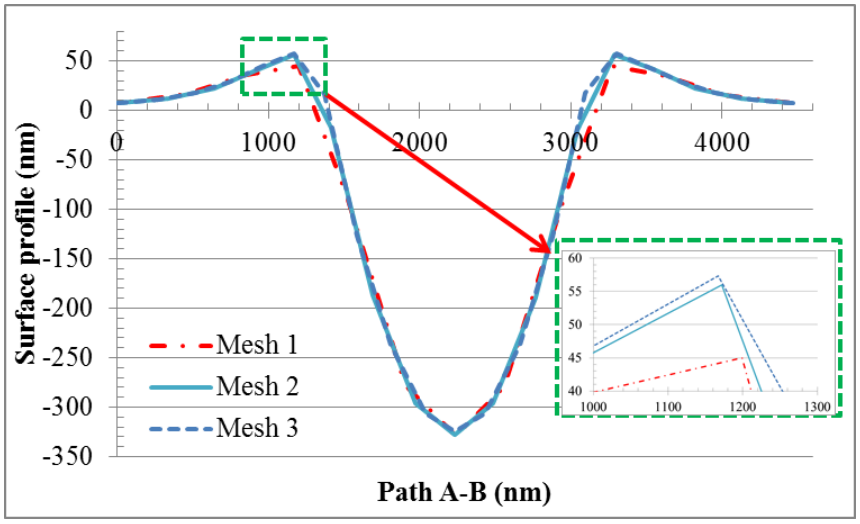

Figure 6-9: Pile-up profiles of indents along path A-B (Figure 6-6) for different FE meshes

Of another special interest here is the computational time of discussed simulations. All the simulations in this section were accomplished with 3 computational nodes, each having two six-core Intel Westmere Xeon X5650 CPUs (2.66 GHz) and 24 GB of memory. Table 6-3 shows the computational time for simulations with different element sizes. It is evident that the computational time increased more than two-fold when Mesh 3 was used rather than Mesh 2, though both meshes gave almost similar results. A mesh with a minimum element size of 150 nm, therefore,

enables us to reduce the overall computational time for dozens of simulations needed to be performed in the next sections.

Table 6-3: Comparison of computational time of simulations with different FE meshes

	Mesh 1	Mesh 2	Mesh 3
CPU time (s)	9631	22713	47064

6.3 Effect of friction

In this section, the effect of a friction at the indenter-workpiece interface is studied. Three different idealised friction conditions are considered. First, the effect of a well-lubricated indenter-workpiece interface, i.e. $\mu = 0$, is analyzed, followed by a two dry non-lubricated interface conditions: $\mu = 0.05$ and $\mu = 0.3$.

Figure 6-10 demonstrates the obtained load-displacement curves from the nanoindentation simulations for (0.641 0.078 0.764) orientation. This plot indicates that the introduction of friction does not influence significantly the load-displacement behaviour of indentation process at the first 250 nm of the indentation depth (Figure 6-10). Similar observations were also reported by Gerday *et al*. (2009), Wang *et al*. (2004), Liu *et al*. (2005) and Zahedi *et al*. (2012). However, with an increase in the indenter penetration, the indented surface starts to form a pile up profile, which, in turn, leads to a relative motion between the indenter's surface and the workpiece material. It is, therefore, observed an increase in the obtained force value after 250 nm indentation depth with an increase in μ. It must be emphasized that the influence of friction on the deformation behaviour of a material is less pronounced in crystal-plasticity constitutive approaches compared to that in the J2-based isotropic continuum scheme (Wang *et al*., 2004). Dève *et al*. (1988) and Harren and Asaro (1989) ascribed this by the characteristics of the crystal-plasticity theory itself, where the material is restricted to flow on discrete planes and directions leading to a reduction in the material's degree of freedom. In other words, the characteristic symptoms of the influence of friction, such as non-

uniform deformation and strain localization, are accounted for naturally in the crystal-plasticity theory.

The effect of friction on the shape of obtained surface profile was also studied. Since the pronounced effect was found to be different for different orientations, two crystallographic orientations were considered, namely (0.641 0.078 0.764) and (100). With an increase in the friction coefficient, it is to be expected that the relative motion (displacement) between the indenter's surface and the workpiece material will be increasingly hindered during the process. It is, therefore, observed a decrease in the pile-up height with a growing coefficient of friction at the workpiece-indenter interface (Figure 6-11). These results suggest that the pile-up height is larger for (100) orientation compared to that for (0.641 0.078 0.764) due to the fact that the former is the plane with higher resistance to slip compared to the latter plane. Detailed information regarding the influence of orientation on pile-up height is given in Section 6.6.

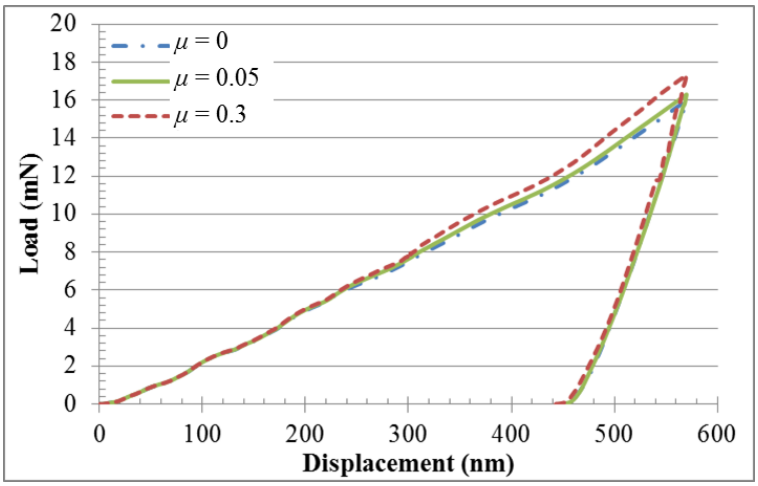

Figure 6-10: Load-displacement curves obtained from nanoindentation simulations for different friction conditions

The change in the spatial position of the pile-up tip for different contact conditions is investigated for (0.641 0.078 0.764) orientation. A quantitative measure of the spatial location for the pile-up tip was the horizontal coordinate of the tip location (x in Figure 6-6). This peak point lies symmetrically on the right- and left-hand

sides of the indenter tip with a distance of 1978.06 nm when $\mu = 0$, whereas it is 1989.33 nm, when $\mu = 0.3$. This result shows that increased friction at the workpiece-indenter interface moves the pile-up tip downwards but at larger distance from the indentation axis (Demiral *et al*., 2010).

The diamond indenter and workpiece material in the experiments are identical to contacting bodies used in the micro-pillar-compression experiment, where the analysis demonstrated that $\mu = 0.05$ characterized the friction characteristics at the indenter-pillar interface. The same contact condition was therefore used in the nano-indentation model.

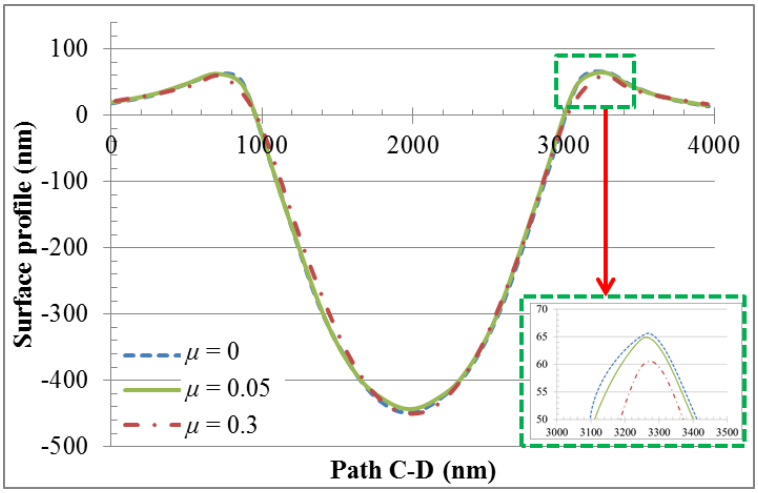

(a)

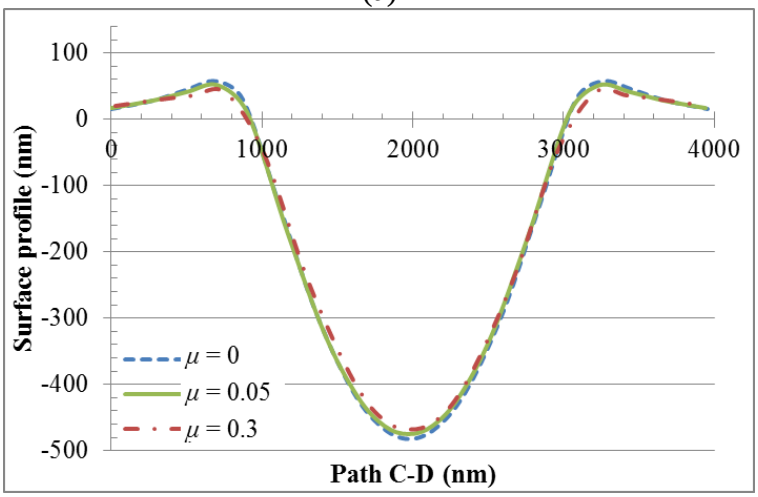

(b)

Figure 6-11: Pile-up profiles of indented surfaces with different orientations - (0.641 0.078 0.764) (a) and (100) (b) - along path C-D (Figure 6-6) for different contact conditions

6.4 Sensitivity study of material parameters in nano-indentation model

In the previous chapter the material parameters of the b.c.c. single-crystal Ti alloy were identified using micro-pillar-compression experiment. As explained at the beginning of this chapter, the pre-existing strain gradients in the pillar body are believed to be absent in the indented workpiece due to two reasons: on the one hand, the free surfaces in the indented workpiece are far from the workpiece center leading to negligibly small strain gradients; on the other hand, as specimens for indentation are not produced in the same way as pillars (e.g. with FIB), it is unlikely that GNDs may be introduced in the body during manufacturing. In this chapter, material parameters of the Ti alloy are characterized from nano-indentation experiment, where incipient strain gradients do not exist. The determination of parameters such as strain-rate sensitivity of material n and Taylor coefficient α_T is left in this chapter as the influence of those parameters is more profound in a nano-indentation model compared to the micro-pillar-compression model.

In this section, the sensitivity analysis of material parameters such as n, α_{T}, τ_0, τ_{s} and h_0 is first performed to get an insight about their influence on the material's behaviour of the single-crystal Ti alloy. It is well known that good knowledge of the deformation zone around an indent is of great importance in nano-indentation experiments as the shape of the surface profile determines the actual contact area and gives hints about the local fields. Here, the surface profile of the workpiece material is therefore mainly focused on. The load-displacement behaviour is not demonstrated here unless it is required as their general behaviour is similar to the character of stress-strain curves in pillar-compression experiments for different material parameters presented in the previous chapter. The results presented in this

section are obtained for indentation of a single-crystal of the Ti alloy in the (0.641 0.078 0.764) orientation, with a zero frictional coefficient being assumed. The parameters presented in Table 6-1 are used in the simulations except $g_T^\alpha\,|_{t=0} = \tau_0 = 300$ MPa and $g_T^\alpha\,|_{\text{sat}} = \tau_s = 400$ MPa.

6.4.1 Effect of strain-rate sensitivity of the material

As explained in Section 5.4.2, n is the strain-rate-sensitivity parameter. In fact, n is a numerical parameter used to satisfy the Schmid`s law in the MBSGCP theory (equation 3-63). When n is equal to infinity, the Schmidt law is satisfied accurately. By contrast, n =1 implies that shear stress (τ^α) is proportional to the shear-strain-rate ($\dot{\gamma}^\alpha$) corresponding to a case of a Newtonian fluid, which is unrealistic for crystal-plasticity. Serious convergence issues arise if infinite n is implemented in numerical computations. This is due to the fact that when the value of τ^α becomes slightly larger than the strength of the slip system g_T^α as a result of a finite strain increment in FE calculations, $\dot{\gamma}^\alpha$ becomes almost infinite causing termination of the analysis. To avoid this, finer strain increments, and, hence, ultra-fine time increments, should be used, leading to dramatically long computational times. On the other hand, according to equation 3-63 the ratio of $|\tau^\alpha / g_T^\alpha|$ is either less than, or equal to, 1 as the stress state of a deformed elastic-plastic material cannot exceed the yield, i.e. the stress-state point can be either inside the yield surface or on it. For instance, when n is big enough (≥ 10), inside the yield surface, the plastic strain-rate becomes infinitesimal, so that almost no shearing occurs, whereas on the yield surface, the plastic shear-strain-rate becomes constant ($\dot{\gamma}^\alpha = \dot{\gamma_o}^\alpha$, see equation 3-63). This is particularly useful to specify a constant slip-rate in the simulations to represent the experiment, where the loading rate is kept constant. In other words, in strain-rate-insensitive materials the shear on the slip system occurs only when τ^α equals to g_T^α, whereas in strain-rate sensitive materials the slip occurs not only on the yield surface but also inside the yield surface.

The surface profile of indented workpiece material was studied for different n values such as $n = 5, 15, 25$. Figure 6-12 (a) and (b) demonstrates the

displacement distribution in y-direction along path C-D (Figure 6-6) at full loading and complete unloading, respectively. The maximum indentation depth was 570 nm at full loading and reduces to less than 500 nm at complete unloading. The amount of spring-back was observed to increases with a decrease in the value of n. Especially noteworthy here is that although the piling-up is a common surface profile at the complete unloading for different n values, at full loading the pile-up behaviour was observed only when $n = 10$ and $n = 15$ and sink-in occured when $n = 5$. So, it was concluded that $n = 5$ indeed represented the well-annealed single-crystal Ti alloy, whereas other cases represented the strain-hardened behaviour.

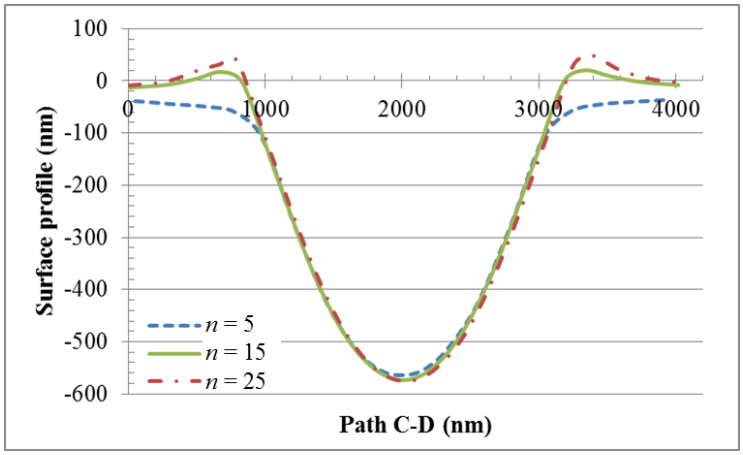

(a)

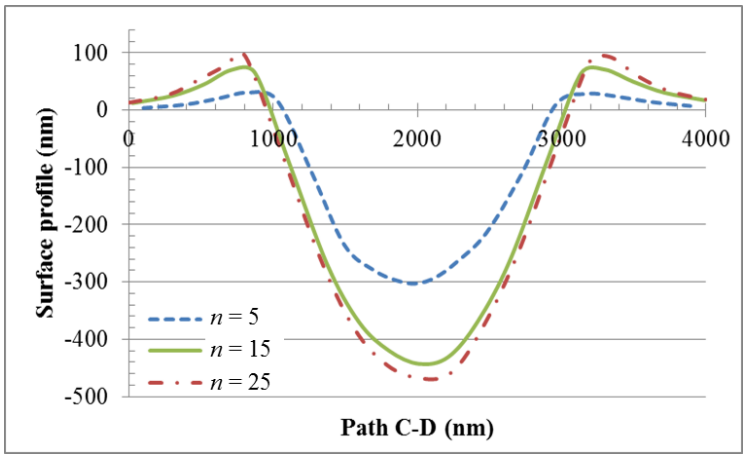

(b)

Figure 6-12: Pile-up profile of indent along path C-D (Figure 6-6) at full loading (a) and complete unloading (b) at different n values

These different types of material behaviour can be summarized briefly as follows. For strain-hardened materials, the volume of material displaced by the indenter is pushed out to its sides and forms a pile-up profile. On the other hand, for well annealed soft metal possessing a high strain-hardening reserve, the displaced volume is accommodated mainly by far-field elastic displacements leading to sink-in behaviour. The reader is referred to Section 2.3.1 for extended information.

As explained at the beginning of this section, a larger value of n leads to higher computational times. This is also confirmed in our simulations. Table 6-4 demonstrates the total computational time accomplished with 12 processors for different n values. It is obvious that the calculation cost increases with an increase in the value of n.

Based on the above analysis, it was decided to use $n = 15$ as the material's plastic parameter for the studied single-crystal Ti alloy since this value, on the one hand, represents the stain-rate-insensitive material behaviour and, on the other hand, it is computationally less expensive.

Table 6-4: Comparison of computational time of simulations with different material strain-rate-sensitivity parameter

	n = 5	n = 15	n = 25
CPU time (s)	6536	8476	15436

6.4.2 Effect of Taylor coefficient

The influence of α_T value on a surface profile of the indented single-crystal Ti alloy is studied in this section. Extended information about α_T can be found in section 5.4.3. Three different values of α_T are considered, viz. 0.0, 0.8 and 1.6. Here, α_T = 0.0 represents the solution obtained using the CP theory and others represents the EMSGCP theory. Figure 6-13 demonstrates that with an increase in α_T value, the pile-up height decreases. The reason for this observation is that as the shear-strain values are averaged in the EMSGCP theory, the gradients in the local

fields, e.g. strain fields, are lessened, which, in turn, leads to a smoother strain distribution. Therefore, the surface profile becomes more flat in simulations employing the EMSGCP theory compared to that for the CP theory. Another observation in Figure 6-13 is the increase in the amount of spring-back for larger values of α_{T}. As demonstrated in Figure 5-18, with an increase in α_{T} value the hardening reserves of the material increases, hence resulting in the well-annealed soft material's behaviour. It is therefore observed that the amount of spring back increases when the strain gradients are more pronounced in the model, i.e. when α_{T} is larger.

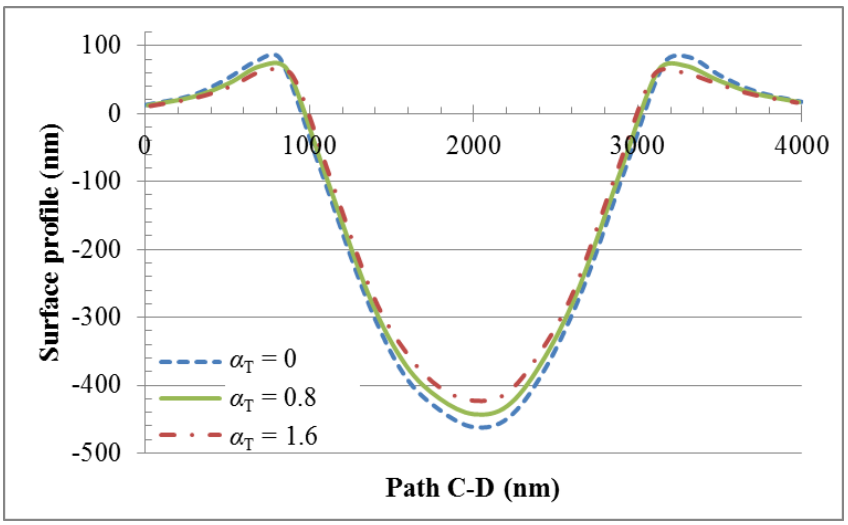

Figure 6-13: Pile-up profiles of indents along path C-D (Figure 6-6) for different α_T values

6.4.3 Effect of different plastic parameters

Selection of τ_0 value affects the surface profile of indented material considerably. Depending on relative amounts of elastic and plastic components in the deformation process, characterized by the ratio of elastic modulus to yield stress, E/σ_Y, the surface either piles-up or sinks-in. Johnson (1974) characterized this ratio as the reciprocal of the level of elastic strain at the yield point representing the amount of deformation accommodated elastically during indentation. In the limit of $E/\sigma_Y = 0$, the deformation is purely elastic leading to a sink-in surface profile,

whereas in the limits of $E/\sigma_Y = \infty$, deformation is rigid-plastic, with an extensive piling-up of material around the indent.

In this section three different values of τ_0, viz. 150 MPa, 250 MPa and 350 MPa are considered in order to examine its role on the deformation behaviour of the single-crystal Ti alloy. Figure 6-14 demonstrates that all the considered values of τ_0 lead to a pile-up surface profile and the height of pile-up increases with an increase in the value of τ_0. The latter observation here indeed seems to contradict with the study of Johnson (1974). According to it, the pile-up height should decrease with an increase in the value of τ_0 as the ratio of E/σ_Y approaches zero as opposed to the behaviour shown in Figure 6-14. The magnitude of pile-up height for different τ_0 values, however, here is determined by the respective values of τ_0 and τ_s, where $\tau_s = 400$ MPa. When τ_0 and τ_s values are close to each other, the extent of strain-hardening is less compared to the case when τ_0 and τ_s values differs significantly (Figure 5-19). As explained in the previous section, when the strain-hardening reserves are smaller, a pile-up surface profile occurs. It is, therefore, observed that the pile-up height is the highest when τ_0=350 MPa, i.e. the difference with τ_s is only 50 MPa, corresponding to a smaller hardening reserves, followed by the pile-up height when τ_0 =300 MPa and τ_0 =250 MPa. This observation is consistent with the study of Taljat and Pharr (2004), where the effects of different material behaviours on the surface profile in indentation were studied. In this study different elastic-plastic materials were investigated, e.g. an ideal elastic material with a strain-hardening exponent n=1 corresponding to a larger strain-hardening reserves, and a rigid-plastic material with n =0 corresponding to zero strain-hardening reserves as well as strain-hardening materials, where n ranges between 0 and 1 (Figure 6-15). It should be emphasized that n value there represented the strain-hardening exponent in the power law and was different from that in the EMSGCP theory. This study demonstrates that the material with a smaller strain-hardening reserves piles-up more compared to that with a larger strain-hardening reserves.

The effect of τ_s value on the surface profile of the indented material was also studied. For fixed $\tau_0 = 300$ MPa, an increase in τ_s shifted the response to that of a material with a higher hardening exponent (Figure 5-20(a)). The pile-up height, therefore, becomes smaller for such material behaviours as seen in Figure 6-16 (a). As demonstrated in Section 6.4.1, smaller values of n represent the material with a larger hardening reserves such as in case of a well-annealed Ti alloy, and for such materials a significant elastic spring back or recovery of the indented material occurs (Figure 6-12). Similar results were also observed here. For fixed τ_0 an increase in τ_s leads to increasing recovery at full unloading of the indenter (Figure 6-16).

The influence of initial hardening moduli h_0 on the surface profile of the indented material is similar to that of τ_s. For constant values of τ_0 and τ_s, a higher value of h_0 represents the soft-metal behaviour with a larger strain-hardening reserves (Figure 5-20(b)); hence, a lower pile-up deformation pattern and increasing recovery at full unloading of the indenter are expected to occur with an increase in h_0 value. Figure 6-16 (b) demonstrates that such an increase causes a growth of the amount of elastic recovery as expected; however, the change in h_0 does not change the pile-up height significantly.

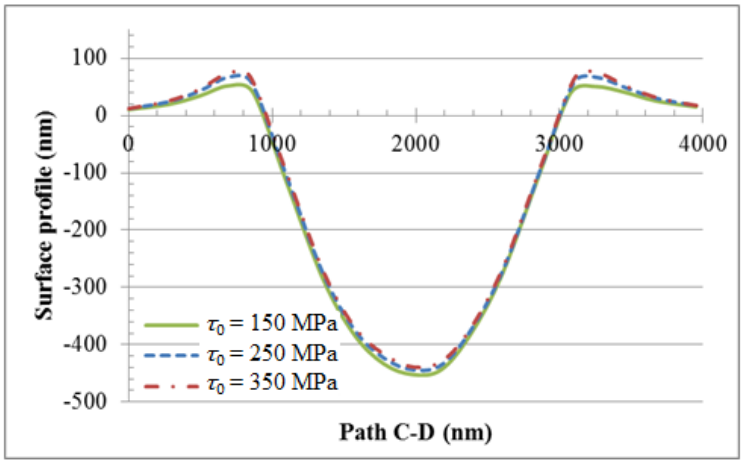

Figure 6-14: Pile-up profiles of indents along path C-D (Figure 6-6) for different τ_0 values

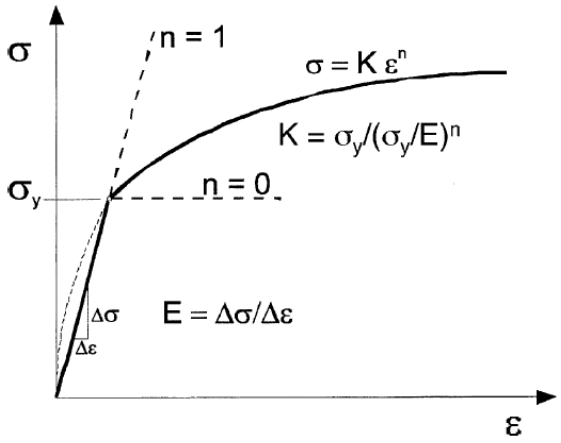

Figure 6-15: Elastic-plastic constitutive law used in finite-element simulations. *n* = 0 represents elastic-perfectly-plastic materials, *n* = 1 represents purely elastic material and 0 < *n* < 1 elastic-plastic material. Reprinted with permission from (Taljat and Pharr, 2004)

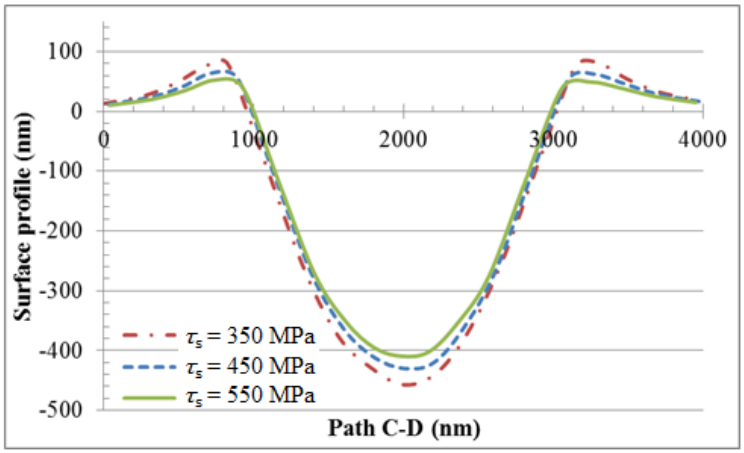

(a)

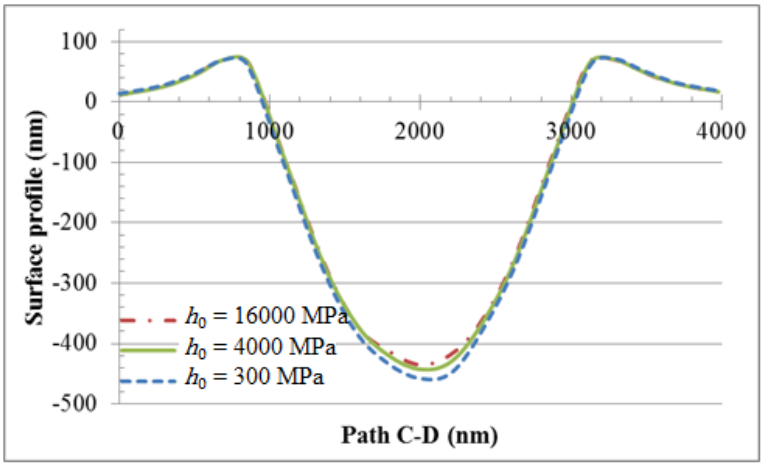

(b)

Figure 6-16: Pile-up profiles of indents along path C-D (Figure 6-6) for different values of τ_s (a) and h_0 (b)

6.5 Determination of material's plastic parameters

In this section the material parameters of the studied single-crystal Ti alloy are determined through multiple trial runs by calibrating the obtained load-displacement curves and the surface profile of the single-crystal Ti alloy indented in (0.641 0.078 0.764) orientation in numerical simulations with the experiments. The sensitivity analysis of material parameters performed in the previous section provides us hints while identifying the material parameters of the single crystal Ti alloy. Using the parameters given in Table 6-5, a reasonably good agreement between experiments and simulations was obtained (Figure 6-17 and Figure 6-18). It should be emphasized that as the indent profiles were imaged with the blunt indenter tip in the experiments, the pit apex appears point-like as seen in Figure 6-18. This fact indeed explained the difference between the experiments and the simulations in the obtained surface profile. Using a sharp indenter, this profile can be scanned more accurately (Altebaeumer *et al.*, 2008).

Additional nano-indentation tests were also conducted in different orientations such as (0.114 0.107 0.988) and (0.579 0.417 0.702) to check the validity of the developed FE model. Using the same material parameters, the experimental load-displacement curves for those orientations were predicted accurately (Figure 6-19 and Figure 6-21). The corresponding surface profiles also demonstrate a reasonable match with the experiments (Figure 6-20 and Figure 6-22). These results at this scale lending further confirmation on the appropriateness of the selected material's parameters. The obtained results were also compared to those in the literature.

Different authors studied nanoindentation of single-crystals for different materials. For instance Wang *et al.* (2004) studied the influence of crystallographic orientation on pile-up patterns and micro-textures using a CP FE model for single-crystal copper. In that study, a correct numerical prediction of the surface pile-up patterns was achieved; however, deviation on the order of a magnitude in the load-

displacement curve between experiments and simulations was reported. Liu *et al*. (2008), on the other hand, did the similar study using a spherical indenter instead of a conical one, where a satisfactory agreement between the numerical and experimental load-displacement curves was demonstrated. In that study different friction coefficients were used to represent the contact condition between the indenter's tip and the workpiece material for different orientations to match the numerically obtained surface profiles with the experimental data; however, an error of up to 50% for the maximum pile-up was observed. In the present study, where the strain gradient theory was incorporated into the constitutive laws, the maximum error was 3% for the load-displacement curve and 19% for the maximum pile-up height. These results confirm the robustness of the developed FE model.

Table 6-5: Material parameters of single-crystal Ti-15-333 obtained using nano-indentation experiments

Elastic constants	$C_{11} = 127740$ MPa
	$C_{12} = 118850$ MPa
	$C_{44} = 43997$ MPa
Hardening parameters (PAN model)	$\dot{a} = 0.0001$
	$n = 15$
	$q = 1$
	$h_0 = 10000$ MPa
	$g_T^\alpha \mid_{t=0} = \tau_0 = 150$ MPa ($K = 0.0392$ MPa.mm)
	$g_T^\alpha \mid_{\text{sat}} = \tau_s = 170$ MPa
Strain gradient parameters	$\alpha_T = 0.7$
	$\mu_s = 13980$ MPa
	$b = 2.802 \times 10^{-7}$ mm

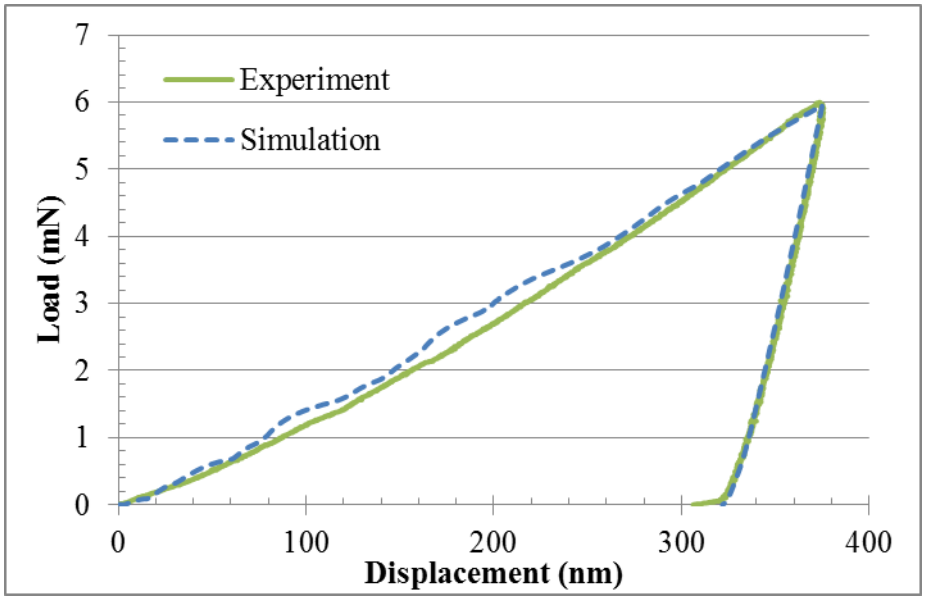

Figure 6-17: Load-displacement curves obtained for nanoindentation of (0.641 0.078 0.764) surface from experiment and simulation

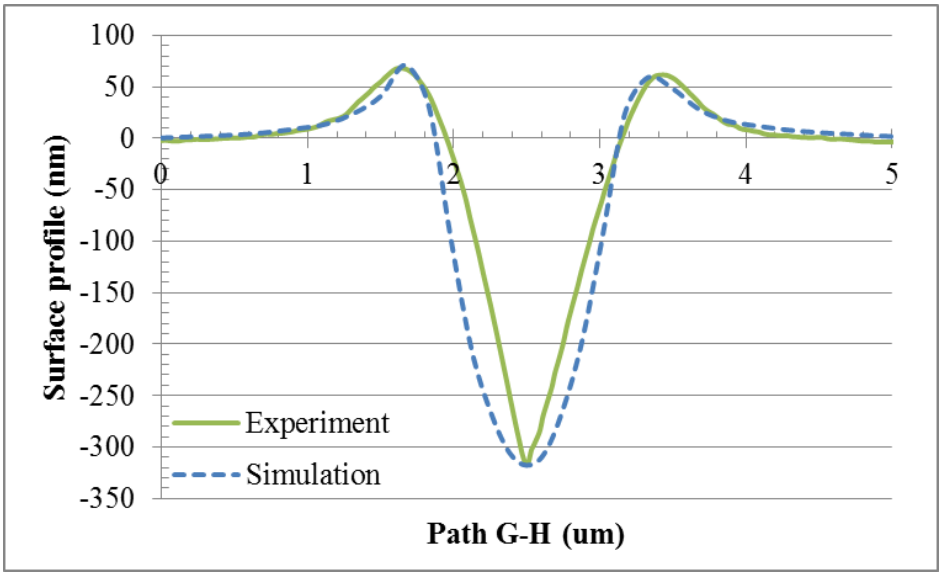

Figure 6-18: Pile-up profiles of indented (0.641 0.078 0.764) surface along path C-D (Figure 6-24) obtained from experiment and simulation

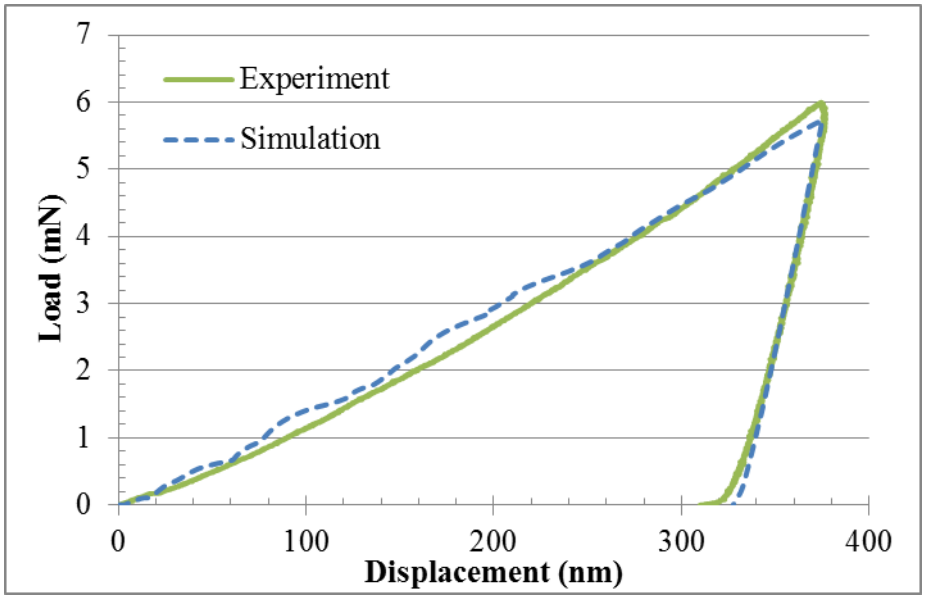

Figure 6-19: Load-displacement curves obtained for nanoindentation of (0.114 0.107 0.988) surface from experiment and simulation

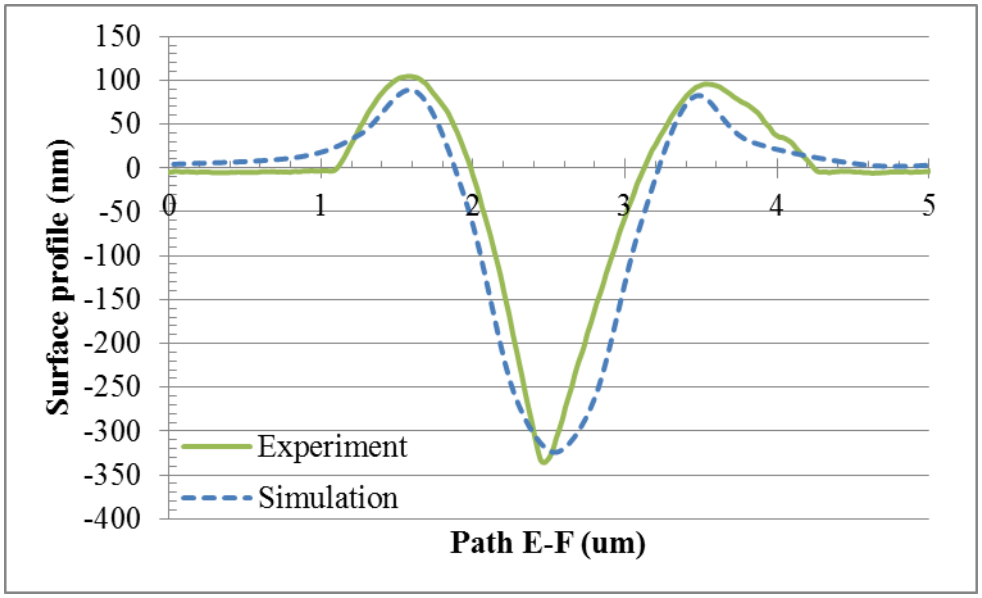

Figure 6-20: Pile-up profiles of indented (0.114 0.107 0.988) surface along path C-D (Figure 6-24) obtained from experiment and simulation

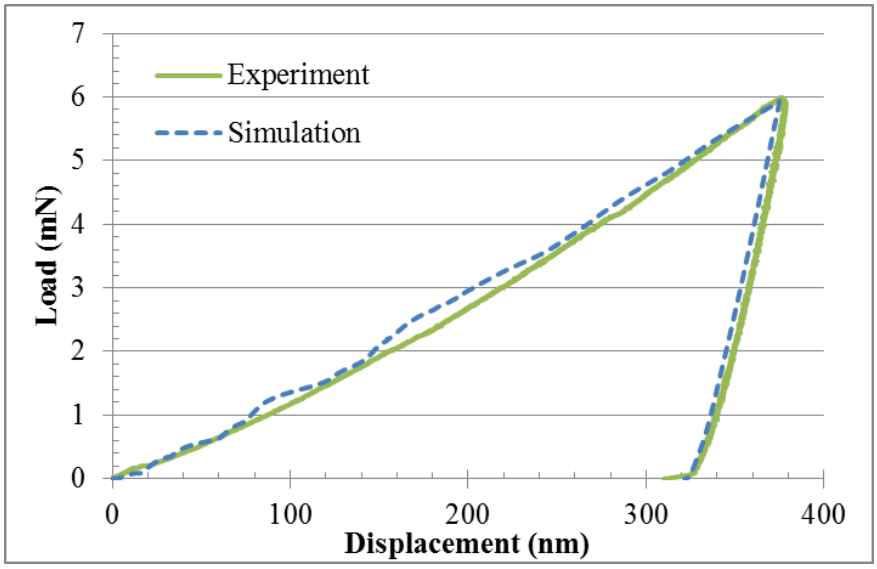

Figure 6-21: Load-displacement curves obtained for nanoindentation of (0.579 0.417 0.702) surface from experiment and simulation

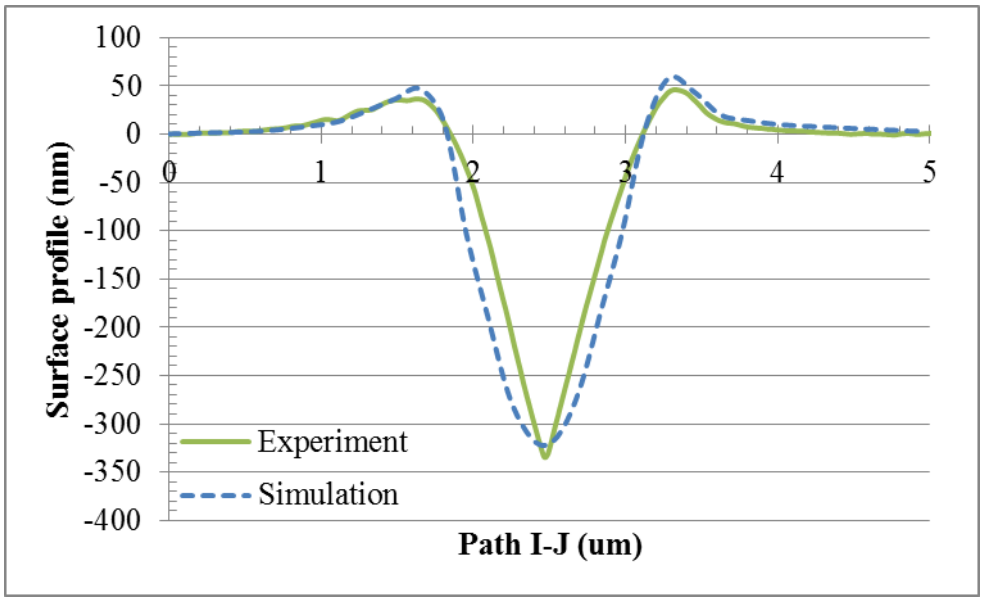

Figure 6-22: Pile-up profiles of indented (0.579 0.417 0.702) surface along path C-D (Figure 6-24) obtained from experiment and simulation

6.6 Mechanical behaviour of single-crystal Ti alloy at nano scale

The performed nanoindentation experiments revealed anisotropy of the single-crystal Ti alloy. In this section, an in-depth analysis of mechanical behaviour of

this alloy is undertaken in order to understand the underlying mechanisms in nano-indentation experiments for different crystallographic orientations. Figure 6-23 shows images obtained with an atomic force microscope (AFM) of the indents on various crystallographic surfaces after full unloading of the indenter. After the nano-indentation tests, the Ti alloy samples were imaged using a digital instrument Hitachi SEM S4800 to determine the surface topography (Figure 6-23). These different types of surface profiles were also obtained with our numerical simulations (Figure 6-24).

As the sample studied here was work-hardened, all profiles demonstrate the pile-up behaviour instead of sink-in. It should be emphasized that the studies of Pharr *et al*. (1992) and Chaudri and Winter (1988) suggested that the pile-up or sink-in behaviour around the indent was primarily affected by the strain-hardening rate of the indented material: the soft metals having sufficient hardening reserves showed a sink-in behaviour, whereas strain-hardened materials such as alloys and metallic glasses exhibiting a low strain-hardening reserve showed a pile-up behaviour. In the study of Lim and Chaudri (1999), a pile-up around an indent in work-hardened oxygen-free copper and sink-in around an indent in annealed oxygen-free copper were observed. However, the observation of Wang *et al*. (2004) is inconsistent with this classical picture, where a pile-up surface profile was reported for the indentation of a soft copper single-crystal with considerable strain-hardening reserves. That study suggested that the different patterns were strongly related to the indented crystallographic planes and all the patterns were pile-ups occurring in the well-defined areas and not sink-in patterns. In short, the interpretation of the pile-up versus sink-in behaviour for the soft material remains more speculative.

The active glide systems for a b.c.c. single-crystal Ti alloy consists of {1 1 2} glide planes and <111> slip directions as a total of 12 slip systems as explained in Section 6.1. Table 6-6 shows the Schmid factor of the slip systems for different orientations. For instance, for crystal orientation (0.641 0.078 0.764), the slip systems (1 2 1) [1 -1 1] and (1 -2 1) [1 1 1] are expected to be active as they have the highest Schmid factor. Figure 6-25 demonstrates the shear-strain distributions

on (0.641 0.078 0.764) surface after full unloading for different slip systems. It is clear that the fifth and the seventh slip systems were the most active ones, whereas the contribution of other slip systems was comparatively small. Here, the primary slip planes (1 2 1) and (1 -2 1) intersected the plane of indentation along the [-1.204 0.102 1] and [-1.180 -0.090 1] directions necessitating a two-fold in-plane symmetry. It is worth noting that the first, third, sixth, eighth and eleventh slip systems also partially contributed to the total deformation although they are considered to be inactive according to Table 6-6 as the corresponding Schmid factor is less than 0.1. Likewise, the contribution of second and forth slip systems are compatible with those of other non-primary slip systems, whereas they are supposed to have a larger contribution. The underlying reason for those discrepancies arises from the fact that the Schmid factors calculated in Table 6-6 are based on the simplifying assumption of uniaxial compression. However, the contribution of slip systems to the overall deformation in FE simulations is computed by imposing boundary conditions locally. That means that in the course of deformation the boundary conditions of the material points start to change as a result of strong strain gradients introduced by the indenter's tip; hence, the Schmid factors start to evolve with deformation and deviate from their starting values.

Table 6-6: Schmid factor of different slip systems for different crystallographic orientation

Slip system							Schmid factor		
Number	plane			direction			(0.641 0.078 0.764)	(0.114 0.107 0.988)	(0.579 0.417 0.702)
1	1	1	2	1	1	-1	-0.024	-0.397	0.166
2	-1	1	2	1	-1	1	0.302	0.462	0.252
3	1	-1	2	-1	1	1	0.099	0.458	0.199
4	1	1	-2	1	1	1	-0.283	-0.500	-0.163
5	1	2	1	1	-1	1	0.488	0.308	0.430
6	-1	2	1	1	1	-1	-0.003	-0.197	0.066
7	1	-2	1	1	1	1	0.436	0.253	0.179
8	1	2	-1	-1	1	1	0.002	-0.153	0.090
9	2	1	1	-1	1	1	0.101	0.306	0.289
10	-2	1	1	1	1	1	-0.154	0.247	-0.016
11	2	-1	1	1	1	-1	-0.021	-0.200	0.100
12	2	1	-1	1	-1	1	0.186	-0.153	0.177

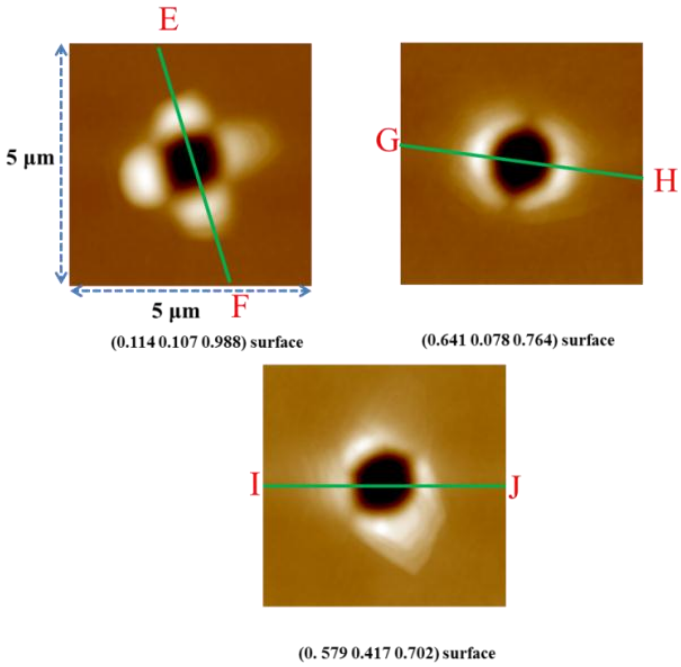

Figure 6-23: Pile-up structures of imprints taken with AFM for different crystallographic orientations (Experiments were performed at EMPA, Switzerland.)

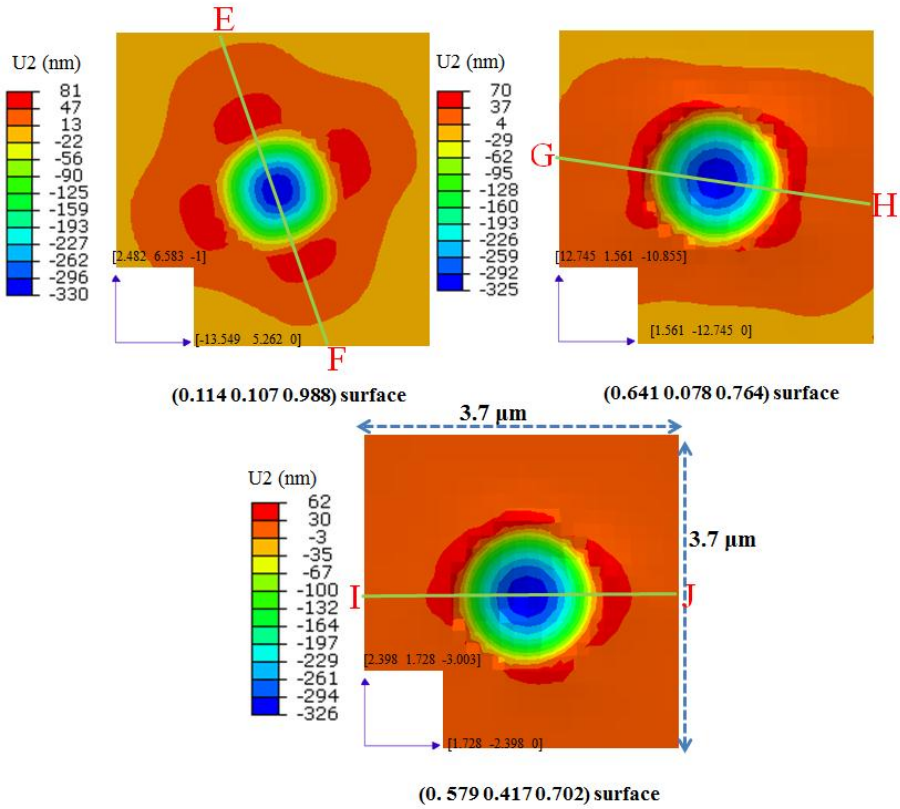

Figure 6-24: Pile-up structures of imprints obtained from FE simulations for different crystallographic orientations

Figure 6-25 also justifies the advantage of FE simulations, where the individual contributions of different slip systems to the overall deformation can be obtained that cannot be achieved in the experiments.

Similar characteristics are also observed for other orientations. For the indented (0. 114 0.107 0.988) surface, the first four slip systems are expected to be the dominant slip systems, i.e., the primary slip systems, as their Schmid factors are higher than those of other slip systems (Table 6-6). However, the FE simulations suggest that all the slip systems become active during deformation (Figure 6-26). On the other hand, the pile-up profiles presented in Figure 6-24 are more likely to be governed by these first four slip systems as the zones where those slip systems were active are identical to the zones, where the maximum pile-up heights were observed, namely on the E-F path in Figure 6-24 and on the path normal to it. This leads us to conclude that the fifth, eight, tenth and eleventh slip systems contributed partially on the pile-up profile. For the indented (0. 114 0.107 0.988) surface, the first four slip planes - (1 1 2) (-1 1 2) (1 -1 2) and (1 1 -2) - intersected the plane of indentation along [-110.57 108.57 1], [-3.502 -5.502 1], [-5.439 -3.439 1] and [-171.714 173.714 1] directions and resulted in a four-fold in-plane symmetry.

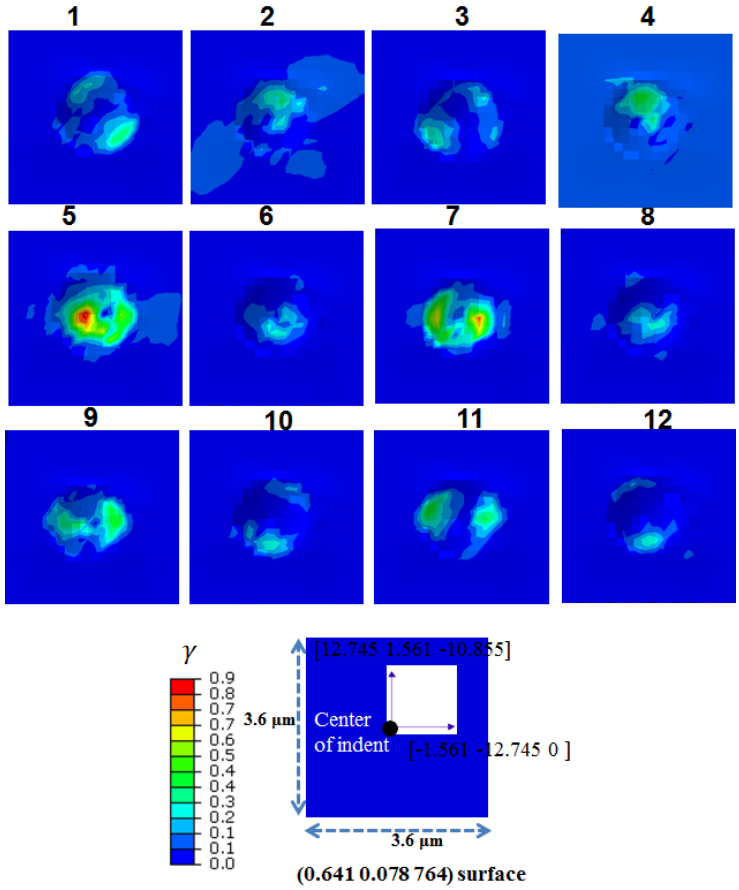

Figure 6-25: Distribution of shear strains on 12 slip systems predicted with FE simulation on indented (0.641 0.078 0.764) surface

For the indented (0.579 0.417 0.702) surface, the fifth, seventh and ninth slip systems were found to be the primary slip systems, whereas the first, forth, tenth and eleventh slip systems can be considered as the secondary active slip systems (Figure 6-27). Here, the intersection of primary slip planes (1 2 1), (1 -2 1) and (2 1 1) with the plane of indentation occured along three directions - [-1.600 0.300 1], [-1.156 -0.078 1] and [0.899 -2.798 1] - and led to a three-fold symmetry. The corresponding Schmid factors in Table 6-6 suggest that the second slip system seems to be more active compared to the seventh slip system. However, Figure 6-27 demonstrates the opposite behaviour, where the latter instead of the former became significant with an evolution of local boundary conditions and, hence, contributed to the overall deformation together with the fifth and ninth slip systems,

which were active from the very beginning. Such a controversy similar to above mentioned was also reported by Zaafarani *et al*. (2006).

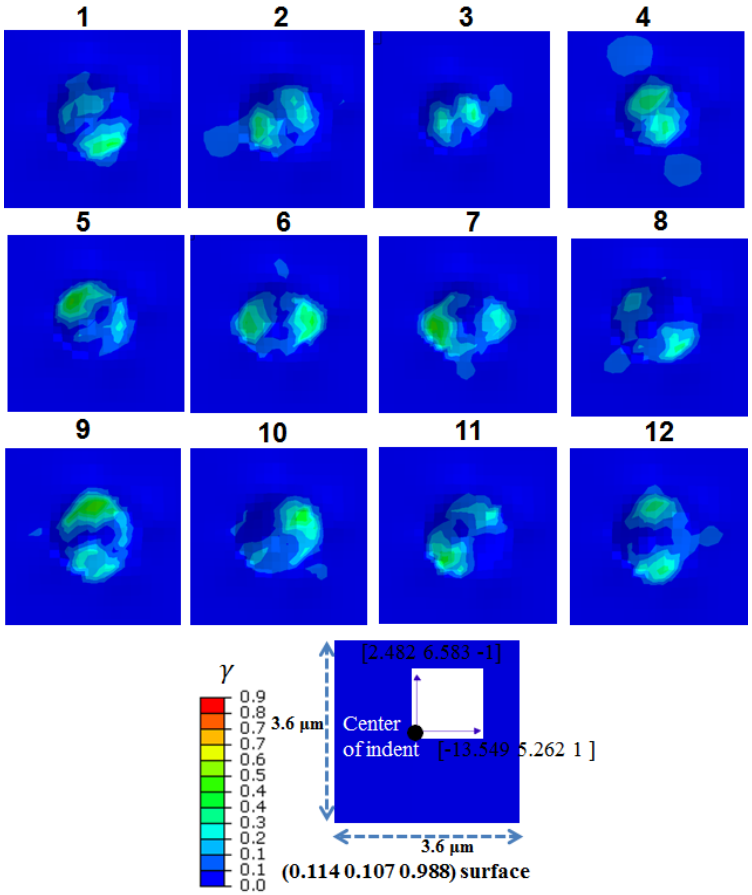

Figure 6-26: Distribution of shear strains on 12 slip systems predicted with FE simulation on indented (0.114 0.107 0.988) surface

Another point to mention here is the total number of active slip systems during indentation for different crystallographic orientations. This number was 12 in indentation for (0.114 0.107 0.988) orientation, whereas it was 7 with three primary and four secondary slips systems in indentation for (0.579 0.417 0.702) orientation. On the other hand, in indentation for (0.641 0.078 0.764) orientation, the total number of active slip systems was 10 since the sixth and tenth slip systems were inactive. Smith *et al*. (2003) demonstrated that the occurrence of cross slip was very high when more slip systems were active due to their involvement to the overall deformation, which, in turn, led to larger pile-up heights. This explains why

the highest pile-up was observed in the indentation of (0.114 0.107 0.988) orientation followed by (0.641 0.078 0.764) orientation with the lowest for (0.579 0.417 0.702) orientation in the experiments and simulations (Figure 6-20 and Figure 6-22).

In the following section, the exact orientations - (010), (101) and (111) - will be used to demonstrate the influence of orientation on the mechanical behaviour of the single-crystal Ti alloy accurately, which cannot be achieved using the orientation of the crystals in the experiments as they are comparatively less stable orientations.

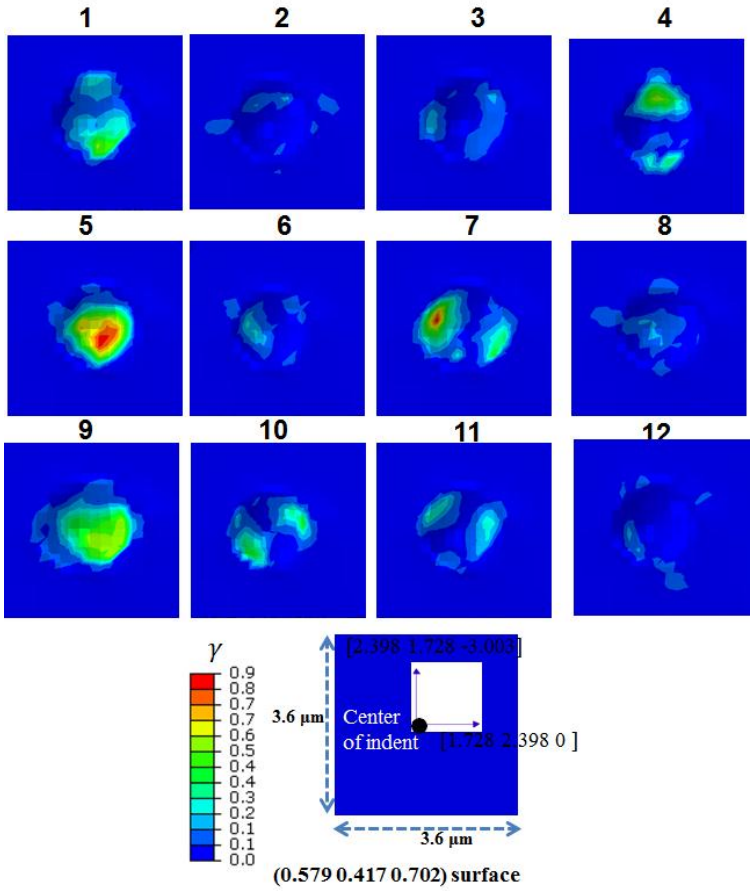

Figure 6-27: Distribution of shear strains on 12 slip systems predicted with FE simulation on indented (0.579 0.417 0.702) surface

6.6.1 Evolution of crystallographic texture of nano-indents

An induced lattice rotation below an indent is of great interest to improve micromechanical understanding of indentation experiments since crystalline

reorientation occurs as a result of crystallographic shear. Figure 6-28 shows the lattice distribution of misorientation for (101) orientation on the cutting plane (-1 0 1). The colour code is linked to the accumulated orientation change with respect to starting orientation of the crystal. This figure shows that the change in local rotational fields varies between -30° and 30° except for the regions adjacent to the indenter directly below its tip, where extreme reorientation occurs. The corresponding orientation change in regions A and C was less, between -10° and 10°, whereas higher texture evolution is observed in region B. Figure 6-29 demonstrates the extent of texture evolution on path O-P shown in Figure 6-28. It should be emphasized that while 0.07 μm distance to the right and left of the center of path corresponds to region A, the remaining part to region B. This plot indicates that the orientation change on this path in region A is less than 10°. Figure 6-29 suggests that steep gradients in the crystalline reorientation exist in region B. Such a distribution of texture evolution below the indent was also observed by Zaafarani *et al*. (2006), where the texture and microstructure below a nano-indent in a (111) Cu single-crystal was investigated using 3D EBSD and crystal-plasticity FE simulations. The experimental part of that study revealed that there were multiple transition regimes with steep orientation gradients and frequent changes in the sign of rotation directions (Figure 6-30). In that study, the FE simulations predicted a similar pattern for the absolute orientation changes but failed to predict the frequent changes in the sign of rotation field. However, this trend was predicted more accurately in this study as shown in Figure 6-28 and 6-30. On the other hand, Zaafarani *et al*. (2006) carried out isotropic plasticity simulations of the indentation process and compared the local rotational fields with the CP simulations. That study revealed that the rotation zones tangent to the indenter directly below its tip was observed in both simulations; however, the inner rotation zones cannot be obtained in an isotropic case. That comparison suggested that the rotations in the former zones were not a purely crystalline phenomenon, whereas the rotations in the inner rotation zones were justified to occur due to crystalline discreteness of the plastic slip.

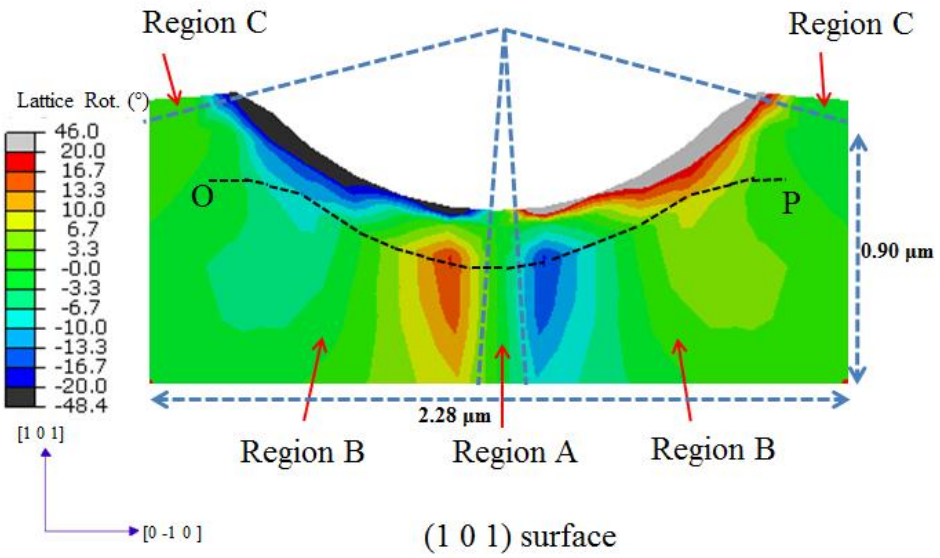

Figure 6-28: Rotation angles and rotation directions predicted by FE simulations using EMSGCP theory in (-1 0 1) plane

The FE simulations were also performed using the CP constitutive laws to demonstrate the influence of strain gradient effects on crystalline reorientation. The corresponding texture evolution on path O-P is plotted in Figure 6-29. The local rotational fields are closer to those obtained with the EMSGCP constitutive laws at some regions, however, they are mostly over predicted (Figure 6-28 and 6-30). The reason for this discrepancy arises from the fact that GNDs are not accounted for in the CP constitutive equations. In indentation model rapid spatial changes occurs in the local texture evolution due to imposed boundary conditions as observed in Figure 6-30. The resulting mismatches in the lattice spin for neighbouring material portions can be accommodated by GNDs. As this is accounted for in the SGCP formulations, the orientation change is predicted accurately compared to CP as also suggested by Zaafarani *et al*. (2006). Lattice rotations on the indented surfaces were also investigated.

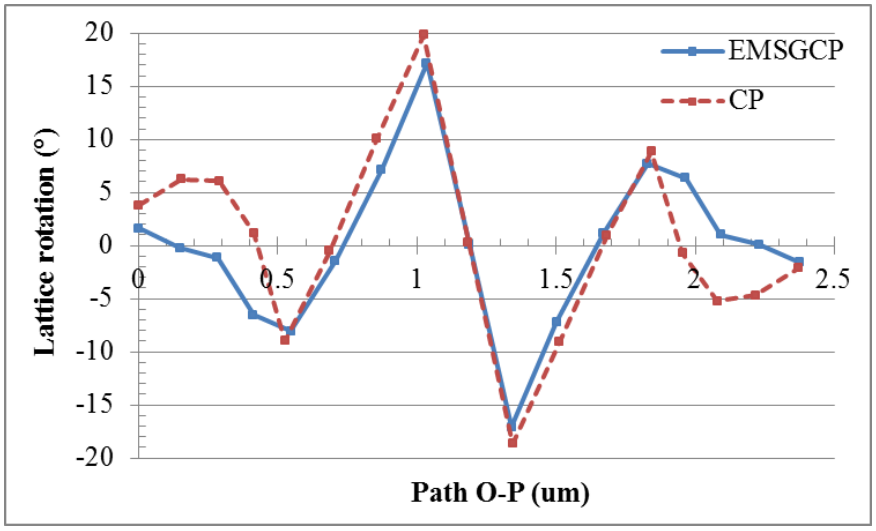

Figure 6-29: Lattice rotation angles obtained using EMSGCP and CP theories along path O-P (see Figure 6-28)

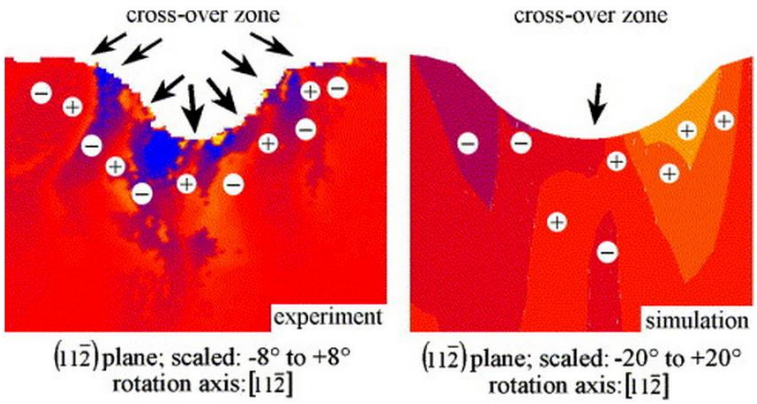

Figure 6-30: Rotation angles and rotation directions in the (1 1 -2) plane obtained from experiment and simulation. Reprinted with permission from (Zaafarani et al., 2006)

Figure 6-31 provides a view of simulation results for the distribution of crystalline reorientation around the indents for three exact orientations. In this figure plots on the left-hand side are rotations w.r.t. y-axis defined for each orientation separately and plots on the right-hand side are rotations w.r.t. x-axis. This figure clearly indicates that there exists high symmetry in the texture evolution of indented (010) surface w.r.t. both x- and y-axis, where the magnitudes of rotations are almost identical.

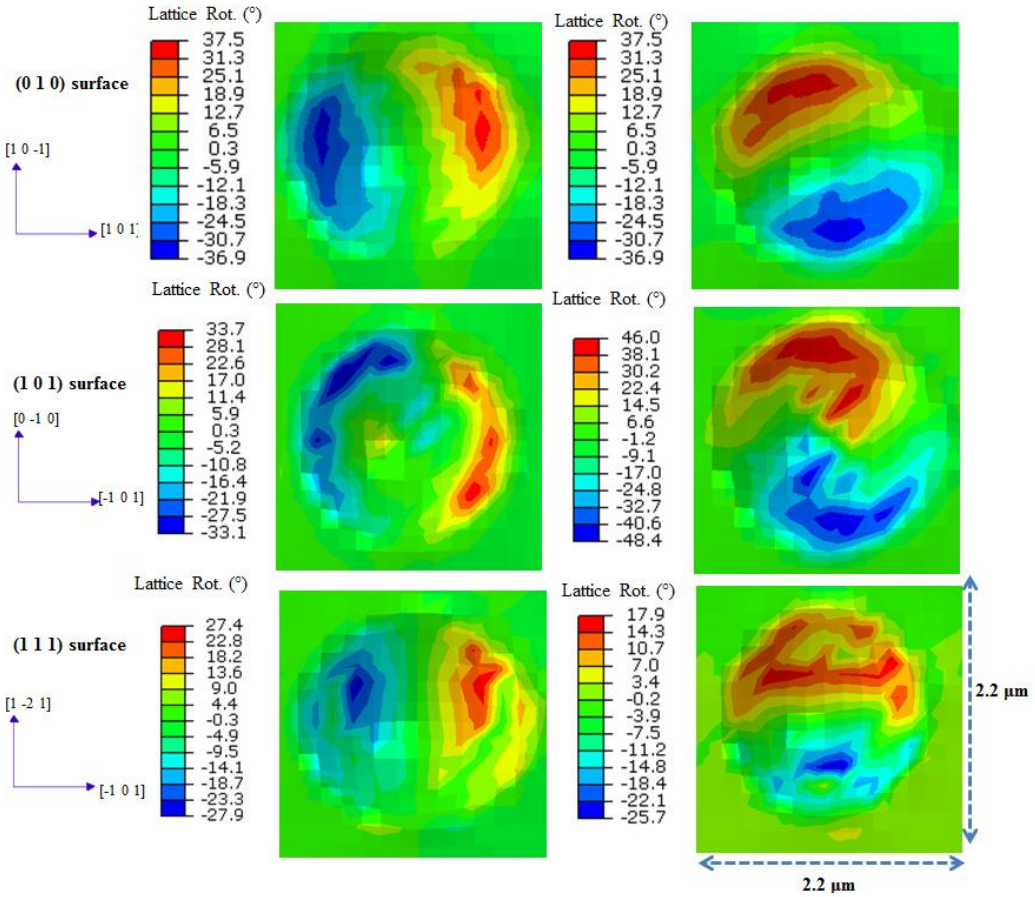

Figure 6-31: Rotation angles and rotation directions predicted with FE simulations of indentation for different crystallographic orientation. Top row: rotations on (0 1 0) surface w.r.t. [1 0 -1] (left) and [1 0 1] (right). Middle row: rotations on (1 0 1) surface w.r.t. [0 -1 0] (left) and [-1 0 1] (right). Bottom row: rotations on (1 1 1) surface w.r.t. [1 -2 1] (left) and [-1 0 1] (right)

Symmetry here is meant as the similarity of the absolute values of rotations at opposite sides. Similarly, the similar symmetry was also observed for the indented (101) surface, where, however, rotations in x-direction were more pronounced compared to those in y-direction. The symmetry, on the other hand, for the indented (111) surface was observed only in y-direction, with different absolute values of rotations w.r.t. x-direction at two opposite sides. These observations can be explained by the pile-up patterns obtained for different orientations (Figure 6-32). Since the surface profile for the indented (010) surface is symmetric w.r.t.

both [1 0 -1] and [1 0 1] axes and the maximum pile-up height is identical at four peak points, the obtained rotational fields have the same characteristics. On the other hand, the maximum-pile up regions in the indented (101) surface occurs w.r.t. [-1 0 1] axis rather than [0 -1 0] axis (Figure 6-32). A higher lattice rotation w.r.t. the former axis is therefore observed compared to the latter one, according to which the pile-up heights are smaller; hence, lower rotations were observed. With the same idea, as the region, where the piling ups were observed on the indented (111) surface, is not symmetric w.r.t. [-1 0 1] axis, but located significantly to the left of [-1 0 1] axis, larger rotations were observed on that side compared to the opposite side. On the other hand, the surface profile is symmetric w.r.t. [1 -2 1] axis; hence, the obtained rotation fields are symmetric.

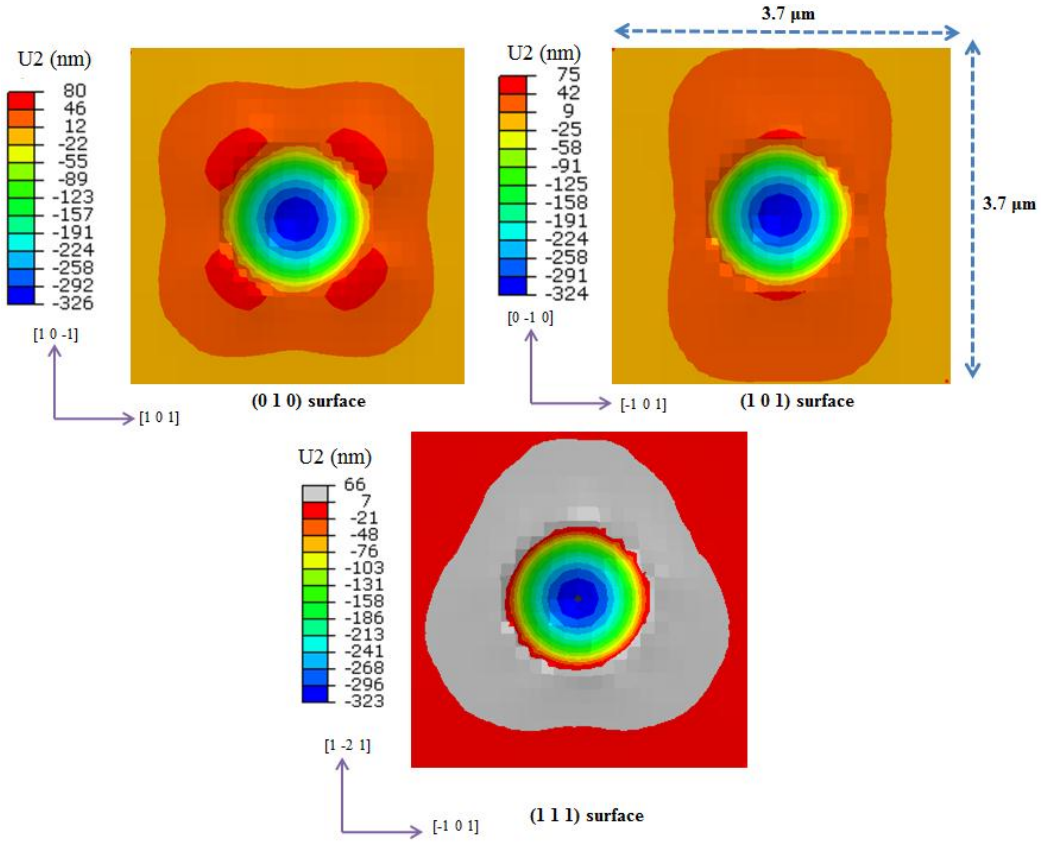

Figure 6-32: Pile-up structures of imprints obtained with FE simulations for different crystallographic orientations

6.7 Size effects in nano-indentation of single-crystal Ti alloy

In this section, the size effect in indentation of the single-crystal Ti alloy is investigated using the material parameters determined in Section 6.5. Size dependency in nano-indentation experiments can be considered as the change in material properties such as yield strength and hardness, with respect to indentation depth and indenter's radius. Therefore, the response of the single-crystal Ti alloy is investigated, namely, hardness changes, on the one hand, with a change in the indentation depth and, on the other hand, with a change in indenter's radius. Spherical indenters with two different diameters - 2.25 μm and 4.5 μm - are considered. The hardness values are calculated as the ratio of the imposed indentation force to the respective projected contact area. To determine the projected contact area, a CAREA option in ABAQUS (Systemes, 2010) was first considered, which calculates the total area in contact. However, the contact area reported by CAREA is, generally, slightly larger than the true contact area for reasonably meshed contact surfaces; therefore, interpretation of CAREA should be done with care (Systemes, 2010). Instead, here the ABAQUS contact variable COPEN outputting the clearance between surfaces was employed to accurately calculate the contact areas of each surface element (Figure 6-33). A very strict threshold value of 10^{-5} mm is considered for COPEN variable; it means that if the clearance between indenter tip and the workpiece material is more than 10^{-5} mm, this part of the element was not accounted for in the area calculation as shown in Figure 6-33. The overall projected contact area, based on summation over all areas of elements in contact, was calculated using the PLOTDIGITIZER program, which digitizes scanned plots of functional data (Huwaldt, 2005).

Figure 6-34 demonstrates the simulation results on the variation of mean pressure, i.e. hardness, with the ratio of the indent's radius a to the indenter tip radius R for two different indenter radii. The definition of a and R is given in Figure 6-35. The first observation in Figure 6-34 is that the hardness value increases with an increase in the a/R ratio for both indenters as the total dislocation density increases with

such an increase. Johnson (1974) estimated the average plastic strain underneath a spherical indenter of radius R as

$$\varepsilon^{\mathrm{p}} \approx \frac{a}{5R}. \qquad 6\text{-}1$$

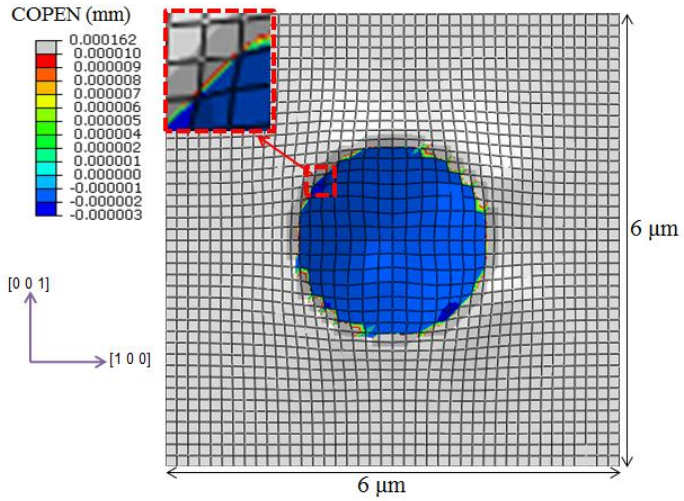

Figure 6-33: Contact area and contact openings for spherical indenter's tip of radius 2.25 µm

As ρ_S is proportional to plastic strain, an increase in the a/R ratio increases ρ_S, according to Equation 6-1. On the other hand, the average density of GND is calculated by Swadener *et al*. (Swadener *et al*., 2002) as

$$\rho_G \approx \frac{\bar{r}}{bR}, \qquad 6\text{-}2$$

where $\bar{r}$ corresponds to the Nye factor and b is the Burgers vector. This equation indicates that ρ_G is independent of a/R ratio, but increases when the indenter's radius decreases. In total, the sum of ρ_S and ρ_G increases with an increase in the a/R ratio; hence, an increase in hardness value is observed for both spherical indenters (Figure 6-34).

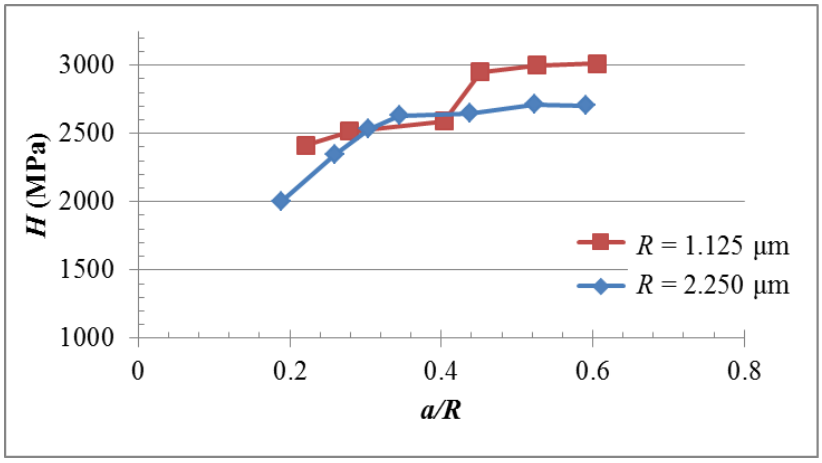

Figure 6-34: Numerical results on variation of hardness with a/R for spherical indenters with different radii

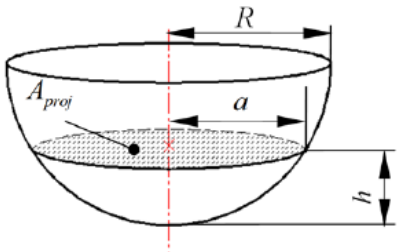

Figure 6-35: Geometry of spherical indenter used in nanoindentation (Fischer-Cripps, 2002)

Equation 6-2 explains partially our second observation in Figure 6-34: at a fixed a/R ratio, an indenter with a smaller tip radius gives a larger hardness value compared to that for a larger radius. Since ρ_G is larger for smaller indenter, the total dislocation density becomes larger, hence does the hardness value. It is worth mentioning that ρ_S is independent of indenter radius.

The change in indentation hardness with the a/R ratio was also investigated by employing the CP theory to make a comparison with the results obtained using the EMSGCP theory. Surprisingly, it was found that very close trends were obtained for hardness values (Figure 6-36). The obtained hardness values were identical up to the a/R ratio of 0.40, whereas beyond that ratio, the hardness values for CP were smaller. To get an idea about the underlying reason, the force-displacement

diagram was plotted using both theories for the indenter's radius of 1.125 μm (Figure 6-37). In this figure the indentation depth of approx. 265 nm corresponds to the a/R ratio of 0.6. It is clearly visible that there is no appreciable difference in the obtained force value using CP and EMSGCP theories up to 180 nm ($a/R \approx 0.4$), after which the force-displacement curve started to diverge. This result explains why identical hardness values were obtained using two theories up to the a/R ratio of 0.40 and divergence in the hardness values for larger values.

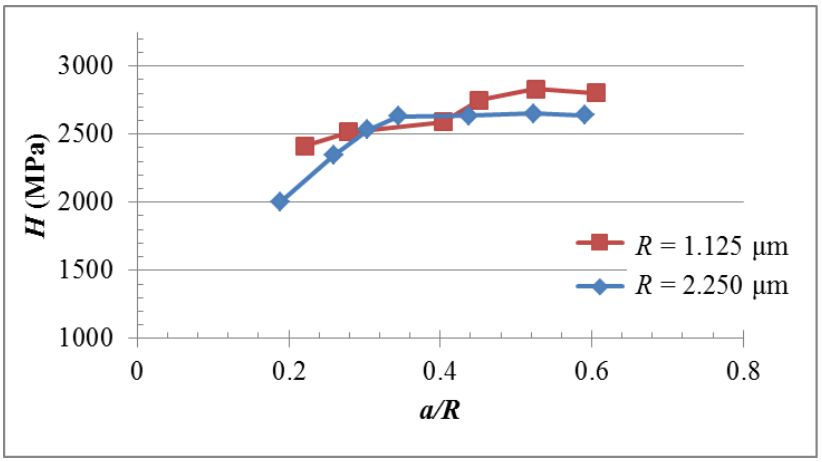

Figure 6-36: Numerical results on variation of hardness with a/R using CP theory for spherical indenters with different radii

In the CP theory the effect of ρ_G is not accounted for; only the contribution of ρ_S is taken into account (see section 3.3). As ρ_S is proportional to the a/R ratio, compatible hardness values were predicted for both spherical indenters (Figure 6-36). This explanation is also valid for the EMSGCP theory up to the a/R ratio of 0.40. However, when the a/R ratio exceeds this threshold value, strain gradients start to become significant (Figure 6-37). Larger hardness values were therefore observed for the EMSGCP theory. As mentioned above, since ρ_G increases with a decrease in the indenter's radius, the hardness values were larger for a smaller indenter when the EMSGCP theory was used (Figure 6-34).

Following equation explains how the strength of a slip system α is calculated.

$$g_T^\alpha = \tau_0 + \sqrt{(\Delta g_s^\alpha)^2 + (\alpha_T \mu)^2 b n_G^\alpha}. \qquad 6\text{-}3$$

At the onset of plastic deformation there are no strain gradients, $g_T^\alpha(t=0) = \tau_0$ (see beginning of this chapter). In the course of deformation, strain gradients start to evolve with an increase in plastic strain. The first term in the square root of Equation 6-3 represents hardening due to SSDs and the second term represents the hardening due to GNDs. As the deformation advances, these two terms start to contribute to hardening of each slip system by competing with each other. However, their contribution occurs gradually since their overall magnitude is comparatively small compared to τ_0 ($g_T^\alpha|_{t=0}$). Differences in the solutions were observed for simulations using CP and EMSGCP theories at later deformation instances (Figure 6-37). It should be pointed out that when a smaller value of τ_0 is used, the influence of strain gradients in the solution can manifest itself at earlier deformation stages. In summary, as the influence of ρ_G is negligibly small at the beginning of plastic deformation, the size effects in indentation at those deformation level cannot be captured using the EMSGCP theory. However this can be captured at higher deformation levels, where ρ_G starts to govern hardening of slip systems (Figure 6-34).

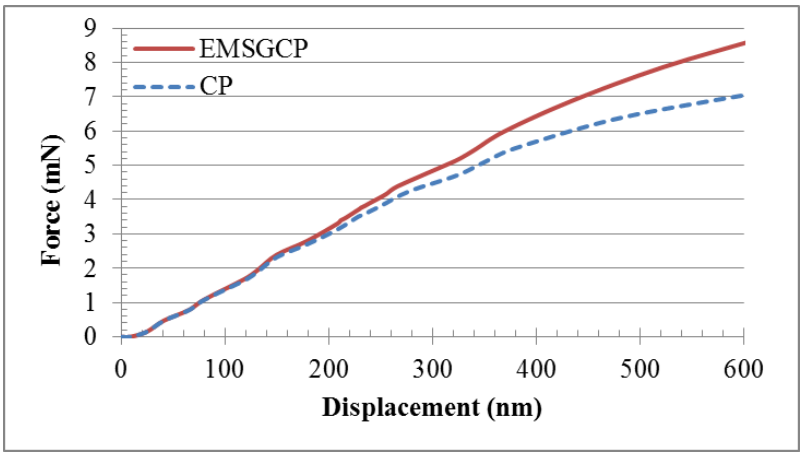

Figure 6-37: Load-displacement curves obtained from FE simulations using CP and EMSGCP theories for spherical indenter with radius of 1.125 µm

Contrary to the case of spherical indenter, indentation hardness for sharp indenters decreases with an increase in penetration depth. Due to self-similarity of sharp indenters (e.g. conical or Berkovic) the average density of SSDs is independent of the indentation depth while the density of geometrically necessary dislocations is inversely proportional to h as

$$\rho_G \approx \frac{3\,(\tan\theta)^2}{2bh}, \qquad 6\text{-}4$$

where θ corresponds to the angle between the surface of the conical indenter and the plane of the indented surface (Nix and Gao, 1998). As the total density decreases with an increase in the indentation depth, the hardness value decreases (Figure 2-13). Since the contribution of GNDs at the beginning of the plastic deformation due to the above-mentioned fact is insignificant, the size effects in the case of sharp indenter cannot be captured using the EMSGCP theory. To sum up, the EMSGCP theory allows us to characterize the size effects in nano-indentation when the GNDs become significant and affect the strength of the slip systems.

6.8 Conclusions

In this chapter the material behaviour of beta phase of the single-crystal Ti alloy in nano-indentation experiments was investigated. The performed experiments revealed different pile-up patterns for different crystallographic orientations justifying strong crystallographic anisotropy of the out-of plane displacements around the indents. A 3D EMSGCP FE model of this test was developed. The numerical model enables, on the one hand, to characterize relative contributions of different slip systems during deformation and, on the other hand, to obtain local fields of stresses and strains inside the sample. The material parameters were obtained by calibrating the developed numerical model with the experiments employing the obtained load-displacement curves and surface profiles. The obtained $\rho_S|_{t=0}$ here helps to characterize the contribution of $\rho_S|_{t=0}$ and $\rho_G|_{t=0}$ to the CRSS of slip systems in the micro-pillar-compression experiment. Similarly,

the Taylor coefficient α obtained here also allows quantifying the WHR in micro-pillars of different sizes. In summary, nano-indentation tests were used to describe the size effect in micro-pillar compression experiments.

The investigation of contribution of different slip systems to the overall deformation in FE simulations demonstrated that the Schmid factor of the slip systems determined their contributions to the materials behaviour. It evolved with deformation, i.e. the slip system active at the very beginning may become inactive at advanced deformation levels, and vice versa. This brought the conclusion that predictions of active slip systems based on the simplifying assumption of uniaxial compression may not be always accurate; whereas, the local boundary conditions in connection with the deformation level need to be taken into account. On the other hand, in nano-indentation experiments, due to imposed boundary conditions rapid changes occurs in the local spatial texture evolution. The resulting mismatches in the lattice spin for neighbouring parts of material can be accommodated by GNDs. As this was accounted for in the EMSGCP constitutive laws, the corresponding simulations describe the local fields of lattice rotations and, hence, strains and stresses accurately compared to solutions obtained using the CP constitutive laws. The size effect in nano-indentation experiments was studied numerically. It was concluded that ISE could be predicted using the EMSGCP theory when a spherical indenter is used, but this was not possible in the case of a sharp indenter.

CHAPTER VII

7 Conclusions and future work

In this chapter a general conclusion on the work done is presented. Although effort is made here to circumnavigate discussions already presented in individual chapters, it should be noted that some amount of duplication is unavoidable. The future work of this thesis is given at the end.

7.1 Conclusions

A novel model of strain-gradient theory to predict the size effect, which is observed in the micro-pillar compression experiments of the studied Ti alloy, is introduced in this thesis. Since background information is vital to understand the underlying mechanisms for this phenomenon, a thorough literature review was given in the first chapter. As the investigated material, Ti-15-3-3-3, has a b.c.c. crystalline structure, the crystal-plasticity theory within the framework of FEM was planned to be used at the initial stage. However, as there is no length scale in its constitutive description, it cannot explain the dependence of mechanical response on a specimen's size. This was circumvented by using a non-local continuum MBSGCP

theory. However, as the CRSS value of the slip systems in this theory is independent of the pillar size, in contrast to observations in the experiments, this theory was also found to be insufficient to explain the size effect. A novel enhanced model of strain-gradient crystal-plasticity theory was suggested, where the initial microstructure of pillars was accounted for, based on some experimental evidences (Maass *et al*., 2006; 2007; 2009). This was explained by the following. During the fabrication process of pillars, e.g. with the FIB method, pillars become work-hardened; hence, finite stresses evolve in their body. It is well known that traction-free surfaces of pillars dictate a zero stress value on their surfaces. This difference in the stress distribution results in stress gradients, i.e. strain gradients in the body, which can be accommodated by GNDs. For instance, for the smaller pillar size, where the traction-free surfaces are closer to the pillar's axis and pillar's surface-to-volume ratio is higher, physically (and numerically) strain gradients become more pronounced compared to larger pillar sizes. Accordingly, the smaller the size of pillar is, the higher the density of GNDs and thus higher its strength. In this theory, the incipient density of GNDs is considered to be a function of surface-to-volume ratio. It is worth mentioning that the initial density of SSDs is independent of the pillar size. The relative contribution of incipient $\rho_S|_{t=0}$ and $\rho_G|_{t=0}$ to the CRSS needs to be addressed in the EMSGCP theory. In principle, $\rho_G|_{t=0}$ is infinitesimally small in the initial microstructure of bulk large-size pillars; hence, incipient $\rho_S|_{t=0}$ can be characterized for such pillars using this experiment. However, their production is difficult. Instead, here a novel technique was employed, in which the combination of nano-indentation experiments and simulations with EMSGCP theory were used to determine $\rho_S|_{t=0}$ since $\rho_G|_{t=0}$ is infinitesimally small in the samples in nano-indentation experiments due to their negligibly small surface-to-volume ratio. In other words, nano-indentation experiments, which are simple to perform, were used to study the size effect in pillars. The numerical results demonstrated that the experimental stress-strain curves for pillars were predicted appropriately using EMSGCP theory. The results also demonstrated that although the deformation was applied uniaxially in micro-pillar compression experiments, heterogeneity evolved during loading due to

boundary conditions and orientation of the pillar itself, leading, in its turn, to strain gradients. These findings also justified that it was appropriate to use the strain-gradient theories to explain the size effect in micro-pillar compression experiments as they are being used to explain this phenomenon in nano-indentation, bending or torsion experiments. It should be emphasized that the experimental study of the b.c.c. Ti alloy revealed that only the slip system {112} <111> was active during loading; hence, only this set among the potential three different sets in the FE simulations was switched on.

The study about the critical edge length (l_c) of the pillar, below which the relative change in the corresponding CRSS value was less than 5%, demonstrated that 8 μm was the value of l_c for the studied Ti alloy. In other words, for the pillars with an edge length of less than 8 μm, the EMSGCP theory should be used, whereas for the larger pillar sizes, the MBSGCP theory can be used as it is degenerated from the EMSGCP theory (Figure 7-1). It was also observed that l_c was a function of material parameters $\rho_S|_{t=0}$, $\rho_G|_{t=0}$ and β_1, whereas it was insensitive to parameter *K*.

It was concluded from the FE simulations of nano-indentation experiments that the local fields of lattice rotations and, hence, strains and stresses can be predicted accurately by using the EMSGCP theory as GNDs accommodating the mismatches in the lattice spin for neighbouring parts of material are accounted for in contrast to the CP theory. The size effect in nano-indentation (ISE) experiments was studied numerically. It was concluded that ISE could be predicted accurately using the EMSGCP theory when a spherical indenter was used, but this was not possible for a sharp indenter.

In summary, the combination of micro-pillar-compression and nanoindentation experiments with their FE models employing the EMSGCP theory were used to predict the real-life deformation behaviour of Ti-15-3-3-3 at micron scale under quasi-static loading conditions. Manufacturers and designers can facilitate the introduced methodology and framework to design and optimize their crystalline materials (even for f.c.c. and h.c.p.) for different applications, spanning from

micro-scale such as MEMS, medical devices, thermal barrier coatings, optics, electronics, etc. It is worth noting that the user subroutine (UMAT) should be amended for h.c.p. crystal structures to account for crystal aspect ratio while determining the slip systems.

7.2 Future Work

In the future work, the applicability of the developed EMSGCP theory to nano-size pillars can be checked. To achieve this, additional compression tests for nano-size pillars of Ti alloy can be carried out and compared with the numerical model (Figure 7-1). This study can help to determine the limit of applicability of the EMSGCP theory since in the sub-micron scales the discrete dislocation events become more significant and the continuum models do not describe the materials behaviour correctly. A similar work can be made for f.c.c. pillars. It is known that the deformation mechanism in f.c.c. micron-sized pillars is not similar to that in nano-sized pillars, unlike b.c.c. pillars with the same mechanism at both scales (Brinckmann *et al.*, 2008). This can lead to differences in the limits of EMSGCP theory for different crystal orientations.

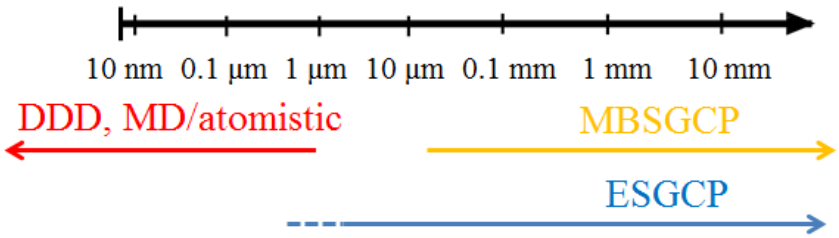

Figure 7-1: Length scales in the pillar compression experiments for Ti alloy

It is also well known that single-crystal components used in high-technology applications such as MEMS, gems industry and medical devices can be exposed to dynamic loading in their service life; the responses under such loading circumstances need to be identified to enhance their dynamic performances. In the future work, dynamic behaviour of the single-crystal Ti alloy at different length scales can be investigated both experimentally and numerically. To achieve this, pillars of different sizes can be compressed dynamically (i.e. at higher strain rates),

where material inertial effects become significant, and the obtained results can be compared with those obtained with FE simulations using the EMSGCP theory. In the numerical model, the CRSS value and strain-hardening of the involved slip systems can be implemented as strain-rate dependent.

References

Abu Al-Rub, R.K., 2007, Prediction of micro and nanoindentation size effect from conical or pyramidal indentation: Mechanics of Materials, v. 39, no. 8, p. 787-802.

Abu Al-Rub, R.K., and Voyiadjis, G.Z., 2004, Analytical and experimental determination of the material intrinsic length scale of strain gradient plasticity theory from micro- and nano-indentation experiments: International Journal of Plasticity, v. 20, no. 6, p. 1139-1182.

Acharya, A., and Bassani, J., 2000, Lattice incompatibility and a gradient theory of crystal-plasticity: Journal of the Mechanics and Physics of Solids, v. 48, no. 8, p. 1565-1595.

Acharya, A., and Beaudoin, A., 2000, Grain-size effect in viscoplastic polycrystals at moderate strains: Journal of the Mechanics and Physics of Solids, v. 48, no. 10, p. 2213-2230.

Ai, K., and Dai, L., 2008, Numerical study of pile-up in bulk metallic glass during spherical indentation: Science in China Series G: Physics Mechanics and Astronomy, v. 51, no. 4, p. 379-386.

Aifantis, E., 1999, Strain gradient interpretation of size effects: International Journal of Fracture, v. 95, no. 1, p. 299-314.

Aifantis, E., 1984, On the microstructural origin of certain inelastic models: Journal of Engineering Materials and Technology, v. 106, p. 326.

Akarapu, S., Zbib, H.M., and Bahr, D.F., 2010, Analysis of heterogeneous deformation and dislocation dynamics in single-crystal micro-pillars under compression: International Journal of Plasticity, v. 26, no. 2, p. 239-257.

Albrecht, H.J., Hannach, T., Häse, A., Juritza, A., Müller, K., and Müller, W., 2005, Nanoindentation: a suitable tool to determine local mechanical properties in microelectronic packages and materials?: Archive of Applied Mechanics, v. 74, no. 11, p. 728-738.

Alcala, J., Barone, A., and Anglada, M., 2000, The influence of plastic hardening on surface deformation modes around Vickers and spherical indents: Acta materialia, v. 48, no. 13, p. 3451-3464.

Altebaeumer, T., Gotsmann, B., Knoll, A., Cherubini, G. and Uerig, D., 2008, Self-similarity and finite size effects in nano-indentation of highly cross-linked polymers: Nanotechnology, v. 19, p. 475301.

Antunes, J., Menezes, L., and Fernandes, J., 2007, Influence of Vickers tip imperfection on depth sensing indentation tests: International Journal of Solids and Structures, v. 44, no. 9, p. 2732-2747.

Antunes, J., Menezes, L., and Fernandes, J., 2006, Three-dimensional numerical simulation of Vickers indentation tests: International Journal of Solids and Structures, v. 43, no. 3, p. 784-806.

Arsenlis, A., and Parks, D., 1999, Crystallographic aspects of geometrically-necessary and statistically-stored dislocation density: Acta Materialia, v. 47, no. 5, p. 1597-1611.

Arsenlis, A., and Parks, D., 2002, Modelling the evolution of crystallographic dislocation density in crystal plasticity: Journal of the Mechanics and Physics of Solids, v. 50, no. 9, p. 1979-2009.

Asaro, R.J., 1983, Micromechanics of crystals and polycrystals: Advances in Applied Mechanics, v. 23, p. 1-115.

Ashby, M., 1970, The deformation of plastically non-homogeneous materials: Philosophical Magazine, v. 21, no. 170, p. 399-424.

Asif, S.A.S., and Pethica, J., 1998, Nano scale indentation creep testing at non-ambient temperature: The Journal of Adhesion, v. 67, no. 1-4, p. 153-165.

Asif, S.A.S., and Pethica, J., 1997, Nanoindentation creep of single-crystal tungsten and gallium arsenide: Philosophical Magazine A, v. 76, no. 6, p. 1105-1118.

Bassani, J., 2001, Incompatibility and a simple gradient theory of plasticity: Journal of the Mechanics and Physics of Solids, v. 49, no. 9, p. 1983-1996.

Bathe, K.J., 1996, Finite-element procedures, Prentice hall Englewood Cliffs, NJ 2.

Beaudoin, A., and Acharya, A., 2001, A model for rate-dependent flow of metal polycrystals based on the slip plane lattice incompatibility: Materials Science and Engineering: A, v. 309, p. 411-415.

Begley, M.R., and Hutchinson, J.W., 1998, The mechanics of size-dependent indentation: Journal of the Mechanics and Physics of Solids, v. 46, no. 10, p. 2049-2068.

Bei, H., Shim, S., Miller, M., Pharr, G., and George, E., 2007, Effects of focused ion beam milling on the nanomechanical behavior of a molybdenum-alloy single-crystal: Applied Physics Letters, v. 91, no. 11, p. 111915.

Beltz, G., Rice, J., Shih, C., and Xia, L., 1996, A self-consistent model for cleavage in the presence of plastic flow: Acta materialia, v. 44, no. 10, p. 3943-3954.

Bennett, V.P., and McDowell, D.L., Polycrystal orientation distribution effects on microslip in high cycle fatigue: International Journal of Fatigue, v. 25, p. 27-39.

Benzerga, A.A., and Shaver, N.F., 2006, Scale dependence of mechanical properties of single-crystals under uniform deformation: Scripta Materialia, v. 54, no. 11, p. 1937-1941.

Berke, P., Tam, E., Delplancke-Ogletree, M.P., and Massart, T., 2009, Study of the rate-dependent behavior of pure nickel in conical nanoindentation through numerical simulation coupled to experiments: Mechanics of Materials, v. 41, no. 2, p. 154-164.

Bhattacharya, A., and Nix, W., 1988, Finite-element simulation of indentation experiments: International Journal of Solids and Structures, v. 24, no. 9, p. 881-891.

Bocciarelli, M., Bolzon, G., and Maier, G., 2005, Parameter identification in anisotropic elastoplasticity by indentation and imprint mapping: Mechanics of Materials, v. 37, no. 8, p. 855-868.

Brenner, S., 1958, Growth and Properties of" Whiskers": Science, v. 128, no. 3324, p. 569.

Brenner, S., 1956, Tensile strength of whiskers: Journal of Applied Physics, v. 27, no. 12, p. 1484-1491.

Brinckmann, S., Kim, J.Y., and Greer, J.R., 2008, Fundamental differences in mechanical behavior between two types of crystals at the nanoscale: Physical Review Letters, v. 100, no. 15, p. 155502.

Bucaille, J.L., Stauss, S., Felder, E., and Michler, J., 2003, Determination of plastic properties of metals by instrumented indentation using different sharp indenters: Acta materialia, v. 51, no. 6, p. 1663-1678.

Busso, E.P., Meissonnier, F.T., and O'Dowd, N.P., 2000, Gradient-dependent deformation of two-phase single-crystals: Journal of the Mechanics and Physics of Solids, v. 48, no. 11, p. 2333-2361.

Cai, X., 1993, Effect of friction in indentation hardness testing: a finite-element study: Journal of Materials Science Letters, v. 12, no. 5, p. 301-302.

Callister, W.D., , Materials science and engineering–an introduction. 1997.

Carpinteri, A., and Puzzi, S., 2006, A fractal approach to indentation size effect: Engineering Fracture Mechanics, v. 73, no. 15, p. 2110-2122.

Cermelli, P., and Gurtin, M.E., 2002, Geometrically necessary dislocations in viscoplastic single crystals and bicrystals undergoing small deformations: International Journal of Solids Structure, v. 39, no. 26, p. 6281-6309.

Chaudhri, M., and Winter, M., 1988, The load-bearing area of a hardness indentation: Journal of Physics D: Applied Physics, v. 21, p. 370.

Chen, S., and Wang, T., 2002, A new deformation theory with strain gradient effects: International Journal of Plasticity, v. 18, no. 8, p. 971-995.

Chen, C.Q., Pei, Y.T., and De Hosson, J.T.M., 2010, Effects of size on the mechanical response of metallic glasses investigated through in situ TEM bending and compression experiments: Acta Materialia, v. 58, no. 1, p. 189-200.

Cheng, C.M., and Cheng, Y.T., 1997, On the initial unloading slope in indentation of elastic-plastic solids by an indenter with an axisymmetric smooth profile: Applied Physics Letters, v. 71, p. 2623.

Cheng, Y.T., 1999, Scaling relationships in conical indentation of elastic-perfectly plastic solids: International Journal of Solids and Structures, v. 36, no. 8, p. 1231-1243.

Cheng, Y.T., and Cheng, C.M., 2004, Scaling, dimensional analysis, and indentation measurements: Materials Science and Engineering: R: Reports, v. 44, no. 4, p. 91-149.

Cheong, K.S., Busso, E.P., and Arsenlis, A., 2005, A study of microstructural length scale effects on the behaviour of FCC polycrystals using strain gradient concepts: International Journal of Plasticity, v. 21, no. 9, p. 1797-1814.

Chokshi, A., Rosen, A., Karch, J., and Gleiter, H., 1989, On the validity of the Hall-Petch relationship in nanocrystalline materials: Scripta Metallurgica, v. 23, no. 10, p. 1679-1684.

Clark, B.G., Gianola, D.S., Kraft, O., and Frick, C.P., 2010, Size Independent Shape Memory Behavior of Nickel–Titanium: Advanced Engineering Materials, v. 12, no. 8, p. 808-815.

Cleveringa, H., Van der Giessen, E., and Needleman, A., 1999, A discrete-dislocation analysis of bending: International Journal of Plasticity, v. 15, no. 8, p. 837-868.

Columbus, D., and Grujicic, M., 2002, A comparative discrete-dislocation/nonlocal crystal-plasticity analysis of plane-strain mode I fracture: Materials Science and Engineering: A, v. 323, no. 1–2, p. 386-402.

Dao, M., Chollacoop, N., Van Vliet, K., Venkatesh, T., and Suresh, S., 2001, Computational modeling of the forward and reverse problems in instrumented sharp indentation: Acta materialia, v. 49, no. 19, p. 3899-3918.

De Borst, R., and Mühlhaus, H.B., 1992, Gradient-dependent plasticity: Formulation and algorithmic aspects: International Journal for Numerical Methods in Engineering, v. 35, no. 3, p. 521-539.

Demiral, M., Roy, A., and Silberschmidt, V., 2010, Repetitive indentation of Ti-based alloys: A numerical study, *in* IOP Conference Series: Materials Science and Engineering, IOP Publishing, p. 012105.

Deshpande, V., Needleman, A., and Van der Giessen, E., 2005, Plasticity size effects in tension and compression of single-crystals: Journal of the Mechanics and Physics of Solids, v. 53, no. 12, p. 2661-2691.

Dève, H., Harren, S., McCullough, C., and Asaro, R.J., 1988, Micro and macroscopic aspects of shear band formation in internally nitrided single-crystals of Fe-Ti-Mn alloys: Acta Metallurgica, v. 36, no. 2, p. 341-365.

Dimiduk, D., Uchic, M., and Parthasarathy, T., 2005, Size-affected single-slip behavior of pure nickel microcrystals: Acta Materialia, v. 53, no. 15, p. 4065-4077.

Doerner, M., and Nix, W., 1986, A method for interpreting the data from depth-sensing indentation instruments: Journal of Materials Research, v. 1, no. 04, p. 601-609.

Dou, R., and Derby, B., 2009, A universal scaling law for the strength of metal micro-pillars and nanowires: Scripta Materialia, v. 61, no. 5, p. 524-527.

Duesbery, M., and Vitek, V., 1998, Plastic anisotropy in bcc transition metals: Acta Materialia, v. 46, no. 5, p. 1481-1492.

Durban, D., and Masri, R., 2008, Conical indentation of strain-hardening solids: European Journal of Mechanics-A/Solids, v. 27, no. 2, p. 210-221.

Dunne, F.P.E. and Petrinic, N., 2005, Introduction to Computational Plasticity, Oxford University Press.

Dunne, F.P.E., Rugg, D., Walker, A., 2007 (a), Length scale-dependent, elastically anisotropic, physically-based hcp crystal plasticity: Application to cold-dwell fatigue in Ti alloys, International Journal of Plasticity, v. 23, p. 1061-1083.

Dunne, F.P.E., Wilkinson, A.J., Allen, R., 2007 (b), Experimental and computational studies of low cycle fatigue crack nucleation in a polycrystal. International Journal of Plasticity, v. 23, p. 273-295.

Evers, L., Parks, D., Brekelmans, W., and Geers, M., 2002, Crystal-plasticity model with enhanced hardening by geometrically necessary dislocation accumulation: Journal of the Mechanics and Physics of Solids, v. 50, no. 11, p. 2403-2424.

Fan, Z., Swadener, J., Rho, J., Roy, M., and Pharr, G., 2002, Anisotropic properties of human tibial cortical bone as measured by nanoindentation: Journal of Orthopaedic Research, v. 20, no. 4, p. 806-810.

Fan, H., Li, Z., and Huang, M., 2012, Size effect on the compressive strength of hollow micro-pillars governed by wall thickness: Scripta Materialia, v. 67, no. 3, p. 225-228.

Felippa, C.A., 2007, Overview of Nonlinear Problems, University of Colorado at Boulder, USA.

Fischer-Cripps, A., 2003, Use of combined elastic modulus in depth-sensing indentation with a conical indenter: Journal of Materials Research, v. 18, no. 05, p. 1043-1045.

Fischer-Cripps, A., 2002, Nanoindentation Springer-Verlag: New York.

Fischer-Cripps, A., 2001, Use of combined elastic modulus in the analysis of depth-sensing indentation data: JOURNAL OF MATERIALS RESEARCH-PITTSBURGH-, v. 16, no. 11, p. 3050-3052.

Fleck, N., and Hutchinson, J., 2001, A reformulation of strain gradient plasticity: Journal of the Mechanics and Physics of Solids, v. 49, no. 10, p. 2245-2271.

Fleck, N., and Hutchinson, J., 1997, Strain gradient plasticity: Advances in Applied Mechanics, v. 33, p. 295-361.

Fleck, N., and Hutchinson, J., 1993, A phenomenological theory for strain gradient effects in plasticity: Journal of the Mechanics and Physics of Solids, v. 41, no. 12, p. 1825-1857.

Fleck, N., Muller, G., Ashby, M., and Hutchinson, J., 1994, Strain gradient plasticity: theory and experiment: Acta Metallurgica et Materialia, v. 42, no. 2, p. 475-487.

Foerster, C., Stankievicz, J., Serbena, F., Lepienski, C., and Zawislak, F., 2007, Flat end and Berkovich instrumented indentation of N and Si irradiated polyethylene–viscoelastic behavior, hardness and elastic modulus: Nuclear Instruments and Methods in Physics Research Section B: Beam Interactions with Materials and Atoms, v. 257, no. 1, p. 510-514.

Fourie, J., 1967, The Plastic Deformation of Thin Copper Single-crystals: II. An Electron Microscope Study of the Surface Structure: Canadian Journal of Physics, v. 45, no. 2, p. 777-786.

Frick, C., Orso, S., and Arzt, E., 2007, Loss of pseudoelasticity in nickel-titanium sub-micron compression pillars: Acta materialia, v. 55, no. 11, p. 3845-3855.

Frick, C.P., Clark, B.G., Orso, S., Schneider, A.S., and Arzt, E., 2008, Size effect on strength and strain-hardening of small-scale [1 1 1] nickel compression pillars: Materials Science and Engineering: A, v. 489, no. 1–2, p. 319-329.

Gao, H., and Huang, Y., 2003, Geometrically necessary dislocation and size-dependent plasticity: Scripta Materialia, v. 48, no. 2, p. 113-118.

Gao, H., Huang, Y., and Nix, W., 1999a, Modeling plasticity at the micrometer scale: Naturwissenschaften, v. 86, no. 11, p. 507-515.

Gao, H., Huang, Y., Nix, W., and Hutchinson, J., 1999b, Mechanism-based strain gradient plasticity--I. Theory: Journal of the Mechanics and Physics of Solids, v. 47, no. 6, p. 1239-1263.

Gerday, A.F., 2009, Mechanical behavior of Ti-5553 alloy. Modeling of representative cells.

Gerday, A.F., Ben Bettaieb, M., Duchêne, L., Clément, N., Diarra, H., and Habraken, A., 2009, Interests and limitations of nanoindentation for bulk multiphase material identification: Application to the β phase of Ti-5553: Acta Materialia, v. 57, no. 17, p. 5186-5195.

Giannakopoulos, A., and Suresh, S., 1999, Determination of elastoplastic properties by instrumented sharp indentation: Scripta Materialia, v. 40, no. 10, p. 1191-1198.

Gouldstone, A., Chollacoop, N., Dao, M., Li, J., Minor, A.M., and Shen, Y.L., 2007, Indentation across size scales and disciplines: Recent developments in experimentation and modeling: Acta Materialia, v. 55, no. 12, p. 4015-4039.

Greer, J.R., and Nix, W.D., 2006, Nanoscale gold pillars strengthened through dislocation starvation: Physical Review B, v. 73, no. 24, p. 245410.

Greer, J.R., and De Hosson, J.T.M., 2011, Plasticity in small-sized metallic systems: Intrinsic versus extrinsic size effect: Progress in Materials Science, v. 56, no. 6, p. 654-724.

Greer, J.R., Oliver, W.C., and Nix, W.D., 2005, Size dependence of mechanical properties of gold at the micron scale in the absence of strain gradients: Acta Materialia, v. 53, no. 6, p. 1821-1830.

Greer, J.R., Weinberger, C.R., and Cai, W., 2008, Comparing the strength of f.c.c. and b.c.c. sub-micrometer pillars: Compression experiments and dislocation dynamics simulations: Materials Science and Engineering: A, v. 493, no. 1–2, p. 21-25.

Gröger, R., Bailey, A., and Vitek, V., 2008, Multiscale modeling of plastic deformation of molybdenum and tungsten: I. Atomistic studies of the core structure and glide of 1/21 1 1 screw dislocations at 0 K: Acta Materialia, v. 56, no. 19, p. 5401-5411.

Groma, I., 1997, Link between the microscopic and mesoscopic length-scale description of the collective behavior of dislocations: Physical Review B, v. 56, no. 10, p. 5807.

Groma, I., Csikor, F., and Zaiser, M., 2003, Spatial correlations and higher-order gradient terms in a continuum description of dislocation dynamics: Acta Materialia, v. 51, no. 5, p. 1271-1281.

Guo, W., 2010, On the influence of indenter tip geometry on the identification of material parameters in indentation testing.

Gurtin, M.E., 2003, On a framework for small-deformation viscoplasticity: free energy, microforces, strain gradients: International Journal of Plasticity, v. 19, no. 1, p. 47-90.

Gurtin, M.E., 2002, A gradient theory of single-crystal viscoplasticity that accounts for geometrically necessary dislocations: Journal of the Mechanics and Physics of Solids, v. 50, no. 1, p. 5-32.

Gurtin, M.E., 2000, On the plasticity of single-crystals: free energy, microforces, plastic-strain gradients: Journal of the Mechanics and Physics of Solids, v. 48, no. 5, p. 989-1036.

Guruprasad, P., and Benzerga, A., 2008, Size effects under homogeneous deformation of single-crystals: a discrete-dislocation analysis: Journal of the Mechanics and Physics of Solids, v. 56, no. 1, p. 132-156.

Hall, E., 1951, The deformation and ageing of mild steel: III discussion of results: Proceedings of the Physical Society.Section B, v. 64, p. 747.

Han, S.M., Bozorg-Grayeli, T., Groves, J.R., and Nix, W.D., 2010, Size effects on strength and plasticity of vanadium nanopillars: Scripta Materialia, v. 63, no. 12, p. 1153-1156.

Han, C., Gao, H., Huang, Y., and Nix, W.D., 2005a, Mechanism-based strain gradient crystal-plasticity—I. Theory: Journal of the Mechanics and Physics of Solids, v. 53, no. 5, p. 1188-1203.

Han, C., Gao, H., Huang, Y., and Nix, W.D., 2005b, Mechanism-based strain gradient crystal-plasticity—II. Analysis: Journal of the Mechanics and Physics of Solids, v. 53, no. 5, p. 1204-1222.

Harren, S.V., and Asaro, R.J., 1989, Nonuniform deformations in polycrystals and aspects of the validity of the Taylor model: Journal of the Mechanics and Physics of Solids, v. 37, no. 2, p. 191-232.

Harsono, E., Swaddiwudhipong, S., and Liu, Z., 2009, Material characterization based on simulated spherical-Berkovich indentation tests: Scripta Materialia, v. 60, no. 11, p. 972-975.

Harsono, E., Swaddiwudhipong, S., and Liu, Z., 2008, The effect of friction on indentation test results: Modelling and Simulation in Materials Science and Engineering, v. 16, p. 065001.

Havner, K., and Shalaby, A., 1978, Further investigation of a new hardening law in crystal-plasticity: Journal of Applied Mechanics, v. 45, p. 500.

Hengsberger, S., Enstroem, J., Peyrin, F., and Zysset, P., 2003, How is the indentation modulus of bone tissue related to its macroscopic elastic response? A validation study: Journal of Biomechanics, v. 36, no. 10, p. 1503-1509.

Herring, C., and Galt, J., 1952, Elastic and plastic properties of very small metal specimens: Physical Review, v. 85, no. 6, p. 1060.

Hill, R., 1967, The essential structure of constitutive laws for metal composites and polycrystals: Journal of the Mechanics and Physics of Solids, v. 15, no. 2, p. 79-95.

Hill, R., 1966, Generalized constitutive relations for incremental deformation of metal crystals by multislip: Journal of the Mechanics and Physics of Solids, v. 14, no. 2, p. 95-102.

Hill, R., , The mathematical theory of plasticity, 1950, 328.

Hill, R., and Rice, J., 1972, Constitutive analysis of elastic-plastic crystals at arbitrary strain: Journal of the Mechanics and Physics of Solids, v. 20, no. 6, p. 401-413.

Holzapfel, G.A., 2000, Nonlinear solid mechanics: a continuum approach for engineering.

Horstemeyer, M., Baskes, M., and Plimpton, S., 2001a, Length scale and time scale effects on the plastic flow of fcc metals: Acta Materialia, v. 49, no. 20, p. 4363-4374.

Horstemeyer, M.F., Baskes, M.I., and Plimpton, S.J., 2001b, Computational nanoscale plasticity simulations using embedded atom potentials: Theoretical and Applied Fracture Mechanics, v. 37, no. 1–3, p. 49-98.

Huang, W., Su, J., Hong, M., and Yang, B., 2005, Pile-up and sink-in in micro-indentation of a NiTi shape-memory alloy: Scripta Materialia, v. 53, no. 9, p. 1055-1057.

Huang, Y., 1991, A user-material subroutine incorporating single-crystal-plasticity in the ABAQUS finite-element program: Mech Report, v. 178.

Huang, Y., Gao, H., Nix, W., and Hutchinson, J., 2000, Mechanism-based strain gradient plasticity--II. Analysis: Journal of the Mechanics and Physics of Solids, v. 48, no. 1, p. 99-128.

Huang, Y., Qu, S., Hwang, K., Li, M., and Gao, H., 2004, A conventional theory of mechanism-based strain gradient plasticity: International Journal of Plasticity, v. 20, no. 4, p. 753-782.

Huang, Y., Xue, Z., Gao, H., Nix, W., and Xia, Z., 2000, A study of microindentation hardness tests by mechanism-based strain gradient plasticity: Journal of Materials Research-Pittsburgh-, v. 15, no. 8, p. 1786-1796.

Huber, N., Nix, W., and Gao, H., 2002, Identification of elastic-plastic material parameters from pyramidal indentation of thin films: Proceedings of the Royal Society of London.Series A: Mathematical, Physical and Engineering Sciences, v. 458, no. 2023, p. 1593-1620.

Huebner, K., Dewhirst, D., Smith, D., and Byrom, T., , The finite-element method for engineers. 2001.

Hurtado, D.E., and Ortiz, M., 2012, Surface effects and the size-dependent hardening and strengthening of nickel micro-pillars: Journal of the Mechanics and Physics of Solids, v. 60, no. 8, p. 1432-1446.

Hutchinson, J., 1976, Bounds and self-consistent estimates for creep of polycrystalline materials: Proceedings of the Royal Society of London.A.Mathematical and Physical Sciences, v. 348, no. 1652, p. 101-127.

Hutchungs, I., 2009, The contributions of David Tabor to the science of indentation hardness: Journal of Materials Research, v. 24, no. 3, p. 581-589.

Huwaldt, J., 2005: Plotdigitizer.

Ito, K. and Vitek, V., 2001, Atomistic study of non-Schmid effects in the plastic yielding of bcc metals: Philosophical Magazine, v. 81, no. 5, p. 187-1407.

Jacobsen, A.J., Barvosa-Carter, W., and Nutt, S., 2007, Compression behavior of micro-scale truss structures formed from self-propagating polymer waveguides: Acta Materialia, v. 55, no. 20, p. 6724-6733.

Jardret, V., Lucas, B., Oliver, W., and Ramamurthy, A., 2000, Scratch durability of automotive clear coatings: A quantitative, reliable and robust methodology: Journal of Coatings Technology, v. 72, no. 907, p. 79-88.

Jennings, A.T., Burek, M.J., and Greer, J.R., 2010a, Microstructure versus size: Mechanical properties of electroplated single-crystalline Cu nanopillars: Physical Review Letters, v. 104, no. 13, p. 135503.

Jennings, A.T., and Greer, J.R., 2010, Tensile deformation of FIB-less single-crystalline copper pillars: Philosophical Magazine, v. 91.

Jérusalem, A., Fernández, A., Kunz, A., and Greer, J.R., 2012, Continuum modeling of dislocation starvation and subsequent nucleation in nano-pillar-compressions: Scripta Materialia, v. 66, no. 2, p. 93-96.

Johnson, K., 1974, Contact mechanics, 1985.

Joshi, V.A., 2006, Titanium alloys: an atlas of structures and fracture features, CRC.

Kalidindi, S.R., Bronkhorst, C.A., and Anand, L., 1992, Crystallographic texture evolution in bulk deformation processing of FCC metals: Journal of the Mechanics and Physics of Solids, v. 40, no. 3, p. 537-569.

Ke, M., Hackney, S., Milligan, W., and Aifantis, E., 1995, Observation and measurement of grain rotation and plastic strain in nanostructured metal thin films: Nanostructured materials, v. 5, no. 6, p. 689-697.

Kese, K., Li, Z., and Bergman, B., 2005, Method to account for true contact area in soda-lime glass during nanoindentation with the Berkovich tip: Materials Science and Engineering: A, v. 404, no. 1, p. 1-8.

Kiener, D., Grosinger, W., and Dehm, G., 2009 (a), On the importance of sample compliance in uniaxial microtesting: Scripta Materialia, v. 60, no. 3, p. 148-151.

Kiener, D., Motz, C., and Dehm, G., 2009 (b), Micro-compression testing: A critical discussion of experimental constraints: Materials Science and Engineering A, v. 505, p. 79-87.

Kiener, D., Motz, C., Rester, M., Jenko, M., and Dehm, G., 2007, FIB damage of Cu and possible consequences for miniaturized mechanical tests: Materials Science and Engineering: A, v. 459, no. 1, p. 262-272.

Kim, J.Y., and Greer, J.R., 2009, Tensile and compressive behavior of gold and molybdenum single-crystals at the nano scale: Acta Materialia, v. 57, no. 17, p. 5245-5253.

Kim, J., Jang, D., and Greer, J.R., 2010, Tensile and compressive behavior of tungsten, molybdenum, tantalum and niobium at the nanoscale: Acta Materialia, v. 58, no. 7, p. 2355-2363.

Kröner, E., 1962, Dislocations and continuum mechanics: Appl.Mech.Rev, v. 15, no. 8, p. 599-606.

Kunz, A., Pathak, S., and Greer, J.R., 2011, Size effects in Al nanopillars: Single-crystalline vs. bicrystalline: Acta Materialia, v. 59, no. 11, p. 4416-4424.

Kysar, J., 1997, Addendum to ‘A user-material subroutine incorporating single-crystal-plasticity in the ABAQUS finite-element program: Mech report 178:

Division of Engineering and Applied Sciences, Harvard University, Cambridge, MA.

Ledbetter, H., Ogi, H., Kai, S., Kim, S., and Hirao, M., 2004, Elastic constants of body-centered-cubic titanium monocrystals: Journal of Applied Physics, v. 95, p. 4642.

Lee, G., Kim, J.Y., Budiman, A.S., *et al*., 2010, Fabrication, structure and mechanical properties of indium nanopillars: Acta Materialia, v. 58, no. 4, p. 1361-1368.

Lee, G., Kim, J.Y., Burek, M.J., Greer, J.R., and Tsui, T.Y., 2011, Plastic deformation of indium nanostructures: Materials Science and Engineering: A.

Lee, W., and Chen, Y., 2010, Simulation of micro-indentation hardness of FCC single-crystals by mechanism-based strain gradient crystal-plasticity: International Journal of Plasticity, v. 26, no. 10, p. 1527-1540.

Lewis, A.C., Siddiq, M.Q., and Geltmacher, A.B., 2010, Slip systems and initiation of Plasticity in a body-centered cubic Titanium Alloy: Metallurgical and materials transactions A, v. 41A, p. 2522-2531.

Li, X., and Bhushan, B., 2001, Micro/nanomechanical and tribological studies of bulk and thin-film materials used in magnetic recording heads: Thin Solid Films, v. 398, p. 313-319.

Liang, H., and Dunne, F.P.E., 2009, GND accumulation in bi-crystal deformation: Crystal plasticity analysis and comparison with experiments, v. 51, p. 326-333.

Lilleodden, E., 2010, Microcompression study of Mg (0 0 0 1) single-crystal: Scripta Materialia, v. 62, no. 8, p. 532-535.

Lilleodden, E.T., 2002, Indentation-induced plasticity of thin metal films.

Lim, Y.Y., and Chaudhri, M.M., 1999, The effect of the indenter load on the nanohardness of ductile metals: an experimental study on polycrystalline work-

hardened and annealed oxygen-free copper: Philosophical Magazine A, v. 79, no. 12, p. 2979-3000.

Liu, Y., Varghese, S., Ma, J., Yoshino, M., Lu, H., and Komanduri, R., 2008, Orientation effects in nanoindentation of single-crystal copper: International Journal of Plasticity, v. 24, no. 11, p. 1990-2015.

Liu, Y., Wang, B., Yoshino, M., Roy, S., Lu, H., and Komanduri, R., 2005, Combined numerical simulation and nanoindentation for determining mechanical properties of single-crystal copper at mesoscale: Journal of the Mechanics and Physics of Solids, v. 53, no. 12, p. 2718-2741.

Liu, Z., and Scanlon, M.G., 2003, Modelling indentation of bread crumb by finite-element analysis: Biosystems Engineering, v. 85, no. 4, p. 477-484.

Liu, Z., Harsono, E., and Swaddiwudhipong, S., 2009, Material characterization based on instrumented and simulated indentation tests: Int.J.Appl.Mech, v. 1, p. 61-84.

Louchet, F., Weiss, J., and Richeton, T., 2006, Hall-Petch law revisited in terms of collective dislocation dynamics: Physical Review Letters, v. 97, no. 7, p. 75504.

Lütjering, G., and Williams, J.C., 2007, Titanium, Springer Verlag.

Ma, Q., and Clarke, D.R., 1995, Size dependent hardness of silver single-crystals: Journal of Materials Research, v. 10, no. 04, p. 853-863.

MaaB, R., Van Petegem, S., Grolimund, D., Van Swygenhoven, H., Kiener, D., and Dehm, G., 2008, Crystal rotation in Cu single-crystal micro-pillars: In situ Laue and electron backscatter diffraction: Applied Physics Letters, v. 92, no. 7, p. 071905-071905-3.

Maass, R., Van Petegem, S., Borca, C., and Van Swygenhoven, H., 2009, In situ Laue diffraction of metallic micro-pillars: Materials Science and Engineering: A, v. 524, no. 1, p. 40-45.

Maass, R., Van Petegem, S., Van Swygenhoven, H., Derlet, P.M., Volkert, C.A., and Grolimund, D., 2007, Time-resolved Laue diffraction of deforming micro-pillars: Physical Review Letters, v. 99, no. 14, p. 145505.

Maass, R., Van Petegem, S., Zimmermann, J., Borca, C., and Van Swygenhoven, H., 2008, On the initial microstructure of metallic micro-pillars: Scripta Materialia, v. 59, no. 4, p. 471-474.

Maaβ, R., Grolimund, D., Van Petegem, S., *et al*., 2006, Defect structure in micro-pillars using x-ray microdiffraction: Applied Physics Letters, v. 89, p. 151905.

Mandel, J., 1965, Généralisation de la théorie de plasticité de WT Koiter: International Journal of Solids and Structures, v. 1, no. 3, p. 273-295.

Maneiro, M., and Rodríguez, J., 2005, Pile-up effect on nanoindentation tests with spherical–conical tips: Scripta Materialia, v. 52, no. 7, p. 593-598.

Manonukul, A., Dunne, F.P.E., 2004, High and low-cycle fatigue crack initiation using polycrystal plasticity: Proceeding of The Royal Society London A, v. 460, no. 2047, p. 1881-1903.

Mara, N., Bhattacharyya, D., Hoagland, R., and Misra, A., 2008, Tensile behavior of 40 nm Cu/Nb nanoscale multilayers: Scripta Materialia, v. 58, no. 10, p. 874-877.

Mata, M., and Alcala, J., 2004, The role of friction on sharp indentation: Journal of the Mechanics and Physics of Solids, v. 52, no. 1, p. 145-165.

Mata, M., Anglada, M., and Alcalá, J., 2002a, Contact deformation regimes around sharp indentations and the concept of the characteristic strain: Journal of Materials Research, v. 17, no. 05, p. 964-976.

Mata, M., Anglada, M., and Alcalá, J., 2002b, A hardness equation for sharp indentation of elastic-power-law strain-hardening materials: Philosophical Magazine A, v. 82, no. 10, p. 1831-1839.

McElhaney, K., Vlassak, J., and Nix, W., 1998, Determination of indenter tip geometry and indentation contact area for depth-sensing indentation experiments: Journal of Materials Research, v. 13, no. 05, p. 1300-1306.

Menzel, A., and Steinmann, P., 2000, On the continuum formulation of higher gradient plasticity for single and polycrystals: Journal of the Mechanics and Physics of Solids, v. 48, no. 8, p. 1777.

Meyers, M.A., Mishra, A., and Benson, D.J., 2006, Mechanical properties of nanocrystalline materials: Progress in Materials Science, v. 51, no. 4, p. 427-556.

Muhlhaus, H.B., and Alfantis, E., 1991, A variational principle for gradient plasticity: International Journal of Solids and Structures, v. 28, no. 7, p. 845-857.

Nakada, Y., and Keh, A., 1966, Latent hardening in iron single-crystals: Acta Metallurgica, v. 14, no. 8, p. 961-973.

Narutani, T., and Takamura, J., 1991, Grain-size strengthening in terms of dislocation density measured by resistivity: Acta metallurgica et materialia, v. 39, no. 8, p. 2037-2049.

Ng, K., and Ngan, A., 2009, Deformation of micron-sized aluminium bi-crystal pillars: Philosophical Magazine, v. 89, no. 33, p. 3013-3026.

Ng, K., and Ngan, A., 2008, Breakdown of Schmid's law in micro-pillars: Scripta Materialia, v. 59, no. 7, p. 796-799.

Nix, W.D., 1998, Yielding and strain-hardening of thin metal films on substrates: Scripta Materialia, v. 39, no. 4, p. 545-554.

Nix, W.D., 1989, Mechanical properties of thin films: Metallurgical and Materials Transactions A, v. 20, no. 11, p. 2217-2245.

Nix, W.D., and Gao, H., 1998, Indentation size effects in crystalline materials: a law for strain gradient plasticity: Journal of the Mechanics and Physics of Solids, v. 46, no. 3, p. 411-425.

Nix, W., Gibeling, J., and Hughes, D., 1985, Time-dependent deformation of metals: Metallurgical and Materials Transactions A, v. 16, no. 12, p. 2215-2226.

Nix, W.D., and Gao, H., 1998, Indentation size effects in crystalline materials: A law for strain gradient plasticity: Journal of the Mechanics and Physics of Solids, v. 46, no. 3, p. 411-425.

Norfleet, D.M., Dimiduk, D.M., Polasik, S.J., Uchic, M.D. and Mills, M.J., 2008, Dislocation structures and their relationship to strength in deformed nickel microcrystals: Acta Materialia, v. 56, p. 2988-3001.

Nowag, K., Ghisleni, R., Michler J., 2012, Effect of crystal orientation on slip-band formation and deformation of a bcc titanium alloy : Acta Materialia (to be submitted).

Ogden, R.W., 1997, Non-linear elastic deformations, Dover Pubns.

Oka, F., Yashima, A., Sawada, K., and Aifantis, E., 2000, Instability of gradient-dependent elastoviscoplastic model for clay and strain localization analysis: Computer Methods in Applied Mechanics and Engineering, v. 183, no. 1, p. 67-86.

Oliver, W.C., and Pharr, G.M., 1992, Improved technique for determining hardness and elastic modulus using load and displacement sensing indentation experiments: Journal of Materials Research, v. 7, no. 6, p. 1564-1583.

Oyen, M.L., and Cook, R.F., 2003, Load–displacement behavior during sharp indentation of viscous–elastic–plastic materials: Journal of Materials Research, v. 18, no. 01, p. 139-150.

Parthasarathy, T.A., Rao, S.I., Dimiduk, D.M., Uchic, M.D., and Trinkle, D.R., 2007, Contribution to size effect of yield strength from the stochastics of dislocation source lengths in finite samples: Scripta Materialia, v. 56, no. 4, p. 313-316.

Peirce, D., Shih, C.F., and Needleman, A., 1984, A tangent modulus method for rate dependent solids: Computers & Structures, v. 18, no. 5, p. 875-887.

Peirce, D., Asaro, R.J., and Needleman, A., 1982, An analysis of nonuniform and localized deformation in ductile single-crystals: Acta Metallurgica, v. 30, no. 6, p. 1087-1119.

Petch, N., 1953, The cleavage strength of polycrystals: J.Iron Steel Inst, v. 174, no. 1, p. 25-28.

Pethicai, J., Hutchings, R., and Oliver, W., 1983, Hardness measurement at penetration depths as small as 20 nm: Philosophical Magazine A, v. 48, no. 4, p. 593-606.

Pharr, G., 1998, Measurement of mechanical properties by ultra-low load indentation: Materials Science and Engineering: A, v. 253, no. 1, p. 151-159.

Pharr, G., Oliver, W.C., and Brotzen, F., 1992, On the generality of the relationship among contact stiffness, contact area, and elastic modulus during indentation: Journal of Materials Research, v. 7, no. 3, p. 613-617.

Poon, B., Rittel, D., and Ravichandran, G., 2008, An analysis of nanoindentation in elasto-plastic solids: International Journal of Solids and Structures, v. 45, no. 25-26, p. 6399-6415.

Prakash, A., 2009, Computational micromechanics of polycrystals: Special emphasis on twinning and recrystallization in Mg alloys and TWIP steels, Shaker.

Qu, S., Huang, Y., Pharr, G., and Hwang, K., 2006, The indentation size effect in the spherical indentation of iridium: A study via the conventional theory of mechanism-based strain gradient plasticity: International Journal of Plasticity, v. 22, no. 7, p. 1265-1286.

Rabe, R., Breguet, J.-M., Schwaller, P., Stauss, S., Haug, F.-J., Patscheider, J., and Michler, J., 2004, Observation of fracture and plastic deformation during indentation and scratching inside the scanning electron microscope: Thin Solid Films, v. 469-470, p. 206-213.

Raabe, D., Ma, D., and Roters, F., 2007, Effects of initial orientation, sample geometry and friction on anisotropy and crystallographic orientation changes in single-crystal microcompression deformation: A crystal-plasticity finite-element study: Acta Materialia, v. 55, no. 13, p. 4567-4583.

Rabkin, E., Nam, H.S., and Srolovitz, D., 2007, Atomistic simulation of the deformation of gold nanopillars: Acta materialia, v. 55, no. 6, p. 2085-2099.

Randall, N., and Consiglio, R., 2000, Nanoscratch tester for thin film mechanical properties characterization: Review of Scientific Instruments, v. 71, p. 2796.

Rao, S.I., Dimiduk, D., Parthasarathy, T.A., Uchic, M., Tang, M., and Woodward, C., 2008, Athermal mechanisms of size-dependent crystal flow gleaned from three-dimensional discrete-dislocation simulations: Acta Materialia, v. 56, no. 13, p. 3245-3259.

Rao, S.S., 1999, The finite-element method in Engineering: Butterworth-Heinemann.

Regueiro, R.A., Bammann, D.J., Marin, E.B., and Garikipati, K., 2002, A nonlocal phenomenological anisotropic finite deformation plasticity model accounting for dislocation defects: Journal of engineering materials and technology, v. 124, p. 380.

Rice, J.R., 1971, Inelastic constitutive relations for solids: an internal-variable theory and its application to metal plasticity: Journal of the Mechanics and Physics of Solids, v. 19, no. 6, p. 433-455.

Rice, J.R., 1970, On the structure of stress-strain relations for time-dependent plastic deformation in metals: Journal of applied mechanics, v. 37, p. 728.

Saha, R., and Nix, W.D., 2002, Effects of the substrate on the determination of thin film mechanical properties by nanoindentation: Acta Materialia, v. 50, no. 1, p. 23-38.

Sakharova, N., Fernandes, J., Antunes, J., and Oliveira, M., 2009, Comparison between Berkovich, Vickers and conical indentation tests: A three-dimensional

numerical simulation study: International Journal of Solids and Structures, v. 46, no. 5, p. 1095-1104.

Schiøtz, J., Vegge, T., Di Tolla, F., and Jacobsen, K.W., 1999, Atomic-scale simulations of the mechanical deformation of nanocrystalline metals: Physical Review B, v. 60, no. 17, p. 11971.

Schulze, D., 1979, P. Paufler, GER Schulze, Physikalische Grundlagen mechanischer Festkörpereigenschaften. Bünde 229 (I) und 238 (II) der wiss. Taschenbücher, Akademie-Verlag, Berlin 1978 143 bzw. 190 Seiten, 50 bzw. 100 Abbildungen, 16 bzw. 19 Tabellen, Preis je Band 8,-M: Kristall und Technik, v. 14, no. 7, p. K42-K42.

Schuster, B.E., Wei, Q., Hufnagel, T.C., and Ramesh, K.T., 2008, Size-independent strength and deformation mode in compression of a Pd-based metallic glass: Acta Materialia, v. 56, no. 18, p. 5091-5100.

Shade, P.A., Wheeler, R., Choi, Y.S., Uchic, M.D., Dimiduk, D.M., and Fraser, H.L., 2009, A combined experimental and simulation study to examine lateral constraint effects on microcompression of single-slip oriented single-crystals: Acta Materialia, v. 57, no. 15, p. 4580-4587.

Shan, Z., Li, J., Cheng, Y., Minor, A., Asif, S.A.S., Warren, O., and Ma, E., 2008, Plastic flow and failure resistance of metallic glass: Insight from in situ compression of nanopillars: Physical Review B, v. 77, no. 15, p. 155419.

Shan, Z., Mishra, R., Asif, S.A.S., Warren, O., and Minor, A., 2008, Nature Materials, v. 7, no. 2, p. 115-119.

Shizawa, K., and Zbib, H., 1999, A thermodynamical theory of gradient elastoplasticity with dislocation density tensor. I: Fundamentals: International Journal of Plasticity, v. 15, no. 9, p. 899-938.

Shu, J.Y., and Fleck, N.A., 1999, Strain gradient crystal-plasticity: size-dependentdeformation of bicrystals: Journal of the Mechanics and Physics of Solids, v. 47, no. 2, p. 297-324.

Siddiq, M.A., 2006, Modelling of crystal-plasticity effects in the fracture of a metal/ceramic interface - bridging the length scales: PhD thesis, Stuttgart University - Mechanical Engineering.

Siddiq, A., Schmauder, S., and Huang, Y., 2007, Fracture of bicrystal metal/ceramic interfaces: A study via the mechanism-based strain gradient crystal-plasticity theory: International Journal of Plasticity, v. 23, no. 4, p. 665-689.

Siemers, C., 2010, Milestone Ti-1: Chip formation of Titanium Alloy: MAMINA internal report.

Simo, J., and Hughes, T.J.R., 1998, Computational Inelasticity, volume 7 of Interdisciplinary Applied Mathematics.

Smith, G., Tadmor, E., Bernstein, N., and Kaxiras, E., 2001, Multiscale simulations of silicon nanoindentation: Acta materialia, v. 49, no. 19, p. 4089-4101.

Smith, R., Christopher, D., Kenny, S., Richter, A., and Wolf, B., 2003, Defect generation and pileup of atoms during nanoindentation of Fe single-crystals: Physical Review B, v. 67, no. 24, p. 245405.

Smyshlyaev, V., and Fleck, N., 1996, The role of strain gradients in the grain size effect for polycrystals: Journal of the Mechanics and Physics of Solids, v. 44, no. 4, p. 465-495.

Sneddon, I.N., 1965, The relation between load and penetration in the axisymmetric Boussinesq problem for a punch of arbitrary profile: International Journal of Engineering Science, v. 3, no. 1, p. 47-57.

Spear, K.E., 1989, Diamond—ceramic coating of the future: Journal of the American Ceramic Society, v. 72, no. 2, p. 171-191.

Stelmashenko, N., Walls, M., Brown, L., and Milman, Y.V., 1993, Microindentations on W and Mo oriented single-crystals: an STM study: Acta Metallurgica et Materialia, v. 41, no. 10, p. 2855-2865.

Stölken, J., and Evans, A., 1998, A microbend test method for measuring the plasticity length scale: Acta Materialia, v. 46, no. 14, p. 5109-5115.

Sun, Q., Guo, Q., Yao, X., Xiao, L., Greer, J.R., and Sun, J., 2011, Size effects in strength and plasticity of single-crystalline titanium micro-pillars with prismatic slip orientation: Scripta Materialia, v. 65, no. 6, p. 473-476.

Suzuki, H., Ikeda, S., and Takeuchi, S., 1956, Deformation of thin copper crystals: Journal of the Physical Society of Japan, v. 11, no. 4, p. 382-393.

Swadener, J., George, E., and Pharr, G., 2002, The correlation of the indentation size effect measured with indenters of various shapes: Journal of the Mechanics and Physics of Solids, v. 50, no. 4, p. 681-694.

Systemes, D., 2010, Abaqus 6. 10 Analysis User Manual.

Tabor, D., 1951, The hardness of metals, Oxford University Press.

Takeuchi, S., 2001, The mechanism of the inverse Hall-Petch relation of nanocrystals: Scripta Materialia, v. 44, no. 8-9, p. 1483-1488.

Taljat, B., and Pharr, G., 2004, Development of pile-up during spherical indentation of elastic–plastic solids: International Journal of Solids and Structures, v. 41, no. 14, p. 3891-3904.

Tang, H., Schwarz, K., and Espinosa, H., 2007, Dislocation escape-related size effects in single-crystal micro-pillars under uniaxial compression: Acta materialia, v. 55, no. 5, p. 1607-1616.

Taylor, S.G.I. and Elam, C.F. 1926, The distortion of iron crystals: Proceedings of the Royal Society of London Series A, v.112, no.761, p.337-361.

Taylor, S.G.I., 1938, Plastic strain in metals.

Tegner, B.E., Zhu, L., and Ackland, G.J., 2012, Relative strength of phase stabilizers in titanium alloys: Physical Review B, v. 85, no. 21, p. 214106.

Telford, M., 2004, The case for bulk metallic glass: Materials today, v. 7, no. 3, p. 36-43.

Tsagrakis, I., and Aifantis, E.C., 2002, Recent developments in gradient plasticity—Part I: formulation and size effects: Journal of engineering materials and technology, v. 124, p. 352.

Tymiak, N., Kramer, D., Bahr, D., Wyrobek, T., and Gerberich, W., 2001, Plastic strain and strain gradients at very small indentation depths: Acta Materialia, v. 49, no. 6, p. 1021-1034.

Uchic, M.D., and Dimiduk, D.M., 2005, A methodology to investigate size scale effects in crystalline plasticity using uniaxial compression testing: Materials Science and Engineering: A, v. 400, p. 268-278.

Uchic, M.D., Dimiduk, D.M., Florando, J.N., and Nix, W.D., 2004, Sample dimensions influence strength and crystal-plasticity: Science, v. 305, no. 5686, p. 986-989.

Uchic, M.D., Shade, P.A., and Dimiduk, D.M., 2009, Plasticity of micrometer-scale single-crystals in compression: Annual Review of Materials Research, v. 39, p. 361-386.

Van Swygenhoven, H., and Derlet, P., 2001, Grain-boundary sliding in nanocrystalline fcc metals: Physical review B, v. 64, no. 22, p. 224105.

Van Swygenhoven, H., Derlet, P., and Hasnaoui, A., 2002, Atomic mechanism for dislocation emission from nanosized grain boundaries: Physical Review B, v. 66, no. 2, p. 024101.

VanLandingham, M.R., 2003: Review of instrumented indentation.

VanLandingham, M.R., Villarrubia, J.S., Guthrie, W.F., and Meyers, G.F., 2001, Nanoindentation of polymers: an overview, *in* Macromolecular symposia, p. 15-44.

Varshni, Y., 1970, Temperature dependence of the elastic constants: Physical Review B, v. 2, no. 10, p. 3952-3958.

Vitek, V., Perrin, R. and Bowen, D.K., 1970, Philosophical Magazine A, v. 21, p. 1049.

Voyiadjis, G.Z., Al-Rub, R.K.A., and Palazotto, A.N., 2003, Non-local coupling of viscoplasticity and anisotropic viscodamage for impact problems using the gradient theory: Archives of Mechanics, v. 55, no. 1, p. 40-90.

Voyiadjis, G.Z., Deliktas, B., and Aifantis, E.C., 2001, Multiscale analysis of multiple damage mechanisms coupled with inelastic behavior of composite materials: Journal of Engineering Mechanics, v. 127, p. 636.

Wang, W., Askes, H., and Sluys, L., 1998, Gradient viscoplastic modelling of material instabilities in metals: Metals and Materials International, v. 4, no. 3, p. 537-542.

Wang, Y., Raabe, D., Klüber, C., and Roters, F., 2004, Orientation dependence of nanoindentation pile-up patterns and of nanoindentation microtextures in copper single-crystals: Acta materialia, v. 52, no. 8, p. 2229-2238.

Weinberger, C.R., and Cai, W., 2008, Surface-controlled dislocation multiplication in metal micro-pillars: Proceedings of the National Academy of Sciences, v. 105, no. 38, p. 14304.

Wk, 2008, http://en.wikipedia.org/wiki/File:Vector_de_Burgers.PNG.

William, F.S., and Javad, H., 2004, Foundations of materials science and engineering.

Wu, T.Y., Bassani, J.L., and Laird, C., 1991, Latent hardening in single-crystals I. Theory and experiments: Proceedings of the Royal Society of London.Series A: Mathematical and Physical Sciences, v. 435, no. 1893, p. 1-19.

Xue, Z., Huang, Y., Hwang, K., and Li, M., 2002, The influence of indenter tip radius on the micro-indentation hardness: Journal of engineering materials and technology, v. 124, p. 371.

Yamakov, V., Wolf, D., Phillpot, S.R., Mukherjee, A.K., and Gleiter, H., 2002, Dislocation processes in the deformation of nanocrystalline aluminium by molecular-dynamics simulation: Nature Materials, v. 1, no. 1, p. 45-49.

Yefimov, S., Groma, I., and Van der Giessen, E., 2004, A comparison of a statistical-mechanics based plasticity model with discrete-dislocation plasticity calculations: Journal of the Mechanics and Physics of Solids, v. 52, no. 2, p. 279-300.

Yin, Z., Tao, S., Zhou, X., and Ding, C., 2007, Evaluating microhardness of plasma sprayed Al2O3 coatings using Vickers indentation technique: Journal of Physics D: Applied Physics, v. 40, p. 7090.

Yoshioka, N., and Yoshioka, M., 1995, Dynamic observation of indentation process: Geophysical Research Letters, v. 22, no. 2, p. 113-116.

Yuan, H., and Chen, J., 2001, Identification of the intrinsic material length in gradient plasticity theory from micro-indentation tests: International Journal of Solids and Structures, v. 38, no. 46, p. 8171-8187.

Zaafarani, N., Raabe, D., Singh, R., Roters, F., and Zaefferer, S., 2006, Three-dimensional investigation of the texture and microstructure below a nanoindent in a Cu single-crystal using 3D EBSD and crystal-plasticity finite-element simulations: Acta materialia, v. 54, no. 7, p. 1863-1876.

Zahedi, A., Demiral, M., Roy, A., Babitsky, V.I., and Silberschmidt, V.V., 2012, Indentation in FCC Single-crystals: Solid State Phenomena, v. 188, p. 219-225.

Zhang, X., and Aifantis, K., 2011, Interpreting strain bursts and size effects in micro-pillars using gradient plasticity: Materials Science and Engineering: A.

Zhang, H., Schuster, B.E., Wei, Q., and Ramesh, K.T., 2006, The design of accurate micro-compression experiments: Scripta Materialia, v. 54, no. 2, p. 181-186.

Zhang, X., and Aifantis, K.E., 2011, Interpreting strain bursts and size effects in micro-pillars using gradient plasticity: Materials Science and Engineering: A, v. 528, no. 15, p. 5036-5043.

Zhu, T., Bushby, A., and Dunstan, D., 2008, Materials mechanical size effects: a review: Materials Technology: Advanced Performance Materials, v. 23, no. 4, p. 193-209.